

NAVAL POSTGRADUATE SCHOOL

Monterey, California



DISSERTATION

GRAIN BOUNDARY DEVELOPMENT IN SUPERPLASTIC ALUMINUM ALLOYS

by

Michael Edward McMahon

December 1996

Thesis Advisor:

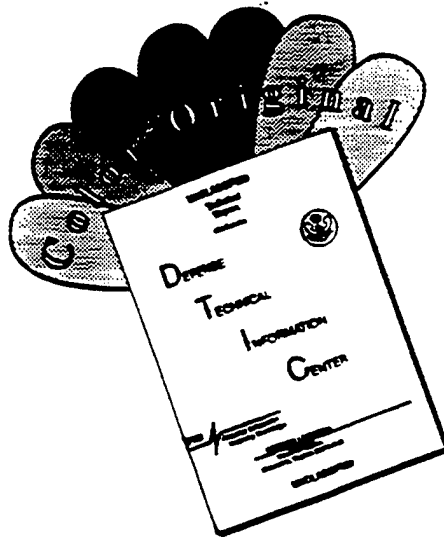
T.R. McNelley

Approved for public release; distribution is unlimited.

19970520 057

DTIC QUALITY INSPECTED 4

DISCLAIMER NOTICE



THIS DOCUMENT IS BEST QUALITY AVAILABLE. THE COPY FURNISHED TO DTIC CONTAINED A SIGNIFICANT NUMBER OF COLOR PAGES WHICH DO NOT REPRODUCE LEGIBLY ON BLACK AND WHITE MICROFICHE.

REPORT DOCUMENTATION PAGE			Form Approved OMB No. 0704-0188	
Public reporting burden for this collection of information is estimated to average 1 hour per response, including the time for reviewing instructions, searching existing data sources, gathering and maintaining the data needed, and completing and reviewing the collection of information. Send comments regarding this burden estimate or any other aspect of this collection of information, including suggestions for reducing this burden, to Washington Headquarters Services, Directorate for Information Operations and Reports, 1215 Jefferson Davis Highway, Suite 1204, Arlington, VA 22202-4302, and to the Office of Management and Budget, Paperwork Reduction Project (0704-0188), Washington, DC 20503.				
1. AGENCY USE ONLY (Leave blank)	2. REPORT DATE December 1996	3. REPORT TYPE AND DATES COVERED Doctoral Dissertation		
4. TITLE AND SUBTITLE Grain Boundary Development in Superplastic Aluminum Alloys		5. FUNDING NUMBERS		
6. AUTHOR(S) McMahon, Michael E.				
7. PERFORMING ORGANIZATION NAME(S) AND ADDRESS(ES) Naval Postgraduate School Monterey, California 93943-5000		8. PERFORMING ORGANIZATION REPORT NUMBER		
9. SPONSORING / MONITORING AGENCY NAME(S) AND ADDRESS(ES)		10. SPONSORING / MONITORING AGENCY REPORT NUMBER		
11. SUPPLEMENTARY NOTES The views expressed in this dissertation are those of the author and do not reflect the official policy or position of the Department of Defense or the U.S. Government.				
12a. DISTRIBUTION / AVAILABILITY STATEMENT Approved for public release; distribution is unlimited.		12b. DISTRIBUTION CODE		
13. ABSTRACT (Maximum 200 words) Recently developed computer-aided electron microscopy diffraction analysis methods have been applied to investigate the role of grain boundaries in a variety of superplastic aluminum alloys. Aluminum alloys 2519, 5083, and 7475 are observed to transform to a refined, superplastically-enabled microstructure by a Gibbs I type of transformation involving discontinuous recrystallization by the formation and migration of high-angle grain boundaries (HAB's). These microstructures consist, predominantly, of disordered, HAB's with characteristically high interfacial energy and mobility. The distribution of grain boundary misorientation follows the random distribution predicted by Mackenzie for randomly-oriented cubes. Such microstructures are observed to exhibit only moderate superplastic performance at relatively high forming temperatures. Following TMP, SUPRAL 2004 and Al-10.0 wt% Mg - 0.1 wt% Zr are observed to follow a Gibbs II, continuous-refinement microstructural transformation resulting in the development of a bi-modal distribution of grain boundary misorientation with peaks centered near 10° and 45° misorientation. The significant fraction of moderately-misoriented ($5^\circ < \theta \leq 15^\circ$) boundaries exceeds the number expected from random processes even given the preferred orientation present and may be attributed to short-range mechanistic processes involving dislocation-boundary and boundary-boundary interactions. The grain boundary distributions in these microstructures are of lower interfacial energy character and mobility. Enhanced grain refinement and increased superplastic flow at higher deformation rates are observed in these later materials.				
14. SUBJECT TERMS Superplastic, Aluminum, Grain Boundary			15. NUMBER OF PAGES 233	
			16. PRICE CODE	
17. SECURITY CLASSIFICATION OF REPORT Unclassified	18. SECURITY CLASSIFICATION OF THIS PAGE Unclassified	19. SECURITY CLASSIFICATION OF ABSTRACT Unclassified	20. LIMITATION OF ABSTRACT UL	

Approved for public release; distribution is unlimited.

GRAIN BOUNDARY DEVELOPMENT IN SUPERPLASTIC ALUMINUM ALLOYS

Michael E. McMahon
Commander, United States Navy
B.S., University of Colorado, 1979
M.S., Naval Postgraduate School, 1986

DOCTOR OF PHILOSOPHY IN MECHANICAL ENGINEERING

from the

NAVAL POSTGRADUATE SCHOOL
December 1996

Author: _____

Michael E. McMahon

Approved by: _____

Alan G. Fox
Professor of
Mechanical Engineering

Van E. Henson
Professor of
Mathematics

Michael E. Kassner
Professor of Mechanical
Engineering, Oregon State Univ.

Young W. Kwon
Professor of
Mechanical Engineering

Gerald H. Lindsey
Professor of Aeronautics
and Astronautics

Terry R. McNelley
Professor of
Mechanical Engineering

Approved by: _____

Terry R. McNelley, Chairman, Department of Mechanical Engineering

Approved by: _____

Maurice D. Weir, Associate Provost for Instruction

TABLE OF CONTENTS

	Page
I. INTRODUCTION.....	1
A. A HISTORICAL REVIEW OF SUPERPLASTICITY.....	1
B. APPLICATIONS OF SUPERPLASTIC TECHNOLOGY.....	5
C. REQUIREMENTS FOR FINE-STRUCTURE SUPERPLASTICITY.....	6
D. DEVELOPMENT OF FINE-GRAINED SUPERPLASTIC ALUMINUM ALLOYS.....	8
E. RELEVANCE OF THIS RESEARCH.....	10
II. THEORETICAL ASPECTS OF SUPERPLASTIC FLOW AND SUPERPLASTICALLY ENABLED MICROSTRUCTURES.....	11
A. OVERVIEW.....	11
B. CONSTITUTIVE EQUATIONS TO DESCRIBE SUPERPLASTIC FLOW.....	12
C. MODELS DESCRIBING SUPERPLASTIC FLOW.....	16
1. The Ball and Hutchison and Related Models.....	16
2. The Ashby and Verrall Model.....	17
D. MICROSTRUCTURAL REFINEMENT.....	18
1. Discontinuous Recrystallization.....	18
2. Continuous Recrystallization.....	21
3. Geometric Dynamic Recrystallization.....	21
E. THE ROLE OF GRAIN BOUNDARIES IN SUPERPLASTICITY.....	22
1. The Coincident Site Lattice Model.....	23
2. Energy Aspects of Special Grain Boundaries.....	26
3. Grain Boundary Mobility.....	29
4. The Influence of Grain Boundary Structure on GBS.....	30

F. APPROACH OF THIS RESEARCH.....	32
III. ELECTRON BACK SCATTER DIFFRACTION (EBSD).....	35
A. OVERVIEW.....	35
B. THE EBSD SYSTEM.....	38
1. System Appartus.....	38
2. Extraction of Data from the EBSP.....	41
3. The Interactive EBSD System at the Naval Postgraduate School.....	47
C. DEVELOPMENT OF METHODOLOGIES FOR STUDIES OF FINE- GRAINED METALS USING EBSP TECHNIQUES.....	50
1. Preparation of Specimens for EBSD Examination.....	52
2. EBSD Examination Procedure.....	53
D. INTERPRETATION AND ANALYSIS OF EBSP DATA.....	58
1. Use of Orientation Information to Analyze Microtexture.....	58
2. Use of Orientation Information to Analyze Mesotexture	66
E. ACCURACY, SOURCES OF ERROR AND LIMITATIONS.....	68
1. Limitations Imposed by the EBSD System	68
2. Limitations and Error Imposed by the User and Examination Methodology.....	69
IV. MICROTEXTURE AND BOUNDARY DEVELOPMENT DURING PROCESSING AND SUPERPLASTIC DEFORMATION OF Al - 10.0wt%Mg - 0.1wt%Zr.....	71
A. INTRODUCTION.....	71
B. EXPERIMENTAL PROCEDURE.....	74
C. RESULTS.....	75
1. Microstructure of Areas Examined.....	75
2. Microtexture.....	77
3. Boundary Character Data.....	82

D. DISCUSSION.....	90
E. OBSERVATIONS FROM THIS STUDY.....	94
V. MICROTTEXTURE AND BOUNDARY EVOLUTION DURING MICROSTRUCTURAL REFINEMENT PROCESSES IN SUPRAL 2004.....	95
A. INTRODUCTION.....	95
B. EXPERIMENTATION.....	97
1. Experimental Procedure.....	97
C. MECHANICAL BEHAVIOR AND MICROSTRUCTURE.....	100
D. MICROTTEXTURE AND MESOTEXTURE.....	102
1. In As-Processed Material.....	102
2. Following Static Annealing.....	105
3. Results from the Isochronol Examination of a Deformed Tensile Specimen.....	106
4. Results from the Cooperative Research.....	112
E. DISCUSSION.....	115
F. CONCLUSIONS.....	118
VI. GRAIN BOUNDARY DEVELOPMENT FOLLOWING PROCESSING, ANNEALING, AND SUPERPLASTIC DEFORMATION OF ALUMINUM ALLOY 2519.....	119
A. INTRODUCTION.....	119
B. THERMOMECHANICAL PROCESSING.....	120
C. EXPERIMENTAL PROCEDURE.....	121
D. MECHANICAL BEHAVIOR AND MICROSTRUCTURE.....	122
E. GRAIN BOUNDARY AND MICROTTEXTURAL DATA.....	127
1. As-Processed Material.....	127
2. Microstructural Development During Static Annealing.....	131

3. Deformed Regions.....	134
F. DISCUSSION.....	136
VII. THE INFLUENCE OF GRAIN BOUNDARY CHARACTER DEVELOPED IN COMMERCIALY PROCESSED, SUPERPLASTIC 5083 ALUMINUM.....	143
A. INTRODUCTION.....	143
B. EXPERIMENTAL PROCEDURE.....	144
C. MECHANICAL BEHAVIOR AND MICROSTRUCTURE.....	145
D. MICROTTEXTURAL AND MESOTEXTURAL RESULTS.....	148
E. DISCUSSION AND OBSERVATIONS.....	155
VIII. GRAIN BOUNDARY DEVELOPMENT FOLLOWING ALTERNATE THERMOMECHANICAL PROCESSING IN COMMERCIAL, SUPERPLASTIC 7475 ALUMINUM.....	159
A. INTRODUCTION.....	159
B. ALLOY CHEMICAL AND MECHANICAL DATA.....	160
C. EXPERIMENTAL PROCEDURE.....	161
D. MICROSTRUCTURE.....	162
E. MICROTTEXTURAL AND MESOTEXTURAL RESULTS.....	165
F. DISCUSSION.....	169
IX. SUMMARY OF RESULTS - THE INFLUENCE OF GRAIN BOUNDARIES IN SUPERPLASTIC ALUMINUM ALLOYS	175
A. ALTERNATE MICROSTRUCTURES FOR SUPERPLASTICITY IN ALUMINUM ALLOYS.....	175
B. GRAIN BOUNDARY EVOLUTION DURING SUPERPLASTIC FLOW.....	185
X. CONCLUSIONS.....	193
LIST OF REFERENCES.....	195

INITIAL DISTRIBUTION LIST.....	205
--------------------------------	-----

LIST OF FIGURES

	Page
Figure 1.1 The number of publications on the topic of superplasticity from 1960-1990.....	3
Figure 1.2 Illustration of some SPF processes and techniques.....	7
Figure 2.1 Data for the diffusion-compensated strain rate versus modulus- compensated flow stress behavior for aluminum and solid-solution strengthened aluminum-magnesium alloys.....	14
Figure 2.2 Schematic representation of the strain rate versus flow stress behavior for superplastic materials.....	15
Figure 2.3 Schematic illustration of the Ball-Hutchison model describing superplastic flow.....	16
Figure 2.4 Schematic illustration of the Ashby-Verall model for superplastic flow involving grain rotation and rearrangement aided by diffusion.....	18
Figure 2.5 Schematic representation of the superlattice construction in the CSL model.....	25
Figure 2.6 Experimental data of boundary interfacial energy based on direct energy measurements in aluminum.....	28
Figure 2.7 Data for grain boundary sliding rates as a function of boundary character.....	31
Figure 3.1 Schematic diagram illustrating the formation of Kikuchi line pairs in reciprocal lattice space.....	37
Figure 3.2 An example of a back-scatter electron diffraction pattern.....	39
Figure 3.3 Schematic representation of the basic components of an EBSD system.....	40

Figure 3.4 Schematic diagram illustrating the specimen position with respect to the incident beam and the diffraction pattern	41
Figure 3.5 Initial calibration specimen arrangement in the SEM.....	43
Figure 3.6 Geometrical aspects of the Kikuchi bands in the EBSP for (a) interplanar spacing between two bands and (b) interplanar spacing for the crystallographic plane associated with the specific band.....	46
Figure 3.7 EBSP images illustrating the sequence in the identification of Kikuchi bands leading to orientation determination; (a) as-captured, (b) identification of the seven bands of highest intensity, and (c) indexed.....	48
Figure 3.8 The EBSD system in place at the Naval Postgraduate School.....	50
Figure 3.9 Schematic diagrams detailing the alignment of specimen axes for a sectioned tensile specimen. Here, a 90 degree rotation about the rolling direction is required to enable the rolling and normal directions to be in the plane formed by the camera axis and the incident electron beam.....	54
Figure 3.10 A BSE micrograph with a typical data collection pattern superimposed. As-captured and indexed diffraction patterns from two neighbor orientations (a) and (b) are shown.....	56
Figure 3.11 Regions examined using EBSP methods.....	57
Figure 3.12 Excerpt from an EBSD data file.....	60
Figure 3.13 Illustration of the construction of a pole figure.....	62
Figure 3.14 Calculation of the three Euler angles.....	63
Figure 3.15 The $\varphi_2 = 0^\circ$ section of an Euler plot.....	64
Figure 3.16 The Euler plot in three-dimensional format with texture fibers shown.....	65
Figure 3.17 The variation of spatial resolution (μm) for EBSD in aluminum	

(a) with accelerating voltage and (b) with working distance at standard SEM working conditions of 20KV accelerating voltage, 15mm working distance and a specimen tilt of 70°	70
Figure 4.1. Mechanical property data illustrating the variation in mechanical behavior at 300C for the two processing schedules.....	72
Figure 4.2. Schematic diagram detailing the processing routes TMP2 (5 minute inter-pass reheat time) and TMP6 (30 minute inter-pass reheat time)...	75
Figure 4.3. BSE micrographs of the regions of deformed tensile specimens examined in this study; (a) TMP2 grip, (b) TMP6 grip, (c) TMP2 gage, and (d) TMP6 gage. The rolling (tensile) direction is horizontal (orientation contrast at 5KV working voltage, no etchant)...	76
Figure 4.4 The discrete Euler plot, discrete pole figure, and contour pole figure detailing the microtexture in the as-processed TMP2 material.....	78
Figure 4.5 The discrete Euler plot, discrete pole figure, and contour pole figure detailing the microtexture in the as-processed TMP6 material.....	79
Figure 4.6 Microtexture plots for undeformed grip sections (processed and annealed) of (a) TMP 2 and (b) TMP 6 specimens.....	80
Figure 4.7 Microtexture plots for deformed gage sections of (a) TMP 2 and (b) TMP 6 specimens.....	83
Figure 4.8 Misorientation histograms for the specimens examined.....	84
Figure 4.9. Grain Misorientation Texture for boundaries with misorientations between 55-65° for the undeformed grip section of TMP2 material illustrating: (1) the large fraction (.23) of boundaries with misorientations in this range and (2) that many boundaries with misorientations in this range have a rotation axis near the twin (111) axis ($\Sigma 3$, 60°/<111>) although not all satisfying Brandon nearness criteria.....	86

Figure 4.10	Misorientation histograms for undeformed grip sections with the plot for the uncorrelated data shown.....	88
Figure 5.1	Geometry of the tensile specimen utilized in this study.....	99
Figure 5.2	Photograph of an undeformed tensile coupon and the tensile coupon deformed to an elongation of 756%.....	100
Figure 5.3	BSE micrographs of SUPRAL 2004; (a) as-processed, (b) processed and annealed for 30 minutes at $T = 450^{\circ}\text{C}$, (c) deformed to a strain of 0.16, (d) deformed to a strain of 0.70, and (e) deformed to a strain of 1.32. The deformation temperature was 450°C and the strain rate was $1.0 \times 10^{-2} \text{ s}^{-1}$. The tensile axis (and rolling direction) is the horizontal. Orientation contrast, no etchant.....	101
Figure 5.4	The discrete Euler plot, discrete pole figure, contour pole figure, and boundary misorientation graph for the as-processed material. A significant fraction of LAB's and MMB's in the processed material are observed. The peak fraction of HAB's lie in the 55-60 degree misorientation range.....	103
Figure 5.5	Boundary misorientation plots and discrete pole figures for processed material static annealed for (a) 6 hours and (b) 12 hours. A deformation texture from processing persists. The bimodal boundary misorientation distribution becomes more pronounced.....	104
Figure 5.6	Grain misorientation texture illustrating the distribution of grain rotation axes for boundaries with misorientations of 55° - 62.8° for material statically annealed at 450°C	108
Figure 5.7	BSE micrographs, boundary misorientation plots, and discrete pole figures for regions of a deformed SUPRAL 2004 specimen.....	111
Figure 5.8	Misorientation histograms for specimens/regions examined in	

	SUPRAL 2004. The uncorrelated distribution of misorientations is indicated by the dotted line.....	111
Figure 5.9	Micro- and mesotextural plots for SUPRAL 2004 specimens from the cooperative research; (a) as-processed, (b) processed and annealed for 55 minutes at 480C, (c) deformed to 40% strain, and (d) fractured tip of the deformed tensile specimen. The randomization of texture and boundary misorientation following extensive GBS is evident in (d).....	113
Figure 6.1	Schematic diagram depicting the TMP schedule utilized to process the 2519 material examined.....	121
Figure 6.2	Results from mechanical testing of selected 2519 specimens.....	123
Figure 6.3	Log strain rate vs. log flow stress plot for the TMP25 specimens processed to $\epsilon = 3.3$	124
Figure 6.4	BSE micrographs of 2519 specimens processed following TMP25 to a total strain of 2.2 and annealed (a) 30 minutes and (b) two hours at 400°C. Orientation contrast, no etchant.....	126
Figure 6.5	Discrete Euler plot, contour pole figure (constructed from the discrete data), and boundary misorientation histogram for as- processed (TMP25, $\epsilon=2.2$) material. A weak texture is present consisting, primarily, of orientations near the deformation texture components brass and S. This data indicates that the microstructural refinement process is incomplete in the region examined (t/2). The fraction (0.14) of boundaries with misorientations less than 15 degrees are likely deformation induced structure from TMP.....	128
Figure 6.6	Discrete Euler plot, contour pole figure, and boundary misorientation histogram for as-processed (TMP25, $\epsilon=3.3$) material. The textural components present are the same deformation components present in the less strained ($\epsilon=2.2$) material however the intensity is higher and	

	the orientations are more tightly grouped around the exact brass, S, and copper orientations. A higher fraction of boundaries is evident in the 40-45 and 50-55 degree ranges of misorientation than was observed in the process route with lower total strain.....	129
Figure 6.7	Contour pole figures and boundary misorientation graphs for specimens of 2519 Al TMP 25 ($\epsilon=2.2$); (a) as-processed, (b) processed and annealed 30 minutes at 400°C, and (c) processed and annealed 120 minutes at 400°C.....	132
Figure 6.8	Microtexture and boundary character plots for deformed regions in 2519 tensile coupons; (a) tested at 450°C and (b) tested at 300°C. Deformation conditions in (a) appear to be near the transition area from region I to region II (GBS) behavior based on the mechanical data. The apparent randomization of texture is indicative of GBS. In (b), a $\langle 111 \rangle$ slip texture is apparent in agreement with the mechanical data that the test temperature of 300°C is insufficient for GBS and region III deformation mechanisms are rate-controlling..	135
Figure 7.1	Plots describing the mechanical behavior of SKY5083.....	146
Figure 7.2	BSE micrographs of specimens of SKY 5083 (a) as-processed and (b) processed and annealed for 30 minutes at 535 C. A fine dispersion of Al_6Mn particles is present. The rolling (and tensile) direction is the horizontal. Orientation contrast, no etchant.....	147
Figure 7.3	The discrete Euler plot and contour pole figure for SKY5083 (a) as-processed and (b) following a static anneal for 30 minutes at 535C. The weak deformation texture present in the as-processed material is observed to transition rapidly to a cube texture of moderate strength following the brief anneal. This suggests that the material is not fully recrystallized in the as-processed condition and that recrystallization	

	occurs shortly after post-TMP annealing.....	149
Figure 7.4	Boundary and misorientation graphs and grain misorientation texture plots for (a) as-processed and (b) processed and annealed specimens. GMT plots are shown for the misorientation range where the peak fraction of boundaries was observed. There is a shift upward in this range with prolonged annealing. The GMT plots illustrate that the boundaries are primarily disordered.....	152
Figure 7.5	Discrete pole figures and boundary misorientation graphs for the deformed gage regions in specimens with various strain rates; (a) 10^{-4}s^{-1} , (b) 10^{-2}s^{-1} , and (c) 10^{-1}s^{-1} . The transition of deformation modes from GBS in (a) to (predominantly) slip is shown by the formation of a $\langle 111 \rangle$ fiber texture in (c).....	154
Figure 8.1	Backscatter electron images taken near the EBSD examination regions in as-processed; (a) ACL 7475SP and (b) ALCAN BEST 7475. The rolling direction is horizontal.....	163
Figure 8.2	Backscatter electron images taken near the EBSD examination regions in processed and statically annealed specimens of; (a) KOBE 7475SP and (b) ALCAN BEST 7475. Annealing was conducted at 450C for one hour. The rolling direction is horizontal..	164
Figure 8.3	Discrete Euler plot, contour pole figure, and boundary misorientation angle histogram for data collected at the t/2 region in as-processed ACL 7475SP material.....	166
Figure 8.4	Discrete Euler plot, contour pole figure, and boundary misorientation angle histogram for data collected at the t/2 region in as-processed KOBE 7475SP material.....	168
Figure 8.5	Discrete Euler plot, contour pole figure, and boundary misorientation angle histogram for data collected at the t/2 region in as-processed	

	ALCAN 7475SP processed to the manufacturer's BEST TMP route...	165
Figure 8.6	Microtextural and mesotextural plots for data from examination of annealed specimens of; (a) ACL7475SP, (b) KOBE 7475SP, and (c) ALCAN BEST TMP.....	172
Figure 9.1	Histogram illustrating the population low angle and moderately-misoriented boundaries in as-processed materials examined. Materials classified as transforming by a Gibbs II-type mechanism illustrated retained deformation texture (and no evidence of a recrystallization texture) consistent with homogeneous microstructural refinement.....	177
Figure 9.2	Histogram illustrating the population low angle and moderately-misoriented boundaries in materials TMP'd and annealed. Materials classified as transforming by a Gibbs II-type mechanism illustrated retained deformation texture (and no evidence of a recrystallization texture) consistent with homogeneous microstructural refinement.....	178
Figure 9.3	Boundary misorientation histograms illustrating the static annealing behavior of a superplastic Al-5.0%Ca-5.0%Zn alloy.....	180
Figure 9.4	Histogram illustrating the population density of disordered HAB's (>15 degrees and not near CSL relations up to $\Sigma 49$). Recrystallization mechanisms involving a Gibbs I type process result in microstructures consisting of predominantly disordered HAB's.....	181
Figure 9.5	Graph of the ratio of the fraction of boundaries in the correlated data and the fraction in uncorrelated data versus misorientation angle. The uncorrelated data approximates the random distribution for the data set given the preferred orientation present. The deviation apparent in the excess number of MMB's for Gibb's II-type transformations is indicative of mechanistic rather than random processes.....	183

Figure 9.6	Histogram illustrating the population density of boundaries fulfilling the Brandon nearness criterion for nearness to low-index CSL relations. The frequency of these boundaries was essentially unchanged in all alloys examined regardless of process condition or strain. Dat for as-processed materials is shown here.....	184
Figure 9.7	Grain boundary misorientation histograms of various superplastically-enabled microstructures near the onset of GBS are shown to transition to a common misorientation distribution following significant GBS in region II.....	185
Figure 9.8	Grain boundary misorientation histograms of various superplastically-enabled microstructures are shown to transition to a common misorientation distribution following deformation condtions in the transition region from II-I. A buildup or retention of LAB's and MMB's distinguishes the resulting misorientation distribution here from that for deformation in region II where GBS is thought to be primarily responsible for the deformation strain.....	187

LIST OF SYMBOLS, ACRONYMS, AND/OR ABBREVIATIONS

BSE	Backscatter Electron
CCD	Charge Coupled Device
CODF	Crystallite Orientation Distribution Function
CSL	Coincident Site Lattice
DM	Deformation Microstructure
EBS	Electron Back-Scatter Diffraction
EBSP	Electron Back-Scatter Pattern
FCC	Face Centered Cubic
GBS	Grain Boundary Sliding
GMT	Grain Misorientation Texture
HAB	High Angle Boundary
LAB	Low Angle Boundary
MGRO	Maximum Growth Rate Orientation
MLI	Mean Linear Intercept
MMB	Moderately Misoriented Boundary
PSN	Particle Stimulated Nucleation
SAD	Selected Area Diffraction
SE	Secondary Electron
SEM	Scanning Electron Microscopy
SPF	Superplastic Forming
TEM	Transmission Electron Microscopy
TMP	Thermomechanical Processing
TSL	TexSem Laboratories
UTS	Ultimate Tensile Strength

WD Working Distance
XRD X-Ray Diffraction

ACKNOWLEDGEMENT

I would like to express my sincere gratitude to my dissertation advisor, Professor Terry McNelley for his outstanding professional guidance and for sharing his academic knowledge. I recognize that the time dedicated to oversight of my research was in addition to his duties as Department Chairman. I would also like to thank Professor Alan Fox for sharing his experience in microscopy and his mentorship during the course of this research. My thanks are also offered to Dr. Sarath Menon and Dr. David Field (TexSem Laboratories, Inc.) who both enthusiastically offered their assistance in the research. It has been a great pleasure to work with the distinguished faculty at the Naval Postgraduate School. I shall always be proud to have been associated with them.

I would also like to express my appreciation for my wife Candace who has been understanding and supportive during my tour at the Naval Postgraduate School and throughout our Navy career.

I. INTRODUCTION

A. A HISTORICAL REVIEW OF SUPERPLASTICITY

Superplasticity may be defined as the capability of certain polycrystalline materials to deform to extensive plastic elongations prior to failure, often without formation of a neck. Typically, superplasticity refers to tensile elongations greater than 200%, although some elongations have been reported in excess of 5000% [Ref. 1]. While it has been suggested that bronze metals in use in ancient civilizations may have possessed superplastic properties [Ref. 2], most historical reviews credit the modern-day documentation of superplastic behavior to a paper published in the Journal of the Institute of Metals by G.D. Bengough in 1912 which described extensive elongations in brass [Ref. 3]. Recognition of a stress and strain-rate relationship was first presented qualitatively in a paper by Rosenhain in 1920 which examined a near eutectic Zn-Al-Cu alloy [Ref. 4]. Photomicrographs detailing superplastic grain structures in eutectic Sn-Pb and Bi-Pb alloys deformed to elongations of 2000% were presented in 1934 by Pearson [Ref. 5]. This study was the first to identify an equiaxed grain morphology in the deformed regions and suggest that grain boundary migration may be involved in the deformation processes.

Only a limited amount of interest followed these studies with much of the early research on superplasticity being conducted from 1945 to 1960 in the U.S.S.R. where terminology translated later as "superplasticity" was initially used to describe the extensive plastic elongations observed [Ref. 6]. Wide recognition and interest in superplasticity may be assumed to have commenced following publication of a summary of the Soviet work by Underwood in 1962 [Ref. 7] and publication of research on an Al-Zn alloy of near-eutectic composition by Backofen and colleagues in 1964 [Ref. 8]. The Backofen study was, perhaps, the first to describe superplasticity as elevated-temperature resistance to necking in terms of a strain-rate sensitivity.

Academic and commercial interest in superplasticity increased significantly in the years

following with a primary focus on establishing the fundamental mechanical aspects of superplastic flow. Some of the key conclusions from these studies were:

- Peak superplastic elongations were observed [Ref. 8] to occur at higher levels of strain rate sensitivity, $m \geq 0.4$, where;

$$m = \frac{\partial \ln \sigma}{\partial \ln \dot{\epsilon}} \quad (1)$$

- Superplastic behavior was observed to be strongly dependent on grain size [Ref. 9].
- Deformation mechanisms resulting in superplastic elongations involved grain boundary sliding [Ref. 10].
- A sigmoidal relationship was observed when the logarithms of stress and strain rate were plotted. Peak elongations were observed to occur for strain rates in the vicinity of the maximum slope of the plot [Ref. 11].

With some fundamental mechanical aspects of superplastic behavior identified, considerable research efforts in the latter 1960's and early 1970's were directed to develop models describing superplastic flow. An association of superplastic behavior with the established diffusional creep theories of Nabarro [Ref. 12], Herring [Ref. 13], Coble [Ref. 14], and Lifshitz [Ref. 15] followed due to recognized similarities in the two processes. Important studies during this period attempting to model superplastic flow were presented by Ball and Hutchison in 1968 [Ref. 16], Raj and Ashby in 1971 [Ref. 17], Mukherjee in 1971 [Ref. 18], Ashby and Verrall in 1972 [Ref. 19] and Gifkins in 1976 [Ref. 20]. These models were proposed to detail the mechanisms of deformation in fine-grained superplastic materials and all involve grain boundary sliding (GBS) with accommodation by dislocation slip, dislocation recovery, grain boundary migration, grain boundary diffusion, or bulk diffusion. These studies and others during this period formed the basis of the fundamental theories of micrograin superplastic flow that exist today. Figure 1.1 illustrates the increasing level of interest in superplastic materials since 1960.

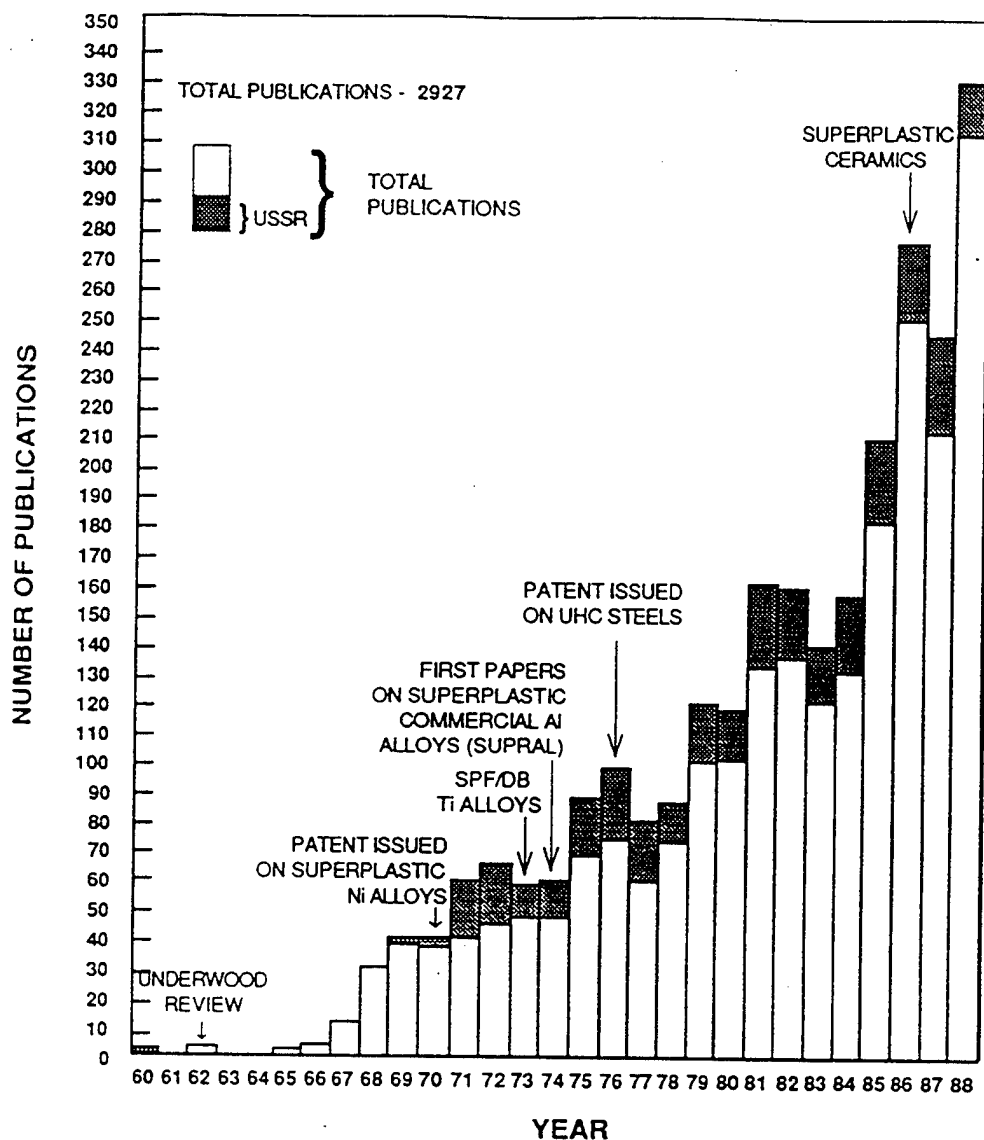


Figure 1.1. The number of publications on the topic of superplasticity from 1960-1989 [Ref.2].

Investigations through the decade of the 1980's may be categorized into two research areas. First, fundamental research to model superplastic flow (*following the onset of GBS*) was continued aided by the use of high-resolution transmission electron microscopy (TEM). This resulted in publications which proposed modifications of earlier models. Arieli and Mukherjee [Ref. 21] proposed one such model in 1980 which described superplastic

deformation as grain boundary shear with concomitant boundary migration and grain rotation accommodated by dislocation climb at grain boundaries. During this period Edington presented a summary and critique of the various theories for the involvement of GBS in superplastic flow [Ref. 22]. The second categorization of research efforts may be described as those which examined the evolution to a superplastically-enabled microstructure (*prior to the onset of superplastic flow*) and sought to model the microstructural refinement processes associated with successful thermomechanical processing (TMP) for fine-grained superplasticity in metals. This research was directly related to improving superplastic performance and the development of additional alloy systems for commercial and defense industry use. Again, TEM was often employed to investigate the role of precipitates in the microstructural refinement processes and the generation of new grains and to investigate the role of grain boundaries. Haasen [Refs. 23, 24], Humphreys [Ref. 25], and others reported studies and proposed models describing the involvement of particles in the recrystallization process. Berger and Wilbrandt [Ref. 26], Sutton and Balluffi [Ref. 27], Wolf [Ref. 28], Dingley and Pond [Ref. 29], Humphrey [Ref. 30], and Wadsworth and Pelton [Ref. 31] reported studies on the influence of grain boundary character on superplastic flow, GBS, boundary migration rates, and interfacial energy levels. Langdon [Ref. 32] has recently summarized the state of research on superplastic materials.

Although superplasticity was, perhaps, thought to be a mature technology in the mid-1980's with limited future growth, recent commercial interest in utilization of aluminum for structural and secondary-structural components in automobiles and optimization of rapid press-forming technology has resulted in renewed interest in the commercial sector. As a result superplastic forming technology has experienced steady growth in the last 10 years. Commercial, application-oriented research has been largely directed toward development of new processing and forming technologies and additional alloy systems. Annual conferences to discuss new topics and summarize research activity in the field continue with the 1997 International Conference on Superplasticity in Advanced Materials (ICSAM) scheduled in

January, 1997 at Bangalore, India.

Continued fundamental research into the microstructural aspects of superplasticity has been limited by the general subdued interest in allocating research support toward fundamental academic research in the absence of obvious potential short-term benefit. Nevertheless, the availability today of ultra-high resolution transmission electron microscopes and orientation imaging systems for scanning electron microscopes provide powerful tools to further earlier research and establish predictive theories which may permit design and optimization of superplastically engineered alloys.

B. APPLICATIONS OF SUPERPLASTIC TECHNOLOGY

Metals processed to exhibit fine-grained superplasticity are predominantly used in near net-shape fabrication of components from sheet material. To a lesser degree some superplastically processed aluminum alloy materials are utilized in hot bending of thicker structural frame sections. The ability to form complex shapes in a single piece of material results in significant weight savings (~ 20% weight reduction is typical), reduced fabrication costs, and improved in-service reliability and corrosion resistance. Additionally, tooling costs associated with superplastic forming (SPF) have been estimated as only 10% of those required for matched die tooling in conventional forming [Ref. 33].

Examples of some recent applications of SPF utilizing aluminum alloys are summarized below categorized by industry [Refs. 34-37]:

- Defense Industry: McDonell-Douglas F-18E/F bomb racks (nose and fairing), various access panels (SUPRAL 2004), T45 nosecone (7475), General Dynamics Tomahawk Missile tailcone assembly (SUPRAL 2004) , Teledyne Ryan UASV 350 (7475), British Aerospace Hawk engine air inlets (7475), SAAB JAS39 Gripen airbraker fairing (7475).
- Commercial aerospace: Boeing 777 - wing tip components, various housing components (3mm sheet SUPRAL 2004-T6), Airbus Industries A330/A340 - Wing

rib components, various housing and ancillary components (SUPRAL 100), De Havilland Learjet 45 - primary structural wing components (7475-T76).

- Electronics: GEC Maarconi, Thorn-EMI, CEL Inc., Ericson Electronics, Inc., and Phillips Electronics Corporation (electronics housing).
- Rapid Transit/Railroad: Structural components for light-rail and metro coaches, seats, and window frames (5083).
- Automotive: Honda Motor Corp.- Acura NSX (5083), Volvo AB Ambulance (5083), Audi A8 (5083), and Jaguar XJ220 (5083).
- Food packaging rigid container sheet (5182/3004).

Figure 1.2 [Ref. 38] illustrates some of the SPF methods currently employed. Processing of near net-shape components from thin sheet material is accomplished in either a male forming method or a female forming method as illustrated. The female forming method is the simpler process, requiring only air pressure to displace the heated sheet into the tool cavity. In the male-forming process tool motion accompanies the displacement of the pressurized surface of the superplastic sheet material.

Cavitation is the formation of microvoids at intergranular locations during superplastic deformation, predominantly at higher homologous forming temperatures. Cavitation has been reported in superplastic aluminum alloys [Refs. 39-41] and is undesirable in service application of superplastically formed structural components and may cause failure during superplastic forming. Imposing a back pressure on the order of the flow stress on the reverse side of the sheet during forming (shown in Figure 1.2 as back-pressure forming) imposes a hydrostatic pressure on the material and has been demonstrated to be effective in suppressing cavitation [Ref. 1]. Diaphragm forming permits a sandwich construction of superplastic sheet material with other alloy or composite material as shown in Figure 1.2.

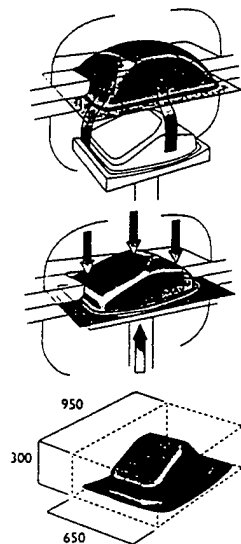
C. REQUIREMENTS FOR FINE-STRUCTURE SUPERPLASTICITY

Langdon [Ref. 32], Edington [Ref. 22], Mukherjee [Ref. 42], Sherby, et al. [Ref. 43],

and Pearce [Ref. 44] have summarized the microstructural prerequisites for fine-grained superplasticity in metals. There is general agreement on some fundamental requirements:

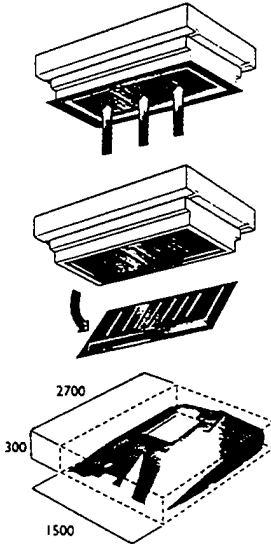
Male Forming Process

In the male forming process shown below, the SPF sheet is heated and formed using a combination of tool movement and air pressure.



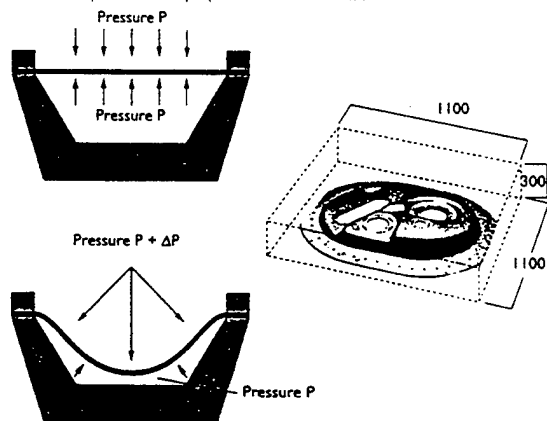
Female Forming Process

In the female forming process shown below, the SPF sheet is heated and forced into the tool cavity using air pressure alone.



Back Pressure Forming

Back Pressure forming (below) was developed for more critical structural components. High pressure is applied to both sides of the sheet and the introduction of a pressure differential provides the forming force. Cavitation, which can deplete material properties is thus inhibited.



Diaphragm Forming

Diaphragm forming (shown below) is used to form non SPF alloys into components requiring uniform thickness by using an SPF sheet as a sacrificial forming surface to force the non SPF material onto the tool.

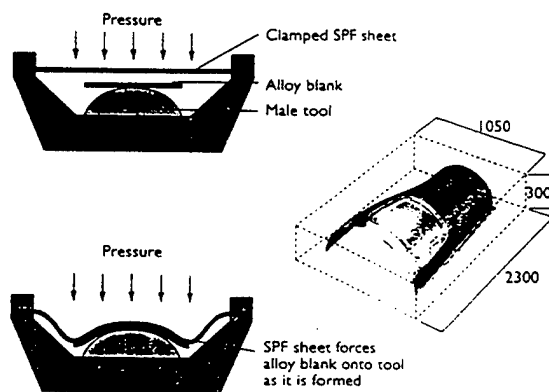


Figure 1.2 Illustrations of some SPF processes and techniques [Ref. 38].

- A fine grain size ($\leq 10\mu\text{m}$) is necessary for extensive superplastic flow. For a given strain rate a decrease in grain size results in an increase in the effective strain rate. At elevated temperature, coarsening of grain size results in hardening and a transition to deformation modes incompatible with those required for superplasticity.
- The presence of a dispersed second phase to inhibit boundary migration and aid in grain refinement. Superplasticity occurs at elevated temperatures where boundary mobility may lead to grain growth and coarsening of the microstructure. Particle size, distribution, and volume fraction are important features of superplastically enabled microstructures.
- A deformation temperature on the order of half of the homologous temperature or greater ($T_{\text{def}} \geq 0.5T_{\text{m}}$). Superplasticity is a diffusion-controlled process requiring generally high rates of material transport in the lattice and during GBS accommodation processes to maintain grain contact.
- A distribution of grain boundaries with the ability to support grain boundary shear without separation and with migration rates sufficient for the associated accommodation processes during superplastic deformation.

D. DEVELOPMENT OF FINE-GRAINED SUPERPLASTIC ALUMINUM ALLOYS

Most of the earlier research on superplasticity was conducted using non-engineering alloys with near eutectic compositions or using "academic", model alloys. Use of eutectic or eutectoid compositions began as early researchers recognized the necessity of a dispersed second phase to inhibit grain growth during the elevated temperature superplastic deformation. Eutectic alloy compositions yielded two-phase microstructures with nearly equal volume fractions of the two phases and subsequent rolling to refine and disperse the second phase produced microstructures capable of superplastic elongations at test temperatures, $T_{\text{test}} \geq 0.5T_{\text{m}}$. The room temperature characteristics of these alloys often made them unsuitable for use as engineering materials as they often contained a large volume

fraction of brittle phases.

Considerable efforts were made in the 1970's to develop alloy systems with military and commercial application potential. The first successful commercial, superplastic aluminum alloy developed was SUPRAL in 1975 by the British Aluminum Company and reported by Grimes [Ref. 45], and Stowell and coworkers [Ref. 46]. The alloy, nominally Al-6.0%Cu-0.4%Zr, has been reported to evolve to a microstructure capable of superplastic flow at commercial forming strain rates, $\dot{\epsilon} \geq 10^{-2} \text{ s}^{-1}$, only upon deformation with a microstructural transition occurring early in the deformation process. The second significant alloy development was achieved using the Rockwell process, developed in 1978 by Paton and Hamilton and initially utilized for processing of aluminum alloy AA7475 [Ref. 47]. This process is thought to involve the development of coarse particles through aging or thermomechanical processing to assist in a discontinuous recrystallization during TMP or post-TMP annealing in a manner which may be described by the particle stimulated nucleation theory of Humphreys [Ref. 25]. Most aluminum alloys thermomechanically processed to achieve extensive fine-grained superplasticity follow routes similar to one of these two basic processing schemes.

A significant effort to develop superplastic Al-Li alloys was made commencing in 1980. Al-Li alloys were perceived to be highly desirable for aerospace applications due to an approximate 12% reduction in weight (for 2.75 wt % Li) and an increase in the modulus of elasticity of $\approx 10\%$. The effort to develop these alloys was viewed with such priority that a series of international conferences were convened from 1982-1985 dedicated to development of formable Al-Li alloys. Wadsworth, et al. [Ref. 48] were among the early researchers and more recently Pu, Liu, and Huang [Ref. 49] have reported on 8090 Al-Li alloys which exhibit low temperature superplasticity (LTSP) following earlier LTSP work on Al-Mg based alloys by McNelley and coworkers [Refs. 50-53]. Efforts to improve superplastic performance and post-superplastically formed (SPF) properties of Al-Li alloys continue. Aluminum alloys 2095/2195, 5083, 6061, and 8090/8091 are examples of recently

developed, commercially available superplastic materials.

E. RELEVANCE OF THIS RESEARCH

It may be stated that the extent of the fundamental understanding of the microstructural transition required to achieve extensive fine-grained superplasticity in aluminum alloys has not appreciably changed in ten years. The microstructural prerequisites, listed previously, have been known for some time and remain the common denominator of successfully processed superplastic aluminum alloys. While progress has been made in the modeling of superplastic flow, the absence of a theory to describe the process whereby a microstructure is superplastically enabled, analogous to the Bain transformation theory modeling the martensitic transformation in steels, has limited the engineering of superplastic aluminum alloys. As a result, the modest superplastic performance of materials currently produced has limited their application and the development of new alloy systems is accomplished by use of an alloy-specific, TMP schedule which is often proprietary to a commercial vendor. A general theory regarding the role of recovery and grain refinement necessary for the transition to a superplastic microstructure is necessary to guide the engineering development of superplastic alloys.

The goal of this research is to expand the fundamental understanding of the microstructural requirements which enable fine-grained superplasticity in aluminum alloys. There is a need to expand beyond the alloy-specific level of engineering utilized today to process and develop superplastic materials. Certainly one obvious need is an expansion of the currently-recognized microstructural prerequisites. Specifically, one goal of this study is a redefinition of the involvement of grain boundaries in developing superplastically-enabled microstructures in aluminum alloys.

II. THEORETICAL ASPECTS OF SUPERPLASTIC FLOW AND SUPERPLASTICALLY ENABLED MICROSTRUCTURES

A. OVERVIEW

The characteristics of high-temperature deformation of fine-grained metals and aspects of microstructural refinement processes leading to superplastically-enabled materials will be reviewed in the first half of this chapter. Theoretical aspects and previous research regarding the role of grain boundaries in superplasticity will then be discussed followed by an overview of the dissertation research.

B. CONSTITUTIVE EQUATIONS TO DESCRIBE SUPERPLASTIC FLOW

Micrograin superplasticity in metals is a thermally-activated, diffusion-controlled process observed at elevated temperatures above approximately one-half of the absolute melting temperature, $0.5 T_m$. At low temperatures the mechanical response during plastic deformation of metals under tensile load may be described by the Holloman equation [Ref. 54]:

$$\sigma = k\epsilon^n \quad (1)$$

where k is a constant and n is the material strain hardening exponent. The motion of dislocations at low temperatures is thought to be restricted to glide and intersection processes [Ref. 55]. At elevated temperatures thermally-activated processes such as dislocation climb and cross-slip may occur readily and the stress-strain relationship must be modified to account for the rate of these processes:

$$\sigma = k\epsilon^n \dot{\epsilon}^m \quad (2)$$

where $\dot{\epsilon}$ is the strain-rate and m is the strain rate sensitivity exponent such that:

$$m = \left(\frac{\partial \log \sigma}{\partial \log \dot{\epsilon}} \right) \quad (3)$$

If it is assumed that the production of dislocations is balanced by the increased mobility such that a nearly constant forest dislocation density results then $n \approx 0$ and equation (2) simplifies to:

$$\sigma = k \dot{\epsilon}^m \quad (4)$$

or

$$\dot{\epsilon} = k \sigma^{n'} \quad (5)$$

where $n' = 1/m$.

The deformation characteristics of superplastic materials were first associated with the established theories of creep by Backofen [Ref. 8]. Initially, superplastic flow was thought to be related to Nabarro-Herring creep [Refs. 12,13] whereby stress imposed self-diffusion of atoms creates a flow of vacancies resulting in creep displacement of the material. Observed superplastic behavior, however, could not be explained by the Nabarro-Herring diffusion creep theory as the predicted linear relationship of strain rate with flow stress was not observed and the maximum strain rates predicted by Nabarro-Herring theory were well below those observed experimentally.

Elevated temperature deformation of polycrystalline metals in the power law regime is thought to be described by the standard equation for high temperature creep [Ref. 32]:

$$\dot{\epsilon} = \frac{ADGb}{kT} \left(\frac{b}{d} \right)^p \left(\frac{\sigma}{G} \right)^n \quad (6)$$

where A, p, and n are constants, G is the shear modulus, b is the Burger's vector, k is the Boltzman's constant, and D is the diffusion coefficient given by $D = D_0 \exp(-Q/RT)$ where Q is the activation energy, R is the gas constant, and T is the absolute temperature. For elevated teperature creep of pure metals $n \approx 5$ while for solid solution alloys the stress exponent is thought to be approximately 3 [Refs. 32, 55-56] due to the solute drag forces on dislocations which result in a required higher flow stress to force dislocations to glide. This power-law dependence of strain rate and flow stress has been shown [Ref. 21] to describe the high temperature creep behavior of class I (alloy) and class II (pure) metals over a wide range of strain ratess. Figure 2.1 illustrates the diffusion-compensated strain rate versus modulus-compensated flow stress behavior of pure aluminum and solid-solution aluminum-magnesium alloys based on the experimental work of Salama and McNelley [Refs. 6,50]. Figure 2.2 shows a schematic illustration of logarithmic strain rate versus flow stress behavior for superplastic materials.

The breakdown of a power law relationship between strain rate and stress is thought to be due to a transition from dislocation climb-controlled creep to obstacle-controlled dislocation glide and generally occurs outside of the superplastic regime at higher stress values where $\sigma/G \approx 5 \times 10^{-4}$ to 1×10^{-3} [Ref. 21]. Wu and Sherby [Ref. 57] have proposed the incorporation of a hyperbolic sine term to describe the elevated temperature creep behavior for both the power-law and power-law breakdown in pure aluminum:

$$\dot{\epsilon} = \frac{K}{\alpha^5} \frac{D_{eff}}{b^2} \left(\sinh \left(\alpha \frac{\sigma}{E} \right) \right)^5 \quad (7)$$

where $\dot{\epsilon}$ is the steady-state creep rate, K is a constant dependent on the stacking fault energy, elastic modulus and Burger's vector, b is the Burger's vector, D_{eff} is the effective diffusivity coefficient, α is the value of (E/σ) at the start of power law breakdown, E is the Young's modulus, and σ is the flow stress.

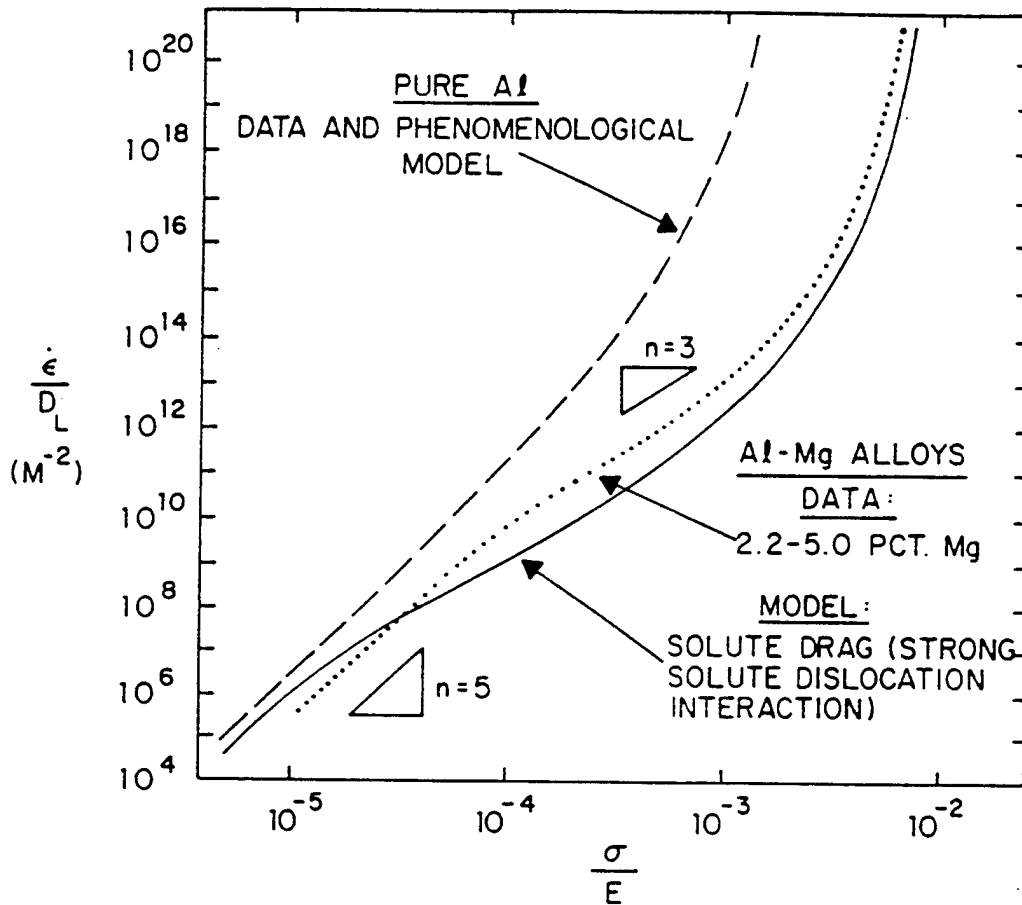


Figure 2.1. Data for the diffusion compensated strain rate versus modulus-compensated flow stress behavior for aluminum and solid-solution strengthened aluminum-magnesium alloys [Ref. 6].

The deformation behavior of fine-grained superplastic metals has been shown [Ref. 58] to follow the phenomenological equation:

$$\dot{\epsilon} = AD_{\text{eff}} \left(\frac{1}{d} \right)^2 \left(\frac{\sigma}{E} \right)^2 \quad (8)$$

where $\dot{\epsilon}$ is the superplastic deformation rate, D_{eff} is the effective diffusion coefficient, A is a constant and approximately equal to 2×10^9 , d is the grain size, E is the Young's modulus, and σ is the flow stress. McNelley, et al. [Ref. 59] reviewed the applicability of equation (8)

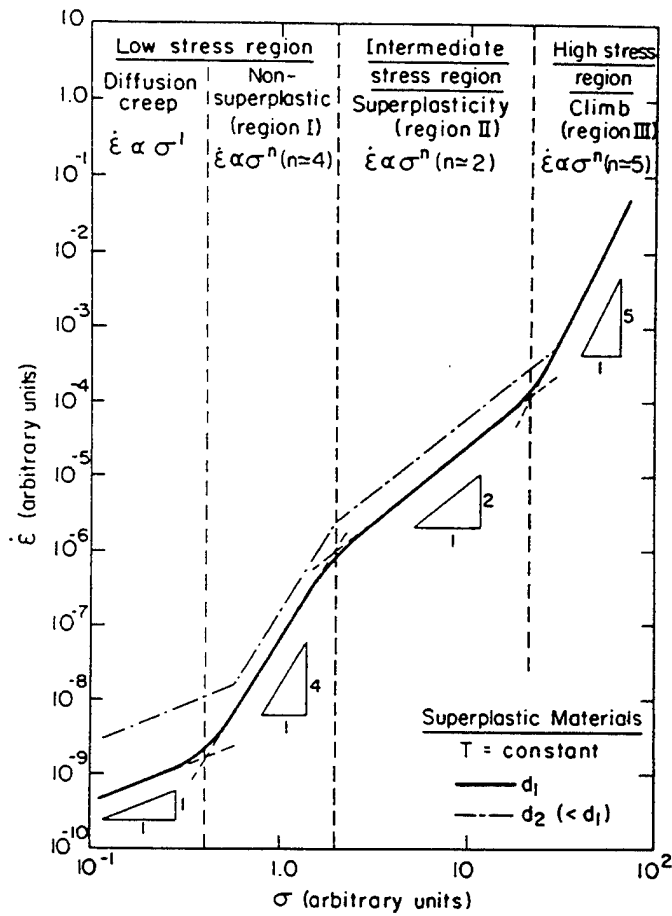


Figure 2.2. Schematic representation of the strain rate versus flow stress behavior for superplastic materials [Ref. 32].

for aluminum with respect to models of superplastic flow by additive contributions of

dislocation accommodated grain boundary sliding aided by diffusion occurring in the mantle region of grains and dislocation creep processes occurring in the core of grains.

C. MODELS DESCRIBING SUPERPLASTIC FLOW

Studies which proposed models to describe region II superplastic flow were identified earlier. The various models may be categorized based on the relative involvement of diffusional flow and dislocation motion in the grain boundary sliding process. Edington [Ref. 22] and, more recently, Langdon [Ref. 32] have reviewed these models. The models will be discussed briefly in the following summary.

1. The Ball and Hutchison and Related Models

Ball and Hutchison [Ref. 16] proposed that GBS proceeded with sliding of grain groups until sliding was blocked by a grain which was unfavorably oriented. An increase in the local stress at the point of blockage was relieved by the activation of dislocation motion in the blocking grain. Motion of the dislocations in the blocking grain, and hence the effective rate of GBS, was controlled by climb of the lead dislocation. Figure 2.3 provides a schematic illustration of the process.

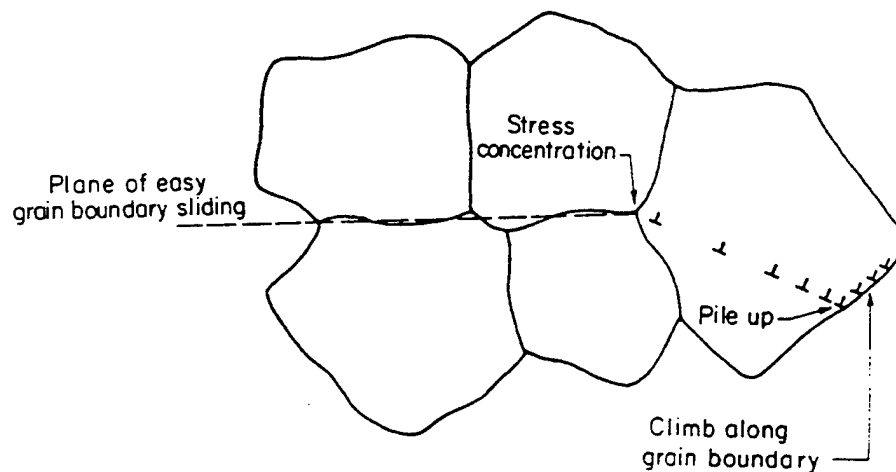


Figure 2.3. Schematic illustration of the Ball and Hutchison model describing superplastic flow [Ref. 32].

Mukherjee [Ref. 18], Gifkins [Ref. 20], and Arieli and Mukherjee [Ref. 21] have proposed modifications to the Ball and Hutchison model. In the Mukherjee model grains were presumed to slide individually with dislocation generation at grain boundary steps and ledges. Dislocation motion proceeded through grains and climb of dislocations piled-up at grain boundaries controlled the rate of GBS. The Gifkins model introduced the core and mantle concept of the grain where the grain is subdivided into the interior region, or core, and the region near the grain boundary, or mantle. In the model, the core region remains essentially dislocation free while accommodation for GBS occurs in the mantle region. For the Gifkins model accommodation occurred at triple junctions with dislocation generation near or within the boundaries. The Arieli and Mukherjee model proposed individual grain rearrangement by a combination of boundary shear and grain rotation with accommodation by dislocation generation and climb at grain boundaries aided by diffusion. These models all involve dislocation motion and predict a stress exponent, $n = 2$, a inverse grain size exponent, $p=2$, in equation (5).

2. The Ashby and Verrall Model

The Ashby and Verrall model [Ref. 19] proposed diffusion-accommodated superplastic flow by grain switching involving topological rearrangement of grains to retain an equiaxed shape. Figure 2.4 schematically illustrates the grain rearrangement. Bulk diffusion and diffusion at grain boundaries accommodate the boundary shear. The constitutive equation for diffusion-accommodated flow predicted an inverse grain size exponent, $p=2$, and a linear relationship of strain rate with flow stress, $n=1$. The authors theorized that superplastic flow is a superposition of dislocation creep and diffusion-accommodated flow.

D. MICROSTRUCTURAL REFINEMENT

Microstructural refinement to produce a grain size less than approximately $10\mu\text{m}$ is a prerequisite for extensive fine-grained superplasticity in aluminum alloys. Thermomechanical

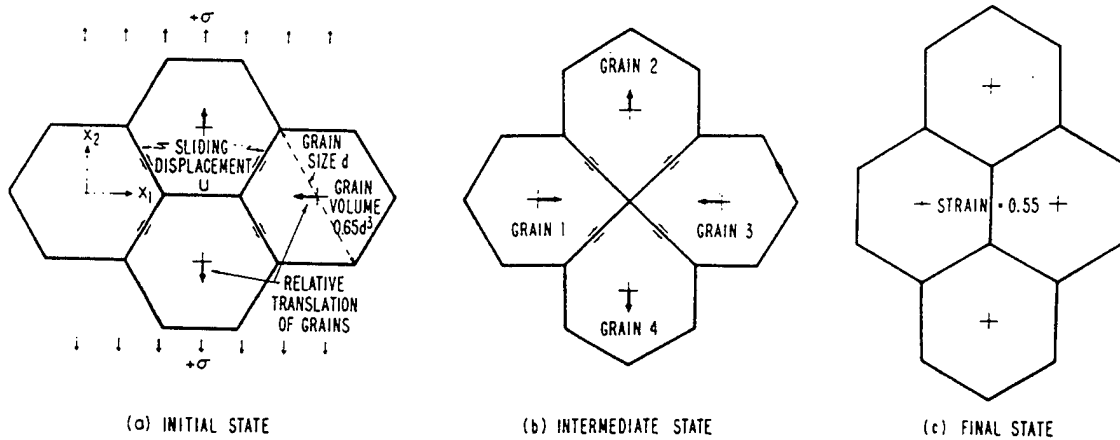


Figure 2.4. Schematic illustration of the Ashby and Verall model for superplastic flow involving grain rotation and rearrangement aided by diffusion [Ref. 32].

processing (TMP) of aluminum alloys involving strain-induced dislocation generation and recovery in the growth of new grains or refinement of the existing grain structure is necessary to produce superplastically enabled microstructures. In an effort to establish standardized criteria to define recrystallization, Doherty, Gottstein, Hirsch, Hutchison, and Lucke [Ref. 60] proposed to restrict the use of the term recrystallization to *"the processes involved in the production and migration of high angle grain boundaries due to the driving pressure of the stored energy of deformation"*. The authors sought to differentiate between processes whereby new high angle boundaries are produced heterogeneously by long-range reactions and migrate (recrystallization) and those whereby deformation microstructure evolves via short-range, recovery-dominated processes in the absence of the formation and migration of new HAB's. In a recent review Doherty [Ref.] refers to the later processes as Gibbs II transformations and those reactions involve recrystallization by the formation and migration of high-angle boundaries in a heterogeneous manner as Gibbs I transformations.

1. Discontinuous Recrystallization

Microstructural refinement for superplasticity in commercial aluminum alloys

processed according to the Rockwell-type process have been reported to occur by discontinuous recrystallization [Ref. 61]. The discontinuous terminology refers to separate nucleation and growth stages in the recrystallization process. Dislocation production during deformation processing results in an accumulation of stored strain energy. Nucleation occurs at regions of local strain-free regions where rapid growth into the adjacent deformation microstructure may occur readily. Nucleation of recrystallization embryo in superplastic aluminum alloys has been reported to occur in the vicinity of non-deforming large particles [Ref. 62-63]. Humphrey's model [Ref. 25] for particle-stimulated nucleation (PSN) involves the accumulation of geometrically necessary dislocations in the vicinity of large, non-deforming particles. In the PSN model the density of the dislocations in the deformation zone around the particles is given approximately by:

$$\rho_g = \frac{8f\gamma}{bd_p} \quad (9)$$

where f is the volume fraction of the precipitate phase, b is the Burger's vector, d_p is the particle diameter, and γ is the shear strain. Strain energy in the deformation zone around the particles is minimized by dislocation rearrangement creating subgrains with local lattice rotations. The critical nucleus size for growth of the embryo into the deformation matrix is given by:

$$\delta_{crit} = \frac{4\Gamma}{E} \quad (10)$$

where δ_{crit} is the size of the nucleus, Γ is the grain boundary interfacial energy, and E is the stored strain energy due to the deformation.

The size of the deformation zone, λ , may be estimated by:

$$\lambda = A d_p \epsilon^{\frac{n}{n+1}} \quad (11)$$

where λ is the size of the deformation zone, A is a material constant, d_p is the particle size, ϵ is the true strain, and n is the strain hardening exponent. A critical particle size may be deduced if it is assumed that the nucleus must equal the size of the deformation zone:

$$d_{p,crit} = \frac{4\Gamma}{AE} \frac{1}{\epsilon^{\frac{n}{n+1}}} \quad (12)$$

and the critical particle size necessary for PSN to occur decreases with increasing strain.

In aluminum and high-stacking fault alloys the nucleus may be a well-developed subgrain of critical size [Ref. 64]. In these materials coalescence of subgrains to achieve the critical particle size may occur readily with a minimum of boundary migration. New grains are produced as the highly mobile nucleated grain grows and consumes the deformation microstructure. In Humphrey's recent review of stability of cellular microstructures [Ref. 64] the increase in boundary energy due to growth has been expressed as:

$$\Delta E_{boundary} = 8\pi\alpha\gamma R\Delta R \quad (13)$$

where R is the radius of the (sub)grain, ΔR is the increase in the subgrain radius due to growth, and α is a constant, and γ is the boundary energy. The accompanying reduction in stored strain energy per unit volume due to the growth is given by:

$$\Delta E_{stored} = 4\pi\beta R^2 E_v \Delta R \quad (14)$$

where β is a constant.

The driving force on the boundary for growth due to a reduction energy may then be expressed as the difference of equation (12) with (13):

$$F = 4\pi\beta E_v R^2 - 8\pi\alpha\gamma R \quad (15)$$

New grains are produced as highly mobile grains grow and consume the deformation microstructure. The driving force must exceed any drag forces imposed by obstacles such as dispersoids.

2. Continuous Recrystallization

Various theories [Ref. 46,51,66-67] have been proposed to describe refinement processes which do not involve the nucleation of new grains by the formation and migration of new high angle boundaries. Continuous recrystallization, in situ recrystallization, and extended recovery have been used to describe these microstructural transformation. In all cases refinement proceeds by dislocation recovery processes in a homogeneous manner and involves limited migration of the evolving boundary.

One model for continuous recrystallization has been proposed [Ref. 51] whereby refinement of the polygonized dislocation structure comprising low angle boundaries is refined via dislocation accumulation. Dislocations produced during plastic straining enter the subboundary network and rearrange to produce a smaller dislocation spacing in the polygonized array. The result is a gradual increase in disorientation of the subgrain boundary concurrent with subgrain coalescence results in the development of moderate to highly misoriented boundaries. Microstructural refinement observed in the commercial superplastic aluminum alloy SUPRAL has been reported [Ref. 46] to result from strain-assisted (dynamic) continuous recrystallization.

3. Geometric Dynamic Recrystallization

McQueen et al. [Ref. 68] proposed a geometric dynamic recrystallization following

investigations of aluminum deformed in torsion at elevated temperature. In this model, initially equiaxed, original grains spiral around the torsion axis and the boundary regions are thinned. Boundaries which are serrated from the earlier formation of subgrains combine with subgrains and the resulting misorientation increases to values typical of HAB's. The formation of new HAB's in this model results from an increase in the HAB area of the elongated grains and not from a gradual increase in misorientation as in the existing continuous recrystallization models. It should be noted that the geometric dynamic recrystallization model as well as the continuous recrystallization model may not satisfy the previously mentioned definition of recrystallization.

E. THE ROLE OF GRAIN BOUNDARIES IN SUPERPLASTICITY

While a fine grain size and the presence of a dispersed second phase have been widely accepted criteria for micrograin superplasticity in metals [Ref. 2,22,32], the role of grain boundary structure in superplasticity has not been as well documented. Grain boundaries are known to be important in a variety of physical phenomena in polycrystalline metals [Ref. 30]. It may be generally summarized that grain boundary structure may influence the development of superplastically-enabled microstructures or the superplastic flow behavior in the following manner:

- Grain boundary interfacial energy has been reported to vary with misorientation and the degree of retained atomic stacking order at the boundary interface [Ref. 26,30,62].
- Grain boundary mobility varies with interfacial energy level and misorientation [Ref. 30,62]. Mobile grain boundaries are necessary to support the grain boundary sliding (GBS) process due to the accommodation required to retain an equiaxed grain structure by boundary rearrangement described in grain boundary shear models [Ref. 2,31]. Grain boundary mobility has been shown to influence growth selection during primary recrystallization [Ref. 23-24,69-70]. Additionally, grain boundary mobility effects the

rate grain growth which may occur at the elevated temperatures required for superplastic deformation and lead to flow hardening.

- Grain boundaries have been shown to be important sites for the nucleation of new grains during primary recrystallization [Ref. 30]. Grain boundary structure determines the size and geometry of the potential nucleation sites. Bishop and Chalmers described the presence of periodic ledges and sites characteristic of each low-index CSL boundary [Ref. 71].
- Grain boundary sliding rates have been related to grain boundary structure [Ref. 29,30].
- The ability of grain boundaries to support boundary shear during GBS without separation is known to be important in superplastic metals [Ref. 2,32].

To specify a particular grain boundary, five degrees of freedom must be identified; the three rotational components of the misorientation between neighboring crystals and two components specifying the boundary plane. The orientation relationship between crystals may be expressed in terms of an axis/angle pair or by a rotation matrix. Determination of the boundary plane is more difficult and experimental difficulties in determining the latter two degrees of freedom are discussed later. The structure or character of the boundary type may be specified by determining the first three degrees of freedom mentioned. Various theories have been developed to quantify the structure present at the interface between two crystals including the coincident site lattice (CSL) model [Freidel, 1926], the O-lattice [Bollman, 1970], plane-matching model [Pumphrey, 1972], and the Rodrigues-Frank vector formulation [Frank et al., 1988]. Although all of these models quantify the degree of atomic registry across the region of disorientation between adjacent crystals in an equivalent manner, the CSL model is the most widely accepted. The Rodrigues formulation is discussed in Chapter 3.

1. The Coincident Site Lattice Model

Grain boundaries have been generally categorized as either low angle, with the

minimum misorientation between adjacent crystals, $\theta \leq 15^\circ$ or high angle with $\theta > 15^\circ$. This categorization may be attributed to the work of Read and Shockley [Ref. 72] who developed and quantified the earlier lattice dislocation models for low angle boundaries formulated by Bragg [Ref. 73] and Burgers [Ref. 74]. The structure of high angle boundaries has not been as well defined. Friedel formulated the coincident site lattice (CSL) model in 1926 (it was later refined by Kronberg and Wilson in 1949) which provided a means to quantify the order at the interfacial plane between adjacent crystals. Essentially the CSL model involves the construction of a super-lattice in the region of the interface between two adjacent crystals by extending the atomic stacking arrangement from each crystal through the region of the boundary and into the adjacent crystal. Lattice points which are common to both grains establish a superlattice. Clearly, not all of the lattice points will be occupied (or there would be no disruption in the arrangement of atoms in the lattice and no boundary) and the density of superlattice sites which are occupied may be calculated:

$$\Sigma = \frac{\text{volume of superlattice cell}}{\text{volume of lattice cell}} \quad (16)$$

Figure 2.5 illustrates schematically the construction of the superlattice for the CSL model. Bollman illustrated that odd integers values result for the inverse density value, Σ [Ref. 26]. It should be mentioned that categorization of boundaries using the CSL model necessitates identification of; (1) the nearness criteria utilized to relate the boundary to the exact CSL relation and (2) the degree of order as determined by Σ . Since it is unlikely that exact coincidence with CSL relations would be satisfied experimentally, nearness criteria are necessary to quantify when a boundary is "close enough" to an exact CSL inverse density relation to possess any associated physical significance. For high-angle boundaries the deviation from exact coincidence is accommodated by arrays of grain boundary dislocations or DSC dislocations following Bollman [Ref. 75]. Brandon [Ref. 76] formulated a nearness

criterion for the CSL model where the allowed deviation from exact coincidence is given by:

$$\Delta\theta = \frac{K}{\Sigma^n} \quad (17)$$

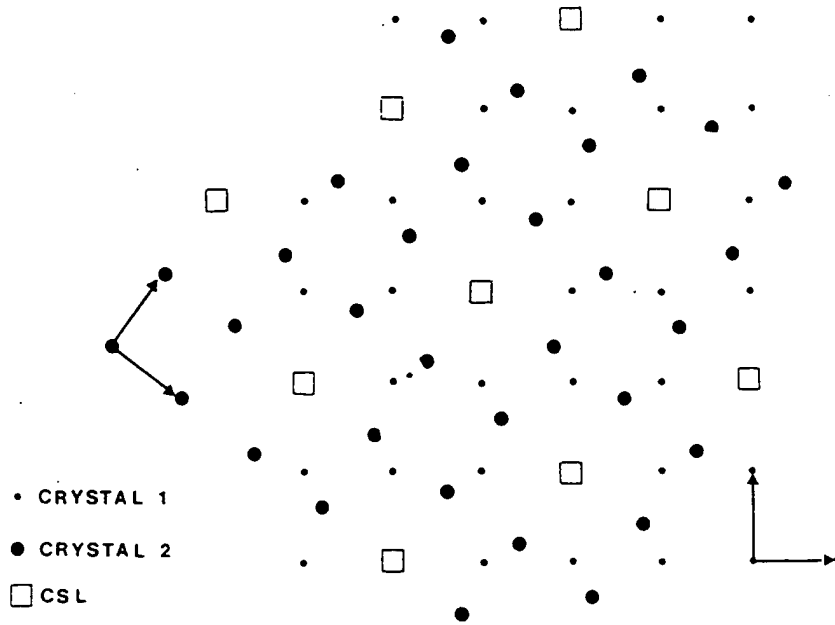


Figure 2.5. Schematic representation of the superlattice in the CSL model [Ref. 77].

where $\Delta\theta$ is the deviation from an exact CSL relation, K is a constant equal to 15° in the Brandon criterion, Σ is the inverse density CSL value, and n is a constant equal to 0.5. Ishida and McLean [Ref. 77] proposed somewhat more restrictive criteria where K is a constant equal to 8° and n is a constant equal to 1.0. High resolution transmission electron microscopy has been utilized and produced data suggesting a K value of 15° and n equal to 0.67 [Ref. 78]. Dechamps, et al. [Ref. 76] and Warrington and Boon [Ref. 79] reviewed and

critiqued the Brandon criterion and other research associated with nearness criteria which relate special grain boundaries to exact CSL values.

Since it has been shown [Ref. 81] that all possible boundaries for a cubic material will lie within 2° of a CSL relation for $\Sigma < 150$, it is also necessary to identify the threshold level for a value of Σ where any physical significance associated with the degree of order at the boundary region may be valid. Watanabe and Haasen have proposed using only low-index ($\Sigma < 30$) CSL relations due to the diminishing degree of order (and presumably reduced physical significance) at higher Σ values [Ref. 23-24,82]. Others have defined low-index CSL relations as $\Sigma \leq 35$ [Ref. 83]. For example, grain boundary interfacial energy cusps unique to special boundaries are observed to be reduced to values within experimental error by $\Sigma \approx 49$ [Ref. 81].

2. Energy Aspects of Special Grain Boundaries

The interfacial energy of a boundary may be estimated by using the Read-Shockley relation:

$$\gamma = \gamma_m \frac{\theta}{\theta_m} \left(1 - \ln \frac{\theta}{\theta_m} \right) \quad (18)$$

where γ is the boundary energy, θ is the boundary misorientation with the subscript indicating the value for a high angle boundary of approximately 15 degrees misorientation. It has been known for some time that low angle boundaries and coherent twin boundaries have low interfacial energy values [Ref. 84]. Wolf [Ref.28] proposed a direct relationship between the coincident site density, Σ^{-1} , and the associated interfacial energy of the grain boundary based on the imposed spacing of lattice planes parallel to the the boundary. Calculations by Hasson and Goux [Ref. 85] have been conducted to determine the influence of Σ on specific grain boundary energy and established that a simple dependence was not apparent. Sutton and Balluffi [Ref. 86] studied geometrical aspects of low boundary interfacial energy based on

structure at the crystal interface. Their studies were extensive and utilized several structure criteria including low reciprocal volume density, high planar density of coincident sites, and interplanar spacing in the interface. Their results revealed the existence of energy cusps for some unique structure-related boundary parameters but concluded that the relationship of boundary interfacial energy was not simply related to structure and that atomistic variables, including bonding, must also be considered. Summaries of work on the relationship between grain boundary structure and interfacial energy values has been presented by Pumphrey [Ref. 30], Berger, et al., [Ref. 26] and Goodhew [Ref. 81].

Although experimental data indicate that grain boundary interfacial energy does not follow misorientation or boundary structure in a simple manner, models have been proposed to predict grain boundary energy based on structure. Goodhew proposed that the energy of any interface may be estimated based on nearness to a CSL relation following the form of Franks [Ref. 87] equation for the energy of a low angle boundary by an equation of the form:

$$\gamma_b = \gamma_{sb} + b\Delta\theta[A - B\ln(\Delta\theta)] \quad (19)$$

where γ_b is the boundary energy, γ_{sb} is the energy of an associated special boundary, $\Delta\theta$ is the deviation from exact coincidence of the special boundary, b is the magnitude of the Burger's vector, A and B are constants which depend on misorientation.

Table 2.2. presents data for the magnitude of interfacial energy cusps observed in symmetrical tilt boundaries in aluminum. Figure 2.6 (a) through (c) illustrate some experimental results for direct energy measurements of boundary interfacial energy in aluminum. Most reported data illustrate that boundary interfacial energy increases with misorientation for low-angled boundaries up to 15° boundary disorientation and then reaches a saturation level where a constant interfacial energy level is sustained with the exception of energy cusps at boundaries with specific structure. The energy of the coherent twin boundary and boundaries near the $\Sigma 3$ relation have low interfacial energy values and are known to have

Boundary Structure	Energy Cusp Depth (mJm ⁻²)
$\Sigma 3$	>500
$\Sigma 5$	114
$\Sigma 9$	83
$\Sigma 11$	71
$\Sigma 13$	54
$\Sigma 17$	49
$\Sigma 19$	43

Table 2.1. Interfacial energy cusps for symmetrical tilt boundaries in aluminum [Ref. 81]. For comparison purposes the average energy of a disordered HAB in this study was 600mJm⁻² and therefore the last three CSL relations cited possessed an energy cusp of less than 10%.

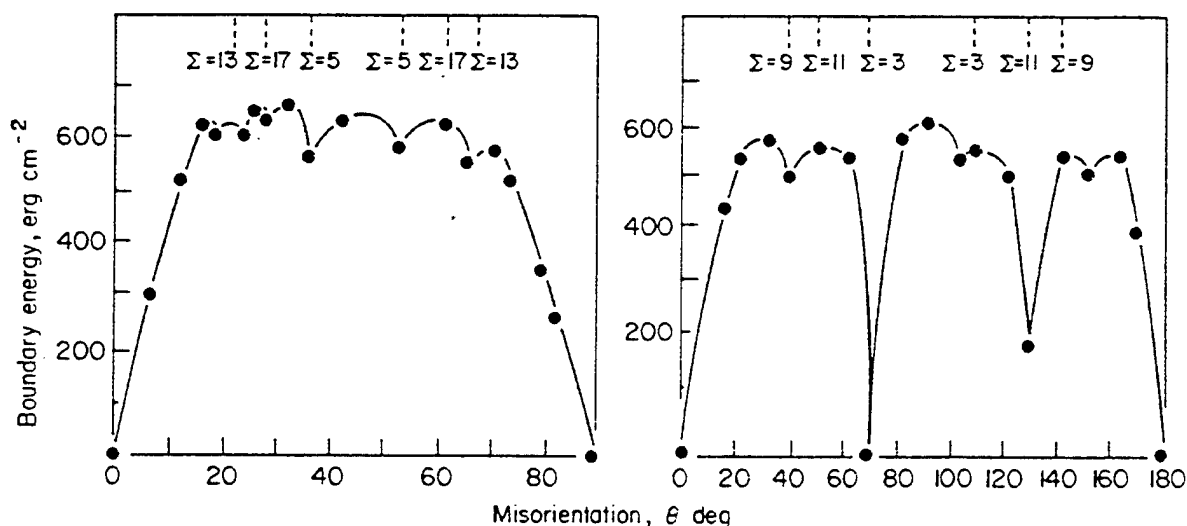


Figure 2.6. Experimental data of boundary interfacial energy based on direct energy measurements in aluminum [Ref. 30,86].

limited mobility [Ref. 30]. A decrease in interfacial energy may provide the driving force for the formation of twin boundaries during annealing [Ref. 88]. Boundary interfacial energy has been found to be sensitive to impurity and solute content [Ref. 89]. Data in these studies

revealed that even a small amounts of solute atoms in the boundary region resulted in lower interfacial energy levels.

3. Grain Boundary Mobility

Grain boundary mobility may influence the superplasticity of an alloy by determining the rate of grain growth (hence influencing the resulting grain size) during static annealing and elevated temperature SPF, by facilitating or inhibiting boundary migration processes associated with GBS, and by influencing grain selection and boundary development during primary and secondary recrystallization. Grain boundary mobility does not follow boundary misorientation in a simple manner. However, Humphreys [Ref. 65] has proposed a phenomenological equation for boundary mobility in aluminum as a function of misorientation:

$$M = M_m \left[1 - e^{-B \left(\frac{\theta}{\theta_m} \right)^n} \right] \quad (19)$$

where M is the boundary mobility, θ is the boundary misorientation, B is a constant approximately equal to 5 and n is a constant approximately equal to 4.

The earlier work of Li [Ref. 64] established boundary mobility as a function of boundary structure. Their results indicated that disordered boundaries and boundaries a few degrees from exact CSL relation possessed fast migration rates while boundaries nearer exact CSL relations were slow moving. As previously mentioned, twin boundaries have been shown to be nearly immobile. Migration rates for low angle boundaries are known to be on the order of 10^3 times slower than for high angle boundaries [Ref. 60].

The Beck experiments [Ref. 69] established certain orientations and boundaries as fast moving in primary recrystallization in aluminum bi-crystals. The maximum growth rate orientation (MGRO) observed, $\Sigma 7$ ($38.2^\circ / \langle 111 \rangle$), has been confirmed in latter studies [Ref. 23-24]. Shewmon illustrated that in a polycrystalline material where the grain boundary plane

is unconstrained, the grains will rotate and boundaries migrate to reduce the free energy [Ref. 90].

Elevated temperatures utilized in TMP and SPF of aluminum alloys facilitate the motion of boundaries while second phase particles and dispersoids inhibit migrating boundaries and advancing reaction fronts of nucleated (sub)grains. Static grain growth may occur during post-TMP annealing or annealing during pre-heat to SPF temperatures. Data has been presented that grain growth kinetics are enhanced by deformation [Ref. 9-10,89]. Flow hardening will result from grain coarsening in superplastic deformation and the associated increase in flow stress may result in an increase in the strain rate sensitivity exponent and a transition from the GBS regime to deformation modes inconsistent with extensive superplasticity.

Studies of grain growth in superplastic deformation of fine-grained metals have shown faster grain growth kinetics under the influence of strain. Deformation-enhanced grain growth during superplastic deformation has been reviewed by Salama [Ref. 6]. One model [Ref. 91], based on investigations of a superplastic Sn-Bi alloy, proposed deformation-enhanced mobility rates resulting from excess vacancy generation (and associated diffusion enhancement) in the grain boundary region due to GBS. Grain growth then proceeds driven by a reduction in surface energy and aided by the elevated temperatures used in SPF. Dynamic grain growth rates were observed to be in excess of static growth rates in the superplastic regime at peak values of strain rate sensitivity.

4. The Influence of Grain Boundary Structure on Grain Boundary Sliding

It has been proposed that disordered HAB's are necessary for superplastic flow [Ref. 2,31]. This was based on the high mobility rates required for grain rotations, grain rearrangements, and stress relaxation at grain junctions during the GBS accommodation processes. Data regarding the influence of boundary structure on grain boundary sliding rates is limited. Figure 2.7 illustrates data from a study by Biscondi and Goux [Ref. 92] for grain boundary sliding rates in aluminum bicrystals. In their data, sliding rates for boundaries

of less than $\approx 15^\circ$ misorientation are on the order of 0.25 of the rates for disordered HAB's, with the rate increasing linearly up to 15° misorientation. In contrast, early research conducted by Weinberg [Ref. 93] revealed evidence of grain boundary sliding in aluminum bi-crystals for boundary disorientation as low as 7° . Distinct cusps in sliding rates for some special boundaries are apparent in Figure 2.7. Other than the $\Sigma 3$ (twin) boundary, the special boundaries with cusps in the sliding rates do not correspond with the special boundaries with observed cusps in mobility rates. Pumphrey [Ref. 30] summarized the influence of boundary structure on grain boundary sliding rates by concluding that, in elevated-temperature deformation of polycrystals, some special boundaries slide more slowly than disordered HAB's with the differences observed to increase with lower deformation temperatures.

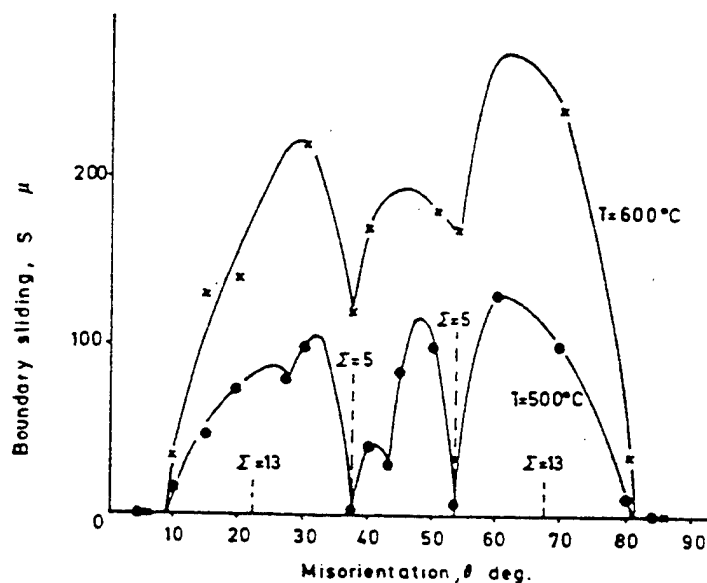


Figure 2.7. Data for grain boundary sliding rates as a function of boundary character [Ref. 92].

Dislocation involvement in the GBS process and the influence of boundary structure are difficult to determine experimentally as defects tend to anneal out of the specimens prior

to TEM examination. However, Dingley and Pond [Ref. 72] studied grain boundaries in polycrystalline aluminum using high-resolution TEM. Their research focused on the character and mobility of grain boundary dislocations and related the motion of grain boundary dislocations to boundary mobility and the GBS process. Their observations were that dislocations may enter into the grain boundary region in both near-coincident boundaries of high order and non-coincident, disordered boundaries. Crystal dislocations were then observed to disassociate into grain boundary dislocations. The authors categorized "hard" boundaries as those for which disassociation is inhibited and "soft" boundaries as those where the disassociation occurs readily. Higher rates of GBS were observed in soft boundaries and this was attributed to the higher degree of accommodation of crystal dislocations in soft boundaries.

EBSP methods have been recently employed to investigate the influence of grain structure in GBS of superplastic alloys. Randle studied the influence of grain boundary structure in a superplastically deformed 8090 aluminum-lithium alloy using EBSP methods [Ref. 94]. The study proposed that the relative contribution of diffusional creep and dislocation creep in the GBS accommodation processes could be concluded based on the character of the structure present at grain junctions. Analysis of the data utilized characterization of the boundary data following O-lattice theory. Diffusion in grain boundaries was concluded to be important in the deformation process when a predominance of boundaries analogous to high interfacial energy, HAB's were evident while dislocation motion in grain boundaries was thought to be important in the deformation process when a low-energy, LAB's were prevalent.

F. APPROACH OF THIS RESEARCH

Studies investigating the role of grain boundaries in superplasticity of modern engineering alloys have not been conclusive. Most data for these studies has been collected using TEM diffraction or SEM with electron channelling pattern methodologies. The time

required for such investigations limited the number of boundaries investigated, the number of alloys systems examined, and the number of processing states for the alloy(s) investigated. Additionally, data from the direct observations was limited to indirect orientation calculation. The result of limitations imposed by these methodologies was a limited amount of comparative data and alloy and process specific results.

The approach of this research is to obtain a wide-range of data regarding the evolution and production of boundaries in processed, annealed, and deformed superplastic aluminum alloys in a variety of important, engineering aluminum alloys. Investigation of superplastic aluminum alloys 2519, 5083, SUPRAL, and 7475 will be conducted as well as examination of a model alloy system, Al-10wt% Mg -0.1wt% Zr. Additionally, cooperative examination of an Al-5.0wt% Ca-5.0wt% Zn alloy was conducted at the Naval Postgraduate School by the author in association with a research partner and will be referenced appropriately.

A feature of the research is to utilize new technology associated with computer-aided backscatter electron diffraction. Post-collection analysis of the orientation data will be conducted in keeping with the previously stated goal to expand the understanding of the microstructural requirements which enable fine-grained superplasticity in aluminum alloys with specific focus on the role of grain boundaries. Concurrent publication of results has been a priority in the execution of the research and, as a result, chapter organization follows the individual alloy studies in a compartmented manner. Summary and integration of the results will follow the studies.

III. ELECTRON BACK-SCATTER DIFFRACTION (EBSD)

A. OVERVIEW

The diffraction of x-rays by a crystal was first demonstrated by von Laue in 1912 and later described analytically by Bragg [Ref. 95] by the relation:

$$n\lambda = 2 d \sin\theta \quad (1)$$

where d is the interplanar spacing, λ is the wavelength of the incident beam, n is the order of reflection and θ is the corresponding Bragg angle. Diffraction by electrons was formulated by de Broglie in 1924 and first demonstrated by Davisson and Germer in 1927 [Ref. 95] and was employed in research to investigate the geometry of crystal structures. Historically, crystal structure investigations using diffraction measurements in metals have been conducted using x-ray diffraction (XRD), neutron diffraction, or electron diffraction in the TEM to obtain macro-texture, crystal structure, and boundary information. Some features of these various methods are summarized in Table 3.1 and Table 3.2.

Use of electrons for diffraction investigations in the scanning electron microscope (SEM) has evolved with SEM technology. Earlier methods of electron diffraction in the SEM utilized selected area channelling techniques whereby the incident beam in the SEM is "rocked" through a fixed angle while focused on a specific area of the specimen. As the degree of "channelling" of the incident electrons through the crystal planes is dependent on the angle of the incident beam, the resultant back-scatter electron image exhibited a contrasted pattern. Crystallographic information, such as the spacing of planes in the crystal lattice, is contained in the channelling patterns. Although back-scattered Kikuchi patterns were reported in 1954 [Ref. 96], back-scatter Kikuchi diffraction (BKD) methods were not widely utilized until the early 1970s. Use of back-scattered electrons in the SEM to produce wide-angle diffraction patterns for data collection was developed by Venables and Harland

Method	Applications	Advantages	Disadvantages
X-ray Diffraction	Macro-texture, lattice parameter determination and crystal structure information.	Apparatus small and relatively inexpensive. Automated.	Bulk texture information only so no boundary information.
Neutron Diffraction	Crystal structure information on heavier elements or thicker specimens. Macro-texture.	Highly penetrating, may investigate light elements and organics.	Need source of thermal neutrons. Apparatus large and expensive.
Electron Diffraction (TEM)	Single crystal orientation. May use to establish beam conditions. Obtain boundary and crystal structure information.	LOR possible to 1.5 angstroms. Micro-diffraction possible to obtain microtexture. Areas of 1nm may be sampled in CBED.	Small specimen size, difficult to automate. Difficult to orient to external reference axes.

Table 3.1. Features of diffraction methods used historically.

in 1973 [Ref. 97]. Development of EBSD methods, building on the work of Venables and Harland, was accomplished by Dingley [Ref. 98] and integrated into the SEM as an automated system by Dingley, Randle, and others [Ref. 99].

PATTERN		INSTRUMENT	HIGHEST SPATIAL RESOLUTION	ANGULAR RESOLUTION (degrees)
Spot {	SAD	HVEM	0.4 μ m	2
	SAD	TEM	1.5 μ m	2
	micro-diff	TEM/STEM	10nm	2
	micro-diff	FEG-STEM	1nm	5
Kikuchi {	SAD	TEM	1.5 μ m	0.2
	micro-diff	TEM/STEM	20nm	0.2
SACP		SEM	10 μ m	>0.5
		SEM/TEM	1-2 μ m	0.5
EBSP		SEM	0.5 μ m	<0.5
Kossel		SEM	10 μ m	0.5

Table 3.2. Accuracy data for various diffraction methods [Ref. 100].

Electron-back scatter diffraction patterns arise as incident electrons penetrate the specimen and diverge in all directions. Some inelastically scattered electrons incident on lattice planes will satisfy the Bragg relation, equation (1), for each plane and will be reflected through the Bragg angle resulting in two cones of diffracted radiation from each set of lattice

planes. Figure 3.1 schematically illustrates the formation of the diffracted cones of radiation in reciprocal lattice space. Usually, the intensity of the diffracted beams along the two cones is not equal as the beam directed onto the reflecting set of planes is not in the same direction as the incident beam onto the specimen. The diffraction image projected onto a two-dimensional screen will depict pairs of Kikuchi lines, one light and one dark, as one cone will be diffracted through a smaller angle than the other and produce a cone of less intensity. The width of the line pairs is related to the spacing of the planes in the crystal and is also a function of the camera distance and specimen working distance in the EBSD system. The angle between two Kikuchi line pairs, or bands, is equivalent to the interplanar angle for the crystal planes associated with each Kikuchi band. The image will contain Kikuchi line pairs

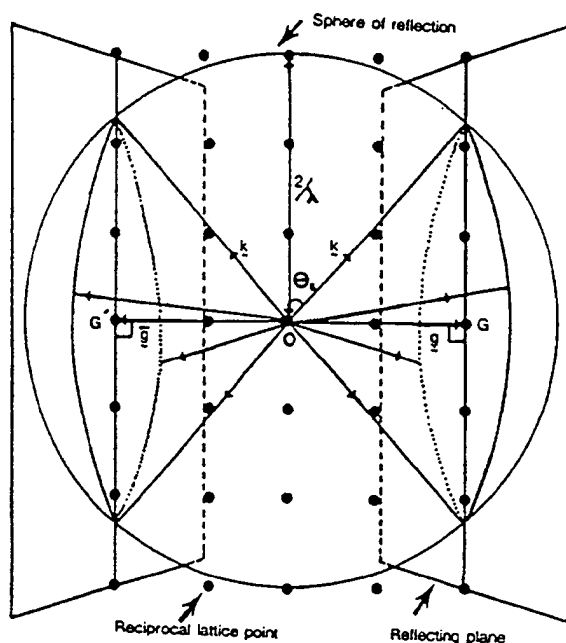


Figure 3.1. Schematic diagram illustrating the formation of Kikuchi line pairs in reciprocal lattice space [Ref. 101].

for all planes for which scattered electrons are incident at the Bragg angle. The diffuse background of the EBSP is a result of other energy loss scattering of electrons and Compton scattering. Higher residual strain in the lattice, deformed surface layers due to mechanical polishing, or surface oxide layers on the specimen will degrade the EBSD pattern due to absorption of the backscattered electrons and line broadening. Some characteristic features of the EBSP are the location of zone axes at major intersections of Kikuchi lines, the angle between the Kikuchi bands, the width of the bands between Kikuchi line pairs, the clarity or sharpness of the pattern, the interzonal distance between zones axes, and the intensity of the pattern. Figure 3.2 illustrates an example of a high quality EBSP collected from a silicon crystal.

Modern crystal orientation studies of fine-grained metals, such as those present in microstructures of superplastic aluminum alloys, have been enhanced within the last five years by use of computer-aided electron back-scatter diffraction systems for the scanning electron microscope (SEM). Some reasons for this:

- Specimens of bulk material may be examined preserving any relationship between the external (global) axes, associated with mechanical processing of the material, and microstructural features, associated with the (local) crystal axes.
- Tens of thousands of neighbor grains may be selected for investigation from a specified region of the bulk material. Computer-aided indexing and analysis is possible.
- Specimens may vary in size and geometry. As such, material from selected regions of processed material or post-form components may be investigated.
- Orientation information may be analyzed to yield microtextural information, boundary information, internal strain measurement, phase identification, and (sub)grain size information.

B. THE EBSD SYSTEM

Figure 3.3 provides a schematic representation of the basic components of an EBSD

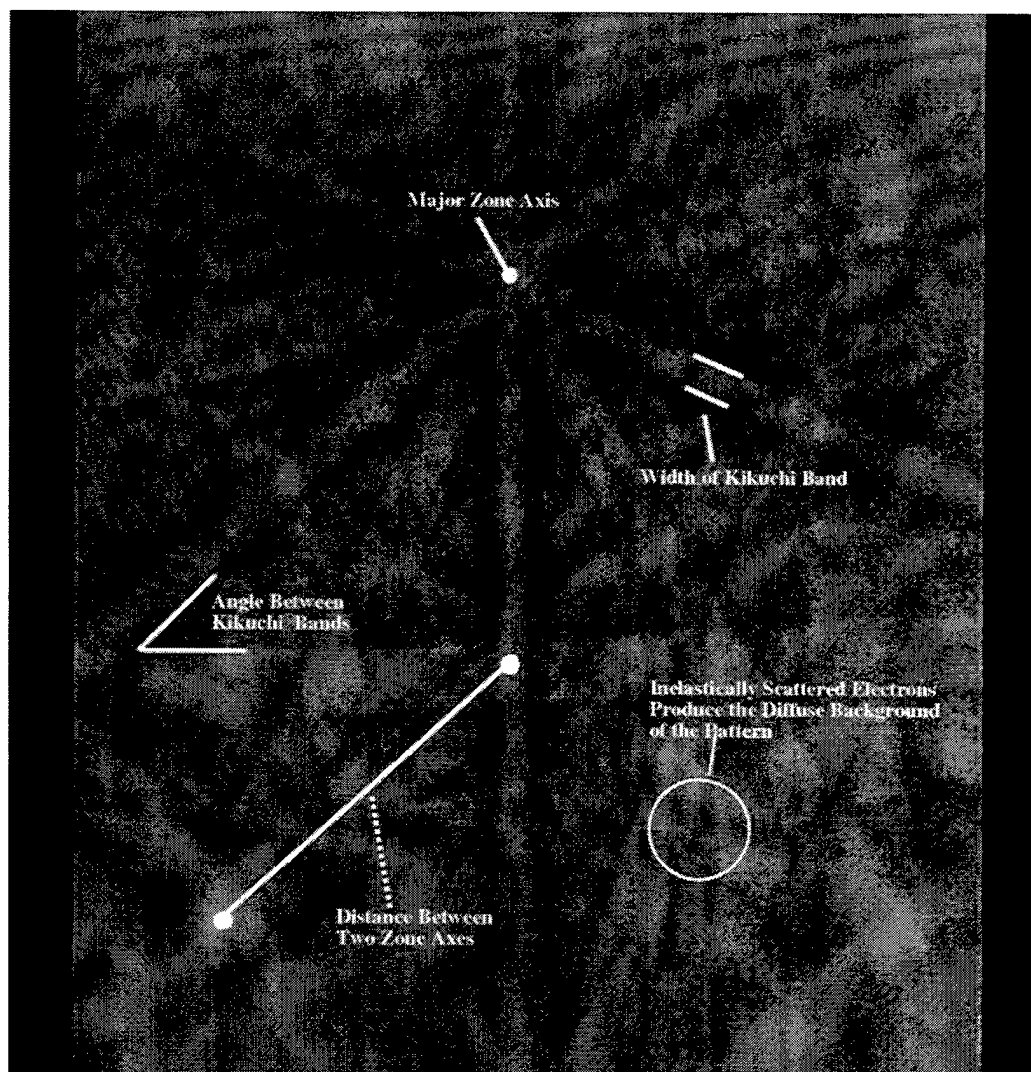


Figure 3.2. An example of an electron back-scatter pattern.

system for a scanning electron microscope.

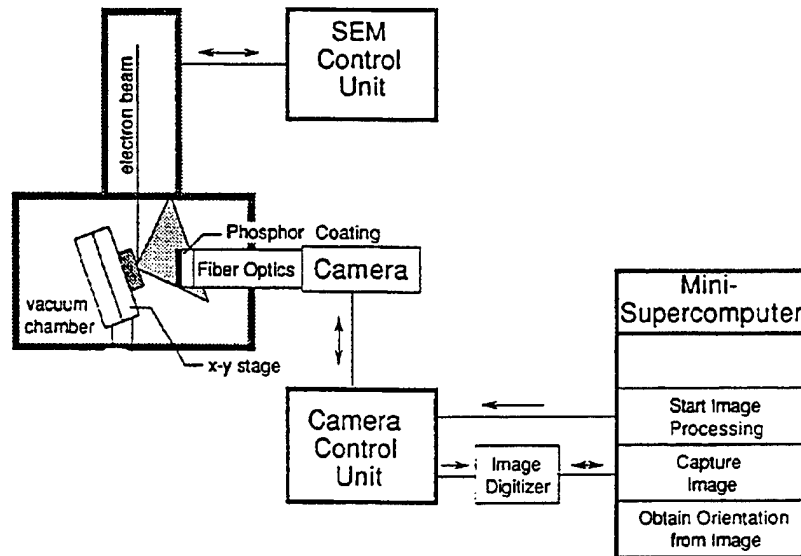


Figure 3.3. Schematic representation of the basic components of an EBSD system [Ref. 101]

Figure 3.4 provides a schematic representation of the specimen position in the SEM for EBSD examination. The incident electron beam strikes the specimen mounted in the special EBSD holder inclined at an elevated angle (typically 70°) and produces the backscattered electron diffraction image. The specimen tilt is optimized to direct the diffraction image to the camera for collection, to achieve maximum contrast, and to produce the widest angle of the Kikuchi pattern. If the specimen were inclined at low angles ($<45^\circ$) the backscattered electron signal would have to pass through more of the specimen and would be more highly absorbed. The diffraction image strikes a phosphor coated lens on the fiber-optic camera and produces an output signal to the camera control unit. The analog signal is received at the camera control unit where the light intensity is measured and may be adjusted. Following integration of the signal and background subtraction, a digital signal is sent to the computer workstation, manually captured in the software, auto-indexed by user command,

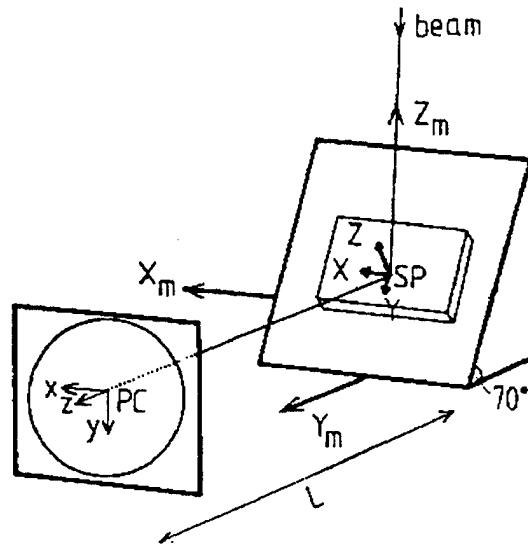


Figure 3.4. Schematic diagram illustrating the specimen position with respect to the incident beam and the diffraction pattern [Ref. 101].

and automatically stored sequentially in a data file. The quantitative data specifying the orientation of each indexed diffraction pattern is stored line by line in the data file. Software installed on the workstation computer also performs subsequent data analysis as well as plotting. Details of the material being examined, such as the crystal system, lattice constant, and reflector groups are entered prior to the start of an examination. Calibration data is required to be input to the software for auto-indexing of the captured pattern. The calibration data specifies values related to the system hardware geometry and working distance to enable interrogation of the EBSP. This will be discussed in greater detail in the next section.

2. Extraction of Data from the EBSP

Following input of the user-defined material information (crystal system, reflector families, and lattice constant) the Kikuchi bands in the EBSP must be recognized and associated with the corresponding lattice plane to enable subsequent determination of the lattice orientation. For an indexed solution of the captured EBSP, the specimen axes relating,

here, to the processing directions, must be rotated into the local crystal axes. The solution will be in the form of a 3x3 orientation matrix containing directional cosines which transform the specimen axes RD, TD, and ND, into the crystal axes, 100, 010, and 001 respectively. Specifically the orientation matrix will be of the form:

$$g = \begin{bmatrix} \cos\alpha_1 & \cos\alpha_2 & \cos\alpha_3 \\ \cos\beta_1 & \cos\beta_2 & \cos\beta_3 \\ \cos\gamma_1 & \cos\gamma_2 & \cos\gamma_3 \end{bmatrix} \quad (2)$$

where α_1 , β_1 , and γ_1 are the angles between 100 and RD, 100 and TD, and 100 and ND, α_2 , β_2 , and γ_2 are the angles between 010 and RD, TD, and ND, and α_3 , β_3 , and γ_3 are the angles between 001 and RD, TD, and ND, respectively.

There are four frames of reference to consider, that of the SEM, the specimen, the phosphor lens of the screen, and the crystal. System software assumes a default alignment of the specimen in the holder such that the RD and ND lie in the plane formed by the camera axis and the electron beam. Calibration parameters are necessary to define the system geometry relative to the specimen being examined. Initial system calibration is performed to determine the position of the pattern source point, SP, (where the electron beam strikes the specimen) the pattern center, PC, (defined as the point on the screen normal to SP) and the distance from the pattern source point to the screen, z^* . Figure 3.5 illustrates the initial system calibration configuration using a silicon single crystal standard in the SEM.

To establish calibration values the single crystal of silicon, having a [001] normal direction, is viewed in the SEM operating in the BKD mode. The specimen holder positions the specimen at an angle of 70.5° to the incident electron beam. The user focuses the beam onto the center of the specimen and adjusts the specimen position such that the [011]

direction is parallel to the horizontal stage direction of the microscope. This will establish [114] as the pattern center of the image as the angle between (001) and (114) is 19.5° (the

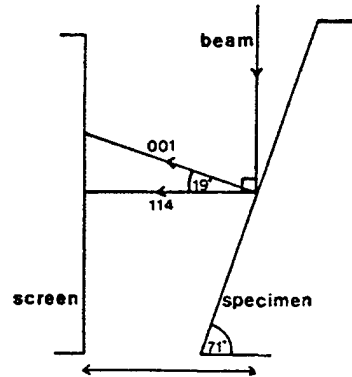


Figure 3.5. Initial calibration specimen arrangement in the SEM.

complement of 70.5° . The program software will require the user to identify the position [001] in the EBSP and will calculate z^* by the relation:

$$z^* = N / (\tan 19.5^\circ) \quad (3)$$

where N is the distance in pixels on the screen between the [114] and [001] zone axes. The value of z^* provides the correlation between the projected angles on the EBSP screen pattern and the true angles in the specimen. The coordinates of PC and the value of z^* remain in memory until the calibration data is updated. Although the EBSD system geometry is fixed, calibration data changes as working distance is varied. Therefore, frequent recalculation of calibration parameters is necessary during an interactive EBSD data run. High quality, captured EBSP's may be utilized for these calibrations during an EBSD data collection session by specifying the current working distance and manually identifying zone axes in the pattern.

Once calibration data is known, identification of the Kikuchi bands in the EBSP is

accomplished through the software calculation of the widths of the Kikuchi bands, the angles between Kikuchi bands, and the positions of Kikuchi bands and zone axes in the EBSP and comparing the values to theoretical values from known crystallographic relations. Referring to Figure 3.6(a), the interplanar angle between two planes represented by the two Kikuchi bands in the EBSP may given by:

$$\cos \gamma = |\mathbf{n}_1 \cdot \mathbf{n}_2| \quad (4)$$

where γ is the interplanar angle for the bands in the EBSP and $\mathbf{n}_1, \mathbf{n}_2$ are given by:

$$\mathbf{n}_1 = \overline{OP} \times \overline{OQ} / (|\overline{OP} \times \overline{OQ}|) \quad (5)$$

and

$$\mathbf{n}_2 = \overline{OR} \times \overline{OS} / (|\overline{OR} \times \overline{OS}|) \quad (6)$$

A corresponding theoretical calculation of the interplanar angle in a cubic system, for example, may be calculated from the Miller indices by the relation:

$$\cos \gamma = (h_1 h_2 + k_1 k_2 + l_1 l_2) / [(h_1^2 + k_1^2 + l_1^2)^{1/2} (h_2^2 + k_2^2 + l_2^2)^{1/2}] \quad (7)$$

Additionally, referring to Figure 3.6(b), the bandwidth angle, β , may be calculated as:

$$\beta = \tan^{-1}(r'/z^*) - \tan^{-1}(r/z^*) \quad (8)$$

where r' is the distance from the pattern center, PC, to the outer Kikuchi line, r is the distance from PC to the inner Kikuchi line, and z^* is the normal distance from SP to PC as previously calculated. The bandwidth angle, β , in the EBSP is related to the interplanar distance of the crystallographic plane associated with the specific Kikuchi band by the relation:

$$\beta = \sin^{-1} (\lambda/2 d_{hkl}) \quad (9)$$

where λ is the wavelength of the electron beam and d_{hkl} is the interplanar spacing. The angle between two zone axes in the EBSP may be derived based on their distance to PC. If two zones axes are at coordinates (x_1, y_1, z_1) and (x_2, y_2, z_2) from the pattern center then the two vectors from PC to the two zone axes in the EBSP may be defined as V_1 and V_2 . The angle between the two zone axes, $\theta_{1,2}$, may be calculated by:

$$\cos \theta_{1,2} = V_1 \cdot V_2 / |V_1 V_2|. \quad (10)$$

In this manner, a calculation of the interplanar angle between the two planes corresponding to the two Kikuchi bands, interplanar spacing of the plane associated with each Kikuchi band, and interzonal angles may be accomplished. For the automatic indexing scheme utilized, selection of the bands for identification from the captured EBSP is determined by identifying the seven bands of highest intensity in a condensed, circular, 100 pixel by 100 pixel image extracted from the original captured image. This identification is conducted automatically and displayed on the monitor.

Once the Kikuchi bands and zone axes in the pattern have been identified, a lattice orientation matrix must be calculated to quantify the orientation data. From a known pair of Kikuchi band normal vectors, calculated previously as, n_1 and n_2 , a mutually orthogonal frame of reference may be constructed by defining the unit vectors:

$$e_1^* = n_1 \quad (11)$$

$$e_2^* = n_1 \times n_2 / |n_1 \times n_2| \quad (12)$$

$$e_3^* = e_1^* \times e_2^* \quad (13)$$

Two matrices of direction cosines may then be calculated relating the new frame of reference

to the that of the specimen;

$$\mathbf{g}_{ij}^I = \mathbf{e}_i^* \cdot \mathbf{e}_j^s \quad (14)$$

and to that of the crystal;

$$\mathbf{g}_{ij}^{II} = \mathbf{e}_i^c \cdot \mathbf{e}_j^* \quad (15)$$

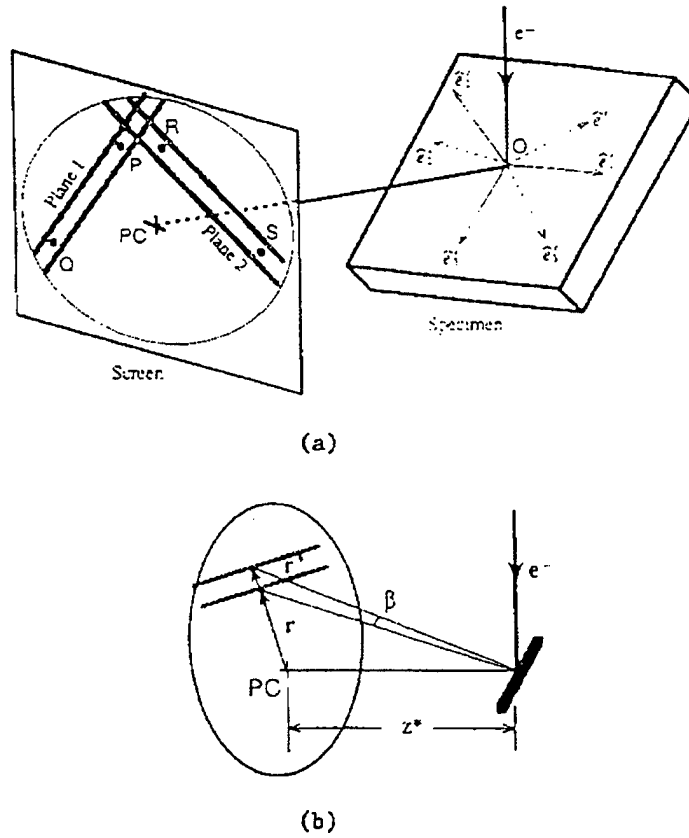


Figure 3.6. Geometrical aspects of the Kikuchi bands in the EBSP for (a) interplanar spacing between two bands and (b) interplanar spacing for the crystallographic plane associated with the specific band [Ref. 101].

The orientation matrix which rotates the specimen axes into the crystal coordinate system is

then given by:

$$g_{ij} = g_{im}^{\text{II}} g_{mj}^{\text{I}}. \quad (16)$$

Figure 3.7 illustrates an example of a captured pattern, the 100 x 100 pixel condensed image from which the Kikuchi bands are selected, and the resultant indexed pattern. Transformation of the orientation matrix into alternate forms to analyze microtextural information will be discussed in the following section. A manual indexing scheme, necessitating user-identification of zone axes, may also be employed to individually index a captured pattern.

In addition to the extraction of quantitative orientation data from the EBSP, the EBSP pattern may be utilized to identify the structure of other phases and to estimate the relative degree of residual strain in the lattice. An image quality factor, shown in the lower left corner of the indexed diffraction image, Figure 3.7(c), is assigned based on the number of bands identified and the number of band triplets in agreement with the indexed solution.

3. The Interactive EBSD System at the Naval Postgraduate School

EBSD systems utilizing automatic control of the electron beam to scan regions to collect tens of thousands of individual orientations in a user-selected grid and step-size to produce orientation "maps" were described formally by Adams, Wright, and Kunze in 1993 [Ref. 102]. Software programs developed for these systems have the ability to interrogate the resultant map to identify specified regions of misorientation, residual strain (as measured by the image quality of the diffraction pattern), to highlight specific boundary types, and produce grain size information files.

The system in use at the Naval Postgraduate School is an interactive system whereby control and positioning of the electron beam onto the specimen as well as "capture" of the resultant diffraction image is determined by the user. There are advantages to each of these two, automatic mapping and interactive, systems. Systems capable of automatic mapping represent the latest in orientation investigation technology, in that mapping parameters for

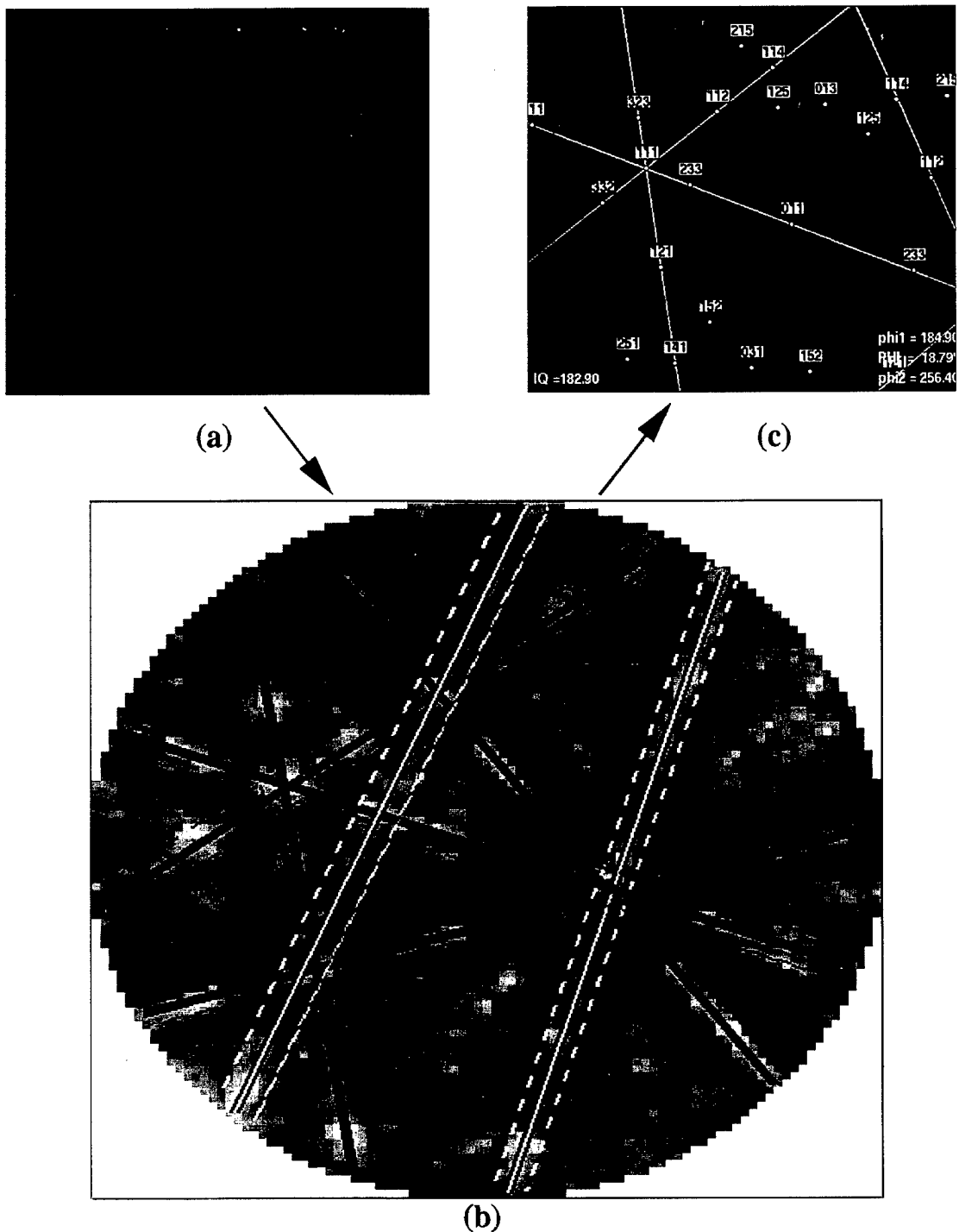


Figure 3.7. EBSD images illustrating the sequence in the identification of Kikuchi bands leading to orientation determination; (a) as-captured, (b) identification of the seven bands of highest intensity, and (c) indexed.

data collection are specified by the user prior to the commencement of analysis and, after initializing the start of data collection, the system will automatically collect data until complete. As such, these data runs are long (~ 8 hours) and are frequently conducted overnight to allow other microscope use during daylight hours. Large data sets of up to $\sim 10^5$ orientations may be collected and stored for analysis and mapping. Additionally, post-collection analysis of the data sets may be conducted to discard orientations with poor image quality or low confidence factor in the indexed solution. Nevertheless, data collection is conducted without user interaction so there is no knowledge whether proper indexing of each orientation has been obtained. Unlike an interactive method of examination where the user may automatically or manually index each captured pattern, in a beam control system only one of the two available indexing transform methods may be pre-selected and may not be changed during the data run. Additionally, the calibration parameters used by the software to properly index the diffraction pattern are sensitive to changes in working distance. If the data collection pattern, or scan, traverses up or down in working distance by a distance of only 1mm, the indexed solution will have a small error.

In an interactive system the data sets are smaller, typically 500 orientations, due to the time required for the user to position the beam spot pixel by pixel and to capture the image. The principle advantage to an interactive method is in the flexibility of technique in scanning the areas selected for data collection. Regions near desired microstructural features may be selected for examination and the data collection scan may be of any geometry. This will be discussed further in the following section on examination methodology. Other benefits are that each pattern is viewed as indexed for accuracy and that calibration settings may be frequently updated. Finally, the interactive system is less expensive as the SEM stage controller and more complex software are not required.

The EBSD system at Naval Postgraduate School utilized for all EBSD data collection in the dissertation research is shown in Figure 3.8. The system includes a Topcon SM-510 scanning electron microscope, a fiber-optic charge-coupled device LTC216 low-light camera

with a phosphor-coated lens, a CCD model 852 camera control unit for light intensity monitoring, analog input signal correction, integration and background subtraction, and digital signal output, and a Silicon Graphics INDY workstation with orientation imaging software from TexSem Laboratories, Inc., Provo, Utah.

C. DEVELOPMENT OF METHODOLOGIES FOR STUDIES OF FINE-GRAINED METALS USING EBSP TECHNIQUES

At the time the EBSD system was installed at the Naval Postgraduate School there were less than ten similar systems operational in the United States, most of which were installed within the three years preceding. As such, there was not a vast amount of published research on EBSD examination methodology, although the fundamentals of the procedures

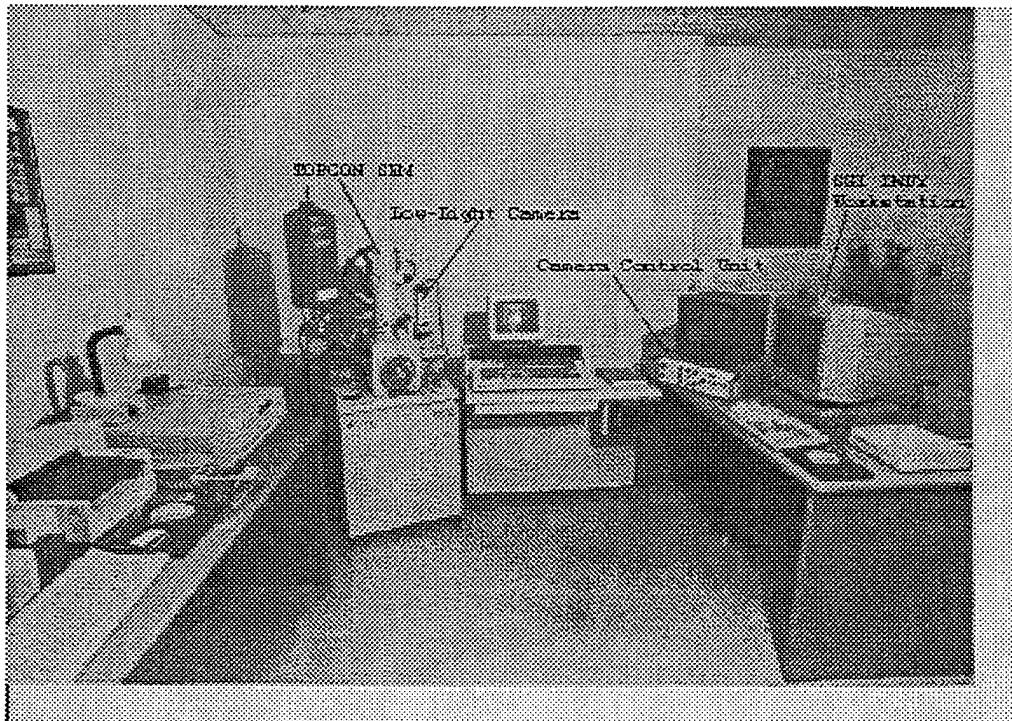


Figure 3.8 The EBSD system in place at the Naval Postgraduate School.

had been outlined by Randle [Ref. 103]. As stated previously, in automatic mapping systems

utilizing beam control the user specifies a choice of grid geometry, usually rectangular or hexagonal, and the step-size between collection points in fractions of a micron before the start of data collection and has no further input until after all of the data is collected. Interactive EBSD examination, however, requires careful choice of a methodology for collection of the EBSD data since the user positions the electron beam spot, captures the pattern, and then must reposition the beam while observing the live diffraction image as it changes. Clearly, in addition to the scan path followed, there are subtle differences in the manner in which data is selected during the capture process that will optimize the data set with respect information desired for the number of orientations collected.

Selection of a scan path is relatively straight forward. If one desired, for instance, to study orientations near a specific feature in the microstructure, such as triple points or large particles, the user may choose a circuitous path about the features desired. For microtexture determination and neighbor (sub)grain orientation comparison a straight line, raster-type path along lines of constant working distance may be selected. In fact, for microtexture determination only, the path followed does not matter at all, only the region examined. As an example, if one desired to investigate microtextural anisotropy in the through-thickness direction of processed plate material, EBSD data sets could be gathered from near the surface, at mid-points to the center, and at the center of the plate thickness.

Selection of a method to capture successive diffraction images to yield information on the boundary between orientations presents more alternatives. To conduct an orientation map, a fixed number of pixels is determined (each pixel shift will represent a fixed distance depending on the magnification used) between image capture points. The user would capture an image, move the spot the pre-determined number of pixels, and recapture. Such a process would, if a small step size was utilized, capture most orientations changes in the region studies including very low angle shifts in orientations, such as those encountered across a subboundary. New versions of orientation imaging software permit step sizes as small as .02 microns and are in use in research and industry to examine thin-film structures, as an example.

In the present study, information was desired regarding the character of well developed boundaries which may influence the mechanical behavior or detail the microstructural refinement processes in superplastically deforming aluminum alloys. Typical grain sizes in the processed aluminum alloys to be examined vary from approximately 1.0 to 15 microns. As such, a methodology was developed building on that utilized by Randle, Skerjvold and Ryum, [Ref. 93, 104]. The method developed at Naval Postgraduate School during this research and described in the following paragraphs was published in the Journal of Metals [Ref. 105] and is described in the following sections.

1. Preparation of Specimens for EBSD Examination

Sample preparation for EBSD examination of the aluminum alloys examined in the scope of the present research is similar to that utilized for backscatter electron imaging (BSE). Specimens were sectioned as required using a Buehler Isomet 11-1180 low speed saw and successively ground using a Struers Knuth-Rotor-3 grinding wheel with 1000, 2400, and 4000 grit silicon carbide paper. Moderate to light pressure was used with nominally 30-45 seconds grinding for each grit size. Specimens were polished initially using 6.0 μ m Metadi diamond compound on a Buehler Chemomet cloth and subsequently polished using 1.0 μ m and 0.25 μ m diamond compound on a Buehler Microtex cloth. Specimens were rinsed with methanol and dried using hot air following each polishing step. For aluminum, at an SEM working voltage of 20KV, the penetration depth of the backscattered electrons is approximately 20-30nm. Therefore, electro-polishing to remove the deformed surface material resulting from the mechanical grinding and polishing is necessary prior to EBSD examination. All specimens examined using either BSE or EBSD were electro-polished using a solution of either 70% methanol-30% nitric acid at a temperature of -20°C and an impressed current of 7V DC or using 90% butoxyethanol-10% hydrochloric acid at a temperature of 0°C and an impressed voltage of 14V DC. Proper removal of any deformed material or oxide layers is essential to EBSD examination therefore specimens were usually examined immediately after polishing although this is not mandatory if specimens are stored

under vacuum.

2. EBSD Examination Procedure

As stated previously, the orientation imaging software assumes a default position for placement of the specimen in 70° holder in the microscope. Specifically, the assumed position is such that the rolling direction and the normal direction of the specimen lie in the plane formed by the camera axis and the electron beam. If the specimen examined is not in the default position, rotation matrices must be applied to the data prior to plotting for textural information. Windows to input the rotation matrices are provided in the software and the resulting rotated file is saved in the program. Figure 3.9 illustrates this adjustment for through-thickness examination of a sectioned tensile specimen extracted from processed sheet material.

Tensile specimens in the present research were sectioned longitudinally along the tensile (also the rolling) direction to reveal the through-thickness direction of the tested coupons. Undeformed sheet materials examined were sectioned along the rolling direction and examined in the through-thickness direction also. Thicknesses of all specimens examined varied from 1.0 mm to 4.0 mm. Working voltage in the SEM was maintained at 20KV for all EBSD examinations. The working magnification selected varied from 1000X to 2000X depending on the microstructure of the specimen. Higher magnifications yield a smaller pixel-to-pixel distance on the SEM viewing screen and facilitated examination of material where orientation changes occurs at distances less than about 1 micron. Selection of microscope magnification specifies the actual distance moved between pixels while operating in the spot mode. EBSD patterns were captured utilizing control of the electron beam in the spot mode to successively position the spot pixel by pixel in a raster pattern. As the specimens were oriented such that the rolling direction was always in the plane of the electron beam and the camera axis, the raster pattern involved, primarily, translation of the spot along lines of constant working distance in the through-thickness direction. This aids in pattern analysis by maintaining constant calibration conditions during translation along such lines and minimizes

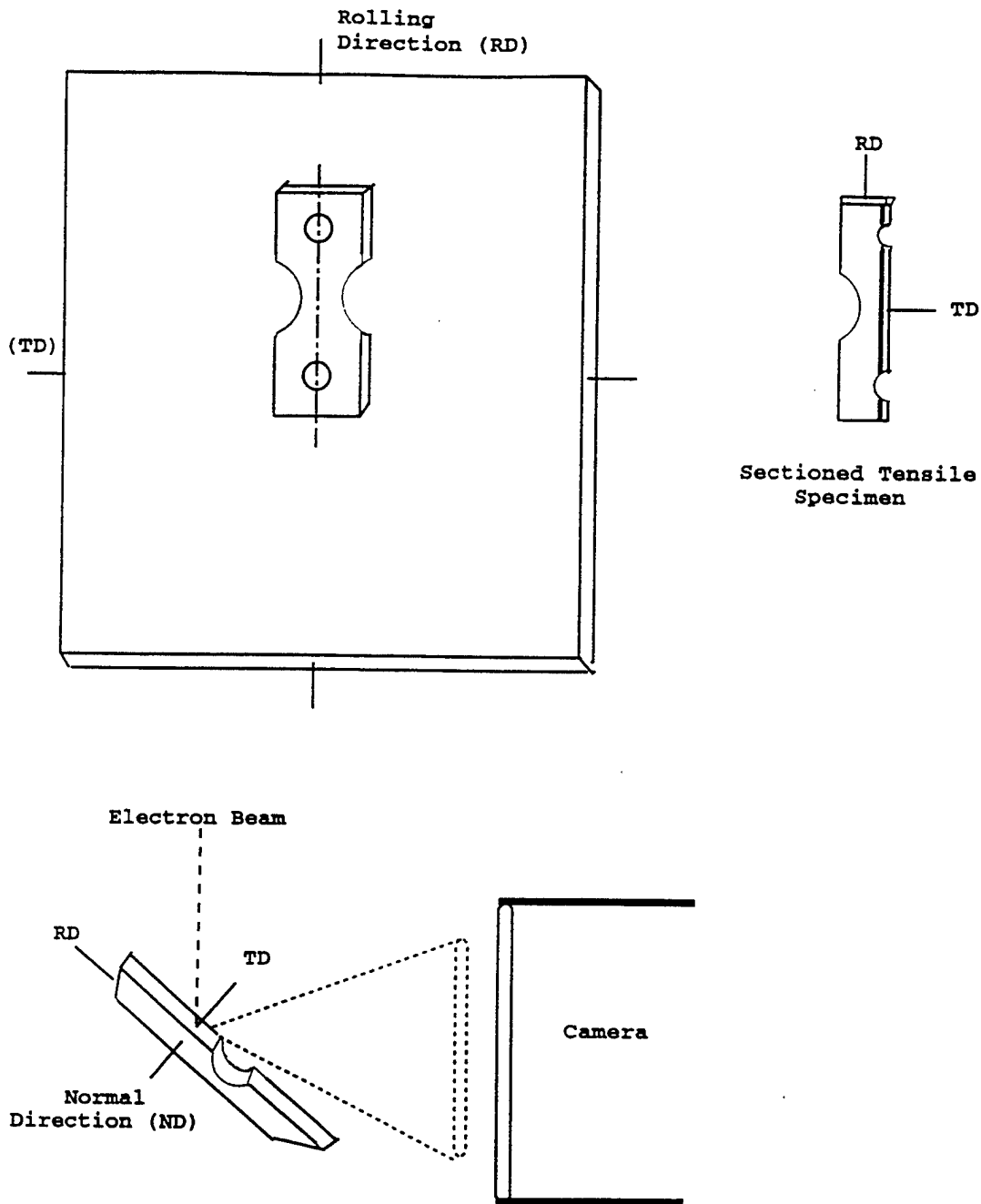


Figure 3.9. Schematic diagrams detailing the alignment of specimen axes for a sectioned tensile specimen. Here, a 90 degree rotation about the rolling direction is required to enable the rolling and normal directions to be in the plane formed by the camera axis and the incident electron beam.

focusing distortions. The electron beam spot was traversed down the specimen (capturing any change in the diffraction pattern) a distance of approximately two to three times the grain size, to avoid capturing the same (sub)grain information twice, to traverse back along another line of constant working distance.

Figure 3.10 illustrates a typical raster-type pattern used for data collection schematically superimposed on a representative BSE micrograph. Two data collection points, labeled (a) and (b), are indicated along with sequentially captured and indexed diffraction patterns. An image quality index is provided in the lower left corner of the indexed pattern and the three Euler angles which describe the crystal orientation relative to the specimen axes are listed in the lower right corner. Again, orientation images were captured sequentially with SEM voltage at 20KV by moving the spot of the electron beam pixel by pixel until a change in the diffraction pattern was noted. The distance between captured patterns was approximated by the distance the spot had been moved and these data may be recorded separately for each captured orientation. Nominally 500 orientations were collected in each EBSD data run.

Accuracy in the indexed solution is important if further analysis of nearest neighbor orientation data is to be accomplished to determine boundary information such as misorientation axis/angle pairs and identification of boundaries meeting CSL nearness criteria. Figure 3.11 shows a low-magnification micrograph of a region examined using EBSD methods described previously in a superplastically processed 5083 aluminum alloy. The data collection path is clearly visible. Some of the individual data collection points are visible on the path as white dots. Some specimen damage results from EBSD examination and this is a potential problem in some research applications.

Post-collection analysis of the orientation data was accomplished using the software. For microtextural analysis, discrete and contoured pole figures (iso-intensity contours normalized to random intensity) and discrete Euler plots were produced for each data set. Misorientation angle data in the form of histograms, representing the minimum rotation angle

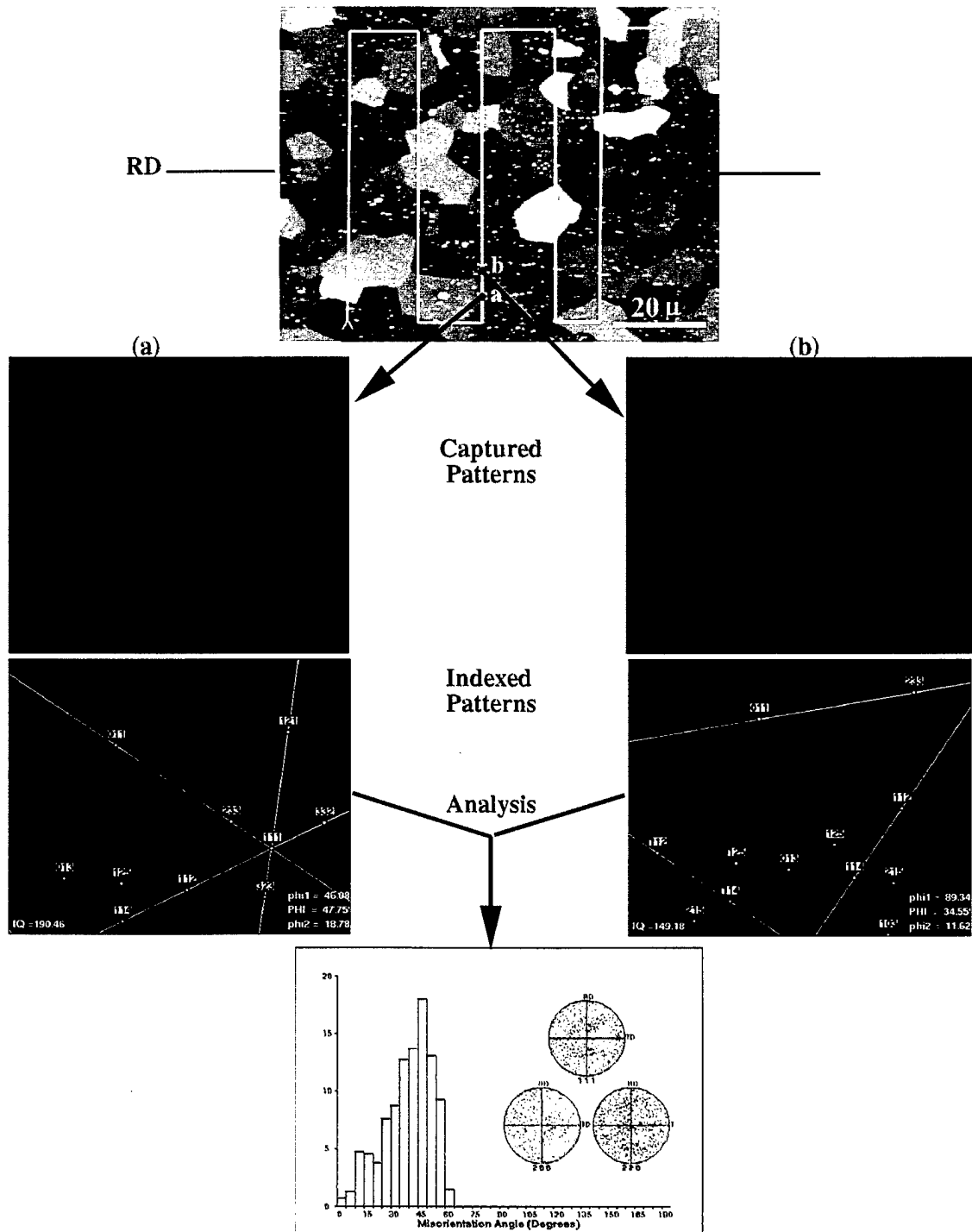


Figure 3.10. Illustration of the interactive EBSD method employed. Two sequentially captured patterns are collected and indexed. Subsequent analysis of the neighbor orientations produces the boundary information. Data illustrated here were collected from a commercial, superplastic 5083 aluminum alloy. The rolling direction is indicated.

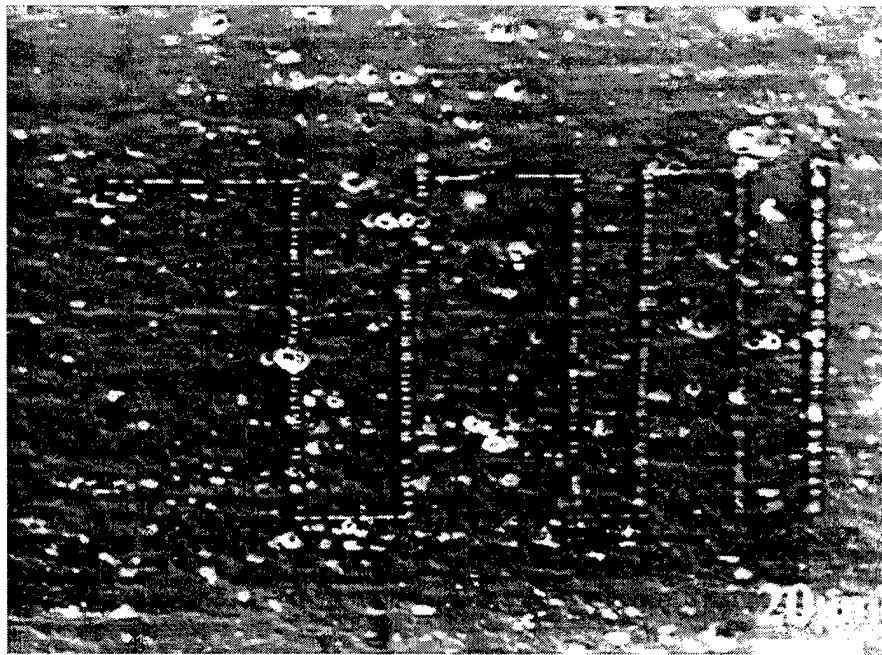


Figure 3.11. A SE image of a regions examined using EBSD.

about an arbitrary axis in order to bring neighboring orientations into coincidence, were produced as well as statistics of boundaries satisfying Brandon criteria for the coincident site lattice model [Ref. 75]. Misorientation data, which may be saved in an axis/angle format, may also be plotted on stereographic triangles to illustrate the distribution of rotation axes present in the examined region. Backscattered electron (BSE) images were acquired with specimens in a flat orientation (specimen normal parallel to the electron beam) to illustrate the microstructure present in the regions of the specimens examined, to examine grain morphology, and estimate the volume fraction, size, and dispersion of second phase particles. Grain size determinations were calculated using the mean linear intercept (MLI) method following Voort [Ref. 106] where the number of grain boundary intercepts, P , were measured for 10 lines with a total length L_{total} at a fixed magnification, M , for six backscatter electron

micrographs of different regions. The mean linear intercept was then calculated as $L_{MLI} = (1/P_L)$ where $P_L = (PM/L_{total})$. The average grain size, d_{av} , was then estimated $d_{av} = 1.773 L_{MLI}$.

D. ANALYSIS AND INTERPRETATION OF EBSP DATA

Collected EBSD data resides in a *.ang file produced by the system software. An example of the format of the data file is provided in Figure 3.12. Following the general information in the heading of the file, information for the specific orientations captured are listed line by line in the sequence as collected. The three Euler angles, ϕ_1 , ϕ , and ϕ_2 , expressed in radians in Bunge format [Ref. 107], are listed in the first three columns followed by two columns with zeros (they would contain the x and y grid coordinates of the captured orientation in a beam control system) then an image quality is listed (a "-1.0" value indicates the pattern was manually indexed), followed, lastly, by a remarks column for a user-defined label. If rotation matrices are applied to the data set a *_rot.ang file will be produced during the plotting procedures. All subsequent analysis utilizes the raw orientation data in the *.ang file. Details of the analysis of the EBSD orientation information will be discussed in the following sections.

1. Use of Orientation Information to Analyze Microtexture

Microtexture refers to the preferred orientation based on a grain-by-grain orientation examination. The formation of preferred orientation of crystals, or texture, in metals during solidification, deformation due to thermo-mechanical processing, annealing, recrystallization, and deformation during testing or forming has been studied extensively. In the thermomechanical processing and deformation of superplastic aluminum alloys, evidence of the mechanisms responsible for the microstructural development which enables superplastic flow may be discerned in the evolution of a complete texture description measured by direct orientation imaging. This may be possible because:

- Single and multiple slip processes on a restricted number of slip systems should result in a stabilization of texture in a limited number of orientations. This should be true for slip in response to applied stress during processing or during subsequent testing or forming. As an example, multiple slip on the $\{111\}\langle 110 \rangle$ system in aluminum alloys may be expected to lead to a $\langle 111 \rangle$ fiber texture and data demonstrating this for aluminum has been presented [Ref. 108].
- Twinning may be a significant influence in the development of texture. Twinning would be expected result in a 180° rotation about the twin plane normal. As the twin plane is the $\{111\}$ plane the 120° $\langle 111 \rangle$ symmetry in the fcc crystal results in rotation of 60° about $\langle 111 \rangle$. Evidence has shown that higher order twinning eventually leads to a complete randomization of texture and the production of boundaries with limited mobility [Ref. 69]. Populations of such boundaries in processed materials may influence the mechanical behavior during superplastic deformation if the deformation mechanisms involve grain boundary sliding.
- Components of texture associated with recrystallization should be discernable and from the texture of the deformation microstructure. Evidence of static, dynamic, or continuous recrystallization processes may be distinguishable from a study of the textural evolution. The formation of a cube texture, $\{001\}\langle 010 \rangle$, has been associated with discontinuous recrystallization of rolled fcc metals, for instance [Ref. 108].
- Mechanisms of deformation associated with superplastic flow, such as grain boundary sliding (GBS), are thought to involve grain rotations and slip accommodation resulting in a weakening of texture and a randomization of the distribution of orientations. Evidence of these processes may be discernable in microtexture of deformed regions in tested specimens.
- Studies have presented evidence that a relationship exists between grain orientation and grain boundary interfacial energies which may influence grain growth and grain boundary mobility [Ref. 99].

```
# WorkDirectory      /usr/people/naval/2519
# OIMDirectory       /usr/OIM
# x-star             296
# y-star             175
# z-star             430
# WorkingDistance    24
# MaterialName       fcc_generic
# Symmetry            43
# LatticeConstants   4.000 4.000 4.000 90.000 90.000 90.000
# NumberFamilies     4
# hklFamilies        1 1 1
# hklFamilies        2 0 0
# hklFamilies        2 2 0
# hklFamilies        3 1 1
#
0.433 0.246 1.472 0.000 0.000 136.7 0.000 01
1.614 1.019 0.338 0.000 0.000 119.7 0.000 02
2.639 0.469 4.974 0.000 0.000 135.6 0.000 03
1.860 0.234 6.088 0.000 0.000 97.7 0.000 04
5.164 0.166 2.580 0.000 0.000 101.2 0.000 05
5.148 0.174 2.596 0.000 0.000 152.7 0.000 06
2.783 0.708 5.116 0.000 0.000 112.9 0.000 07
2.786 0.706 5.117 0.000 0.000 129.1 0.000 08
0.820 0.662 0.866 0.000 0.000 121.7 0.000 09
1.208 0.153 0.078 0.000 0.000 116.5 0.000 010
2.088 0.078 5.368 0.000 0.000 92.8 0.000 011
1.279 0.679 0.744 0.000 0.000 123.4 0.000 012
6.238 0.550 1.861 0.000 0.000 117.8 0.000 013
2.721 0.582 5.727 0.000 0.000 84.4 0.000 014
1.862 0.689 0.125 0.000 0.000 139.1 0.000 015
1.658 0.623 0.043 0.000 0.000 157.4 0.000 016
1.781 0.660 6.163 0.000 0.000 126.3 0.000 017
0.472 0.460 0.239 0.000 0.000 115.9 0.000 018
1.528 1.009 6.182 0.000 0.000 129.0 0.000 019
1.287 0.854 6.167 0.000 0.000 134.1 0.000 020
2.016 0.269 0.202 0.000 0.000 99.5 0.000 021
1.605 0.526 5.979 0.000 0.000 134.4 0.000 022
0.931 1.090 1.233 0.000 0.000 124.5 0.000 023
2.471 0.532 5.979 0.000 0.000 120.3 0.000 024
0.412 0.246 1.491 0.000 0.000 129.2 0.000 025
1.605 1.011 0.339 0.000 0.000 123.9 0.000 026
1.579 1.151 0.167 0.000 0.000 118.2 0.000 027
1.593 1.100 0.159 0.000 0.000 124.6 0.000 028
2.570 0.826 5.494 0.000 0.000 134.8 0.000 029
5.979 0.698 1.990 0.000 0.000 150.2 0.000 030
5.147 0.171 2.595 0.000 0.000 123.4 0.000 031
2.786 0.706 5.117 0.000 0.000 129.8 0.000 032
1.707 1.320 5.657 0.000 0.000 145.1 0.000 033
3.707 0.306 3.762 0.000 0.000 150.4 0.000 034
1.708 1.319 5.659 0.000 0.000 139.9 0.000 035
3.738 0.307 3.726 0.000 0.000 123.8 0.000 036
0.745 1.221 0.118 0.000 0.000 73.0 0.000 037
1.311 0.935 0.203 0.000 0.000 120.6 0.000 038
0.743 1.223 0.117 0.000 0.000 114.4 0.000 039
3.697 0.527 4.366 0.000 0.000 96.6 0.000 040
```

Figure 3.12. Excerpt from an EBSD data file

Description of texture in metals has historically been presented by the use pole figures where the distribution of a certain type of pole is plotted onto a stereographic projection. The pole figure is referenced to an external set of axes to provide a visual relationship between the orientation of planes in the crystals to the reference material axes, such as rolling,

normal, and transverse axes for processed sheet material subjected to rolling. As such, the conventional pole figure does not describe individual crystal orientations directly but, rather, the distribution of selected planes for the orientation. The multiplicity of poles is reflected in the pole figure. Typically the three pole figures of lowest multiplicity are displayed. In the case of a fcc crystal the (200), (111), and (220) pole figures are often represented. Figure 3.13 schematically illustrates the construction of the pole figure. The macrotextural data used to construct the conventional pole figure is, typically, based on intensity data from x-ray diffraction from specified planes in a volume of material containing tens of thousands of grains. Pole figures may also depict discrete data, based on single EBSD measurements of individual orientations. Discrete pole figures may also be smoothed, where a smoothing function is used to produce iso-intensity contours of the pole distribution density. Smoothing and filtering methods to represent the discrete data have been reported by Matthies and Vinel [Ref. 109]. It should be mentioned that there are many other methods to obtain macro and microtextural data, a few of which were discussed briefly in section 3.1.

Alternately, the crystal orientation may be directly described by a series of three rotational operations to bring the external axes associated with the material being examined into coincidence with reference directions of the local crystal axes, $\langle 100 \rangle$, $\langle 010 \rangle$, and $\langle 001 \rangle$. Figure 3.14 illustrates the three operations to define the three Euler angles, ϕ_1 , ϕ , and ϕ_2 in the format developed by Bunge [Ref. 107]. Plotting crystal orientations in Euler space requires a three-dimensional display to plot the three Euler angles as Cartesian coordinates. In general, all possible orientations in Euler space fall within the range $0 < \phi_1 < 360^\circ$, $0 < \phi < 180^\circ$, $0 < \phi_2 < 360^\circ$. For cubic systems, all Euler angles vary from 0° to 90° . The Euler plot displays three-dimensional information in a two-dimensional format by plotting windows of constant ϕ_2 sections, usually in increments of 5 degrees, where ϕ_1 is plotted on the abscissa and ϕ is plotted on the ordinate.

EBSD systems permit the collection of orientation information from small regions of less than $1.0 \mu\text{m}^2$. The "micro-texture" of such a small region may be displayed by use of

discrete or contour Euler plots using the three Euler angles for each measured orientation. Figure 3.15 shows one of the "windows", $\phi_2=0^\circ$, of an Euler plot with the ideal crystal

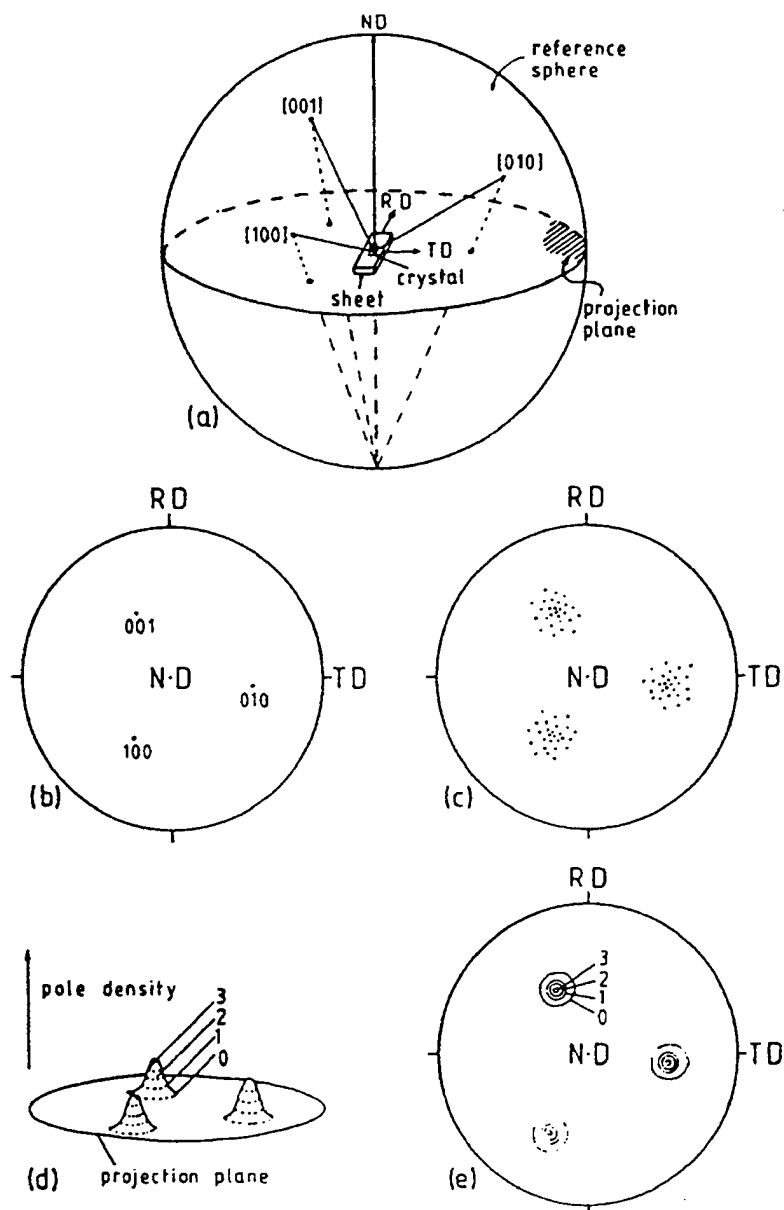
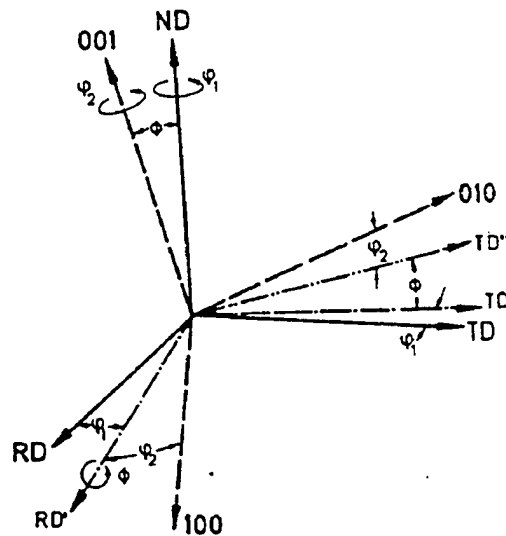


Figure 3.13. Illustration of the construction of a pole figure [Ref. 110].

orientations of the form $\{hkl\} \langle uvw \rangle$ superimposed onto the plot. Identification of some common ideal orientations, such as the $\{011\} \langle 211 \rangle$ Brass orientation, may be located in this manner. To facilitate the interpretation of texture in latter discussions, it is convenient to visualize the windows of constant φ_2 on the Euler plot being "stacked" onto each other to construct a three-dimensional cartesian set of axes and then to consider "fibers" or "tubes" of orientation running continuously through the sections. Figure 3.16 shows the Euler plot in a three-dimensional cartesian format with various fibers identified.

Alternate methods of displaying discrete orientation data are available including discrete inverse pole figures and the Rodriguez representation. In Rodriguez formulation, whether representing an single orientation or a misorientation across a boundary, a description



1. First a rotation of φ_1 about the normal direction (ND) transforms the original transverse direction (TD) and rolling direction (RD) to TD' and RD' . The magnitude of φ_1 is such that RD' is perpendicular to the plane formed by ND and the local crystal direction $[001]$.
2. A rotation φ about RD' such that the original ND is transformed into the $[001]$ crystal direction.
3. A third rotation φ_2 around ND' such that RD' is transformed into $[100]$. This also results in TD'' transforming into $[010]$.

Figure 3.14. Calculation of the three Euler angles.

using Rodriguez formulation involves the construction of a Rodriguez vector such that:

$$R = l \tan (\theta/2) \quad (17)$$

where θ is the net misorientation from the reference orientation and l is the vector of the directional cosines of the axis of the disorientation. In the case of Rodriguez vector to express an orientation, the reference orientations are the $\langle 100 \rangle$, $\langle 010 \rangle$, and $\langle 001 \rangle$ directions of the unit cube. In the case of the Rodriguez representation of a misorientation across a boundary, one of the neighbor crystal orientations is the reference and so it becomes simply an axis/angle description of the boundary in vector format.

In order to use discrete data consisting of individual orientation measurements to specify the texture representative of the material, clearly, a minimum number of individual orientations must be obtained to provide confidence that; (1) all texture components present in the bulk material are represented and (2) the texture components are described at or near

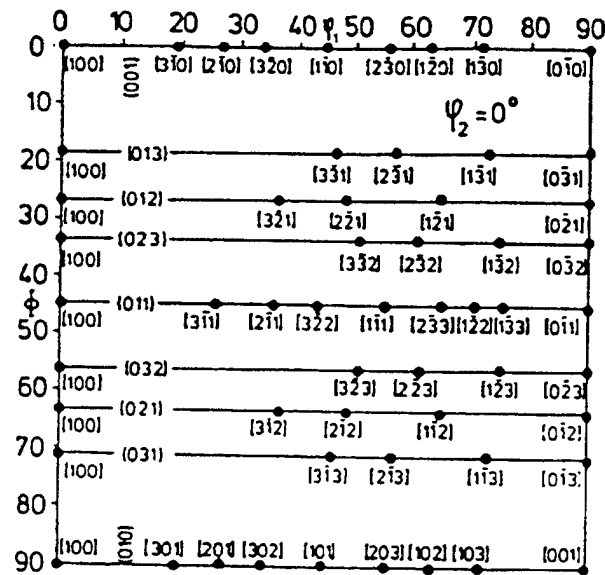


Figure 3.15. The $\phi_2=0^\circ$ section of an Euler Plot.

the correct intensity level in which they exist in the bulk material. This is particularly true for materials with only a moderate degree of texture strength. For the purposes of this research,

it was necessary to know the appropriate number of individual orientations to obtain for each data set before commencing data collection. This issue was addressed in investigations by Randle, Adams, and Wright [Ref. 111]. It was found that, for rolled aluminum, most texture components were identified in only 100 orientation measurements. Saturation of the intensity

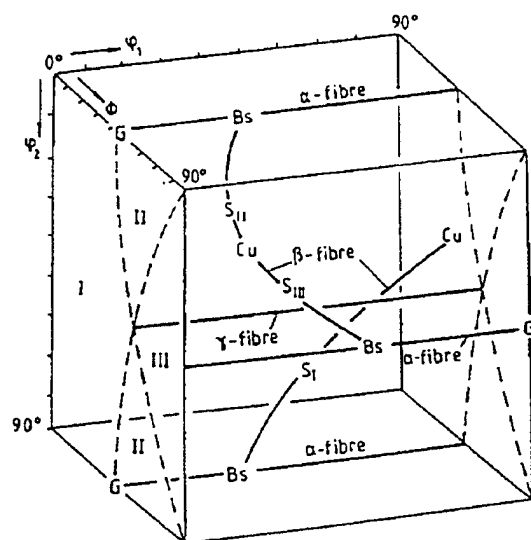


Figure 3.16. The Euler plot displayed in three-dimensional format with texture fibers shown.

levels of the individual components, however, required up to 750 orientations. Data was presented suggesting that, for a material of very weak texture, up to 2400 orientations may be required to match intensity peaks of the all texture components with continuous data from XRD. For the materials examined in the present research, with peak texture intensities from 2.0 to 6.0 times random, it was estimated that 500 orientations would correctly represent the texture components present in their represented intensity levels. This hypothesis was substantiated by a comparison of XRD intensity data with EBSD microtextural data for an Al-10Mg-0.1Zr TMP6 data set for which XRD data was known.

2. Use of Orientation Information to Analyze Mesotexture

Mesotexture refers to the grain boundary information resulting from the analysis of microtextural information. Individual orientations gathered utilizing EBSD may be, if the orientation data points are neighboring points, analyzed to obtain information about the character of the boundary, or degree of disorientation if there is no boundary, that exists between the two points. As in orientation information, the grain boundary character may be described in terms of Euler angles, axis/angle pairs describing the minimum rotation about an arbitrary axis to bring the two orientations into coincidence with consideration of crystal symmetry, or in terms of a Rodriguez vector. It should be stated that five degrees of freedom must be specified to completely define a unique boundary; the directional components of the axis of the misorientation, the magnitude of the angle of misorientation, and the normal of the plane of the grain boundary. Mesotextural data from analysis of orientation information does not provide information on the boundary plane normal. Calculation of the boundary plane normals is possible using serial sectioning techniques in the SEM, stereo viewing with Kikuchi line analysis in the TEM, and other techniques [Ref. 103]. These methods require difficult specimen preparation and are limited, in that information is usually obtained at a rate of only tens of boundaries examined per day. Characterization of boundaries, without specification of the boundary plane normal, may be accomplished through comparisons of orientations to fix the four degrees of freedom associated with the axis/angle pair and may be conducted using computer-aided EBSD systems to describe the thousands of boundaries possible in an EBSD data set.

By selecting to extract misorientation data from the *.ang data file the user may calculate misorientation data for pairs of data points (i.e., #1-#2, #3-#4, and so on) or sequentially analyze all data in sequence (i.e., #1-#2, #2-#3, and so on). A misorientation file is created, *.mis, in either Euler angle, axis/angle pair, or Rodriguez format. The boundary misorientation may be calculated by forming a boundary misorientation matrix, ΔG , which rotates the previously calculated grain misorientation matrix, G , of one (sub)grain onto the

grain misorientation of the adjacent (sub)grain with consideration of the crystal symmetry or:

$$\Delta G = G_1 G_2^{-1} \quad (18)$$

The orientation matrix for cubic crystal systems may be equivalently expressed in 24 ways. The misorientation matrix that is selected is that which results in the smallest magnitude of rotation about any arbitrary axis in an axis/angle representation.

Further analysis of the misorientation data may also be accomplished to identify special boundaries fulfilling user-defined nearness criteria to coincident site lattice inverse density values, Σ . The Brandon criterion, $\Delta\theta = 15^\circ/(\sqrt{\Sigma})$, is the default nearness criterion, where $\Delta\theta$ is the maximum deviation from exact coincidence; 15° is the magnitude of boundary misorientation in the Read-Shockley model [Ref. 75] where dislocation spacing in the boundary network is reduced such that dislocation cores overlap and description of a boundary by dislocation models is assumed to be invalid.

Graphical representation of misorientation data may be made by use of misorientation histograms or McKenzie plots. A Rodriguez misorientation plot in Rodriguez-Frank space may also be used to graphically depict misorientation data in three dimensions. Histograms detailing the distribution of boundary misorientation by displaying the misorientation range on the abscissa and the fraction of boundaries on the ordinate may be displayed using the boundary misorientation data calculated sequentially from the collected orientation data. Such data may be termed uncorrelated in that the misorientations calculated from neighboring orientations are displayed without consideration to the influence of texture in the population of orientations present in the data set. In the course of this research, an algorithm was proposed to obtain an uncorrelated distribution of misorientation from the collected EBSD data set. The scheme involved comparison of each orientation with all orientations in the data set to produce boundary misorientation data. In a 500-orientation data set, for example, the first orientation data point would be compared to numbers 2 through 500 to yield 499

boundaries. The complete data set would then yield 499^2 or 249,001 boundaries. The distribution of this large data set would then provide an uncorrelated distribution reflecting the influence of preferred orientation in the distribution of boundaries.

McKenzie calculated the uncorrelated probability distribution of misorientation for randomly-oriented neighbor cubes based on geometrical considerations only [Ref. 112]. Comparison of the uncorrelated misorientation distributions with the correlated distribution and geometrical distribution of McKenzie may provide evidence of mechanisms responsible for the evolution of boundaries during processing and deformation. The distribution of rotation axes may be also plotted for all misorientation ranges based on the axis/angle data in the misorientation file.

E. ACCURACY, SOURCES OF ERROR AND LIMITATIONS

The intent of this brief section is to identify EBSD system limitations and establish the accuracy and error associated with the EBSD system hardware and examination methods utilized. Accuracy and sources of error, in general, of EBSP analysis have been discussed by Randle [Ref. 103].

1. Limitations Imposed by the EBSD System

Clearly, the EBSD system components influence the accuracy of the results. Improved low-light cameras may improved the signal strength provided to the image analyzer and reduce any non-linearity in the low-light camera used in the system to collect the back scatter electrons. The source of electrons in the SEM, by field-emission, LaB_6 filament or W filament, will influence the intensity, stability, and energy coherency of the electron beam. Additionally, the spatial resolution required to obtain an EBSP from as small a volume as possible is influenced by working distance, accelerating voltage, probe current, and specimen tilt angle. For the present research on specimens examined at the Naval Postgraduate School, ingot metallurgical specimens with a grain size $\geq 1\mu\text{m}$, a tungsten filament was utilized.

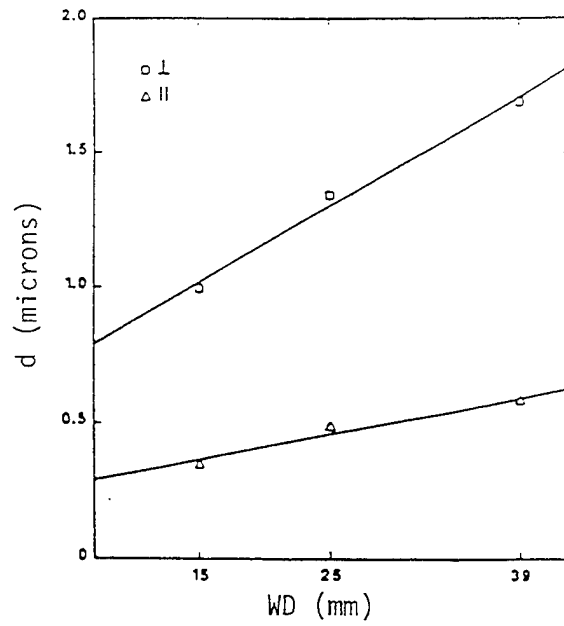
The variation of spatial resolution for EBSD has been summarized by Randle [Ref.

103]. Figures 3.17 (a) and (b) illustrate the variation of spatial resolution with working distance and accelerating voltage in aluminum. The optimum spatial resolution for the aluminum alloys is estimated to be $0.7\mu\text{m}$.

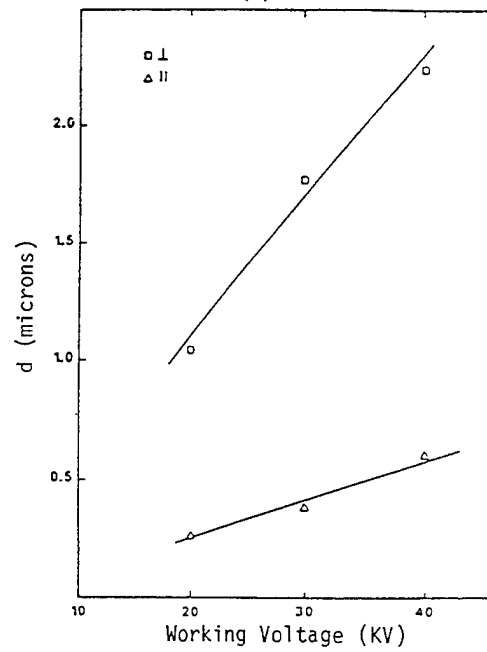
2. Limitations and Error Imposed by the User and Examination Methodology

Interactive EBSD examination, unlike automatic mapping systems using beam control, are sensitive to the user proficiency. Specimen positioning errors may be made in the initial placement of the specimen in the EBSD holder. The surface of the specimen being examined must be normal to the camera axis. As specimen size is typically small, any deviation from a normal orientation to the camera axis may result in a error of several degrees in the EBSP pattern. This error may be compensated for by applying a rotation matrix to the collected data. Such an error, if uncompensated, would only effect the microtextural analysis and not the mesotextural data. As previously stated, maintenance of accurate calibration parameters is essential to precise indexing of the EBSP. Focusing distortions, resulting in poorer quality EBSP's, may result unless refocusing is accomplished each time the working distance is varied.

For the method and materials in this research, it is estimated that misorientation changes $\geq 2^\circ$ could be consistently be identified, even for lower quality EBSP's. In specimens with a higher residual strain in the crystal lattice the EBSP may become diffuse with lower intensity and broadening/blurring of the Kikuchi bands. The rotation and/or translation of the two-dimensional backscattered diffraction pattern resulting from a change in orientation of less than 2° was not reliably discernable in these specimens.



(a)



(b)

Figure 3.17. The variation of spatial resolution, d (μm), for EBSD in aluminum (a) with accelerating voltage and (b) with working distance at standard SEM working conditions of 20KV accelerating voltage, 15mm working distance, and a specimen tilt of 70° [Ref. 103].

IV. MICROTTEXTURE AND BOUNDARY DEVELOPMENT DURING PROCESSING AND SUPERPLASTIC DEFORMATION OF Al - 10.0 wt% Mg - 0.1 wt% Zr

A. INTRODUCTION

Previous research [Ref. 50-53, 62] to examine the microstructural development during superplastic thermomechanical processing (TMP) involving warm rolling at 300°C of an Al-10Mg-0.1Zr (wt%) alloy has described the development of refined microstructures in the processed material. For optimum processing conditions cavitation-free tensile elongation of more than 1100% were obtained at 300°C and a strain rate of $2 \times 10^{-3} \text{s}^{-1}$. This research has also illustrated that one modification to the TMP scheme, decreasing the inter-pass anneal (IPA) time from 30 minutes to 5 minutes between successive rolling passes, resulted in a peak elongation of only 280% at 300°C and a strain rate of $4 \times 10^{-4} \text{s}^{-1}$ (Figure 1). Fully annealed material exhibited a peak elongation of 180%. Similarities in the microstructure of the as-processed material for both IPA times included features normally associated with successful superplastic processing such as a refined microstructure ($<5 \mu\text{m}$ mean linear intercept (MLI)) and the presence of a dispersed phase. The principle dispersed phase is the β (Al_3Mg_2).

While a fine grain size and a uniform second-phase dispersion are generally recognized prerequisites in superplastic materials, the character and mobility of grain boundaries are considered to be important factors as well [Ref. 2]. Fine dispersions of second-phase particles have been associated with the control of grain growth by the pinning of boundaries during superplastic deformation, generally at temperatures above $0.5T_m$, of fine-grained materials. Second-phase particles have also been associated with the recrystallization process required to achieve a superplastic microstructure. Humphrey's model [Ref. 25] for particle-stimulated nucleation (PSN) of recrystallization details mechanisms for formation of new grains near larger, non-deforming second-phase particles in deformed aluminum and describes a relationship between particle size and strain for PSN. Recrystallization of aluminum alloys to achieve microstructures capable of supporting superplastic flow may occur during the TMP

or during the superplastic deformation [Ref. 108].

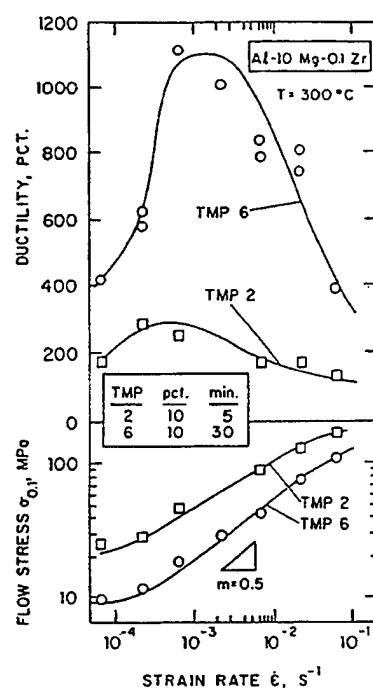


Figure 4.1. Mechanical property data illustrating the variation in mechanical behavior at 300C for the two processing schedules [Ref. 51].

The roles of grain boundary mobility and structure in superplastic flow have not been as well defined. Grain boundary mobility is important in nucleation and growth of new grains, primarily in influencing the growth rate of new grains during recrystallization [Ref. 23-24, 68]. Grain boundary structure, or character, has been described using the coincident site lattice (CSL) model [Ref. 113]. Special boundaries, satisfying nearness criteria to CSL relationships, have been associated with distinct interfacial energy values, rates of mobility, and deformation rates involving mechanisms associated with superplastic flow, such as grain boundary sliding (GBS) [Ref. 30]. It has generally been thought that random (disordered) high angle boundaries (HABs) are desirable for superplastic flow by GBS while low-energy

boundaries, such as coherent twin boundaries, are nearly immobile and do not support superplastic deformation by GBS. Models for GBS have included boundary migration and diffusional accommodation processes but the influence of the ordered structure of special grain boundaries has not been fully distinguished.

Recent research on the alloy of concern in this study has considered the role of boundaries in facilitating superplastic behavior. These studies have been conducted by transmission electron microscopy (TEM) using convergent beam operation in obtaining Kikuchi patterns for neighbor (sub)grains in order to characterize the axis and angle of misorientation for each boundary [Ref. 52, 62]. Table 4.1 provides a summary of the microstructural data obtained via TEM in relation to the mechanical property data for the two TMP routes. Results suggested that high-angle grain boundaries in less ductile material (TMP2, processed with a brief IPA time) were dominated by twin-related boundaries ($\Sigma 3^n$) formed by the twin-chain mechanism. About 18% of boundaries were of less than 5° misorientation. In the more ductile material (TMP6, processed with a longer IPA time) a higher proportion of random high angle boundaries were observed and special boundaries corresponding to the $\Sigma 7$ CSL relation were observed. The difference in uniaxial tensile behavior of the material processed according to the two schedules was ascribed to differences in the grain boundary character distribution and, specifically, the distribution of CSL boundaries.

TMP Route	IPA Time (at 300°C)	Peak Elongation to Failure	Strain Rate	Grain Size (MLI)	Dominant CSL Boundary	Vol. Pct. of β Phase in the As-Processed Condition
2	5 min	280%	$4.5 \times 10^{-4} \text{s}^{-1}$	2.3 μm	$\Sigma 3^n$	2%
6	30 min	1100%	$2.0 \times 10^{-3} \text{s}^{-1}$	2.4 μm	$\Sigma 7, \Sigma 21$	10%

Table 4.1. TMP and Microstructural Data for Al-10Mg-0.1Zr Deformed at 300C.

The limitations of such a study by TEM are that a small region of a thin foil is analyzed and thus relatively few (sub)grains (~ 50) may be examined. In this study, computer-aided Electron Back Scatter Pattern (EBSP) techniques are employed to investigate the role of grain orientation and grain boundary character in these materials.

B. EXPERIMENTAL PROCEDURE

The alloy composition has been previously cited as Al-9.89Mg-0.09Zr (wt%). Figure 4.2 schematically details the thermomechanical processes describing the TMP2 and TMP6 schedules [Ref. 51]. Total true strain for both processes was 2.5. In preparation for EBSP analysis, deformed tensile specimens from each of the TMP2 (5 minute inter-pass anneal) and TMP6 (30 minute inter-pass anneal) materials were sectioned longitudinally along the tensile axis to reveal the through-thickness direction of the processed and tested coupons. The selected specimens were those exhibiting the maximum elongation for each of the two TMPs (Table 4.1). The through-thickness sectioned surface was polished and then electropolished in preparation for EBSP examination using the procedures previously described. Tensile specimens were oriented such that the rolling direction was always in the plane of the electron beam and the camera axis. Tensile testing had been conducted along the rolling direction of the material from which the tensile coupons were extracted. As-processed material (without annealing) was also sectioned and examined in the through-thickness direction. For the EBSD examination, 400-500 orientations were collected in the in the as-processed material, in the undeformed grip section of each tensile specimen and at a position approximately halfway between the shoulder and point of fracture in the deformed gage sections. Back-scatter electron (BSE) microscopy using low accelerating voltage to obtain grain orientation contrast was utilized to detail the microstructure and calculate grain size (MLI) with the specimen in a flat position normal to the electron beam. Standard quantitative microscopy methods utilizing line-intercept methods were used throughout all research to estimate average MLI in this manner [Ref. 106]. Analysis of the orientation data was accomplished

using methods previously described.

C. RESULTS

1. Microstructure of Areas Examined

The microstructure of the four regions examined in this study are presented in Figures 4.3 (a) through (d). Results of quantitative microstructural analysis of as-processed TMP2 and TMP6 materials were summarized in Table 4.1. The undeformed grip regions of the

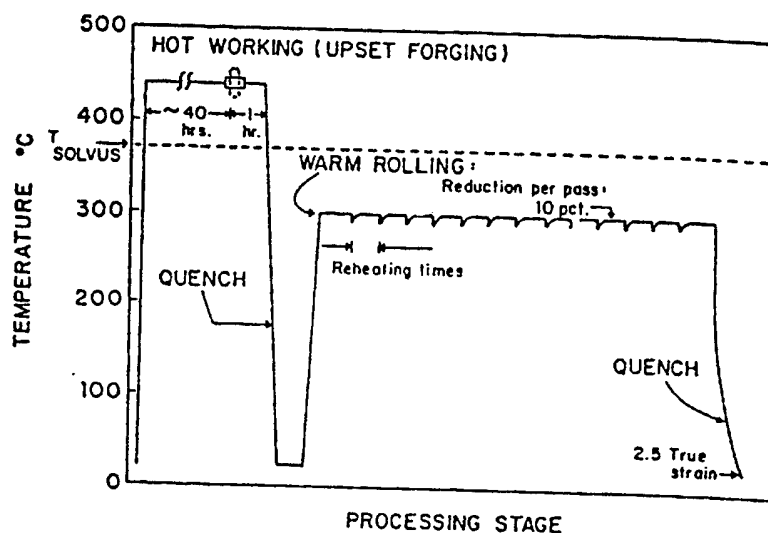


Figure 4.2. Schematic diagram detailing the processing routes TMP2 (5 minute inter-pass reheat time) and TMP6 (30 minute inter-pass reheat time) [Ref. 51].

specimens examined in the current study have experienced more time at temperature than the undeformed as-processed material due to continued annealing during tensile testing at 300°C. Examination of the micrograph of Figure 4.3(a) indicates, however, that the distribution of the β -phase along prior boundaries, observed previously, is still evident. The amount of β -phase has increased from the as-processed TMP2 value of about 2.0 vol. pct. toward the equilibrium value of 10 vol. pct. at 300°C that was observed in the as-processed TMP6

material. Fine, grain boundary β -phase particles that were evident on prior boundaries in the as-processed TMP2 material have coarsened and spheroidized. In Figure 4.3(b), the TMP6 grip material, the grain (sub)structure is well defined, uniform in size, and equiaxed. The β -phase is uniformly distributed near triple points throughout the microstructure and the rolling direction is not readily discernable in the microstructure. Comparison of the deformed gage sections of the TMP2 and TMP6 specimens, Figures 4.3(c) and (d), reveals greater similarities than evident in the undeformed grip sections. While the β -phase appears to be present in

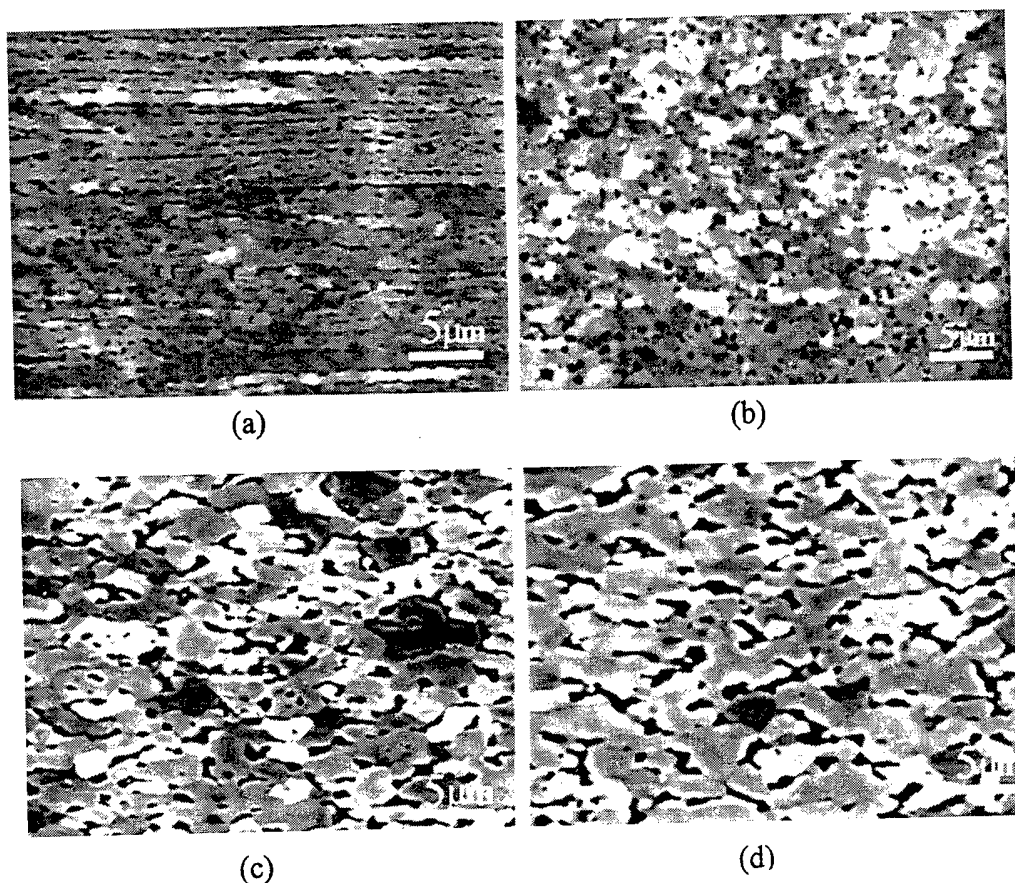


Figure 4.3. BSE micrographs of the regions of deformed tensile specimens examined in this study; (a) TMP2 grip, (b) TMP6 grip, (c) TMP2 gage, and (d) TMP6 gage. The rolling (tensile) direction is horizontal (orientation contrast at 5KV working voltage, no etchant).

nearly the same amount in both gage sections, the particles are of smaller size in the TMP2 material. Some grain growth is evident in both deformed specimens.

2. Microtexture

Microtextural data for the as-processed TMP2 material is presented in Figure 4.4. Smoothing contours illustrated in the contour pole figures have been calculated from the discrete data. The orientations plotted on the discrete Euler plot illustrate that the texture in the as-processed TMP2 material may be described primarily by only two deformation texture components, brass, $\{110\}\langle 112 \rangle$, and S, $\{123\}\langle 634 \rangle$. The spread of orientations is small and all orientations captured are close to the ideal orientation for these two deformation texture components. The S component is slightly stronger than the brass component, as evidenced by the larger number of orientations near the ideal S orientation on the Euler plot. Orientations near the copper component, $\{112\}\langle 111 \rangle$, are also evident and this can be seen in the $\phi_2=25^\circ$ window of the Euler plot. The texture of the as-processed TMP2 material may then be described as deformation texture which extends along the β -fiber and is characteristic of aluminum rolled to a high strain at moderate to low temperatures where limitations on the number of available slip systems and twinning are evident. The texture reflects the processing schedule which consisted of a 5 minute IPA for 12 passes and resulted in a cumulative total time of 60 minutes at a moderate temperature of 300°C . There is no evidence of any recrystallization components. The texture for the as-processed TMP6 material, shown in Figure 4.5, is distinctly different from the TMP2 but remains primarily a deformation texture. Orientations near the brass and S components are still evident. However, there is a stronger copper component in the texture and orientations near the deformation texture component S/B, $\{168\}\langle 211 \rangle$, are evident in the $\phi_2=80^\circ$ window of the discrete Euler plot. There are a few recrystallization orientations present, primarily the recrystallized brass component, Bs_{Rxx} , $\{113\}\langle 112 \rangle$. The stronger copper component of the texture would be expected due to a longer time at elevated temperature enabling the activation of additional slip systems leading to octahedral slip. Peak intensity from the contour pole figures constructed from the discrete

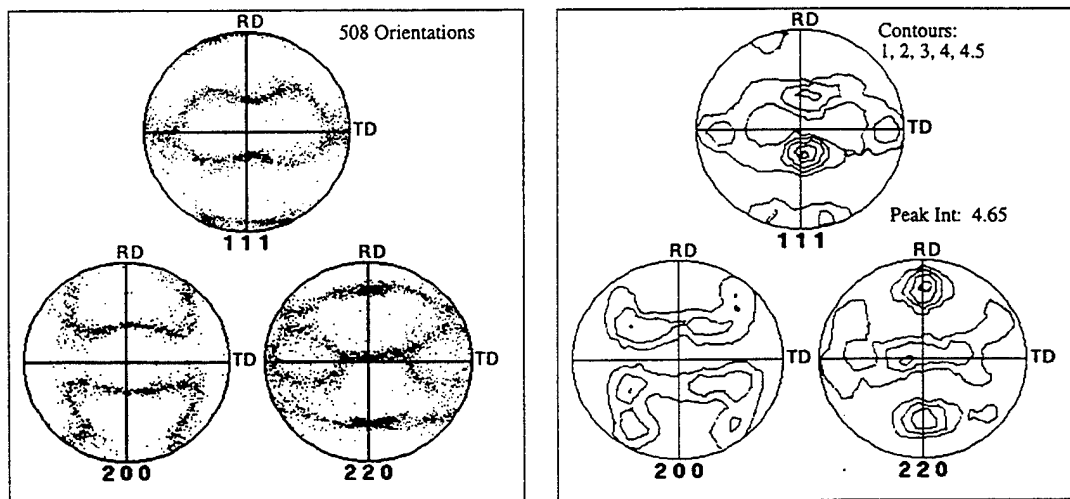
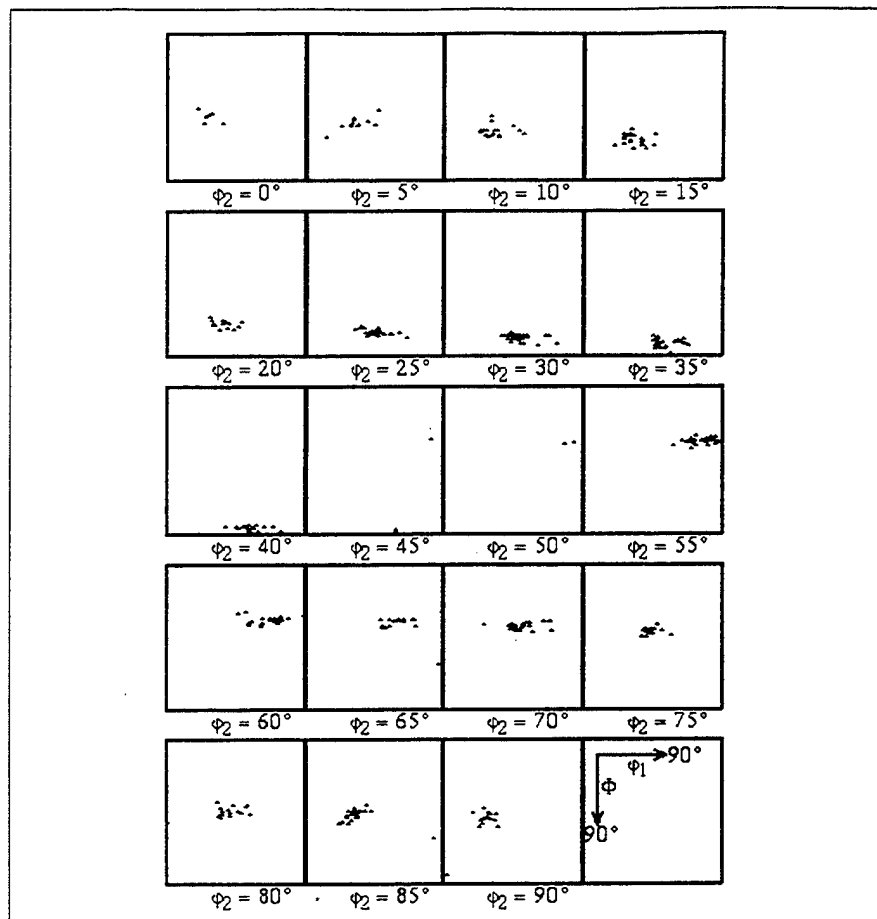


Figure 4.4. The discrete Euler plot, discrete pole figure, and contour pole figure detailing the microtexture in the *as-processed* TMP2 material.

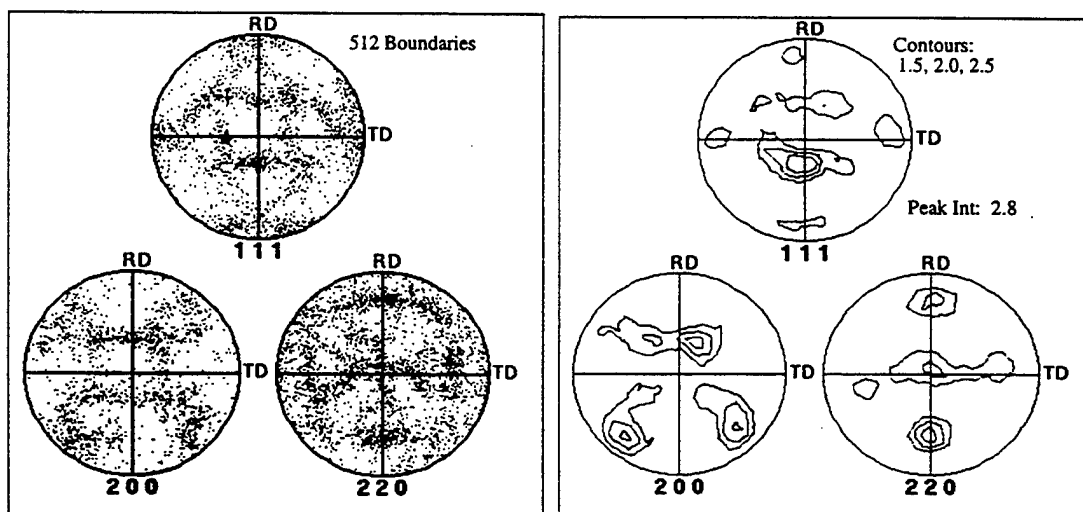
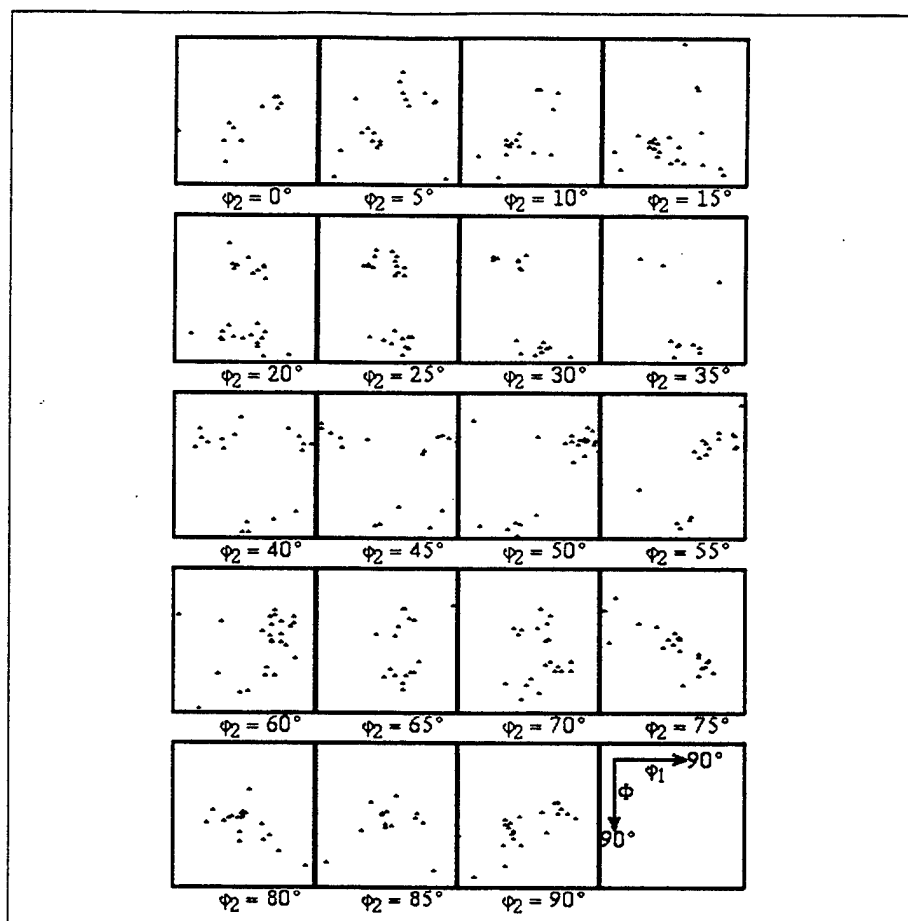


Figure 4.5. The discrete Euler plot, pole figure, and contour pole figure detailing the microtexture in the *as-processed* TMP6 material.

plots suggest the texture is weaker in the TMP6 as-processed material with a peak intensity of 2.8 times random for a 500 orientation data set. Peak intensity for the TMP2 material was 4.65 times random.

Microtexture data for the *undeformed grip sections* (which correspond to a processed and annealed condition) of the TMP2 and TMP6 tensile specimens in the form of discrete pole figures, discrete Euler plots and contour pole figures calculated from the discrete data, are presented for comparison in Figures 4.6(a) and (b). Inspection of the data for the undeformed grip sections indicates that, at the completion of the processing and subsequent annealing at 300°C, the texture is again similar for both TMP2 and TMP6. Most orientations present are near the two deformation texture components brass, $\{110\}\langle 112 \rangle$, and S, $\{123\}\langle 634 \rangle$, but more are near the copper orientation, $\{112\}\langle 111 \rangle$. There are also a few orientations in the vicinity of the recrystallization component R, $\{241\}\langle 112 \rangle$. There is no evidence of a cube component for either process. Additionally, there are no orientations unique to either process. Although the discrete data indicates that there is clearly more spread about the orientations present in the TMP6 material, peak intensity from contour plots calculated from the discrete data indicate a maximum intensity of about 4.3 times random in both cases. The spread in orientations in the TMP6 specimen appears to be concentrated about the aforementioned texture components.

The S and brass orientations have been associated with aluminum alloys deformed to high strain at moderate temperatures. The texture present in the grip sections follows the texture predicted by the Hirsch and Lucke "SC" model which modified Taylor theory by relaxing two of the shear components, ϵ_s and ϵ_c (the transverse and rolling shear components), and is reported to describe the texture developed following severe rolling schedules at moderate temperatures in aluminum alloys [Ref. 114]. Retention of deformation textures in aluminum after annealing has been reported before as has the absence of cube or rotated cube texture in deformed FCC metals following annealing [Ref. 115-116].

Figures 4.7(a) and (b) illustrate the microtexture data obtained from the *deformed*

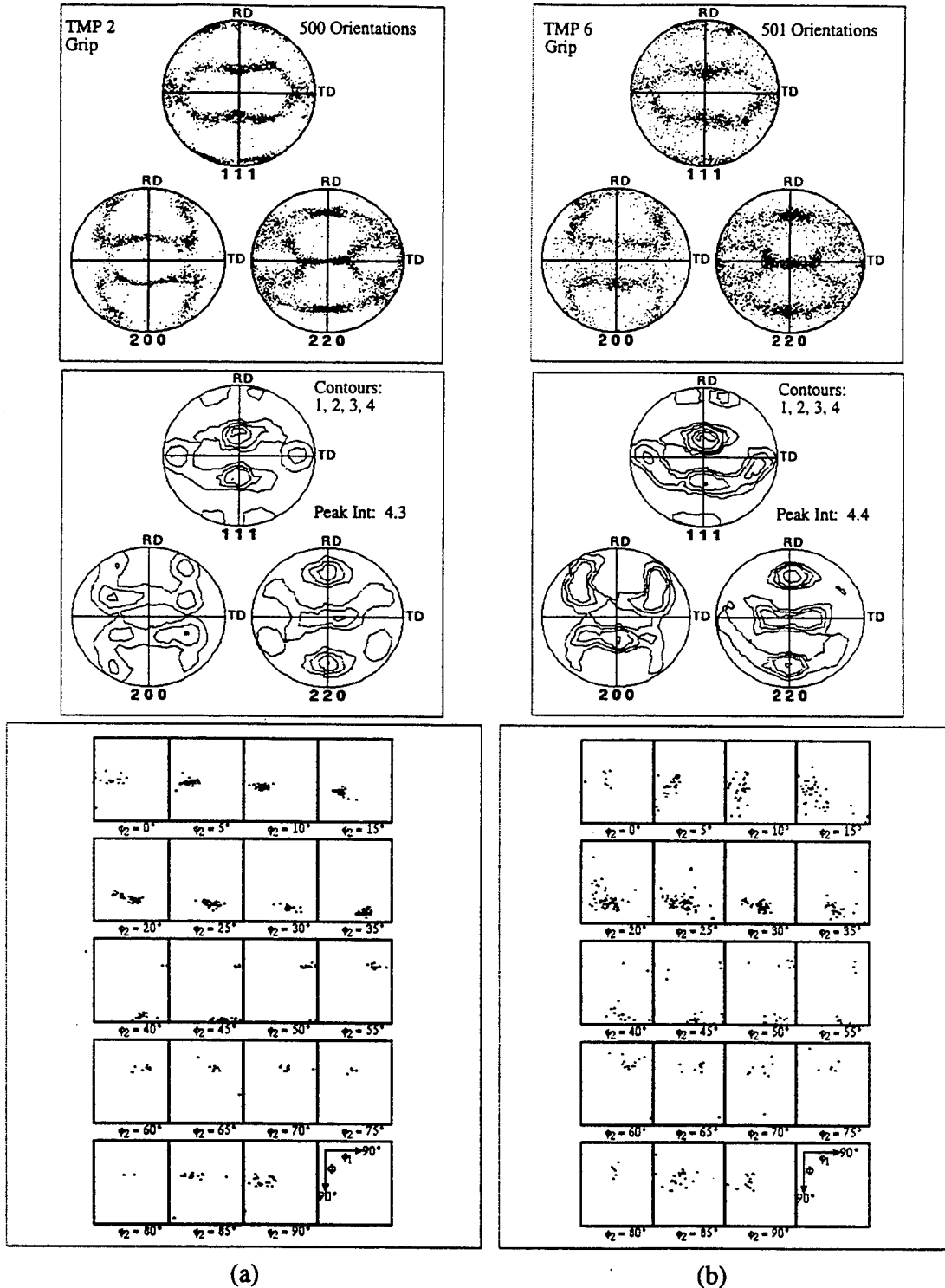


Figure 4.6. Microtexture plots for *undeformed grip sections* (processed and annealed) of (a) TMP 2 and (b) TMP 6 specimens.

gage sections of the tensile specimens from TMP2 and TMP6 processed material. Analysis of the contour plots constructed from the discrete data reveals that the same components of texture are present but with lower intensity. Peak intensity from contour pole figures calculated from the discrete data is approximately 3.0 times random in both cases. Extensive grain rotation has occurred during the deformation as evidenced by the spreading of orientations around the texture components observed in the undeformed grip regions as well as the weakening of the texture components. Randomizing of texture is also evident in that orientation space is becoming more uniformly filled. Such randomizing of orientations resulting in a weakening of texture is characteristic of grain rotations in material deforming by GBS [Ref. 108]. However, multiple twinning has also been shown to result in the randomizing of texture [Ref. 69].

There is no evidence of the formation of a distinct fiber texture in the deformed regions of the less ductile TMP2 specimen. A fiber texture would be expected if deformation by slip were significant. Edington [Ref. 22] discusses changes in texture expected from random grain rotation, recrystallization processes, slip deformation, and accommodation of GBS by slip processes.

3. Boundary Character Data

Figures 4.8 illustrates the distribution of boundary misorientation for the regions examined. Boundary misorientation in these plots is the minimum rotation angle about a common axis to bring the respective crystals into coincidence considering crystallographic symmetry. The dotted line indicates the continuous plot of a random distribution of misorientations predicted by Mackenzie [Ref. 112]. Again, the fraction of boundaries between $0-5^\circ$ is known to be understated due to the difficulty in identifying orientation changes of less than 2° . In the as-processed materials, a similar distribution of boundary misorientation is evident in the plots for the TMP2 and TMP6 materials. One distinguishing feature is the large fraction (0.21) of boundaries near 60° (in the $55^\circ - 62.7^\circ$ range) in the as-processed TMP2 material. Both of these distributions contain a significant fraction (0.22) of

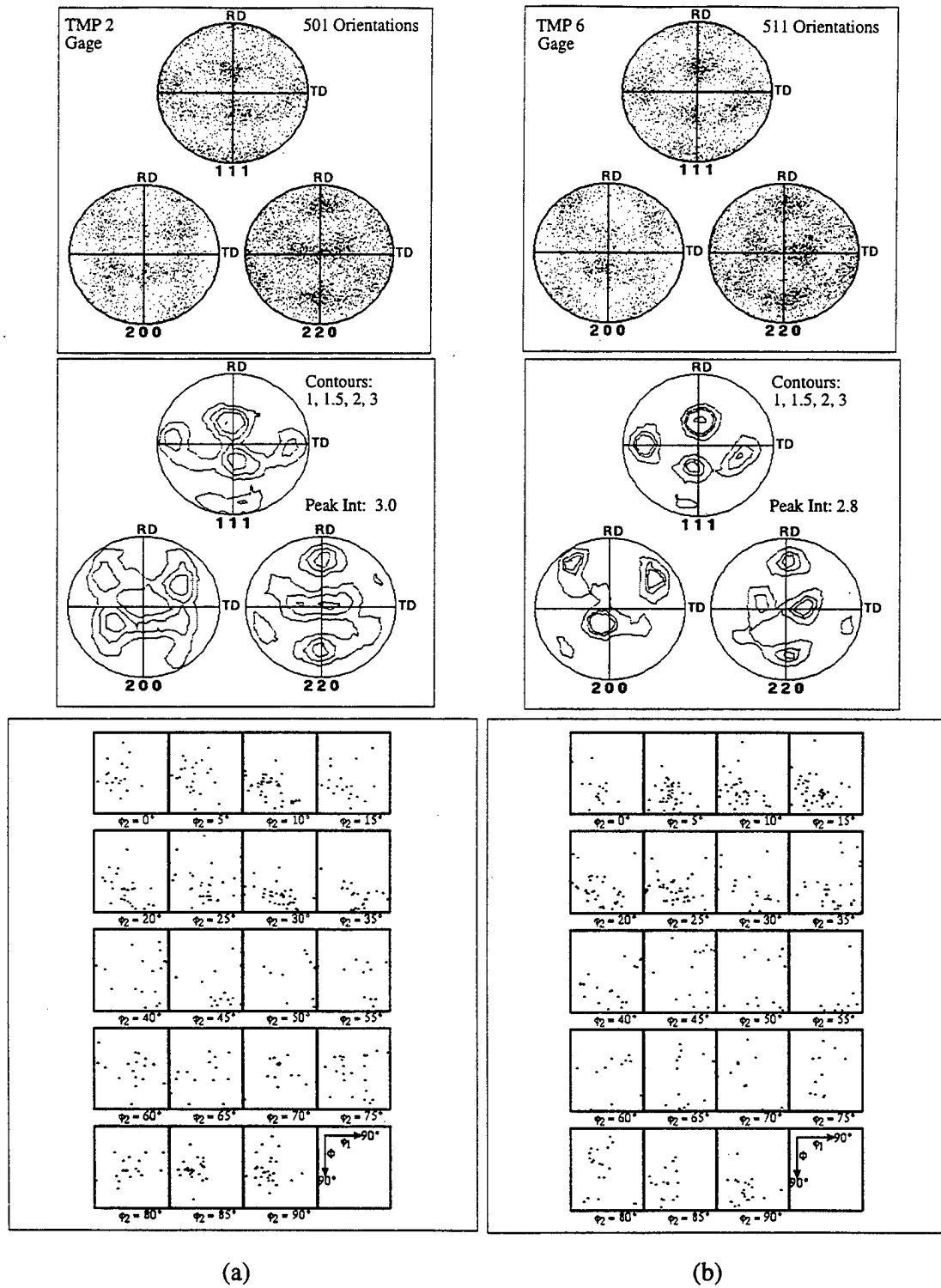


Figure 4.7. Microtexture plots for *deformed gage sections* of (a) TMP2 and (b) TMP 6 specimens.

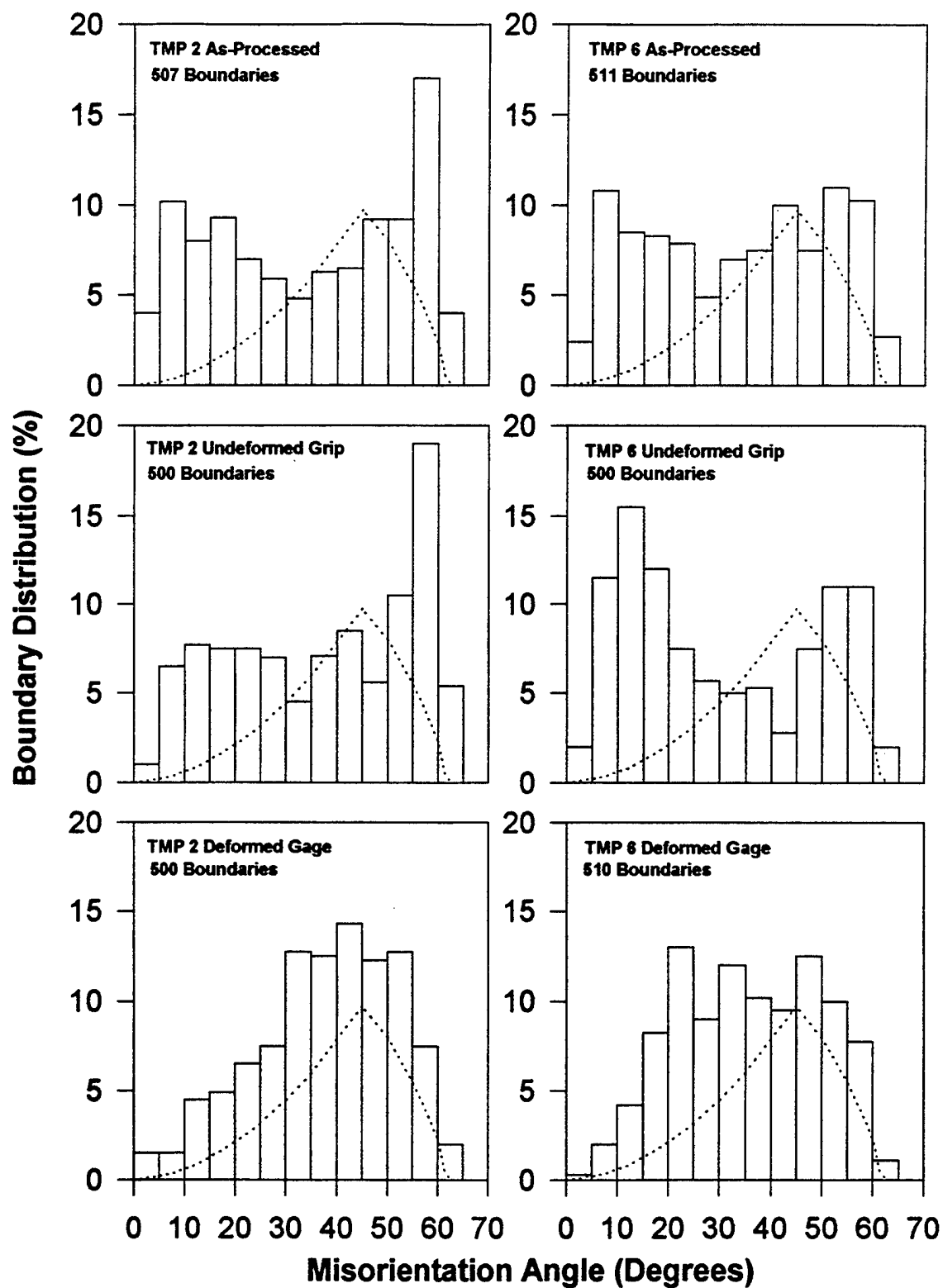


Figure 4.8. Misorientation histograms for the specimens examined.

boundaries in the 2° - 15° misorientation range and do not reflect distributions typical of a recrystallized microstructure where a predominance of HAB's exists. The mesotextural evidence is in agreement with the microtextural evidence and suggests that the alloy does not recrystallize during either TMP.

In the *undeformed TMP2 material* there is a larger fraction (0.23) of boundaries observed near 60° misorientation. These boundaries may be near the $\Sigma 3$ CSL ($60^{\circ}/\langle 111 \rangle$) twin boundary although not all may satisfy the restrictive nearness requirement of the Brandon criteria. Fig 4.9 illustrates the distribution of rotation axes for boundaries in the 55° - 62.7° misorientation range for undeformed TMP2 material. Additionally, 8% of all boundaries in the TMP2 grip specimen have misorientation between 35° - 40° and this group would contain boundaries near the second-order twin, $\Sigma 9$ ($38.9^{\circ}/\langle 110 \rangle$) and the third-order twin $\Sigma 27b$ ($35.4^{\circ}/\langle 210 \rangle$). The boundary misorientation distribution in the *undeformed region of the TMP6 specimen* is distinctly bi-modal, with large fractions of boundaries misoriented in the range 5° - 15° and in the range 50° - 55° . The average misorientation of boundaries in the 5° - 15° range was 10.6° and therefore these boundaries may be described as well developed low-angle boundaries (LAB) with $\theta < 5^{\circ}$ and moderately misoriented boundaries (MMB) with $5^{\circ} \leq \theta \leq 15^{\circ}$.

The misorientation angle distribution in the *deformed TMP2 material* is close to the predicted misorientation distribution for randomly oriented cubes. The large number of boundaries near the $\Sigma 3$ CSL has decreased but the number in the range 30° - 40° , which contains the $\Sigma 9$, $\Sigma 27a$ and $\Sigma 27b$ CSL boundary types, is now about 25% of all boundaries represented in the histogram. In the *deformed region of the TMP6* the distribution has also tended toward random. The large fraction of well-developed LABs and MMB's, evident in the undeformed TMP6 data, is still evident although their misorientation appears to have increased a value in the range 15° - 25° . Also, the number of boundaries remaining in the 2° - 15° misorientation range has decreased significantly and to the about the same level for deformed materials processed by both TMP routes.

As stated previously, Mackenzie's uncorrelated probability distribution for boundary misorientation for adjacent cubes was plotted onto the histograms of Figure 4.8 to provide

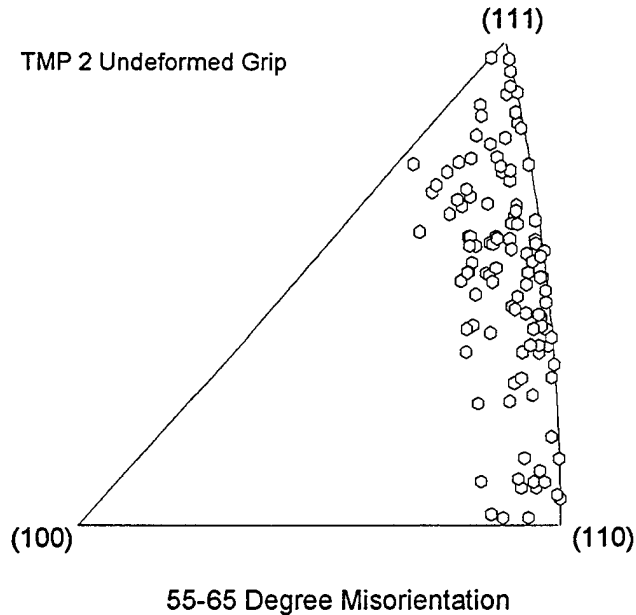


Figure 4.9. Grain misorientation texture for boundaries with misorientations between 55°-65° for the undeformed grip section of TMP2 material illustrating: (1) the large fraction (.23) of boundaries with misorientations in this range and (2) that many boundaries with misorientations in this range have a rotation axis near the twin (111) axis ($\Sigma 3$, $60^\circ/\langle 111 \rangle$) although not all satisfying Brandon nearness criteria.

a reference random distribution considering only geometrical considerations of cubic symmetry. *It should be noted, however, that Mackenzie's random distribution is not, in general, the random distribution for a material examined when it is known to have some texture or preferred orientation as the Mackenzie was based solely on geometrical considerations.* The existence of preferred orientation will result in a different "random" distribution for the material. An algorithm was developed to approximate the random distribution of misorientation for a collected data set with consideration to any preferred

orientation in the data. As stated previously, boundary misorientation is calculated by comparing adjacent orientations. The mesotextural analysis is then *correlated*, in that, the misorientation data is correlated to adjacent orientations. An *uncorrelated* misorientation data set may be constructed by comparing each captured orientation to all other orientations in the data to produce a large misorientation data set. For a 500 orientation data set, a correlated misorientation analysis would yield 499 boundaries for successively captured orientations. The uncorrelated algorithm, which was coded by TexSEM Laboratories, Inc. following recommendations by the author, results in 499^2 or 249,001 boundaries which may be plotted as an uncorrelated misorientation distribution approximating the random misorientation distribution for the material.

Figure 4.10 shows the uncorrelated distribution for TMP2 and TMP6 material approximating a "random" distribution for each material given the orientations with consideration of texture. The boundary misorientation in the TMP2 material follows closely to the expected "random" distribution. This suggests that the boundary structure is dictated by the texture. The TMP6 grip specimen, however, deviates significantly from the uncorrelated plot suggesting that the large fraction of boundaries in the 5° - 20° misorientation range is not a result of the preferred orientation in the material but, rather, evidence of additional mechanisms of boundary development associated with the processing history of the specimen.

Table 4.2 summarizes the results of the (sub)grain boundary characterization based on the misorientation data. The analysis software produces data identifying CSL boundaries to $\Sigma 49$, however, following Watanabe[Ref. 82], these data are displayed for only those CSL's up to $\Sigma 29$. While interfacial energy cusps have been shown to exist in higher- Σ CSL boundaries, the cusps are small and the significance of the cusps has been debated [Ref. 28, 80].

The grain boundary character data (Table 4.2) reveals that a significant fraction (0.28) of boundaries misoriented by 2 - 15° are present in the *undeformed* TMP6 material. These

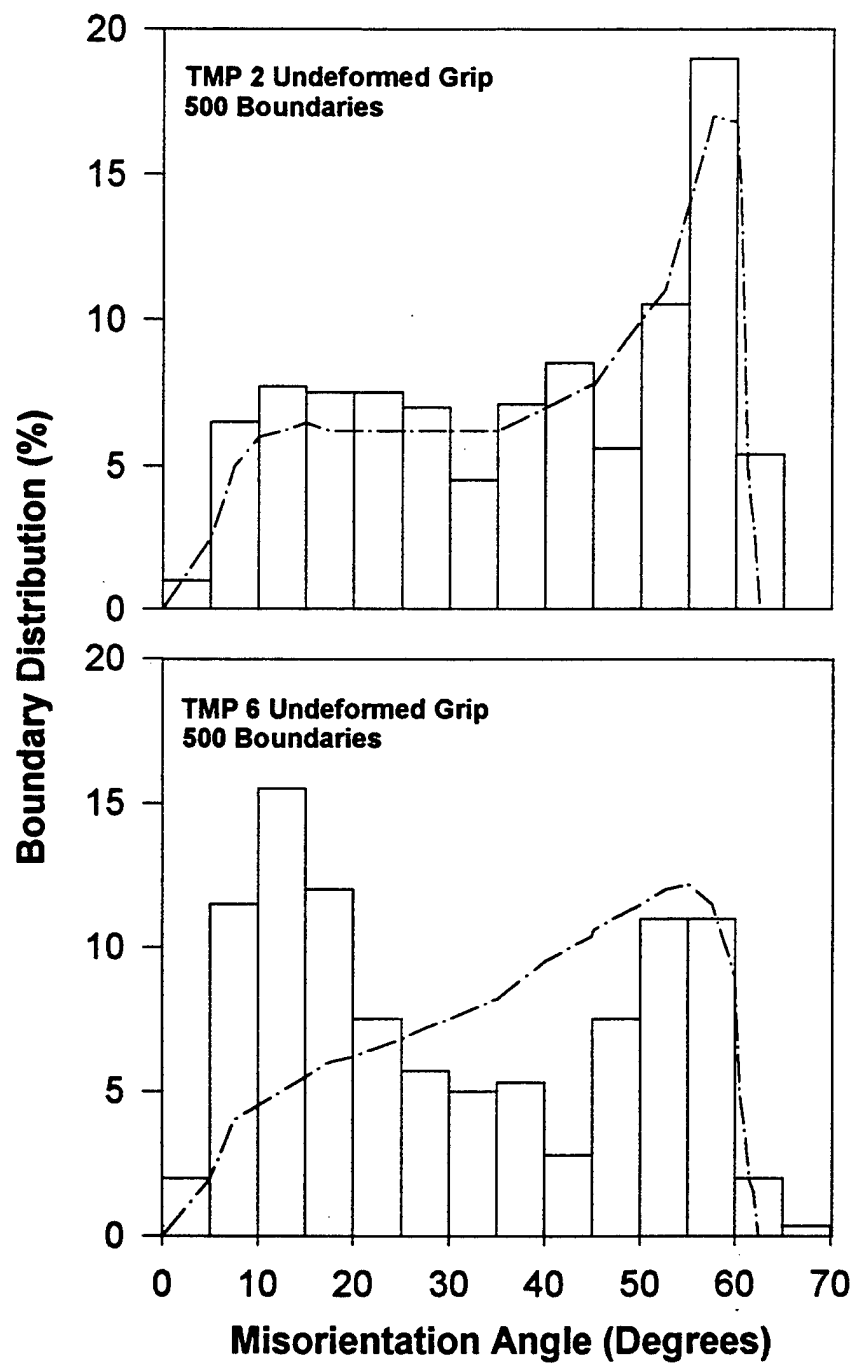


Figure 4.10. Misorientation histograms for undeformed grip sections with the plot for the uncorrelated data shown.

	TMP 2 Grip	TMP2 Gage	TMP6 Grip	TMP6 Gage
Number of Boundaries	499	500	500	510
Number with $2^\circ < \theta < 15^\circ$	84(16%)	38(7.6%)	142(28.4%)	38(7.5%)
Number $\theta > 15^\circ$ Random	335(68%)	372(74.4%)	301(60.2%)	408(80.0%)
Number $\theta > 15^\circ$ CSL	81(16%)	86(10.4%)	52(10.4%)	64(12.5%)
$\Sigma 3$ ($60^\circ / < 111 >$)	15	7	18	10
$\Sigma 5$ ($36.9^\circ / < 100 >$)	2	5	2	7
$\Sigma 7$ ($38.2^\circ / < 111 >$)	4	6	1	3
$\Sigma 9$ ($38.9^\circ / < 110 >$)	8	6	1	6
$\Sigma 11$ ($50^\circ / < 110 >$)	6	3	4	2
$\Sigma 13a$ ($22.6^\circ / < 100 >$)	0	4	0	1
$\Sigma 13b$ ($27.8^\circ / < 111 >$)	6	0	1	3
$\Sigma 15$ ($48.2^\circ / < 210 >$)	0	2	3	4
$\Sigma 17a$ ($28.1^\circ / < 100 >$)	0	1	0	0
$\Sigma 17b$ ($61.9^\circ / < 221 >$)	9	2	3	1
$\Sigma 19a$ ($26^\circ / < 110 >$)	3	5	2	2
$\Sigma 19b$ ($46.8^\circ / < 111 >$)	1	2	2	1
$\Sigma 21a$ ($21.8^\circ / < 111 >$)	1	3	0	1
$\Sigma 21b$ ($44.8^\circ / < 211 >$)	2	1	2	0
$\Sigma 23$ ($40.5^\circ / < 311 >$)	0	1	0	2
$\Sigma 25a$ ($16.3^\circ / < 100 >$)	0	2	0	1
$\Sigma 25b$ ($51.7^\circ / < 331 >$)	1	0	1	2
$\Sigma 27a$ ($31.6^\circ / < 110 >$)	2	4	1	0
$\Sigma 27b$ ($35.4^\circ / < 210 >$)	0	5	0	1
$\Sigma 29a/b$	1/1	0/1	0/0	0/3

Table 4.2. A Partial Summary of Grain Boundary Data

boundaries had an average misorientation of 10.6° and their associated orientations were captured at spacings less than the MLI between HAB's previously reported for this process [Ref. 53]. *Undeformed* TMP2 material was found to possess 84 boundaries in this misorientation range (a fraction of 0.17) but at a spacing nearly equal to the MLI and with a lower average misorientation. Twin boundaries, represented by the $\Sigma 3$ CSL data, were present in both undeformed regions at essentially the same level. However, higher order twins, $\Sigma 3^n$ ($n \geq 2$), were seen primarily in the TMP2 specimens. After the first-order twin boundary type, $\Sigma 3$, the $\Sigma 9$ boundary type was the dominant CSL boundary in TMP2 grip regions and $\Sigma 27a/b$ CSL boundaries dominated all CSL boundaries in the TMP2 gage region. This observation is consistent with the observation of McNelley and Hales [Ref. 53] in their work using TEM that "twin chaining" was a strong influence on the microstructural development in the TMP2 process. There was, however, no correlation with their reported characterization of boundaries in the TMP6 process. Boundaries satisfying the $\Sigma 7$ CSL criteria were present to a greater extent in the *less ductile*, TMP2-processed material here, in contrast to the earlier TEM work. Additionally, there are consistently more CSL boundaries (all Σ) in both TMP2 specimens here than in TMP6 material.

D. DISCUSSION

Both of the TMP schedules produce refined microstructures which exhibit distinctly different response during superplastic deformation. The grain size and microtexture for both are similar while differences in the distribution of the β -phase are noted. The microtexture data suggests that there is no distinguishable recrystallization mechanism unique to either of these TMP processes based on the proposed definition of recrystallization by Doherty, et al. [Ref. 60]. Recent work by Jensen and Hansen [Ref. 61] using EBSD to investigate commercial purity aluminum and aluminum-magnesium-manganese alloys rolled to similar strains as the material of this research and then subsequently annealed, demonstrated the development of moderately strong cube textures, $(001)\langle 100 \rangle$, and recrystallization by the

formation and migration of high-angle boundaries leading to the growth of new grains. The absence here of the cube component in the texture, or the development of any recrystallization orientations during annealing and tensile deformation, is evidence that recrystallization involving formation and migration of high-angle boundaries *may not* be the mechanism responsible for microstructural refinement and responsible for the observed tensile behavior of the more ductile material. The most significant difference in texture observed in the *undeformed* materials is the spread of orientations near the stable rolling texture orientations for the TMP6 material. This may be attributed to the significant fraction (0.28) of well-developed LABs and MMBs within the HAB grain structure.

Data in this study illustrating that there are *fewer* $\Sigma 7$ CSL boundaries, thought to be highly mobile and associated with growth of new grains [Ref. 23-24, 68], in the more ductile TMP6 material is further support for this assertion. It is recognized that $\Sigma 7$ boundaries have been shown to be present only during the early stages of recrystallization and that they are lost as the nucleation and migration processes proceed [Ref. 23-24]. Thus, the presence of more $\Sigma 7$ boundaries in a study of the population of CSL boundaries would not necessarily be sufficient evidence that successful recrystallization has occurred.

The observed increase in the average misorientation of LAB/MMBs for the TMP6 processed material has been previously proposed as evidence of continuous recrystallization wherein subgrain boundaries, stabilized by second-phase particles, increase in misorientation to become moderately misoriented in a refined microstructure [Ref. 51]. Orsund and Nes have suggested "extended recovery" to describe similar processes whereby subgrain growth in heavily deformed metals results in changes in boundary energy character and the development of moderately oriented boundaries through recovery [Ref. 117]. The significant fraction (0.28) of moderately misoriented boundaries observed in the as-processed and processed and annealed TMP6 material (at distances less than the average MLI values) supports the possible involvement of such processes in microstructural evolution during processing and leading to the observed tensile behavior in this more ductile material.

Extended recovery processes leading to the development of moderately oriented boundaries may also result in lowering the dislocation density and residual strain in the interior of the grain and, thus, inhibit the formation of less mobile twin boundaries.

Whether the development of such boundaries constitutes a "recrystallization" mechanism capable of supporting superplastic behavior unique to the TMP6 process cannot be concluded from this study alone. The increase of sub-boundary misorientation due to accumulation of dislocations during recovery has been shown *to have no effect* on the flow stress of pure aluminum deformed to large strains at low strain rates (10^{-4}) at $0.7T_m$ [Ref. 118]. However, those boundaries were in the misorientation range 0.5° - 3° . Little data is available regarding the contribution to mechanical behavior of boundaries with 5° - 15° misorientation. Evidence here does call into question previous theories associating a transition from non-superplastic to superplastic behavior in aluminum alloys with a transition of moderately misoriented boundaries ($\sim 10^\circ$) to disordered HAB's [Ref. 31].

Boundaries between two crystals disoriented by less than 15° are not thought to slide readily [Ref. 30] although early research [Ref. 92] demonstrated GBS in aluminum for boundaries with misorientations as low as 7° . LAB/MMBs are known to have rates of mobility much lower than those of HABs [Ref. 60] and would not be expected to support GBS as readily as higher angle boundaries. This is because extensive boundary migration is required in the accommodation of GBS. There is evidence for boundary migration here in that the grain structure in the BSE micrographs of deformed gage specimens in the TMP6 material has remained equiaxed in spite of the large superplastic strain. Subgrain boundaries have recently been proposed to enhance accommodation during lattice-diffusion controlled GBS by reducing the climb distance for dislocation pile-ups. This constitutes an alternative role for such LAB/MMBs, although the proposed model was specific to powder metallurgy (PM) and mechanically alloyed (MA) materials [Ref. 119]. The presence of the LAB/MMBs may also be a manifestation of the extended recovery during TMP resulting in a reduction of stored strain energy sufficient to inhibit twinning and the production of immobile boundaries.

The randomizing and weakening of texture evident in the deformed gage section of the more ductile TMP6 specimen is most likely due to random grain rotations associated with GBS. Previous research has cited the observation that the strain-rate sensitivity exponent, m , was 0.5 at a strain of 0.02 for the more ductile TMP6 material [Ref. 51] indicating that the microstructure was capable of superplastic response at the commencement of tensile testing. The randomizing of texture in the less ductile TMP2 material may be at least partially due to operation of the twin-chain mechanism described by Gottstein [Ref. 69]. This is reflected here in the presence of $\Sigma 9$, $\Sigma 27a$ and $\Sigma 27b$ in the grain boundary character data for the deformed gage section of the TMP2 material. However, GBS may also contribute as well in the TMP2 material. This is reflected here in the lack of the development of a $\langle 111 \rangle$ fiber component, which would reflect multiple slip during plastic deformation, or increase in the number of orientations near $(110)\langle 112 \rangle$ if single slip were a significant deformation mechanism. Sliding of adjacent grains in low temperature superplastic deformation of aluminum alloys has been observed in conjunction with elongations as low as approximately 200% [Ref. 120]. It is important to note that grain size measurements, i.e. MLI data, are similar for both of these materials. Thus, grain size (MLI) alone is not the only significant microstructural feature and models for superplastic deformation via GBS should consider factors in addition to grain size. The observed strain-rate sensitivity coefficient, m , for the TMP2 material is about 0.33 suggesting a possible contribution to deformation from the solute drag mechanism.

Coalescence of LAB/MMBs in association with GBS may be responsible for the evolution of boundaries initially in the 5° - 15° misorientation range during deformation of the TMP6 material. There was no apparent evidence of a relationship between the distribution of CSL boundaries, with the exception of twin-chain ($\Sigma 3^n$) boundaries, and the tensile behavior of the two processed materials. CSL boundaries, in general, are not thought to slide as readily as random boundaries due to the relatively high degree of atomic registry at such interfaces and data in this study would support this conclusion given the smaller fraction of

CSL boundaries in the more ductile specimens.

E. OBSERVATIONS FROM THIS STUDY

1. The distinguishable feature responsible for the difference in tensile behavior of the two processed materials is the development of moderately (5° - 15°) misoriented within the more ductile TMP6 material. The development of these boundaries reflects extended recovery during the longer IPA time of the TMP utilized with the more ductile material. Whether these boundaries produce microstructural refinement, facilitate dislocation accommodation during GBS or are a by-product of extended recovery processes that simply inhibit development of immobile (twin-chain) boundaries requires further investigation.

2. Formation of twin-chain ($\Sigma 3^n$) boundaries and restricted recovery influenced the less ductile response of material processed with the shorter IPA time.

3. No recrystallization mechanism unique to either process is evident in the microtexture data. The microstructural transition following TMP and annealing in the may be described as a recovery-dominated process.

4. The distribution of non-twin related CSL boundaries is not thought to be an important factor influencing the superplastic deformation of this alloy.

V. MICROTTEXTURE AND BOUNDARY EVOLUTION DURING MICROSTRUCTURAL REFINEMENT PROCESSES IN SUPRAL 2004

A. INTRODUCTION

The SUPRAL aluminum alloys represent the most successful commercial superplastic material developed to date. SUPRAL, a trademark of Alcan Aluminum Inc. subsidiary Superform Metals U.S.A., was developed in 1974 by Stowell, Grimes and co-workers of Tube Investments/British Aluminum Group and secured under a series of U.S. patents from 1975-1978. The alloy is nominally Al - 6.0 wt% Cu - 0.4 wt% Zr. The copper alloying addition is thought to influence recrystallization by lowering the stacking fault energy and results in the formation of a coarse second phase precipitate, θ , Al_2Cu . The zirconium alloying addition results in a uniform dispersion of ultra-fine Al_3Zr precipitates. Such a bi-modal distribution of phases has been thought to result in a more optimum peak strain rate for superplasticity, increasing it to rates experienced in commercial forming processes, $\sim 10^{-1} \text{ s}^{-1}$ [Ref. 2].

SUPRAL has been investigated extensively and reported to be a dynamically recrystallizing alloy which evolves to a microstructure capable of superplastic flow only upon deformation with a microstructural transition reported to occur early in the deformation process [Ref. 45-46, 108]. A comprehensive study, which attempted to describe in more detail the microstructural transition, was conducted by Bricknell and Edington in 1978 utilizing XRD and the crystallite orientation distribution function (CODF) to quantify textural changes associated with the microstructural evolution [Ref. 108]. Their study hypothesized that continuous recrystallization mechanisms involving the movement of dislocations and dislocation networks was associated with the dynamic refinement to a superplastic microstructure. These investigators followed this study with a similar one utilizing TEM to examine the as-processed alloy and found evidence of a banded structure with a large number of low-angle boundaries (LAB's) present from the TMP. Conclusive evidence regarding the

involvement of the LAB's in the superplastic response was lacking due to an absence of boundary evolution data.

Although details of the TMP route for the SUPRAL alloys is proprietary to the manufacturer, details of the processing schedule have been reported [Ref. 45]. To avoid the development of coarse primary Al_3Zr particles upon chill casting a rapid solidification rate is utilized. Homogenization of the cast ingot is conducted to reduce any residual stresses developed in the casting process and to minimize compositional anisotropy. The homogenization temperature is maintained at a lower value than conventional homogenization temperatures in aluminum alloys to inhibit the formation and coarsening of Al_3Zr precipitates from the supersaturated lattice. Processing reduction by warm-rolling at a moderate temperature ($T \approx 300^\circ\text{C}$) follows homogenization and a subsequent cold, cross-rolling to a reduction of approximately 70% is conducted to induce a large degree of strain energy into the microstructure. During the initial rolling process, precise temperature control is maintained to retard the growth of the Al_3Zr particles. Grimes, co-developer of the patented process, has reported that the cold-rolling process is conducted without any inter-pass anneals to inhibit static recrystallization during TMP and to retain sufficient strain energy in the microstructure to enable the reported dynamic recrystallization [Ref. 45]. A post-rolling treatment (details not reported) is incorporated into the TMP scheme prior to delivery.

In the end-use fabrication of near-net shape components, the alloy is highly superplastic at forming temperatures of approximately 450°C and strain rates from $1 \times 10^{-2} \text{s}^{-1}$ to $1 \times 10^{-1} \text{s}^{-1}$. The most-common alloy produced by this process, SUPRAL 2004, is produced in various sheet thicknesses and is used in secondary and tertiary structural applications. Some specific applications were given previously. The ultimate tensile strength of as-processed 2004 is reported as 220 MPa with a UTS of 420 MPa reported for material in the T6 condition [Ref. 38].

The goal of this study is to utilize an interactive electron back-scatter pattern (EBSP) method to detail the microtextural changes and boundary evolution from the as-processed

state, during static annealing, and increasing strain levels up to the onset of GBS. Discrete boundary character data, with the accompanying orientation information, may provide more conclusive evidence to detail the refinement process operative in this alloy. As the material has been reported to be dynamically recrystallizing, application of the EBSP method to investigate small regions of increasing strain in the deformed material would be expected to show the evolution of boundary structure from the as-processed material to a microstructure capable of the high superplastic elongations documented for this material. Ultimately, it may be of interest to modify TMP schemes utilized to process other aluminum alloys to obtain microstructure more closely related to that which results from the SUPRAL process, which apparently yields superior superplastic performance.

B. EXPERIMENTATION

Experimentation was conducted in three phases. First, tensile coupons were machined from sheet material obtained from the manufacturer and deformed at NPS in uniaxial tension at rates corresponding to commercial conditions. A deformed specimen was selected for examination and a series of data sets were taken in regions of increasing strain in the deformed tensile coupon. This examination may be termed isochronal in that all regions examined have experienced the same time at temperature. Second, material was statically annealed at NPS at the prescribed forming temperature for various lengths of time and examined. Finally, under a cooperative research agreement, EBSD data were also taken on a series of SUPRAL 2004 specimens received from The Centro Nacional de Investigaciones Metallurgicas (CNIM) of Consejo Superior de Investigaciones Cientificas (CSIC), a research organization of the government of Spain. The series consisted of SUPRAL 2004 in the following conditions: as-processed; processed and annealed; partially deformed (40% strain); and deformed to failure. The deformation conditions differed from those in the isochronal examination.

1. Experimental Procedure

SUPRAL 2004 material was obtained in 2.0 mm sheet in the as-processed condition from Mr. A.J. Barnes of Superform, USA, Inc. The chemical composition is shown in Table 5.1. Tensile specimens were machined to the geometry illustrated in Figure 5.1 and deformed in uniaxial tension at a constant-crosshead speed on an Model 4527 Instron mechanical testing system utilizing an ATS clamshell furnace for temperature control. Deformation conditions were set at a constant crosshead speed comparing to a nominal strain rate of $1.0 \times 10^{-2} \text{ s}^{-1}$ and deformation temperature of 450°C was maintained $\pm 2^\circ \text{C}$ using 8 thermocouples placed along the extension rod and specimen grips. Tensile specimens were deformed to failure and quenched. The tensile axis was aligned parallel to the final rolling direction. The deformed

	Cu	Zr	Fe	Si	Zn	Mn	Mg	Ti	Li	Al
Cast No. 2004F013	5.66	.37	.14	.06	.029	.013	.003	.005	.0001	bal

Table 5.1 Alloy composition (by wt%) for the as-received SUPRAL 2004.

tensile coupons were sectioned longitudinally, in the tensile direction. Sheet material was also sectioned to obtain samples for annealing. Static annealing was conducted in a Lindberg Model 1442 furnace at a temperature of 450°C for 6 hours, 12 hours and 24 hours. Annealed specimens were quenched and sectioned along the rolling direction. Specimens received in the cooperative research arrived as portions of tensile coupons. These specimens were sectioned longitudinally along the tensile axis also. Standard electropolishing methods described previously were utilized for all BSE and EBSD examinations.

For the isochronal study, EBSD examinations were conducted near the mid-plane ($t/2$) in the grip (undeformed) region and at four regions down into the deformed gage section at increasing levels of strain using the methods discussed in chapter 3. The local level of strain, ϵ_{local} was approximated by measurements of the undeformed and deformed tensile specimen and using the relation:

$$\epsilon_{\text{local}} = \ln (A_{\text{f, local}} / A_{\text{o, local}}) \quad (1)$$

where $A_{\text{f, local}}$ is the final area at the point of measurement and $A_{\text{o, local}}$ is the initial cross sectional area of the coupon. This approximation for local strain assumes a continuous material without the formation of cavities or voids during straining.

EBSD examination was also conducted in a region near the mid-plane ($t/2$) of as-processed, statically annealed, and cooperative research specimens. BSE micrographs were taken adjacent to all regions examined using EBSD to record the grain structure, precipitate size and dispersion. The BSE micrographs were collected using a TOPCON SM-510 SEM

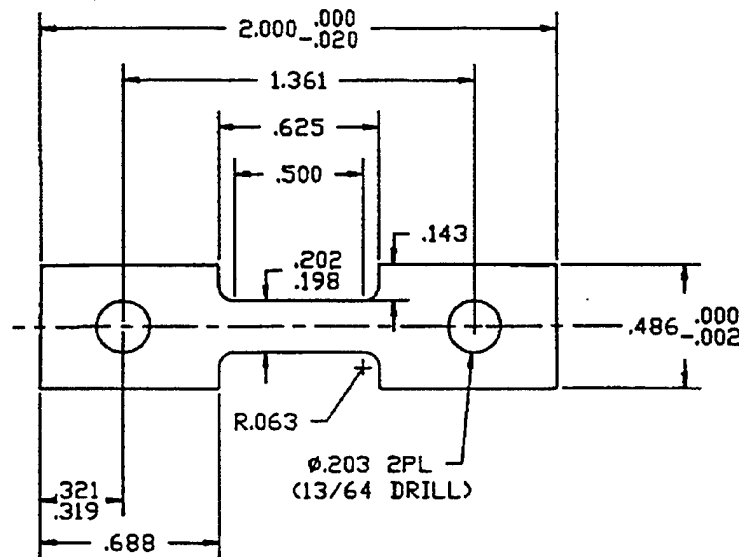


Figure 5.1. Geometry of the tensile specimens utilized in this study.

and were obtained at a working voltage of 5KV to obtain grain orientation contrast as well as atomic number contrast. Microtextural and quantitative boundary character analysis were conducted for each of the orientation data sets. The "random" distribution of boundary

misorientation, with consideration of the influence of the texture present, was calculated for each data set and plotted as the *uncorrelated* distribution of misorientation in a manner consistent with the preceding chapter.

C. MECHANICAL BEHAVIOR AND MICROSTRUCTURE

An elongation of 756% was obtained at the time of fracture for the specimen deformed at $T_{\text{def}} = 450^\circ \text{C}$ and a strain rate of $1.0 \times 10^{-2} \text{s}^{-1}$. In comparison, the material manufacturer reported a tensile elongation of 800% at essentially the same test conditions. Figure 5.2 shows a photograph of the undeformed and deformed tensile specimens from this test.

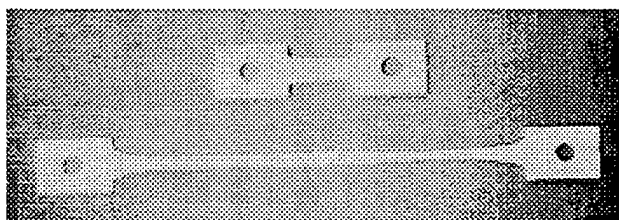


Figure 5.2. Photograph of an undeformed tensile coupon and the tensile coupon deformed to an elongation of 756%.

Figure 5.3 (a) through (e) shows BSE micrographs illustrating the microstructure present in some of the regions selected for examination. The rolling (and tensile) direction is aligned in the horizontal direction on all images. In Figure 5.3 (a), the as-processed material, coarse θ -phase, Al_2Cu , particles are evident (particles in the fine dispersion of Al_3Zr less than approximately $0.1\mu\text{m}$ are not visible at the magnification here). Although grain contrast is not evident in the as-processed material (as previously reported) directionality is apparent in the microstructure, presumably due to mechanical fibering introduced in the final cold rolling process. The original grains are thought to be flattened and thinned by the rolling process and elongated in the (apparent) rolling direction. Figure 5.3 (b) depicts the

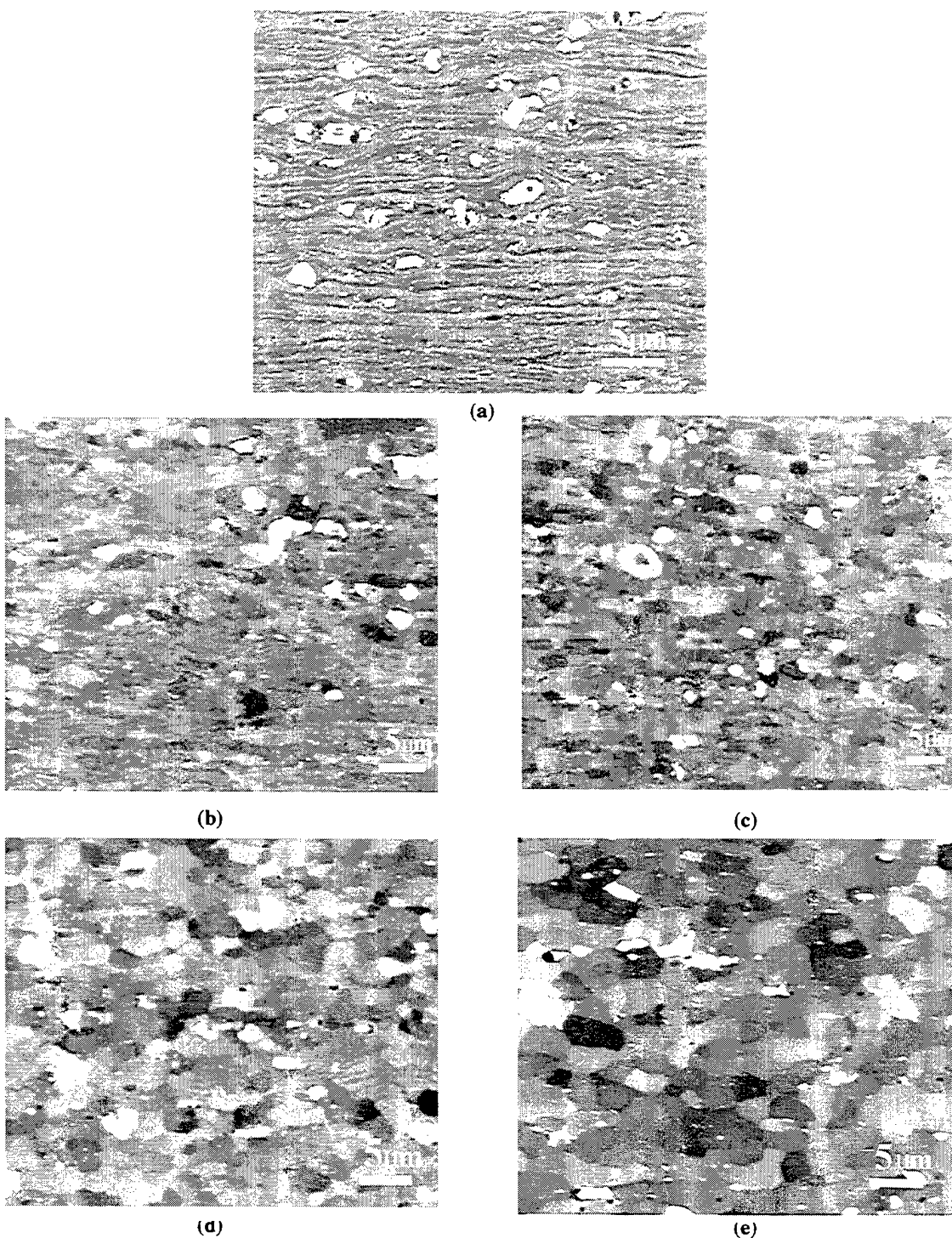


Figure 5.3. BSE micrographs of selected regions examined in SUPRAL 2004; (a) as-processed, (b) processed and annealed for 30 minutes at 450C (grip), (c) deformed to a strain of 0.16, (d) deformed to a strain of 0.70, (e) deformed to a strain of 1.32. The deformation temperature was 450C and the strain rate was $1.0 \times 10^{-2} \text{s}^{-1}$. The tensile axis (and rolling direction) is the horizontal. Orientation contrast, no etchant.

microstructure of the grip region (processed and annealed 30 minutes at 450°C) section. Contrast variation due to various features including LAB's and substructure, found in earlier TEM studies in the as-processed material, have become evident between the bands apparent in (a). The material in region in Figure 5.3 (c) has experienced an approximate local strain of 0.16 and some (sub)grain refinement is apparent. A loss in the previous directionality of the microstructure is also evident. The local strain in (d) was estimated to be 0.70 and grain refinement processes have resulted in an equiaxed grain structure with a fine, uniform grain size. Some of the diffuse boundary structure appears to have sharpened. A mean linear intercept calculation indicated an average MLI value of $L_{av} = 5.26 \mu\text{m}$ for this structure. Figure 5.3 (e) was taken in the region with a local strain of approximately 1.32. The orientation contrast for grains in this image indicated that a higher degree of misorientation may exist than in the previous regions of lower strain.

D. MICROT texture AND MESOT texture

1. In As-Processed Material

Figure 5.4 illustrates the results from examination of the as-processed material. Quantitative boundary data is summarized later in Table 5.2. Analysis of the discrete Euler plot indicates that the microtexture present is a deformation texture consistent with aluminum alloys rolled to high strain at low to moderate temperatures and consistent with results of earlier XRD studies [Ref. 108]. The texture extends along the β -fiber with the strongest component concentration near the S, $\{123\} \langle 634 \rangle$, and brass, $\{011\} \langle 211 \rangle$, orientations. A closely grouped cluster of grains with orientations near S are evident in the $\phi_2=35^\circ$ window of the Euler plot while orientations near brass are identified readily in the $\phi_2=90^\circ$ window. The other significant deformation component is the S/B orientation, $\{168\} \langle 211 \rangle$, identifiable in the $\phi_2=5^\circ$ and $\phi_2=80^\circ$ plots. A few orientations near copper, $\{112\} \langle 111 \rangle$, are evident in the $\phi_2=25^\circ$ plot. This texture formation has been attributed to stable orientations resulting from multiple slip on limited $\{111\} \langle 110 \rangle$ systems and the influence of twinning on generation

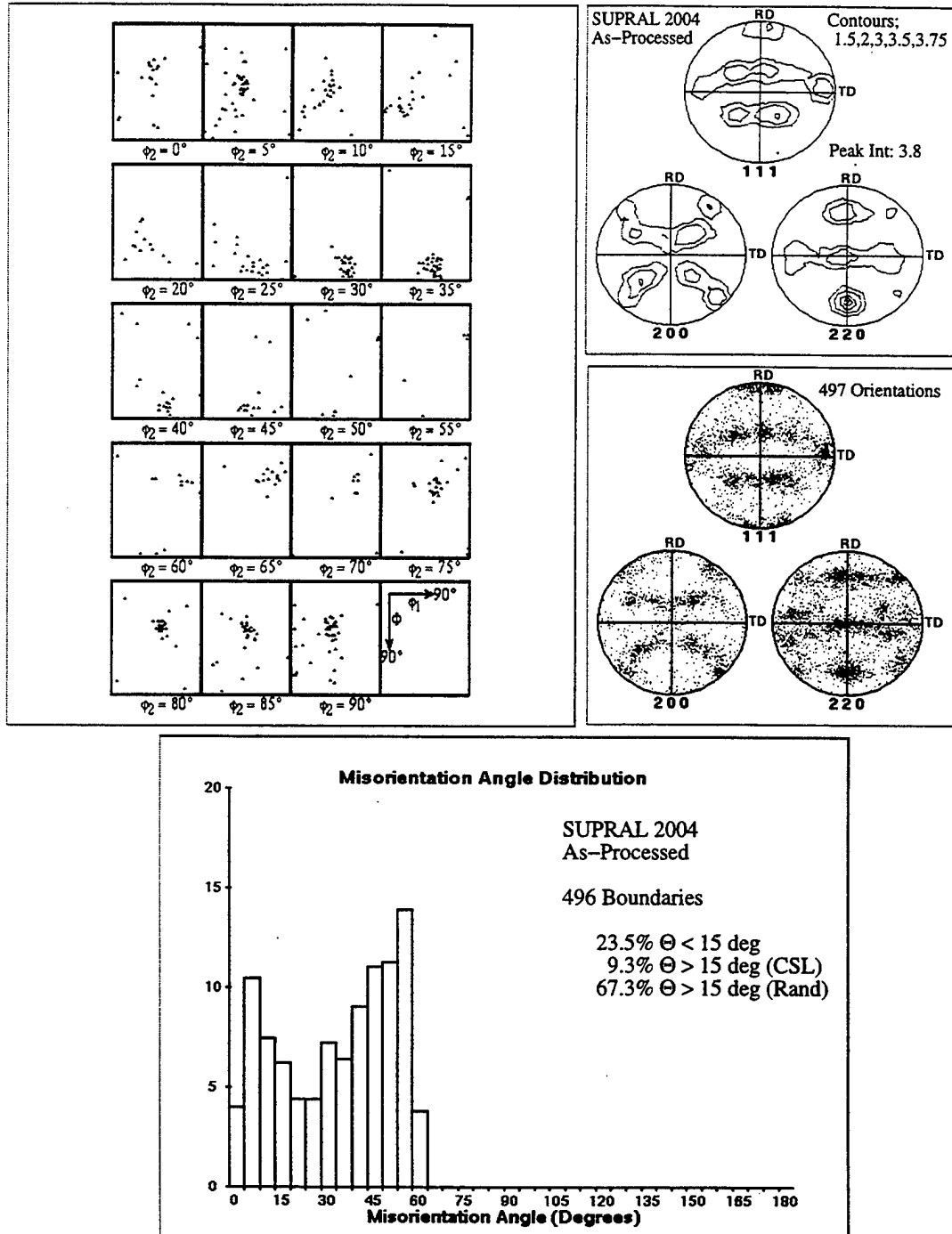


Figure 5.4. The discrete Euler plot, discrete pole figure, contour pole figure, and boundary misorientation graph for the as-processed material. A significant fraction of LAB's and MMB's in the processed material are observed. The peak fraction of HAB's lie in the 55–60 degree misorientation range.

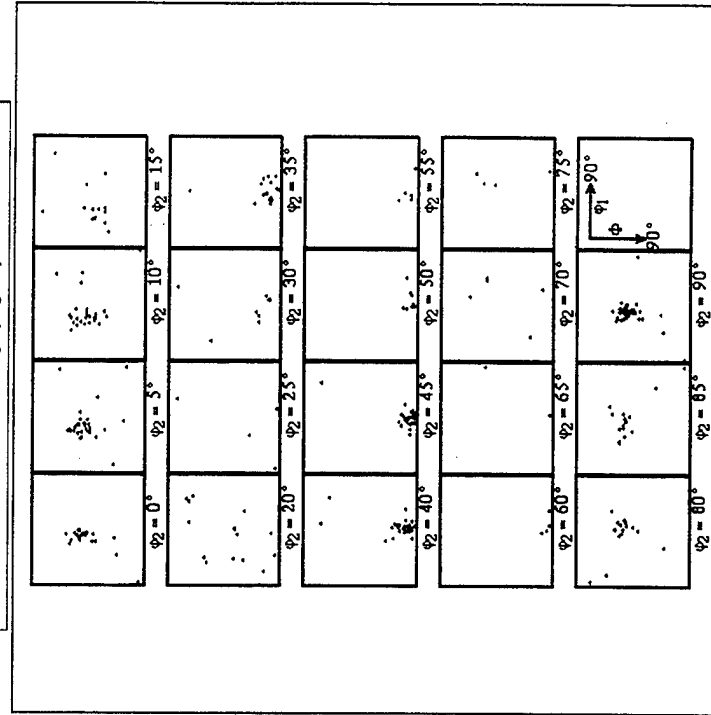
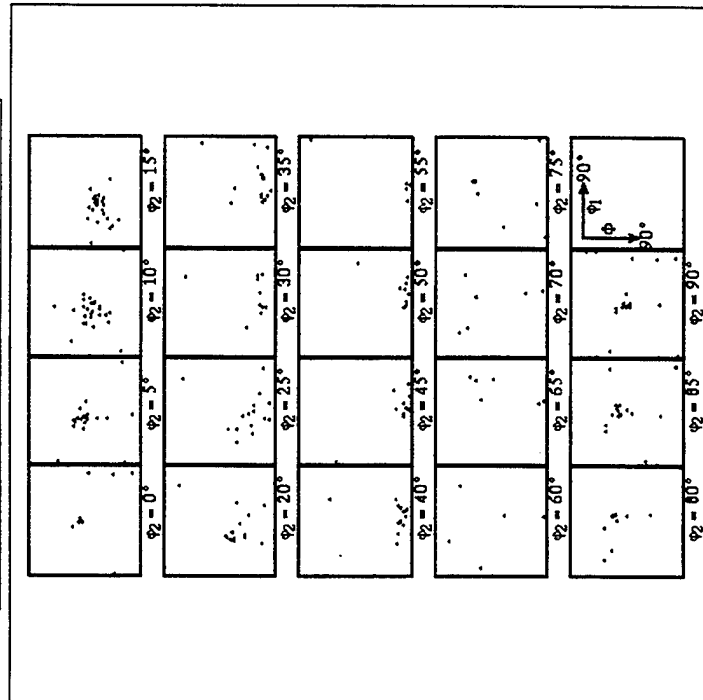
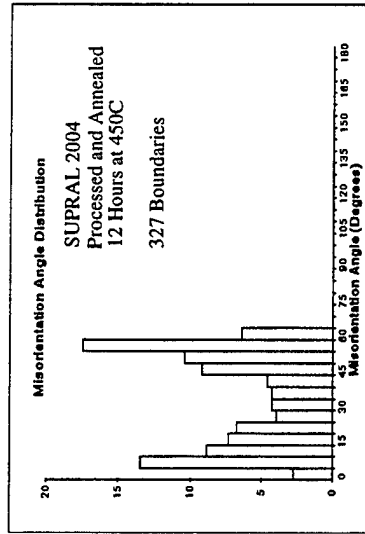
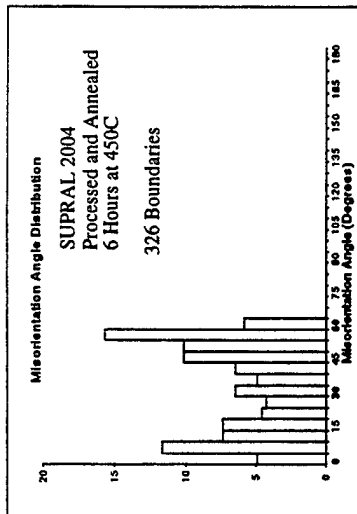


Figure 5.5. Boundary misorientation plots and discrete pole figures for processed material statically annealed for (a) 6 hours and (b) 12 hours. A deformation texture from processing persists. The bimodal shape of the boundary misorientation distribution becomes more pronounced.

of new orientations in f.c.c. metals [Ref. 108, 121]. There are no orientations near components which have been associated with recrystallization in aluminum alloys (and none are expected as the as-processed material does not appear to be recrystallized).

Grain boundary data illustrated in Figure 5.4 indicates that the as-processed material possesses a significant fraction (0.235) of LAB's ($0^\circ < \theta \leq 5^\circ$) and moderately misoriented boundaries, MMB's, ($5^\circ \leq \theta \leq 15^\circ$). Additionally, the peak fraction of the HAB's present lie in the 55° - 62.8° misorientation range, near that expected if twinning were influential in the generation of new orientations. The quantitative data reveals that the number of boundaries satisfying Brandon criteria for nearness to the $\Sigma 3$ CSL is twice the value expected for a random population. During data collection, orientations were captured at spacings of $\approx 0.5 \mu\text{m}$ while the thickness of the pancaked grains is 2-3 μm . Therefore, the misorientation distribution reflects, primarily, deformation induced structure with some prior high-angle grain boundaries and HAB's resulting from twinning. Overall, the distribution of boundaries present in the as-processed material may be described as reflecting a lower interfacial energy character with approximately 50% of all boundaries either LAB, low-index CSL boundaries, or HAB's near the twin relation, $60^\circ / \langle 111 \rangle$.

2. Following Static Annealing

The evolution of micro- and mesotexture during static annealing is summarized in Figure 5.5 (a) and (b). The overall effect of static annealing at the test temperature of 450°C is the persistence of the deformation texture observed in the as-processed material with a slight sharpening in the strength of the texture present and changes in the strengths of individual deformation texture components which lie along the β -fiber. It is noted that there is no evidence of the development of orientation components observed in discontinuous recrystallization during annealing of deformed aluminum alloys, such as cube $\{001\} \langle 100 \rangle$, rotated cube $\{025\} \langle 100 \rangle$, or Goss $\{011\} \langle 100 \rangle$ [Ref. 110, 122].

An analysis of the discrete Euler plots indicate that, as annealing proceeds, most orientations follow along the α -fiber and orientations near brass, $\{011\} \langle 211 \rangle$, dominate the

texture as evidenced in the $\phi_2=0^\circ$ and $\phi_2=90^\circ$ windows of the plot for the material annealed 12 hours. Orientations near the copper component, $\{112\} \langle 111 \rangle$, present in the $\phi_2=25^\circ$ window of the plot for the 6 hour anneal, are absent in the $\phi_2=25^\circ$ window for the 12 hour anneal.

The evolution of boundary misorientation during annealing shows the retention of the bi-modal distribution of boundary misorientation, present in the as-processed material, with an increase in the fraction of LAB's/MMB's and in the average misorientation of the MMB's present. Quantitative boundary analysis, shown in Table 5.2, shows that the percentage of LAB's/MMB's increases during static annealing to a value of 29.1% at an elapsed annealing time of 12 hours. Given that the deformation texture persists during static annealing, the evolution of these boundaries suggests that the refinement processes may not be confined to the dynamic regime and that recovery is important microstructural transition.

Data for the evolution of HAB's during static annealing show that the peak in the histogram for HAB's continue to lie in the 55° - 60° misorientation range and to have increased to approximately 18% of all boundaries. Quantitative boundary analysis (Table 5.2) reveals that over one-fourth of these boundaries (4.7% of all boundaries collected or 3 x random) satisfy the Brandon criteria for nearness to the twin boundary, $\Sigma 3$. Figure 5.6 illustrates the distribution of rotation axes for boundaries in the 55° - 62.8° misorientation range for the material annealed 12 hours. While the $\Sigma 3$ boundary has been reported to have a low interfacial energy, these data show that *many* of the HAB's in the annealed material may be of low-interfacial energy character and formed as a result of annealing twinning.

3. Results from the Isochronal Examination of a Deformed Tensile Specimen

Figure 5.7 provides a visual summary of the isochronal examination of the fractured tensile specimen. The regions examined in the fractured tensile specimen are indicated, accompanied by a BSE image of the region adjacent to the EDSD examination area for the level of local strain approximated by the deformed specimen geometry, along with the discrete pole figure and misorientation angle histograms analyzed from the orientation data set. A

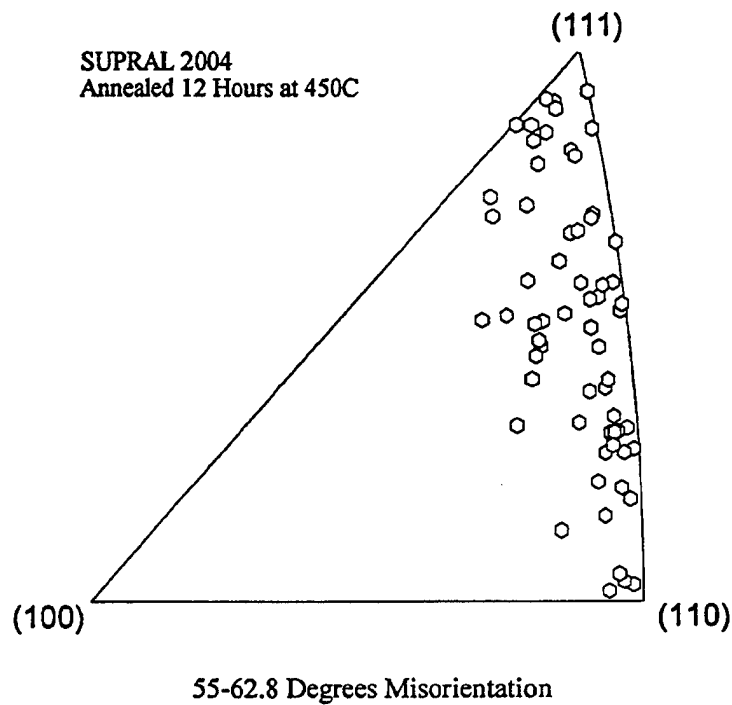


Figure 5.6. Grain misorientation texture illustrating the distribution of grain rotation axes for boundaries with misorientations of 55° - 62.8° for material statically annealed 12 hours at 450°C .

summary of boundaries, categorized by energy character following Watanabe and Haasen [Ref. 23, 81] is provided in the corner of the misorientation angle histogram.

Analysis of the microtexture plots for this examination reveals that the deformation texture present in the as-processed material sharpens during annealing, is observed to spread about the initial principal rolling deformation components, brass and S, and gradually diminishes with increasing strain. Preferential retention of, primarily, orientations near brass, $\{110\} \langle 112 \rangle$, is noted in the data for the region with a local strain of 1.32. Retention of $\langle 121 \rangle$ type orientations during GBS were previously observed and attributed to concurrent deformation by limited or single slip [Ref. 108]. The randomizing of texture, which has been

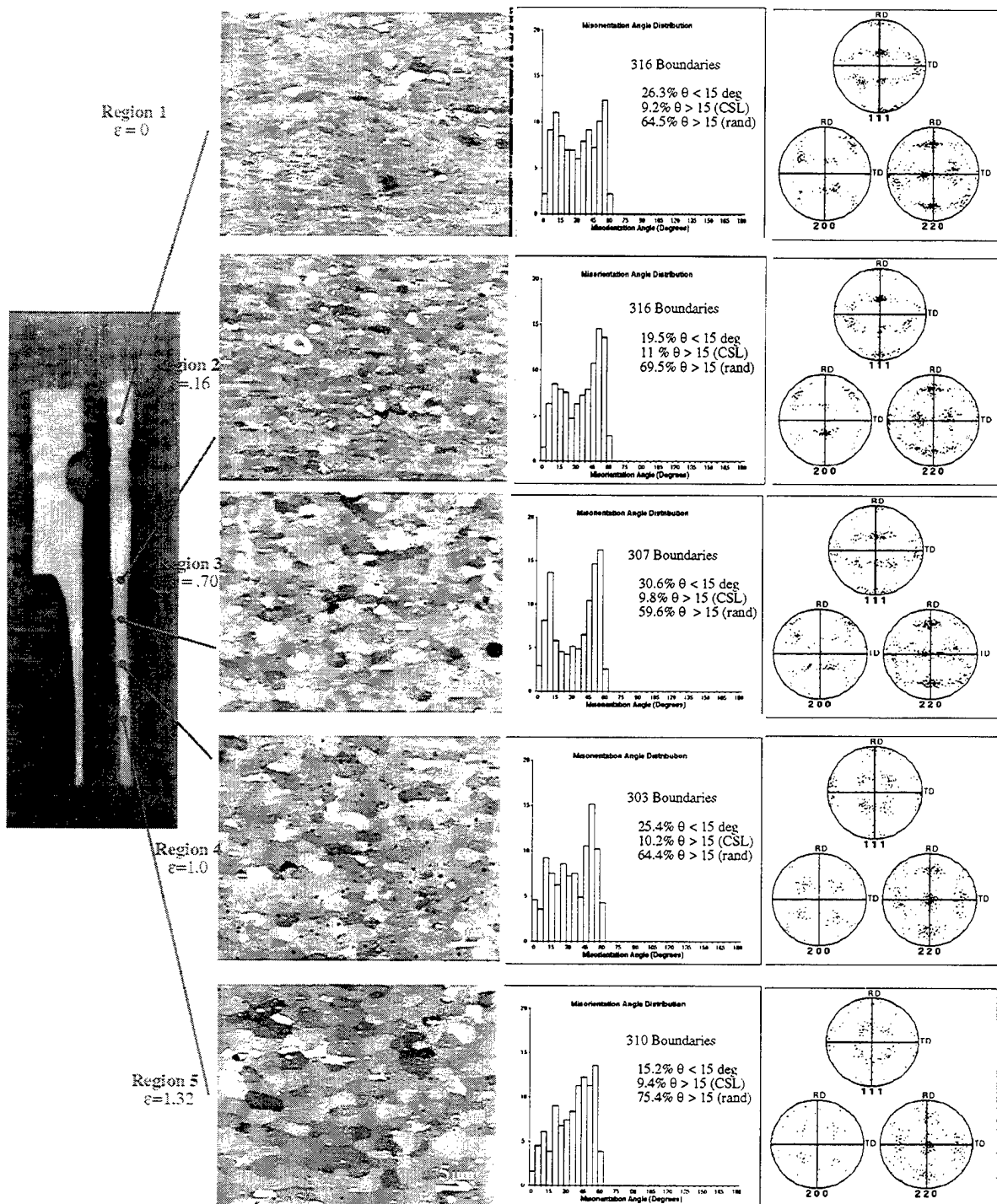


Figure 5.7. BSE micrographs, boundary misorientation plots, and discrete pole figures for regions of a deformed SUPRAL 2004 specimen.

SUPRAL 2004	As-Processed	Annealed 6 Hours at 450C	Annealed 12 Hours at 450 C
Total Number of Boundaries	496	326	327
% with $\theta < 15^\circ$	23.5	28.9	29.1
% with $\theta > 15^\circ$ and CSL ($\Sigma < 31$)	9.3	12.0	12.9
% with $\theta > 15^\circ$ and disordered	67.3	59.1	58.0
% $\Sigma 3$ [1.53]	3.0	3.5	4.7
% $\Sigma 5$ [1.07]	.6	.6	.3
% $\Sigma 7$ [0.86]	.6	.6	.3
% $\Sigma 9$ [0.88]	1.4	1.3	0
% $\Sigma 11$ [0.68]	.4	1.3	4.0
% $\Sigma 13a/b$ [0.59]	.2	.3	.6
% $\Sigma 15$ [0.82]	.2	.3	.3
% $\Sigma 17a/b$ [0.51]	.6	2.5	1.5
% $\Sigma 19a/b$ [0.48]	.4	.3	0
% $\Sigma 21a/b$ [0.66]	.4	.3	.6
% $\Sigma 23$ [0.43]	0	0	0
% $\Sigma 25a/b$ [0.48]	.6	.6	.6
% $\Sigma 27a/b$.2	0	0
% $\Sigma 29a/b$.8	.6	0

Table 5.2. Summary of boundary character data for as-processed and statically annealed specimens examined. The number in brackets [] indicates the % of CSL boundaries (using the Brandon criteria) expected based on random processes [Ref 79].

associated with deformation by GBS, is evident as early as a strain of 1.0 [Ref. 108]. As the data were collected isochronally, with all regions experiencing the same degree of annealing and any associated sharpening of texture, all of the randomizing of texture here may be

attributed to either GBS or generational twinning. Again, there is no evidence of the development of recrystallization texture components during the microstructural refinement processes. Mesotextural data, depicted here in the boundary misorientation plots, illustrates the retention of a significant fraction, approximately 20% to 30%, of MMBs up to the apparent onset of GBS (evidenced by the aforementioned randomization of texture). During the microstructural refinement processes, occurring during early stages of plastic deformation, the misorientation of MMBs is observed to shift to higher values of misorientation. At a strain level near that which has been associated with completion of the dynamic "recrystallization" in this alloy, $\epsilon \approx 0.70$, only 59.6% of the boundaries encountered were disordered HAB's. The fraction of HAB's satisfying nearness to the Brandon criterion to exact CSL values is relatively constant and near that expected from purely geometrical rotations [Ref. 79].

Figure 5.8 is a summary of the misorientation plots for the isochronal data with superimposed plots of the uncorrelated ("random") distributions expected for the material given the preferred orientation present. The random distribution was calculated in the manner described in the previous chapter. Through deformation to strains at which the microstructural refinement processes are thought to be complete, $\epsilon \approx 0.70$, the fraction of boundaries in the LAB/MMB regime (0° - 15° misorientation) is significantly higher than that predicted for a random distribution, even given the effect of texture in the processed material. Since the methodology used in the EBSD examination is known to preclude some boundaries with misorientations less than 2° (discussed in Chapter III), the deviation is likely more pronounced than the plots depict. Additionally, the average misorientation of the MMB's has shifted to higher values with the largest fraction in the 10° - 15° misorientation range. This suggests a mechanism associated with the microstructural refinement process may be responsible for the development of MMB's in the as-processed and processed and annealed regions. At higher strain values, where deformation by GBS is thought to dominate, a reduction of LAB/MMBs occurs concurrent with a shift in the boundary misorientation distribution towards random.

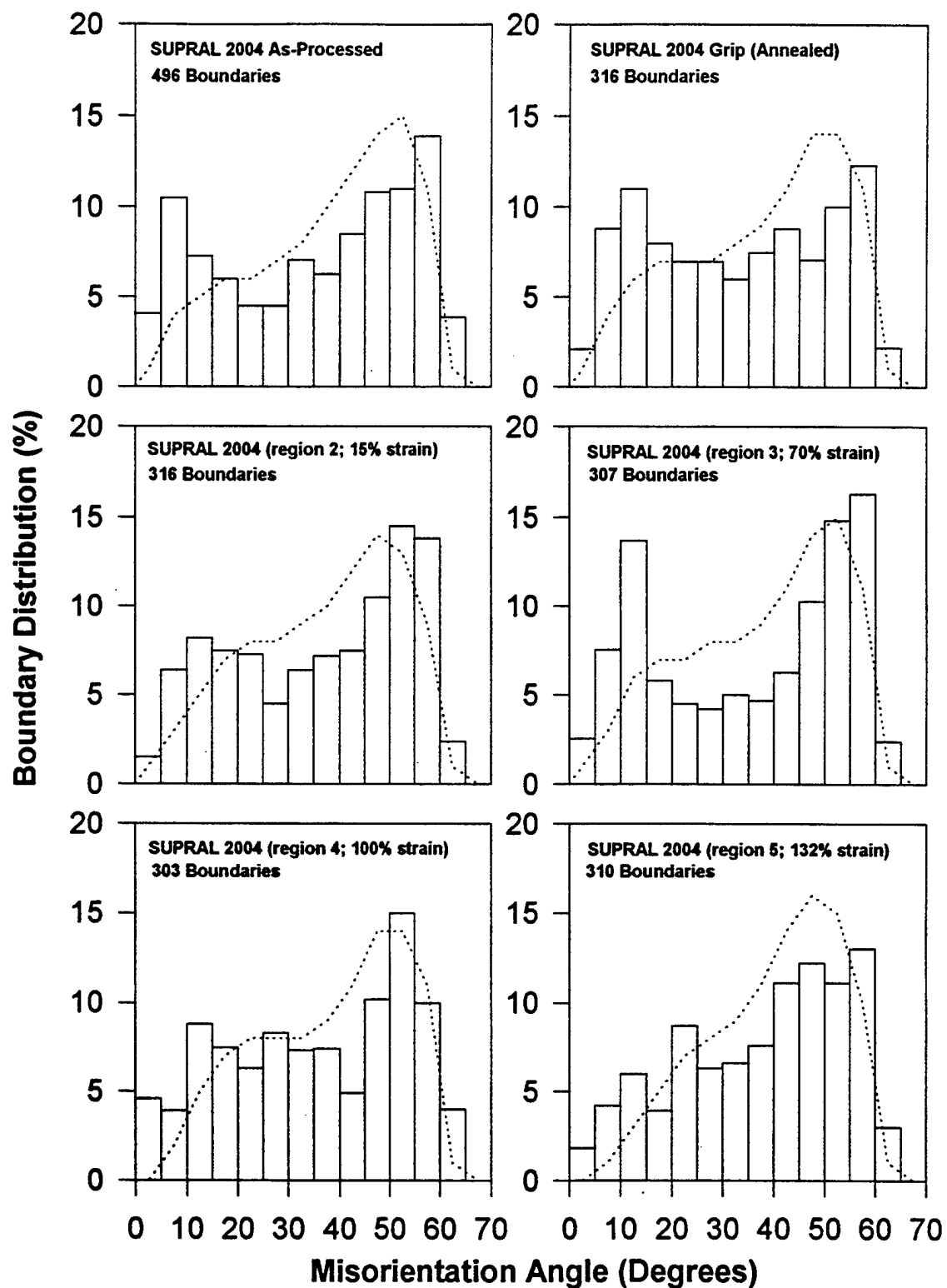


Figure 5.8. Misorientation histograms for specimens/regions examined in SUPRAL 2004. The uncorrelated distribution of misorientation is indicated by the dotted line.

As the degree of texture diminishes, the uncorrelated misorientation plot will approach that described by Mackenzie [Ref. 112].

Table 5.3 summarizes the quantitative boundary data for the isochronal examination. With the exception of LAB's/MMB's ($\Sigma 1$ s) and $\Sigma 3$ boundaries, the CSL data is unremarkable and the *overall fraction* of CSL boundaries with $3 \leq \Sigma \leq 25$ does not deviate significantly from the value predicted by purely geometrical means ($\approx 9.0\%$ for Brandon nearness criterion [Ref. 79]). The absence of higher order, twin related CSL's, particularly $\Sigma 27a/b$, would imply that all of the randomization of texture in the more highly strained regions of the isochronally collected data may be attributed only to GBS. The presence of $\Sigma 3$ boundaries at levels two to three times that expected for a random distributions of orientations again suggests that twinning may be important in the generation of new orientations during the microstructural refinement processes. This observation is consistent with the predominance of a brass component to the texture. The overall distribution of boundaries indicates that the fraction of $\Sigma 1$ boundaries is significantly higher than that predicted by geometrical rotations ($\approx 2.0\%$).

4. Results from the Cooperative Research

Figure 5.9 (a) through (d) illustrates the summary of data for the specimens examined in the cooperative research. A summary of the quantitative data for these examinations is provided in Table 5.4. The deformation temperature here was 480°C and a constant crosshead speed corresponding to a nominal strain rate of $5 \times 10^{-4} \text{ s}^{-1}$ in uniaxial tension was utilized. Data for as-processed material, although obtained earlier in this study from processed sheet material provided from the manufacturer, was taken from an as-processed specimen provided in the cooperative research. This was done to provide the researchers at CSIC a complete study of specimens which they provided. The results for the as-processed material, Figure 5.9 (a), duplicate those from the earlier analysis.

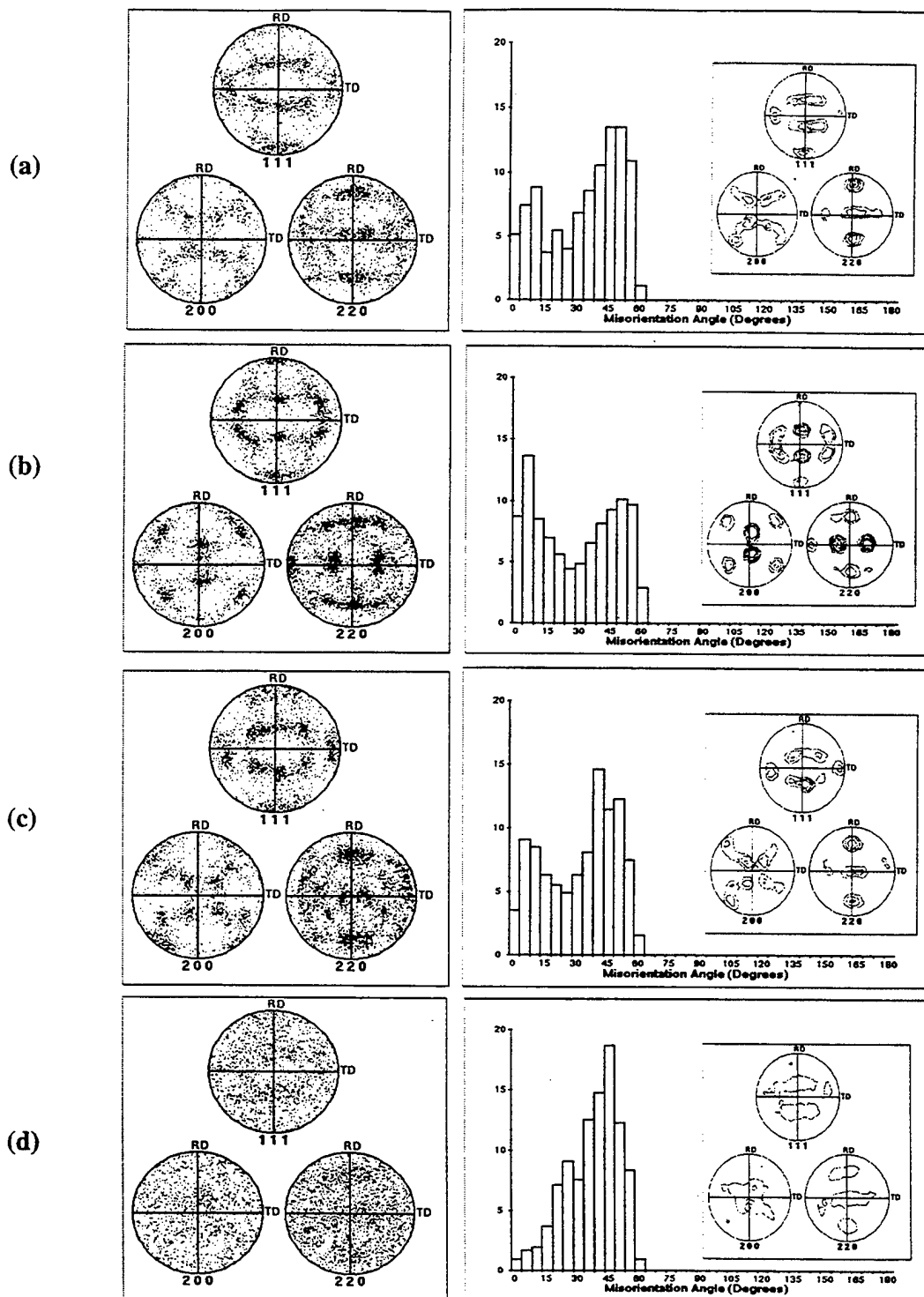


Figure 5.9. Micro and mesotextural plots for SUPRAL 2004 specimens from the cooperative research; (a) as-processed, (b) processed and annealed for 55 minutes at 480 C, (c) deformed to 40% strain, and (d) fractured tip of the deformed tensile specimen. The randomization of texture and boundary misorientation following extensive GBS is evident in (d).

SUPRAL 2004	As- Processed	Annealed 30 min at 450C	Deformed to 16% Strain at 450°C and $10^{-2}s^{-1}$	Deformed to 70% Strain at 450°C and $10^{-2}s^{-1}$	Deformed to 100% Strain at 450°C and $10^{-2}s^{-1}$	Deformed to 132% Strain at 450°C and $10^{-2}s^{-1}$
Total Number of Boundaries	496	316	316	307	303	310
% with $\theta < 15^\circ$	23.5	26.3	20.0	30.6	25.4	15.2
% with $\theta > 15^\circ$ and CSL ($\Sigma < 31$)	9.3	9.2	11.0	9.8	10.2	9.4
% with $\theta > 15^\circ$ and disordered	67.3	64.5	69.0	59.6	64.4	75.4
% $\Sigma 3$ [1.53]	3.0	2.3	2.9	4.1	5.0	2.0
% $\Sigma 5$ [1.07]	.6	1.0	0	0	0	.3
% $\Sigma 7$ [0.86]	.6	1.3	3	1.0	1.1	.7
% $\Sigma 9$ [0.88]	1.4	2.3	0	.3	.4	.3
% $\Sigma 11$ [0.68]	.4	.3	1.3	0	.4	.7
% $\Sigma 13a/b$ [0.59]	.2	.3	1.3	.3	.4	1.0
% $\Sigma 15$ [0.82]	.2	0	1.3	0	0	.3
% $\Sigma 17a/b$ [0.51]	.6	.3	.6	.7	1.1	.7
% $\Sigma 19a/b$ [0.48]	.4	0	.3	.3	0	1.0
% $\Sigma 21a/b$ [0.66]	.4	0	.3	.3	0	1.3
% $\Sigma 23$ [0.43]	0	.3	0	0	1.1	0
% $\Sigma 25a/b$ [0.48]	.6	1.3	.6	1.8	.4	.7
% $\Sigma 27a/b$.2	0	1.0	1.0	.7	0
% $\Sigma 29a/b$.8	0	.6	.3	.4	.7

Table 5.3. Boundary character data for SUPRAL 2004 specimens examined in the isochronal study. The number in brackets [] indicates the % of CSL boundaries (using the Brandon criteria) expected based on random processes [Ref. 79].

In Figure 5.9 (b), material statically annealed for 55 minutes at 480° C, the rapid development of a more pronounce bimodal distribution of boundary misorientation is evident at the slightly higher annealing temperature. Sharpening of the deformation texture is evident as is the change in the textural components due to annealling at the higher temperature.

Again, there are no recrystallization texture components evident in these data. In the data for the specimen deformed to 40% strain, shown in Figure 5.9 (c), the preferential retention of orientations near brass is again evident (as in the earlier data) concurrent with an overall reduction in texture strength, presumably due to the effect of GBS. This provides additional evidence that limited slip (evidenced by retention of the brass components in the texture) occurs concurrently with GBS, either in response to the applied stress or as an accommodation mechanism to the GBS. A mean linear intercept calculation for this specimen revealed a grain size (MLI) of 5.2 μm .

Figure 5.9 (d) provides information not presented in the earlier data. These data were taken at the tip of a fractured specimen deformed in excess of 700%. A significant randomization in texture is obvious as the orientations in the discrete pole figure fill up all of orientation space and the contours shown in the contour pole figure are at only 1.5 times random. As the number of twin and twin-generational boundaries ($\Sigma 3^n$) present is near that of random, the randomization of texture here may be attributed to grain rotations during GBS processes. The distribution of boundary misorientation following extensive GBS is observed to closely follow the random distribution predicted by Mackenzie for adjacent cubes. The observation that the mesotexture tends toward random following GBS is clearly evident in all data collected in this research (for all alloys examined) and has not been reported previously. Such random distributions of misorientation may result as grain rotations cause coalescence of LAB's and imply that only "hard" boundaries (disordered, high-angle boundaries of higher interfacial energy character which predominate in the random distribution) remain after extensive sliding because such boundaries slide most readily.

E. DISCUSSION

Data from this examination of SUPRAL 2004 show that, at the completion of the microstructural refinement processes, there is no evidence of recrystallization involving the formation and migration of high-angle boundaries. Rather, the data suggests that continuous,

recovery-dominated processes occur from the onset of post-TMP heating and result in the formation of a significant fraction (~0.25) of well-developed, moderately-misoriented boundaries and an overall bimodal distribution of boundary misorientation, with low-energy interfacial energy character, in the superplastically enabled material. Given that the fraction

SUPRAL 2004	As-Processed	Annealed 55 minutes at 480 C	Deformed to a Strain of 0.40	Deformed to Failure (Fractured Tip)
Total Number of Boundaries	348	513	505	406
% with $\theta < 15^\circ$	24.3	41.7	24.6	6.9
% with $\theta > 15^\circ$ and CSL ($\Sigma < 31$)	10.7	7.9	9.5	12.3
% with $\theta > 15^\circ$ and disordered	65.0	50.4	65.9	80.8
% $\Sigma 3$ [1.53]	3.2	1.9	1.0	1.8
% $\Sigma 5$ [1.07]	.3	.9	1.0	1.0
% $\Sigma 7$ [0.86]	.3	.9	1.0	2.0
% $\Sigma 9$ [0.88]	1.5	.4	.6	1.0
% $\Sigma 11$ [0.68]	.3	.4	.8	.8
% $\Sigma 13a/b$ [0.59]	.3	.6	1.3	1.5
% $\Sigma 15$ [0.82]	.3	0	.4	.8
% $\Sigma 17a/b$ [0.51]	0	1.0	.8	.2
% $\Sigma 19a/b$ [0.48]	1.4	.4	.8	.5
% $\Sigma 21a/b$ [0.66]	.6	.6	0	1.0
% $\Sigma 23$ [0.43]	.3	0	.8	.2
% $\Sigma 25a/b$ [0.48]	.9	.2	.6	0
% $\Sigma 27a/b$.6	.4	.2	1.0
% $\Sigma 29a/b$.9	.2	.2	.5

Table 5.4. Boundary character data for SUPRAL 2004 specimens examined in the cooperative research. The number in brackets [] indicates the % of CSL boundaries (using the Brandon criteria) expected based on random processes [Ref. 79].

of HAB's fulfilling nearness criteria to non-twin, low-index CSL ($3 < \Sigma < 31$) relations is, essentially, constant and near the level predicted for random rotations and the number of disordered HAB's remains nearly constant until well into the GBS regime, it may be concluded that the evolution of the MMB's to higher levels of misorientation by recovery processes is responsible for the microstructural refinement and reduction in grain size, and may be assumed to be responsible for enabling superplastic behavior.

Given this observation, earlier work attributing the transition to a superplastically capable microstructure to a dynamic recrystallization should be reconsidered and the refinement process viewed as a continuous process which begins during the TMP and with boundary development continuing through static annealing and dynamic straining. The continuous refinement process involves, primarily, the development of MMB's and may be viewed as a recovery-dominated mechanism. Results from the statically annealed specimens support a continuous model in that the evolution of MMB's toward higher misorientation values is observed in the absence of deformation. The evolution of HAB's in the statically annealed material appears to be associated with annealing twinning and not formation of new HAB's during discontinuous recrystallization processes.

Following the (apparent) onset of grain boundary sliding, MMB's coalesce (preferentially those with lower misorientation according to the data) during grain rotation and accommodation processes and a random micro- and mesotexture results. Previous theories detailing the mechanism of GBS have proposed that a predominance of disordered, high angle boundaries was a prerequisite for extensive superplastic flow. The ability of the recovered microstructures observed here, with a characteristically lower boundary interfacial energy distribution, to sustain extensive GBS and the boundary misorientation distribution present following extensive GBS provide evidence that cooperative GBS processes are active in the superplastic flow of this alloy. The preferential retention of brass orientations in deformed regions during randomization of texture due to GBS would strengthen earlier suggestions

[Ref. 108] that slip may be an important accommodation mechanism during GBS processes in these alloys.

F. CONCLUSIONS

1. The microstructural refinement responsible for enabling superplastic behavior in SUPRAL 2004 may be attributed to recovery-dominated processes involving the continuous development of the MMB's found in the as-processed material. The resultant superplastically-enabled microstructure has a characteristically lower boundary-interfacial energy distribution.

2. Recrystallization involving the formation and migration of high-angle boundaries is not responsible for the microstructural refinement processes observed in this alloy.

3. Evidence suggests that GBS is the dominant deformation mechanism by a strain of 1.0 suggesting that the transition to a superplastic microstructure is achieved prior to a strain of 1.0.

4. Cooperative GBS involving, primarily, sliding at disordered HAB's with accommodation by slip may describe the GBS process for this alloy at the deformation conditions in this study.

VI. GRAIN BOUNDARY DEVELOPMENT FOLLOWING PROCESSING, ANNEALING, AND SUPERPLASTIC DEFORMATION OF ALUMINUM ALLOY 2519

A. INTRODUCTION

Aluminum alloy 2519 is a wrought alloy of moderate strength (~ 360 MPa UTS in T42 temper to ~ 470 MPa UTS in T87 temper) with corrosion resistance sufficient for service in marine applications. Among the strongest of the weldable aluminum alloys, the most notable in-service application of the 2519 alloy was in structural material for the external liquid hydrogen tank on the space shuttle. The relatively high content of copper, nominally 6.0 wt%, exceeds the solubility limit of the terminal solid solution and results in the availability of eutectic liquid for backfilling of weld cracks. Also, coarse θ -phase particles, Al_2Cu , will form during solidification incipient and these will remain insoluble during heat treating of the material.

There are similarities between the chemical composition of the 2519 alloy and that of the SUPRAL alloy, discussed in the preceding chapter. The SUPRAL alloy is nominally Al - 6.0wt% Cu - 0.37wt% Zr while the 2519 alloy is nominally Al - 6.0wt% Cu - 0.3wt% Mn (others elements are present to a lesser degree in both alloy systems). The content of magnesium is higher in the 2519 alloy (0.12 wt % compared to 0.003 wt% in SUPRAL). The SUPRAL alloy transitions to a superplastically-enabled microstructure by means of continuous refinement processes in a manner discussed previously. Processing of the 2519 alloy examined in this study to produce thin sheet material for SPF has been accomplished following the Rockwell process, reviewed earlier, and has been reported [Ref. 47] to result in discontinuous recrystallization through a particle stimulated nucleation (PSN) process as suggested by Humphreys [Ref. 25]. The presence of magnesium as an alloy addition may increase recovery kinetics in processed aluminum and aid in recrystallization involving the formation of new high-angle grain boundaries. The higher magnesium content of the 2519

alloy, among other factors, may influence the microstructural response of 2519 to TMP and facilitate the distinctly different refinement process observed.

The TMP route utilized for processing the 2519 alloy involves an overaging treatment following homogenization and a low temperature pre-straining step. The time and temperature of the aging is controlled to produce a uniform dispersion of θ -phase particles of sufficient size as to induce PSN following subsequent deformation processing. When the alloy manganese content in aluminum exceeds 0.25 wt%, MnAl_6 precipitates form as fine particles ($\leq 0.1\mu\text{m}$) as a uniform dispersion during solidification. Thus, the 2519 alloy contains a bi-modal distribution of particle sizes of the second (Al_2Cu) and third (MnAl_6) phases. Aging treatments may be designed to modify particle size and dispersion. If present in a sufficient volume fraction and with sufficiently small interparticle spacing, fine particles may inhibit movement of very low angle boundaries while coarser particles may restrict motion of moderate and high-angle boundaries. With the exception of the SUPRAL alloy, a similar Rockwell-type process is utilized in the processing of most commercial, superplastic aluminum alloys available currently.

The goal of this study is to examine the boundary development and microtextural evolution in a 2519 alloy following TMP, post-TMP static annealing, and deformation within a range of temperatures and strain-rates to assess the influence of the grain boundaries on the superplastic behavior of the material. Specifically, the boundary character and microtexture resulting from a PSN initiated recrystallization following the Rockwell-type TMP will be analyzed.

B. THERMOMECHANICAL PROCESSING

Material was supplied by ALCOA Technical Center, Pittsburgh, Pennsylvania and received as 0.875 inch (22.2mm) rolled plate in the T87 temper condition (470 MPa UTS). Chemical composition data is presented in Table 6.1. The thermomechanical processing route utilized in material examined in this study is presented in Figure 6.1 [Ref.123-124].

Processing was conducted and reported by Zohorsky, Peet, and Stancy [Ref. 123-125]. The TMP route, designated TMP 25, utilized to process material was conducted alternately to two levels of total strain in the warm rolling sequence, $e_{\text{total}} = 2.2$ and $e_{\text{total}} = 3.3$, as indicated in Figure 6.1.

Cu	Mn	Mg	Fe	Zr	V	Si	Ti	Zn	Ni	Be	B	Al
6.06	0.30	0.21	0.16	0.13	0.09	0.07	0.06	0.03	0.01	0.002	0.001	bal

Table 6.1 Alloy composition (by wt%) for the as-cast 2519 Aluminum [Ref. 125].

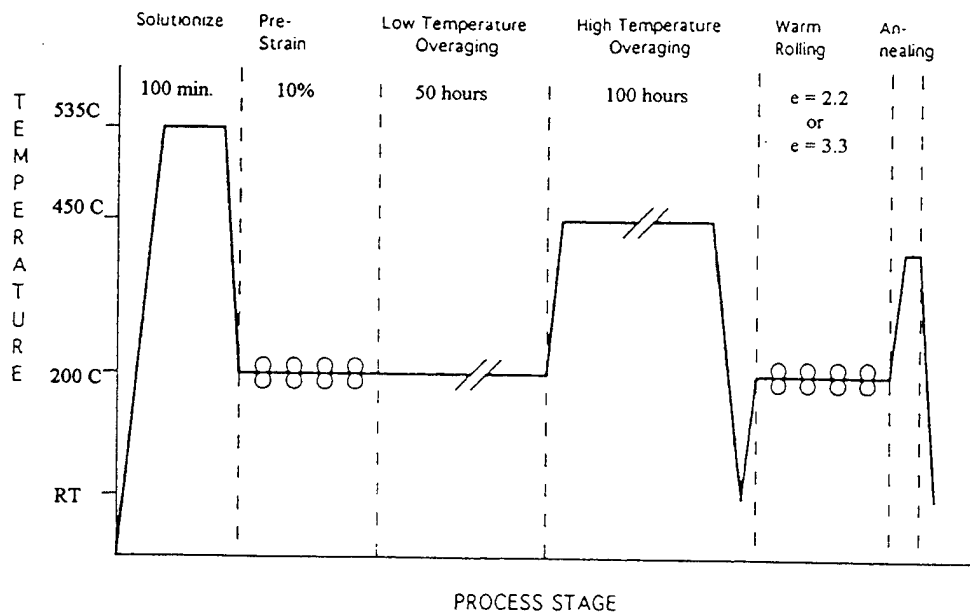


Figure 6.1. Schematic diagram depicting the TMP schedule utilized to process the 2519 material examined.

C. EXPERIMENTAL PROCEDURE

Tensile coupons and specimens of as-processed material were machined and prepared in the manner described in previous chapters. As-processed material and tensile coupons for

both total strain values from the TMP were obtained. Elevated temperature, uniaxial tensile testing was conducted on the system apparatus previously described utilizing a constant crosshead speed. As the material examined here was laboratory processed (versus commercially processed), an objective of the mechanical testing was to ascertain the superplastic regime of the material and obtain specimens for grain boundary investigations over a range of temperatures and strain rates. Tensile testing of material processed to a total strain of 3.3 was conducted at a *fixed, constant crosshead speed* corresponding to a nominal strain rate of $1.0 \times 10^{-4} \text{ s}^{-1}$ at deformation temperatures of 300°C, 400°C, or 450°C. Additionally, tensile testing on material processed to a total strain of 3.3 was conducted at a *fixed deformation temperature* of 450°C at constant crosshead speeds corresponding to nominal strain rates of $1.0 \times 10^{-4} \text{ s}^{-1}$, $1.0 \times 10^{-3} \text{ s}^{-1}$, or $1.0 \times 10^{-2} \text{ s}^{-1}$. Material processed to a total strain of 2.2 was tested at a nominal strain rate of $1.0 \times 10^{-4} \text{ s}^{-1}$ at deformation temperatures of 300°C, 400°C, and 450°C. Additionally, specimens of material processed to a total strain of 2.2 were subjected to *static* annealing at 400°C for periods of 30 minutes, 60 minutes, and 120 minutes, quenched, and prepared for examination.

All specimens were sectioned in a manner consistent with that described in earlier chapters, examined at the t/2 location, and analyzed utilizing EBSD methods previously described. BSE micrographs were obtained near the regions examined for purposes of examining grain morphology, calculation of MLI values, and to examine the distribution, size, and dispersion of the coarse, θ -phase precipitates (the MnAl_6 precipitates may also be observed but it is assumed that only the larger MnAl_6 particles, $\geq 0.1 \text{ }\mu\text{m}$, are evident at the magnifications utilized in this study). A low accelerating voltage of 5 KV was utilized to image the microstructure in the BSE mode of the SEM due to the pronounced atomic number, Z, contrast between the matrix and the θ -phase particles.

D. MECHANICAL BEHAVIOR AND MICROSTRUCTURE

Figure 6.2 illustrates the results of tensile testing. Peak elongations of 293% and

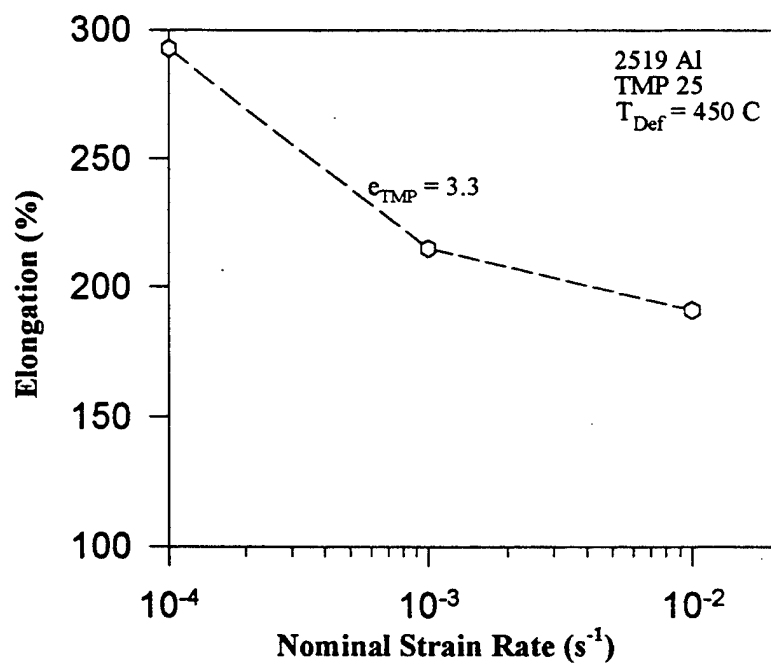
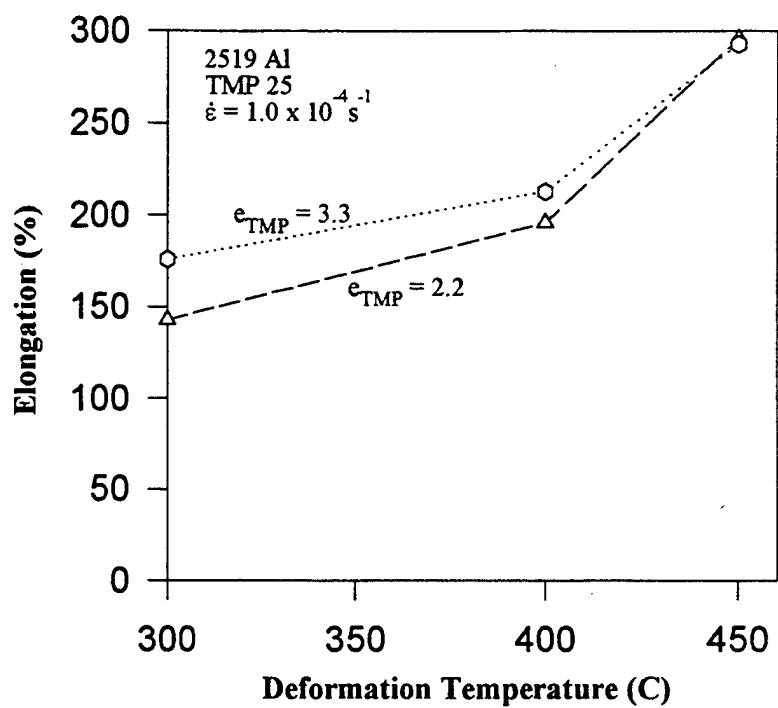


Figure 6.2. Results from mechanical testing of selected 2519 specimens.

296% were attained at the lowest deformation rate, $1.0 \times 10^{-4} \text{ s}^{-1}$, for processing strains $\epsilon_{\text{total}} = 2.2$ and $\epsilon_{\text{total}} = 3.3$ respectively. The effect of higher processing strain is reflected in marginally better elongation behavior at the lower deformation temperatures. Following the PSN model of Humphrey's, the critical particle size to serve as a nucleation site for PSN of recrystallization is a function of processing strain.

Figure 6.3 shows the flow stress versus strain rate on double logarithmic axes for tested specimens of the material processed to a strain of 3.3. A maximum strain rate sensitivity exponent, m , of approximately 0.4 is observed at the lowest test strain rate of $1.0 \times 10^{-4} \text{ s}^{-1}$, marginally within the range where GBS is thought to be the rate-controlling deformation mechanism for superplastic flow. The value of m decreases rapidly at higher strain rates indicating that slip processes likely govern the deformation processes there. The data indicates that higher deformation temperatures may be required for higher values of the

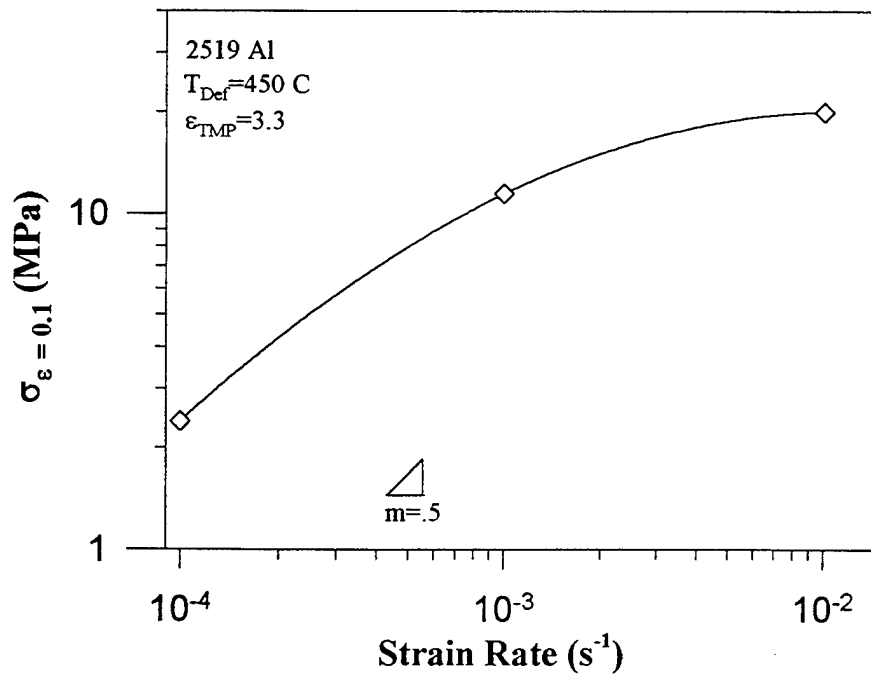


Figure 6.3. Log strain rate versus log flow stress plot for TMP25 specimen processed to $\epsilon=3.3$.

strain rate sensitivity exponent and optimum superplastic performance in this alloy.

The low values and limited range of strain rates in which superplastic flow is observed is consistent with reported values for commercial, superplastic aluminum alloys thermomechanically processed following a Rockwell-type method and may be related to the relatively coarse ($\approx 10\mu\text{m}$) grain size achieved following TMP and recrystallization [Ref. 47]. Table 6.2 summarizes the grain size calculations for various specimens of the alloy []. At elevated temperature, a coarse grain size will result in hardening and limit the superplastic strain-rate range of a material.

2519	As Received	Following Over-Aging	Following TMP 25 to $\epsilon_{\text{total}} = 2.2$	Following TMP 25 to $\epsilon_{\text{total}} = 3.3$	Processed to $\epsilon_{\text{total}} = 2.2$ Annealed 1 hr@400C
Average Grain Size (1.773xMLI)	57.3 μm	21.0 μm	12.7 μm	9.2 μm	13.0 μm

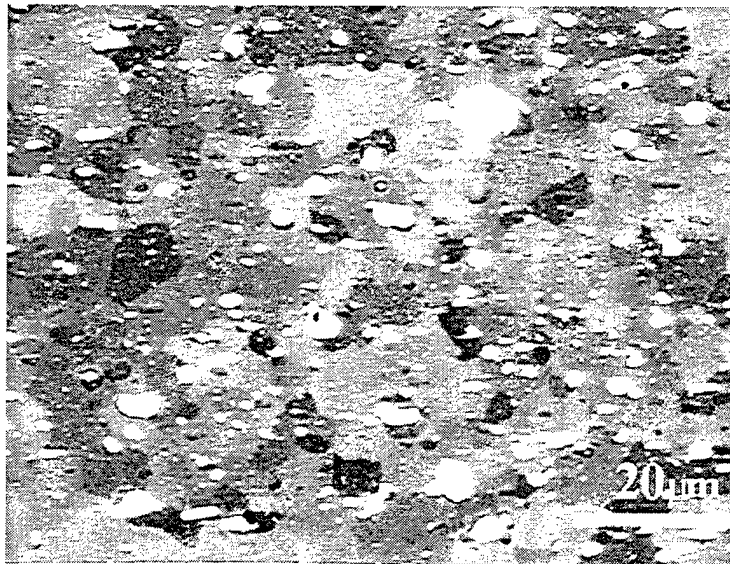
Table 6.2. Calculated grain size data for various specimens of the 2519 alloy studied.

Based on the grain size data, microstructural refinement begins during the prolonged elevated temperature (450°C) prolonged static anneal of the as-received material. Subsequent warm deformation at 200°C , with 30 minute interpass annealing at the rolling temperature, results in continuation of the refinement processes. An apparent effect of rolling to a higher total strain is a reduction in grain size to 9.2 μm . The reduction in grain size with increasing processing strain permits more particles to satisfy critical particle size requirements for participation in the PSN process and results in an increased number of active nucleation sites in the PSN model. Based on the model presented by Humphreys [Ref. 25], the final grain size is closely related to the interparticle spacing following recrystallization involving PSN.

Figure 6.4 (a) and (b) shows BSE micrographs of regions at $t/2$ in the 2519 specimens



(a)



(b)

Figure 6.4. BSE micrograph of a 2519 specimen processed following TMP25 to a total strain of 2.2 and annealed (a) 30 minutes and (b) two hours at 400°C. Orientation contrast, no etchant.

processed following TMP25 to a total strain of 2.2 and annealed (a) 30 minutes and (b) two hours at 400°C. The rolling direction is horizontal. Grain contrast is evident but somewhat masked by the predominance in contrast of the copper-rich, θ -phase particles. The θ -phase particles are observed in a uniform dispersion ranging in size from $\sim 0.5 \mu\text{m}$ to $8.0 \mu\text{m}$. Some of the ultra-fine dispersoids present are likely MnAl_6 particles, however this was not confirmed. Based on previously reported data [Ref. 123-125] most of the MnAl_6 particles are too small to be observed at the magnification here. The grains appear equiaxed and the MLI calculation of average grain size for this specimen was $13.0 \mu\text{m}$.

E. GRAIN BOUNDARY AND MICROTTEXTURAL DATA

1. As-Processed Material

Results from examination of the as-processed material following rolling to a total strain of 2.2 and 3.3 are presented in Figures 6.5 and Figure 6.6, respectively. In both of the as-processed materials the texture present *at the mid-plane* ($t/2$) of the through thickness direction is a deformation texture consistent with deformation to a high strain at elevated temperature and extending along the β -fiber. Orientation concentrations near brass, $\{011\} \langle 211 \rangle$, S $\{123\} \langle 634 \rangle$, and copper, $\{112\} \langle 111 \rangle$, have been highlighted on the discrete Euler plots. The overall texture intensity is slightly higher in the specimen processed to the higher total strain, possibly reflecting longer annealing time at elevated temperature during the additional rolling passes. In both processed materials, orientations near the copper component are predominant with orientations near the ideal S orientation somewhat lower in intensity. Orientations near brass are evident to a lesser degree. Studies have reported [Ref. 126] weak overall texture when PSN is the predominant recrystallization mechanism and, specifically, a weak brass deformation component. The orientations present near the major β -fiber components are more concentrated near the ideal orientations in the case of the more highly strained process condition.

Textural data, therefore, indicates that recrystallization is incomplete in both

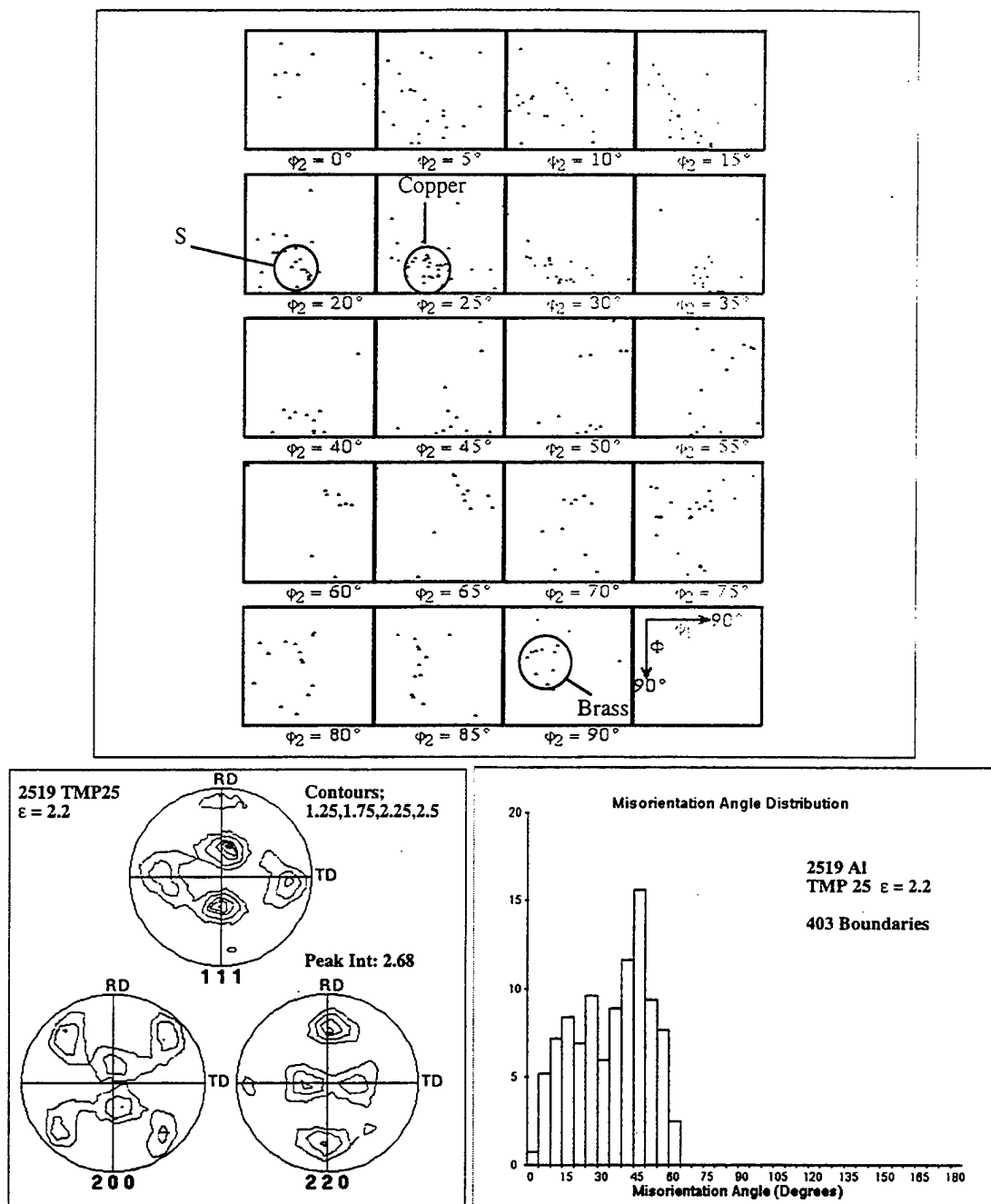


Figure 6.5. Discrete Euler plot, contour pole figure (constructed from the discrete data), and boundary misorientation histogram for as-processed (TMP 25, $\epsilon = 2.2$) material. A weak texture is present consisting, predominantly, of orientations near the deformation texture components brass and S. This data indicates that the microstructural refinement process is incomplete in the region examined ($t/2$). The fraction (0.14) of boundaries with misorientation less than 15 degrees are likely deformation induced structure from TMP.

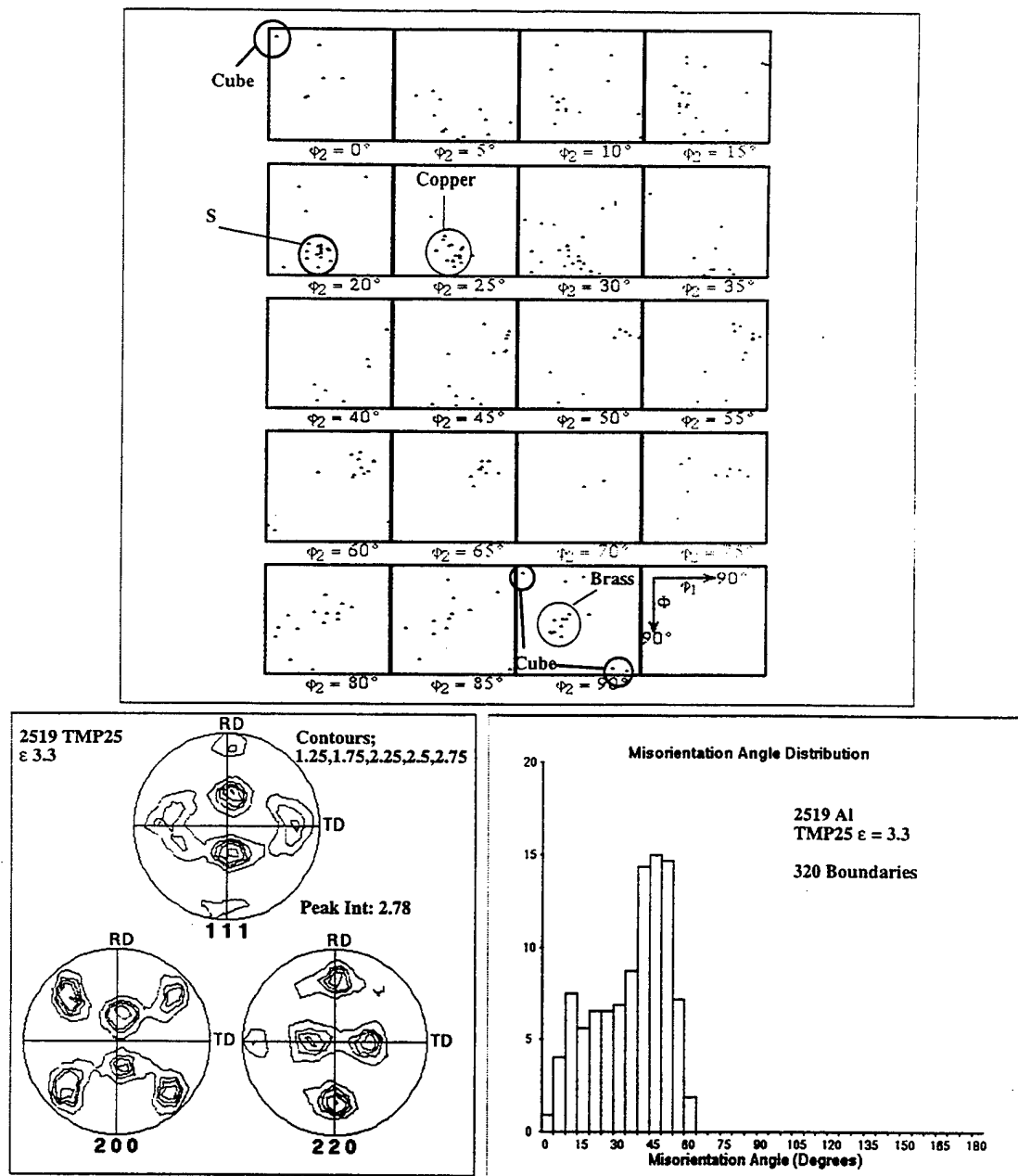


Figure 6.6. Discrete Euler plot, contour pole figure, and boundary misorientation histogram for as-processed (TMP25, $\epsilon = 3.3$) material. The textural components present are the same deformation components present in the less strained ($\epsilon = 2.2$) material however the intensity is higher and the orientations are more tightly grouped around the ideal brass, S, and copper orientations. A higher fraction of boundaries is evident in the 40–45 and 50–55 degree ranges of misorientation than was observed in the process route with lower total strain.

processed materials *at the mid-plane* ($t/2$) where data was collected. A few cube orientations are highlighted in the discrete Euler plot for material processed to the higher strain ($e_{\text{TMP}} = 3.3$). The presence of these recrystallization orientations at the mid-plane may indicate that regions near the surface ($t/4$ and $t/8$) may be either partially or fully recrystallized. Recrystallization would be expected have proceeded further in the more highly strained material if PSN is the dominant recrystallization mechanism as the PSN model predicts that a higher fraction of particles will act as nucleation sites for larger processing strains.

Boundary misorientation information is similar for the both of the as-processed materials. The data indicates that approximately 14% of all boundaries in either as-processed material ($e_{\text{TMP}} = 2.2$ or $e_{\text{TMP}} = 3.3$) are low-angle (LAB) or moderately-misoriented boundaries (MMB). This suggests that deformation during TMP has resulted in the development of a significant volume of deformation structure. Since the as-processed materials are unrecrystallized *at the region of examination*, the HAB's may be attributed to those produced by twinning and those which are prior boundaries.

In the case of the more highly strained ($e_{\text{TMP}} = 3.3$) material there are noticeably more HAB's in the $40^\circ - 45^\circ$ and $50^\circ - 55^\circ$ ranges. In conjunction with the presence of cube orientations, this may be viewed as supporting the observation that partial recrystallization is evident at the $t/2$ region in the more highly strained, as-processed material. The appearance of more boundaries in the $40^\circ - 45^\circ$ and $50^\circ - 55^\circ$ misorientation ranges would be expected for recrystallization involving the formation and migration of HAB's according to a PSN model. Recrystallization following the PSN model has been generally thought to produce grains with random orientations [Ref. 25] as the nuclei formed in the deformation zones around large, non-deforming particles are thought to have random orientations. The resultant grain boundary distribution would be expected to follow that described by Mackenzie [Ref. 112] and with the largest fraction of boundaries lying in the $40^\circ - 45^\circ$ and $50^\circ - 55^\circ$ misorientation range.

The distribution of boundaries satisfying nearness to low-index CSL relations for both

as-processed materials is summarized quantitatively later in Table 6.3. The overall frequency of occurrence of CSL boundaries is near random for both materials. There are more twin ($\Sigma 3$) boundaries in the $e_{\text{imp}}=2.2$ material (1.5 times random) and more $\Sigma 9$, second generation twin boundaries, in the $e_{\text{imp}}=3.3$ than predicted (1.7 times random). The fraction of boundaries near $\Sigma 7$ ($60^\circ/\langle 111 \rangle$) is near that predicted for random rotations. There has been a consensus for many years that the $\Sigma 7$ misorientation is essentially the maximum growth rate orientation (MGRO) in aluminum during primarily recrystallization [Ref. 23-24, 68]. Much of the data for these observations was on single- and bi-crystals. The absence here (at the $t/2$ region in as-processed materials) of the existence of MGRO's suggests that either primary recrystallization has not proceeded to the $t/2$ region, the operative recrystallization mechanism(s) involve growth processes which do not follow the MGRO, or the $\Sigma 7$ orientations are lost in the generation of orientations in a heavily rolled polycrystalline material with a large volume fraction of second phase. The late Dr. Haasen [Ref. 23] similarly reported observing fewer than expected $\Sigma 7$ boundaries and more than expected (2.7 times random here) of twin-modified $\Sigma 7$ boundaries ($\Sigma 21$).

2. Microstructural Development During Static Annealing

Figure 6.7 summarizes the evolution of microtexture and mesotexture during static annealing at 400°C in material thermomechanically processed to a strain of 2.2. Again, all examination were conducted near the $t/2$ region. The uncorrelated distribution of boundary misorientation, calculated from the orientation data set in the manner previously described, has been plotted to overlay the correlated boundary misorientation histogram. Results indicate that the weak deformation texture present in the as-processed material is transformed to a weak cube texture following a brief 30 minute static annealing at 400°C . Continued annealing for 120 minutes results in a slight sharpening of the cube texture intensity to a moderate peak intensity level of 2.9. With the exception of cube, $\{001\} \langle 100 \rangle$, and cube_{ND} (cube rotated about the normal direction), $\{001\} \langle 110 \rangle$, orientations, present at moderate levels, orientations are randomly distributed through Euler space. Therefore, microtextural

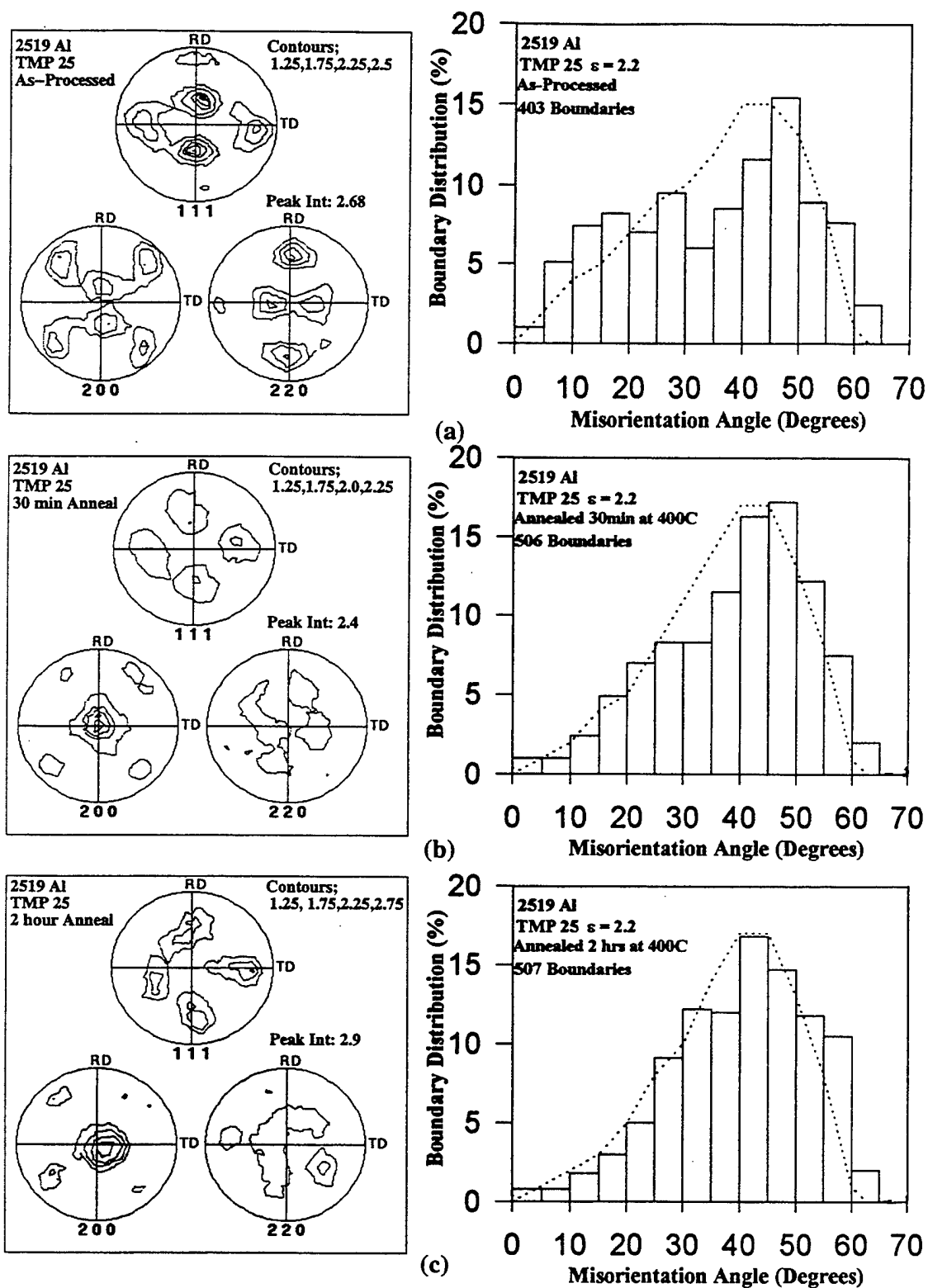


Figure 6.7. Contour pole figures and boundary misorientation histograms for specimens of 2519; (a) as-processed, (b) annealed 30 minutes at 400°C, and (c) annealed 2 hours at 400°C. The uncorrelated misorientation distribution is plotted overlaying the histogram.

data indicates that recrystallization is complete through the thickness of the processed sheet following a 30 minute anneal and that the orientation distribution of recrystallized grains is essentially random with a weak cube texture component.

Analysis of the boundary misorientation distribution data during annealing illustrates the change in grain misorientation which occurs as a result of recrystallization. The grain structure in the as-processed material consisted of deformation and recovery-induced low angle and moderately misoriented boundaries (with $\theta \leq 15^\circ$), original grain boundaries, and twin-modified original boundaries. The distribution of boundary misorientation following recrystallization preferentially consists of high-angle, disordered boundaries which follow both the random distribution predicted by Mackenzie [Ref. 112], based only on geometrical considerations, and the uncorrelated distribution predicted by the orientations present. The close degree of correspondence between the uncorrelated distribution and Mackenzie's random distribution is due to the random nature of the distribution of orientations in Euler space following recrystallization. This suggests that the operative recrystallization mechanism is likely PSN. There is no evidence that a cube recrystallization mechanism is contributing to the generation of new orientations. Nucleation of new grains of cube orientation has been summarized [Ref. 126] to involve either parent, primary cube grains persisting through the deformation process or subgrains of cube orientation within the banded region of the elongated, flattened grains following deformation. In either case, EBSD examination would be expected to reveal the cube orientations in the as-processed material.

LAB and MMB's, to a substantial degree, are not observed in the recrystallized microstructure. Newly recrystallized grains formed by a PSN mechanism for materials processed to the high reductions would be expected to be high-angle in nature, as the increase in misorientation between the matrix and the recrystallized grain increases with processing strain in the deformation zone as suggested in the model of Humphreys [Ref. 25]. Additionally, existing LAB's and MMB's may be lost during the PSN and recrystallization process through coalescence with the reaction front of the newly formed grains. Quantitative

boundary character data, summarized in Table 6.3, suggests that twinning is operative during annealing as evidenced by the presence of boundaries which satisfy nearness criteria to first and second generation twin CSL relations $\Sigma 3$ and $\Sigma 9$ ($\Sigma 3^2$). These are present above random levels in material annealed 30 minutes.

Although the grain boundary structure of the resultant, recrystallized microstructure is dominated by high-angle, disordered boundaries with characteristically high interfacial energy levels and migration rates, grain growth during annealing is modest. The average grain size estimated by MLI calculation is $12.7\mu\text{m}$ for as-processed, $e_{\text{TMP}}=2.2$, material and $13.0\mu\text{m}$ for material statically annealed one hour at 400°C (Table 6.2). Apparently, the distributions of second phase, Al_2Cu , and third phase, MnAl_6 , are effective in inhibiting boundary migration at the annealing temperature.

3. Deformed Regions

Figure 6.8 illustrates discrete pole figures and boundary character data for regions in deformed gage sections of tensile coupons tested at $\dot{\epsilon} = 1.0 \times 10^{-4}\text{s}^{-1}$ at 450°C and 300°C . The microtexture in the deformed regions of the specimens consists primarily of random orientations. The predominantly random distribution of orientations present in the *undeformed*, annealed specimens has persisted during extensive plastic deformation (this specimen elongated 293%). As stated previously, grain rotations required during accommodation processes during GBS have been observed and widely reported to result in a randomization of texture during deformation. However, since the undeformed microstructure at the start of deformation was essentially random (with a weak cube/rotated cube texture) a direct comment regarding the observation of GBS based on the microtextural data may not be made. There is, however, no evidence of textural transitions to stable end-orientations associated with deformation by single slip ($\langle 121 \rangle$ end orientations) or multiple slip ($\langle 111 \rangle$ fiber formation) [Ref. 108]. Given that a strain rate sensitivity value of $m \approx 0.4$ was observed from the mechanical data and an equiaxed grain morphology was observed in the deformed regions, deformation by GBS may be concluded to be a significant deformation mechanism.

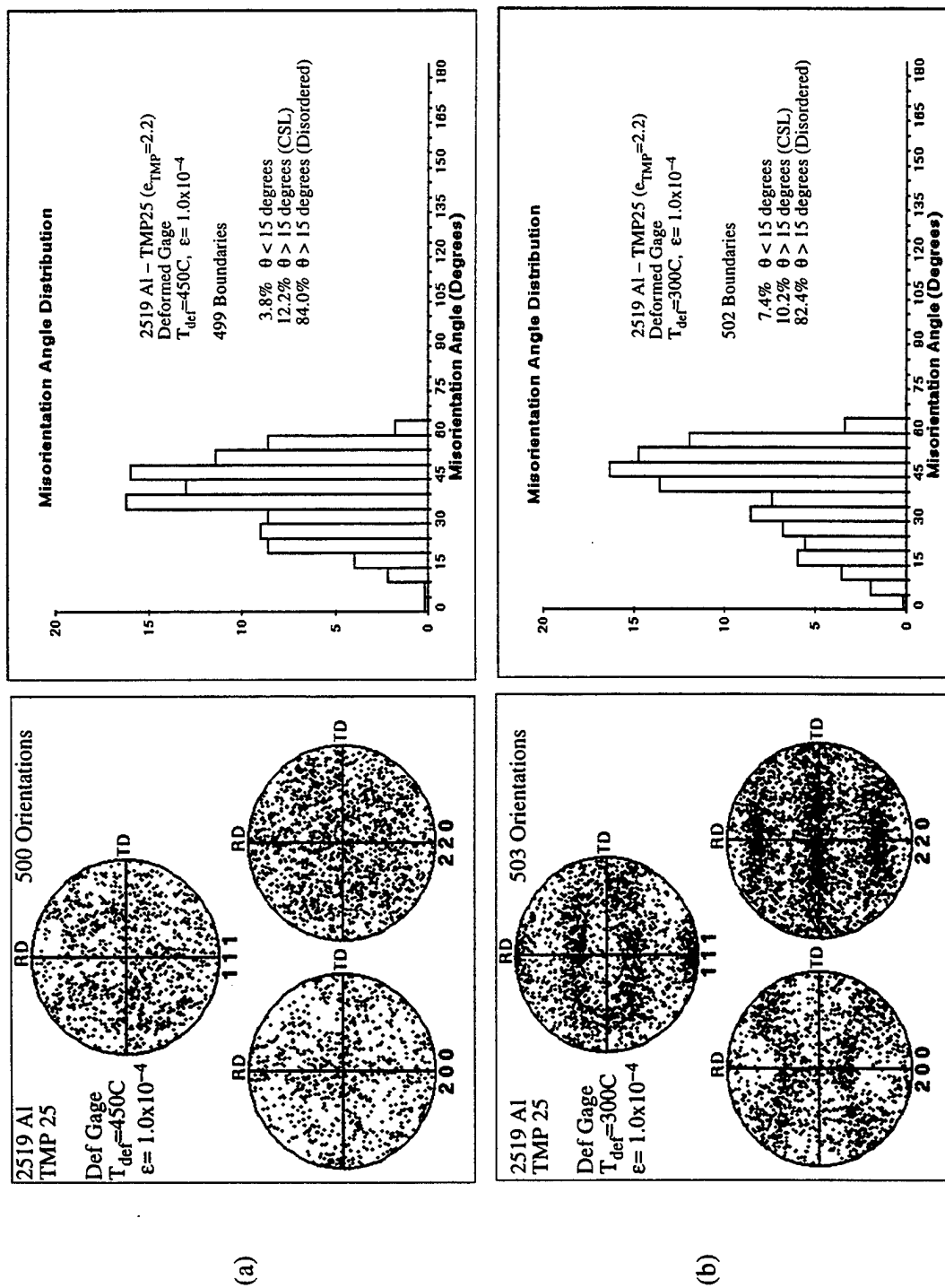


Figure 6.8. Microtexture and boundary character plots for deformed regions in 2519 tensile coupons; (a) tested at 450C and (b) tested at 300C. Deformation conditions in (a) appear to be near the transition area from region I to region II (GBS) behavior based on the mechanical data. The apparent randomization of texture is indicative of GBS. In (b), a $\langle 111 \rangle$ slip texture is apparent. This confirms the mechanical data that the test temperature of 300C may be insufficient for GBS and region III deformation mechanisms are rate-controlling.

In contrast, examination of deformed regions in the tensile specimen tested at 300°C shows clear evidence of the formation of a $\langle 111 \rangle$ fiber texture indicative of deformation by multiple slip.

The grain boundary character data for the deformed regions reveal that deformation by multiple slip results in an increase in the population of LAB's and MMB's. One explanation for this observation is that coalescence of LAB's during the grain rotations which accomodate GBS do not occur during deformation by multiple slip and LAB's present at the onset of deformation are retained. The quantitative data (Table 6.3) shows that twin, $\Sigma 3$ CSL, boundaries are present at two times random in the specimen deformed at 300°C. Given the more limited time at elevated temperature for this specimen (as the elongation was 143% at a strain rate of $\dot{\epsilon} = 1.0 \times 10^{-4} \text{s}^{-1}$ compared to 293% for the specimen deformed at 450°C at the same strain rate) available for formation of annealing twins this suggests that deformation twinning may occur to a limited degree.

F. DISCUSSION

The development of boundaries following TMP and post-TMP annealing may be discussed in terms of the orientations present in microstructure as boundaries may be characterized by a comparison of the associated two neighbor orientations. The orientations identified by EBSD examination of the as-processed material at the mid-plane originate from grains which are retained from the microstructure prior to TMP, orientations from the microstructure prior to TMP which have been modified, and new orientations generated in the deformation microstructure (DM) during TMP and reflect the stable end-orientations for the operative slip processes. The stable end-orientation concentrations present in the as-processed material follow those predicted by Taylor theory and are the major deformation components which lie on the β -fiber; copper, S, and brass, in order of decreasing textural component intensity. The associated deformation mesotexture evident at the mid-plane ($t/2$) of the as-processed material consists of approximately 15% LAB/MMB's ($\theta < 15^\circ$), 11%

2519	As Processed $e_{\text{TMP}}=2.2$	As Processed $e_{\text{TMP}}=3.3$	Annealed 30 min $T_{\text{ann}}=400\text{C}$ $e_{\text{TMP}}=2.2$	Annealed 60 min $T_{\text{ann}}=400\text{C}$ $e_{\text{TMP}}=2.2$	Annealed 120 min $T_{\text{ann}}=400\text{C}$ $e_{\text{TMP}}=2.2$	Deformed Gage $T_{\text{def}}=450\text{C}$ $\dot{\epsilon}=10^{-4}\text{s}^{-1}$	Deformed Gage $T_{\text{def}}=300\text{C}$ $\dot{\epsilon}=10^{-4}\text{s}^{-1}$
Total Number of Boundaries	403	420	506	509	507	499	502
% with $\theta < 15^\circ$ [2.3]	14.8	14.7	5.7	4.9	4.1	3.8	7.4
% with $\theta > 15^\circ$ and CSL ($\Sigma < 31$) [11.3]	10.9	10.6	10.7	9.7	10.8	12.2	10.2
% with $\theta > 15^\circ$ and disordered [86.4]	74.3	74.7	83.6	85.4	85.1	84.0	82.4
% $\Sigma 3$ [1.53]	1.5	1.0	2.0	1.6	1.4	1.6	2.8
% $\Sigma 5$ [1.07]	1.0	0.9	1.2	1.4	1.4	2.4	0.2
% $\Sigma 7$ [0.86]	0.8	0.9	0.4	1.0	0.8	1.4	1.0
% $\Sigma 9$ [0.88]	0.2	1.6	1.8	0.6	1.8	0.4	0.6
% $\Sigma 11$ [0.68]	1.5	0.9	0.6	0.4	0.4	0.8	1.4
% $\Sigma 13\text{a/b}$ [0.59]	0.7	0.6	1.4	1.5	0.6	1.8	0.2
% $\Sigma 15$ [0.82]	0.7	0.9	0.8	0.8	0.8	0.6	0.6
% $\Sigma 17\text{a/b}$ [0.51]	0.5	0.9	0.2	0	0.8	0.6	0.4
% $\Sigma 19\text{a/b}$ [0.48]	0.3	0	0	0.5	1.2	0.4	1.0
% $\Sigma 21\text{a/b}$ [0.66]	1.7	0.6	0.6	0.4	0.2	1.0	0.8
% $\Sigma 23$ [0.43]	0.5	0.3	0	0.8	1.0	0.6	0.2
% $\Sigma 25\text{a/b}$ [0.48]	0	1.2	1.0	0	0.4	0	0.6
% $\Sigma 27\text{a/b}$	0.7	0.3	0.4	0.2	0.2	0.4	0
% $\Sigma 29\text{a/b}$	0.7	0.3	0.4	0.4	0	0.2	0.4

Table 6.3. Summary of boundary character data for the 2519 Al specimens examined. The number in brackets indicates the % of CSL boundaries satisfying the Brandon criterion for random rotations [Ref. 79].

HAB's near low-index CSL relations, and 74% disordered HAB's (in contrast, as-processed SUPRAL consisted of 24% LAB/MMB's, 9.5% HAB's near low-index CSL relations, and 64.5% disordered HAB's). The *overall* fraction of boundaries satisfying the Brandon nearness criterion to low-index CSL relations remains essentially constant in all specimens examined and near that predicted by random rotations. Cube-related orientations and orientations consistent with recrystallization involving the formation and migrations of new HAB's were not present to a significant degree in the as-processed material at the $t/2$ region examined.

Data indicate that recrystallization is complete through the thickness of the processed sheet within 30 minutes of static annealing at the annealing temperature of 400°C. Orientation concentrations associated with the stable end-orientations of the DM are not observed in the recrystallized material but, rather, an orientation distribution that is primarily random with a weak concentration of orientations near the cube and rotated cube components is present.

The grain boundary misorientation distribution following recrystallization is near the random distribution of Mackenzie's [Ref. 112] and consists predominantly of high-angle, disordered boundaries. A random misorientation distribution would be expected to result from a random orientation distribution if no boundary-development process (such as extended recovery in the case of LAB's/MMB's, or extensive twinning in the case of HAB's) were operative in the formation of new boundaries concurrent with the retention of the orientation distribution of the DM. The grain boundary misorientation distribution observed in the recrystallized material may be described by a discontinuous recrystallization process. Following the PSN model of Humphreys [Ref. 25], nucleation of recrystallized grains occurs in deformation zones of high dislocation density and large lattice curvature near non-deforming particles. These nuclei are thought [Ref. 126] to have random orientations. Nucleation from regions near high-angle grain boundaries (such as grain boundary steps) is also thought to produce randomly oriented grain nuclei [Ref. 126].

The selection process for growth of the nucleated grains apparently favors boundaries of with high mobility rates, based on the mesotextural data. Additionally, the microtextural transition from the as-processed condition to the recrystallized state closely follows that described by Berger [Ref. 26] for the idealized transition of deformation microstructure to the recrystallized microstructure in aluminum based on orientation-dependent growth rates. Twin selection, as described by Berger [Ref. 26], does not appear to dominate as the quantitative data (Table 6.3) does not show the presence of twin $\Sigma 3$, twin-chain $\Sigma 3^n$, or twin-modified $\Sigma 3 \times \Sigma N$ *consistently* at levels far above random. Cube selection or generational formation of cube orientations, as described by Nes, et al. [Ref. 126] does not appear to contribute based on the absence of cube orientations in the as-processed material and the limited increase in intensity of the cube component during longer periods of static annealing.

Regardless of the boundary development process during PSN initiated recrystallization, the high interfacial energy character of the resultant boundary distribution in the recrystallized microstructure does not adversely effect the superplastically-enabled microstructure through increased grain growth kinetics. Grain growth during continued elevated temperature annealing is subdued, probably due to effective pinning of boundaries by the Al_2Cu and MnAl_6 particles.

Thus, the grain size resulting from recrystallization may be the limiting microstructural feature for superplastic performance for this alloy at the deformation temperature utilized (cavitation may be a factor at higher temperatures but significant cavitation was not observed in deformed specimens at the test temperatures here). The expected high mobility of the boundaries present following recrystallization would facilitate GBS accomodation processes and would not be expected to limit superplatic flow kinetics. The peak strain rate for superplastic flow has been shown in a previous chapter to be highly sensitive to grain size, however. As previously noted, the grain size resulting from recrystallization involving PSN is thought to be close the the interparticle spacing (of the θ -phase here). Following PSN theory, grain refinement to a lower grain size is possible if the fraction of particles active in

the nucleation of new grains is increased or the interparticle spacing is decreased while retaining the same particle size distribution. The former would involve processing to a higher strain values. The latter would result for a higher volume fraction of second phase and is limited by the amount of copper available from solution.

The foregoing discussion may summarize a fundamental difference in the alternative routes for processing of aluminum alloys for superplasticity, in that processing to achieved grain-refinement with a retained deformation microstructure (such as in the SUPRAL process) may be accomplished by refinement of low-energy boundaries and yield boundaries with lower overall migration and growth rates. Processing to achieve a recrystallized microstructure by the formation and migration of HAB's may require grain growth selection, which favors high mobility and results in a coarse grain size and increased dependence on the presence of dispersoids to inhibit grain growth. Processing to achieve microstructural refinement to a smaller (sub)grain size without a recrystallization involving the production of new HAB's may lead to improved superplastic response if the accomodation process during GBS is sufficiently rapid to accomodate the (presumably) non-sliding (LAB/MMB) boundaries.

Data from EBSD examination of the deformed regions of specimens tested within the GBS regime in the 2519 material and in the SUPRAL 2004 and TMP6 processed Al-10Mg-0.1Zr materials of previous chapters illustrate that, regardless of the mesotexture present at the onset of GBS, the grain boundary misorientation distribution following extensive GBS consists predominantly of disordered, high angle boundaries for which rapid grain boundary shear rates have been reported [Ref. 30]. This suggests that only these boundaries are sliding interfaces in the GBS process.

Apparently, the non-sliding LABs/MMBs are accomodated readily in the SUPRAL material given the higher (by two orders of magnitude) peak superplastic strain rates observed for that material. In the 2519 material, the high volume fraction of dispersoids necessary to restrict migration of new HABs formed during discontinuous recrystallization may inhibit the

GBS process in a manner described by Raj and Ashby [Ref. 17] whereby the particles act like pegs penetrating the sliding boundary plane and result in decreased sliding rates for a given applied shear stress.

VII. THE INFLUENCE OF GRAIN BOUNDARY CHARACTER DEVELOPED IN COMMERCIALY PROCESSED, SUPERPLASTIC 5083 ALUMINUM

A. INTRODUCTION

Recent interest in use of highly-formable aluminum-magnesium alloys in the automotive industry has resulted in efforts to improve the superplastic behavior of the currently available commercial, aluminum-magnesium alloys thermomechanically processed to exhibit fine-grained superplasticity. The 5083 aluminum alloy, nominally Al - 4.7wt% Mg - 0.7 wt% Mn, is a common aluminum-magnesium material and is widely used in moderate strength (~ 200 - 300 MPa) structural applications where corrosion resistance is important. Several commercial, superplastic 5083 materials are currently produced; however, end-use application of these materials has been limited due to the modest superplastic performance of these materials and the relatively high homologous forming temperatures ($\sim 0.82 T_m$) required. As a result, the largest U.S. manufacturer of superplastic materials reports that most superplastically processed 5083 aluminum is utilized in hot-bending applications in non-U.S. railroad industries while use in the automotive industry, although increasing, has been subdued [Ref. 127].

Recent studies of superplasticity in the 5083 aluminum alloy have attributed the transition to a fine-grained structure to static recrystallization occurring during intermediate annealing steps following cold-rolling stages of the TMP scheme. Maximum values of the strain-rate sensitivity exponent, $m \approx 0.5$ - 0.65 , have been observed at strain rates of $\approx 5.0 \times 10^{-4} \text{ s}^{-1}$ in the temperature regime reported for peak elongations ($\sim 525^\circ\text{C}$ - 550°C) [Ref. 128]. These strain rates are well below those utilized in most commercial forming operations.

The goal of this study is to quantify the grain boundary characteristics that result from TMP and the associated grain refinement process and determine the influence of the grain boundaries on the observed superplastic flow. As the material is reportedly recrystallized in

the as-processed state the distribution of boundaries present may be attributed directly to the TMP scheme employed. Evolution of the microstructure and mesotexture in post-processing annealing and during deformation will also be examined.

B. EXPERIMENTAL PROCEDURE

Superplastic 5083 material manufactured by Sumitomo-Kaiser, trade name SKY5083, was obtained from NASA-Langley Research Center and A.S.&M., Inc., Hampton, VA in the as-processed condition as 2.0 mm sheet. Chemical analysis of the received material is presented in Table 7.1. Tensile coupons were machined from the sheet material to the geometry cited in the previous chapter. Elevated temperature, uniaxial tensile testing was conducted at 535°C on the mechanical test apparatus described in the preceding chapter at various constant-crosshead speeds corresponding to nominal strain rates of $1.0 \times 10^{-4}\text{s}^{-1}$, $1.0 \times 10^{-2}\text{s}^{-1}$, and $1.0 \times 10^{-1}\text{s}^{-1}$. An untested coupon was utilized for analysis of the as-processed state.

	Mg	Mn	Cr	Fe	Si	Al
SKY5083	4.48	0.65	0.11	0.07	0.05	bal

Table 7.1 Alloy composition (by wt%) for the as-processed SKY 5083.

Tensile coupons were sectioned longitudinally, prepared and examined using BSE and EBSD methods described previously. Grain size (MLI) was determined for regions adjacent to those specimen areas examined using quantitative methods described earlier. A total of six samples/regions were analyzed: as-processed; the undeformed grip section of the specimen deformed at $\dot{\epsilon}=10^{-4}\text{s}^{-1}$ (corresponding to static annealing 535°C for 11 hours including time for stabilization at the test temperature); the undeformed grip section of the specimen deformed at $\dot{\epsilon}=10^{-2}\text{s}^{-1}$ (corresponding to static annealing for 30 minutes at 535°C); and

regions approximately half-way down the deformed gage section of coupons tested at the three test strain rates utilized. Analysis of the collected orientation data was accomplished using methods described earlier.

C. MECHANICAL BEHAVIOR AND MICROSTRUCTURE

Mechanical testing results are presented in Figure 7.1. Data for testing conducted at NASA-Langley Research Center and A.S.&M., Inc. for other deformation rates has also been included in the graph. Peak elongations were observed at the lowest strain rate utilized in testing, $1.0 \times 10^{-4} \text{ s}^{-1}$, with an associated strain rate sensitivity exponent of $m \approx 0.5$. The mechanical test data indicates that the maximum strain rate at which grain boundary sliding (GBS) is the rate-controlling deformation mechanism, region II, is on the order of 10^{-4} s^{-1} for this alloy at the deformation temperature utilized. For deformation rates of $\dot{\epsilon} \geq 5.0 \times 10^{-3} \text{ s}^{-1}$ elongation remains essentially constant at a marginally superplastic value of $\approx 240\%$ and $m \leq 0.33$, indicating GBS is unlikely the principal deformation mode and a transition from region II (GBS rate controlling) to region I where diffusion-controlled dislocation glide is rate controlling for the plastic flow.

Figure 7.2 (a) and (b) illustrates BSE micrographs for as-processed material and for a region corresponding to static annealing for 30 minutes at 535°C . In (a) a low-volume fraction of coarse, Al_3Mg_5 particles are observed along with a fine (submicron), uniform dispersion of Al_6Mn particles. A refined grain size is evident although the limited contrast in some areas suggests that grain development may be incomplete. A mean linear intercept (MLI) determination of grain size for the as-processed material resulted in a value of $L_{\text{mean}} = 8.96 \mu\text{m}$. In (b) the grain contrast is more pronounced and some grain growth is evident. The MLI calculation for material illustrated in (b) was $L_{\text{mean}} = 12.3 \mu\text{m}$. The significant grain growth (37% increase) observed following the brief anneal suggests that the grain boundaries present in the as-processed material are highly mobile and that the volume fraction of the dispersoids may be insufficient to retard grain boundary migration at the

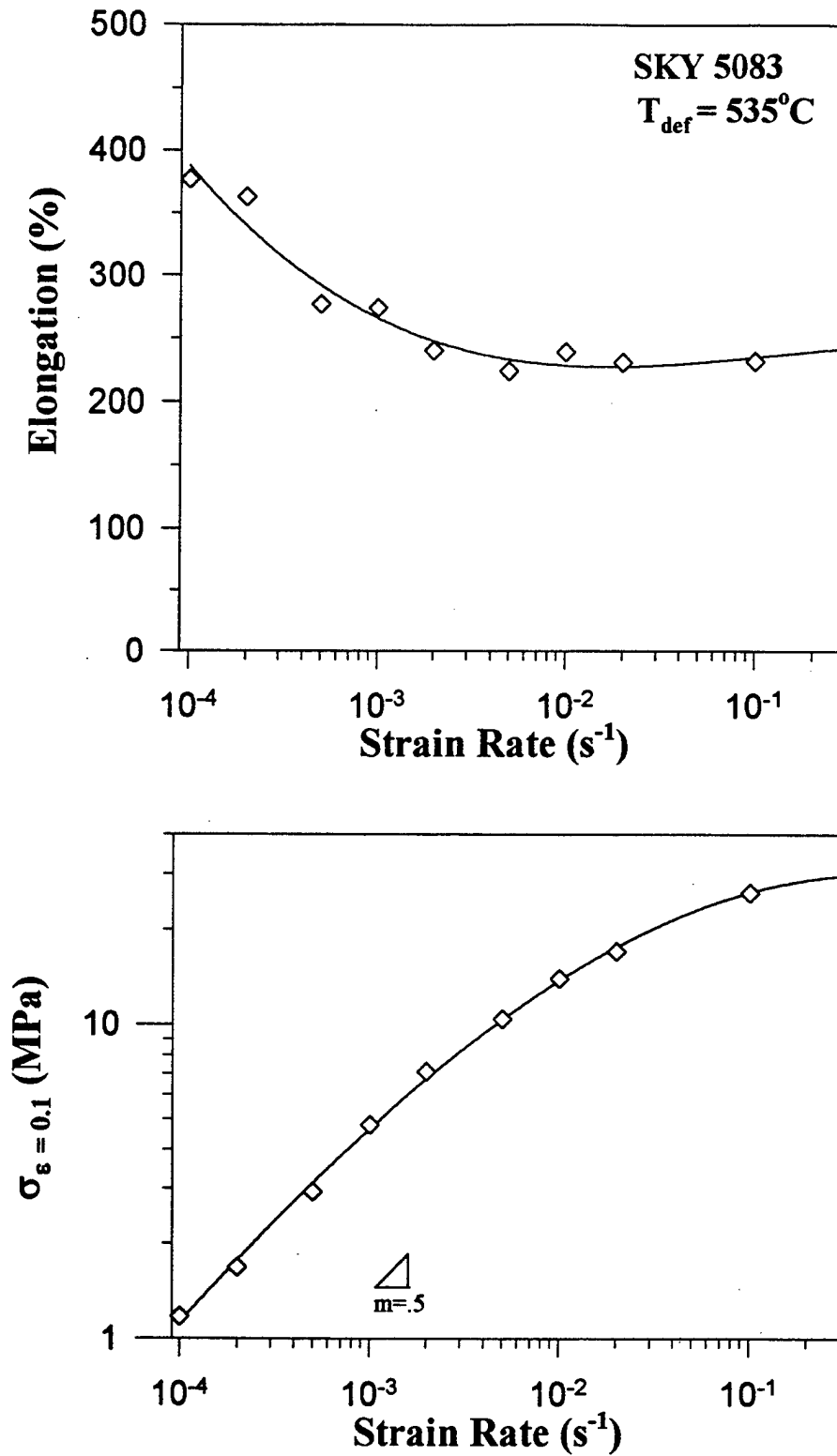
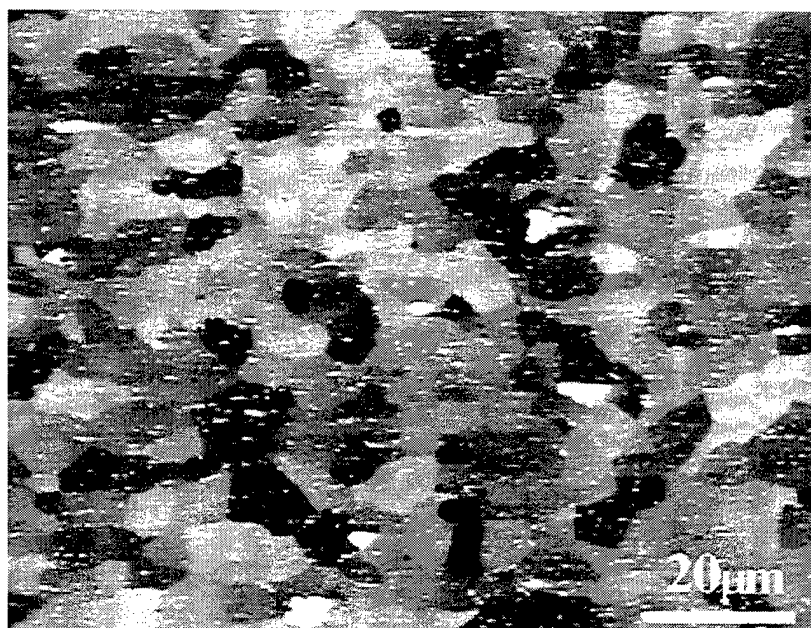
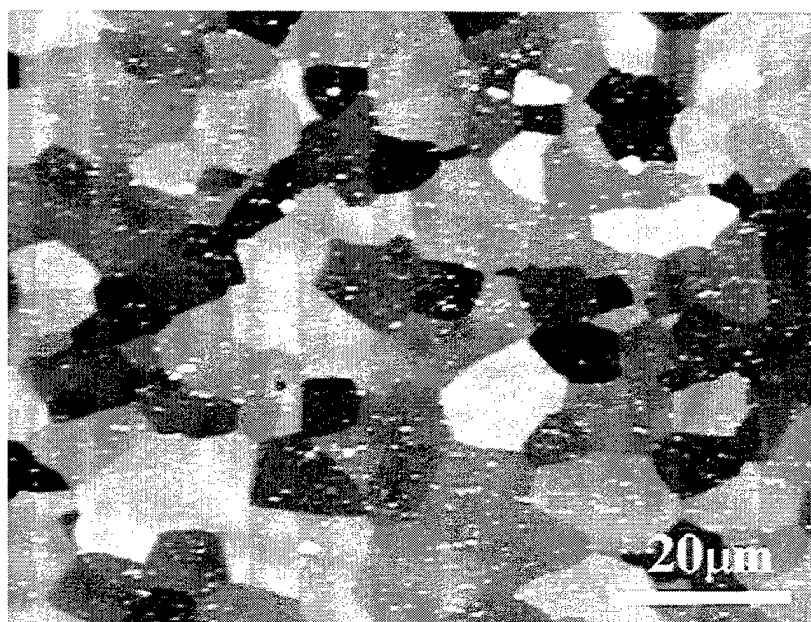


Figure 7.1. Plots describing the mechanical behavior of SKY 5083.



(a)



(b)

Figure 7.2. BSE micrographs of specimens of SKY5083 (a) as-processed and (b) processed and statically annealed for 30 minutes at 535 C. A fine dispersion of Al_6Mn particles is present. The rolling (and tensile) direction is the horizontal. Orientation contrast at 5KV, no etchant.

relatively high homologous temperature ($0.8T_m$).

D. MICROTTEXTURAL AND MESOTEXTURAL RESULTS

Figure 7.3 (a) and (b) illustrates the microtexture present in material as-processed and statically annealed 30 minutes at 535°C respectively. Data reveals that distribution of orientations is near random in the as-processed material with only a weak texture present (peak intensity 2.3 times random). The overall texture may be described as a mixture of rolling and recrystallization components. The rolling components present lie along the β -fiber and are located near brass, $\{011\} \langle 211 \rangle$, and S, $\{123\} \langle 634 \rangle$. Recrystallization orientations near the cube component, $\{001\} \langle 100 \rangle$, rotated cube (cube rotated about the rolling direction, evident along the ϕ axis in the $\varphi_2 = 0^\circ$ and $\varphi_2 = 90^\circ$ windows of the Euler plot), $\{025\} \langle 100 \rangle$, and Goss component, $\{101\} \langle 010 \rangle$ (visible in the $\varphi_2 = 0^\circ$ window at $\phi = 45^\circ$, $\varphi_1 = 0^\circ$) are also evident. The textural evidence here implies that the material is not fully recrystallized in the as-processed state and is indicative of TMP including warm rolling or cold rolling with brief inter-pass anneals at moderate temperatures. As the data were collected at regions near $t/2$, the mid-plane in the processed sheet, the preferred orientation present may be associated with through-thickness textural anisotropy associated with incomplete recrystallization. A recent study on the origin of the cube texture during warm rolling of similarly processed Al-Mg-Mn alloys showed a fully recrystallized microstructure (and an associated cube texture) persisted to a distance of one third of the sheet thickness while the center portion of the material consisted of elongated, recrystallized grains with bands of unrecrystallized material running between the grains [Ref. 97]. Data here is consistent with these observations and suggests that reversible rolling may have been used to induce deformation during TMP.

Following the 30 minute anneal the texture in (b) is observed to undergo a transition to a moderately strong recrystallization texture consisting primarily of cube and RC_{nd} , cube components rotated about the normal direction. RC_{nd} orientations are evident in the $\varphi_2 = 90^\circ$ along the ϕ axis. The texture in (b) was observed to persist throughout longer annealing

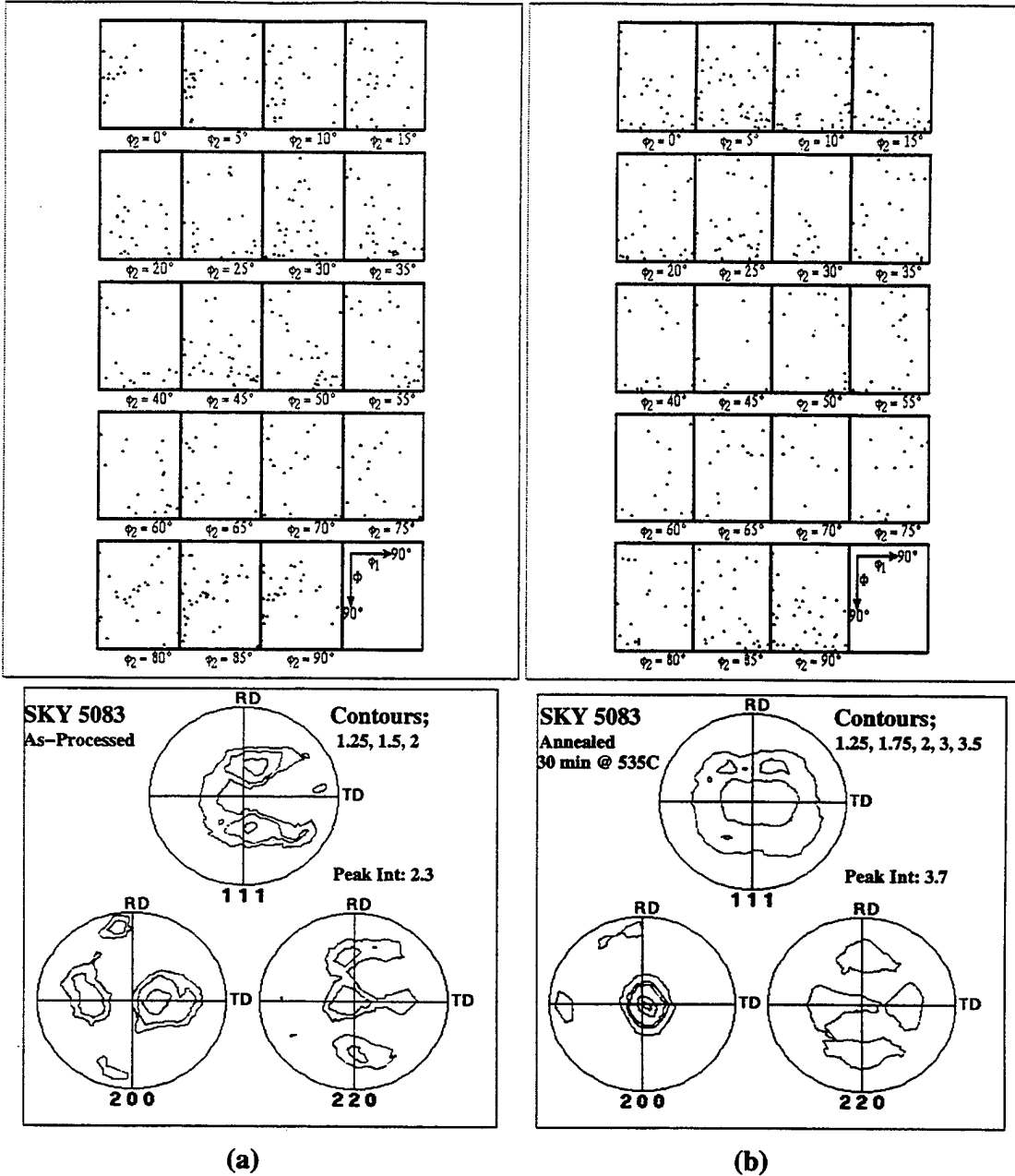


Figure 7.3. The discrete Euler plot and contour pole figure for SKY5083 (a) as-processed and (b) following a static anneal for 30 minutes at 535 C. The weak deformation texture present in the as-processed material is observed to transition rapidly to a cube texture of moderate strength following the brief anneal. This suggests that the material is not fully recrystallized in the as-processed condition and that recrystallization occurs shortly after post-TMP annealing.

periods along with an increase in intensity. The formation of a cube texture has been reported to be associated with discontinuous recrystallization in these alloys during post-TMP annealing [Ref. 97]. During collection of the orientation data, the transition between back-scatter patterns was distinct and the EBSP's were sharp and of high image quality indicating low residual strain in the crystal lattice. Use of such observations has been incorporated into EBSD research methodology in some studies to differentiate primary grains from recrystallized grains [Ref. 122]. In the case here, for the specimen annealed 30 minutes, the observation was that nearly all grains appeared to be recrystallized.

Figure 7.4 illustrates the distribution of boundary misorientation present in (a) as-processed material and (b) material statically annealed for 11 hours at 535°C. The boundary misorientation distribution present in both conditions are essentially the same and are, primarily, high-angle and disordered boundaries. The distribution follows closely the random distribution predicted by Mackenzie based only on geometric considerations. There were relatively few boundaries ($\approx 2.0\%$) with a misorientation of less than 10° and the number of HAB's satisfying nearness criteria to CSL relations ($\Sigma > 1$) was near that expected for random rotations. A summary of the quantitative boundary information is provided later in Table 7.2.

The grain boundary misorientation distribution may be categorized by interfacial energy following Watanabe and Haasen [Ref. 23, 82]. Low-angle boundaries (LABs; $\theta \leq 5^\circ$) and moderately misoriented boundaries (MMBs; $5^\circ < \theta < 15^\circ$) and high-angle boundaries (HABs; $\theta > 15^\circ$) satisfying criteria for nearness to low-index coincident site lattice (CSL) relations up to $\Sigma 29$ are assumed to have lower interfacial energy than random, disordered high-angle boundaries. It is recognized that this is a general categorization as grain boundary energy may not follow in such a simple manner and has been shown to be sensitive to impurity content and specific boundary orientation requiring specification of the remain two degrees of boundary freedom not presented here [Ref. 85]. The data shows that boundary distributions present in the recrystallized 5083 material here are of high interfacial energy character. High boundary interfacial energy has been shown to be associated with fast

boundary migration rates and may be responsible for the rapid grain growth during annealing that was observed here. Additionally, evidence of faster grain growth rates for grains of cube orientations in recrystallized aluminum has been presented recently [Ref. 123].

The grain misorientation texture (GMT) plots shown in Figure 7.4 illustrate the

SKY 5083	As-Processed	Annealed 11 hours $T_{\text{ann}}=535\text{C}$ Undeformed	Annealed 30 min $T_{\text{ann}}=535\text{C}$ Undeformed	Deformed Gage $T_{\text{def}}=535\text{C}$ $\dot{\epsilon}=10^{-4}\text{s}^{-1}$	Deformed Gage $T_{\text{def}}=535\text{C}$ $\dot{\epsilon}=10^{-2}\text{s}^{-1}$	Deformed Gage $T_{\text{def}}=535\text{C}$ $\dot{\epsilon}=10^{-3}\text{s}^{-1}$
Total Number of Boundaries	614	526	528	450	244	242
% with $\theta < 15^\circ$ [2.3]	6.2	8.9	9.1	8.7	6.5	13.6
% with $\theta > 15^\circ$ and CSL ($\Sigma < 31$) [11.3]	10.9	10.8	10.5	10.8	16.0	13.0
% with $\theta > 15^\circ$ and disordered [86.4]	82.9	80.2	80.4	80.5	77.5	74.0
% $\Sigma 3$ [1.53]	1.5	1.5	1.5	2.0	2.6	3.3
% $\Sigma 5$ [1.07]	1.3	1.4	2.0	1.4	3.3	1.3
% $\Sigma 7$ [0.86]	0.8	0.8	0.8	0.7	0.7	0.8
% $\Sigma 9$ [0.88]	1.8	0.6	1.0	0.9	1.3	0.8
% $\Sigma 11$ [0.68]	1.0	1.3	0.4	1.4	0.7	0.4
% $\Sigma 13\text{a/b}$ [0.59]	0.3	0.7	0.4	0.7	1.4	0.8
% $\Sigma 15$ [0.82]	1.1	0.4	0.6	0.7	0.7	0
% $\Sigma 17\text{a/b}$ [0.51]	0.3	0.4	0.2	0.7	0	1.8
% $\Sigma 19\text{a/b}$ [0.48]	0.5	1.1	1.7	0.2	0	0.8
% $\Sigma 21\text{a/b}$ [0.66]	1.0	0.2	0.6	0.5	0.2	0.8
% $\Sigma 23$ [0.43]	0.2	0.4	0.4	0.5	2.0	1.3
% $\Sigma 25\text{a/b}$ [0.48]	0.2	0.6	0.2	0.2	0.7	0
% $\Sigma 27\text{a/b}$	0.4	0.6	0.8	1.2	0.6	0.8
% $\Sigma 29\text{a/b}$	0.3	0.8	0.2	0	0.6	0.4

Table 7.2. Summary of boundary character data for SKY 5083 specimens examined. The number in brackets [] indicates the % of CSL boundaries satisfying the Brandon criterion for random rotations [Ref. 79].

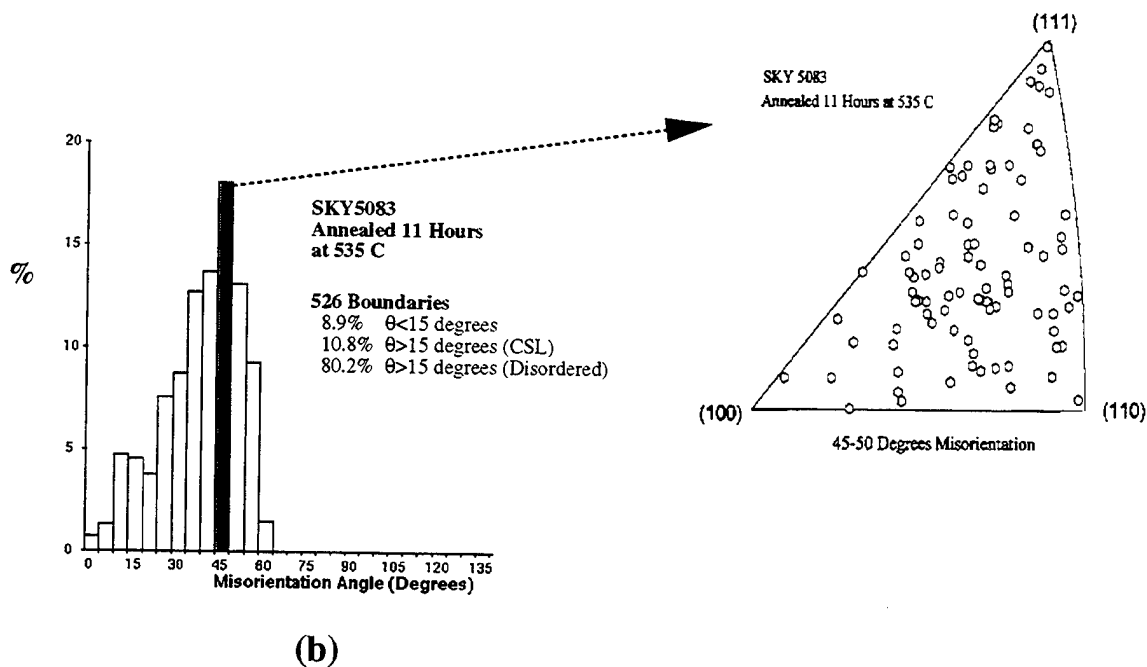
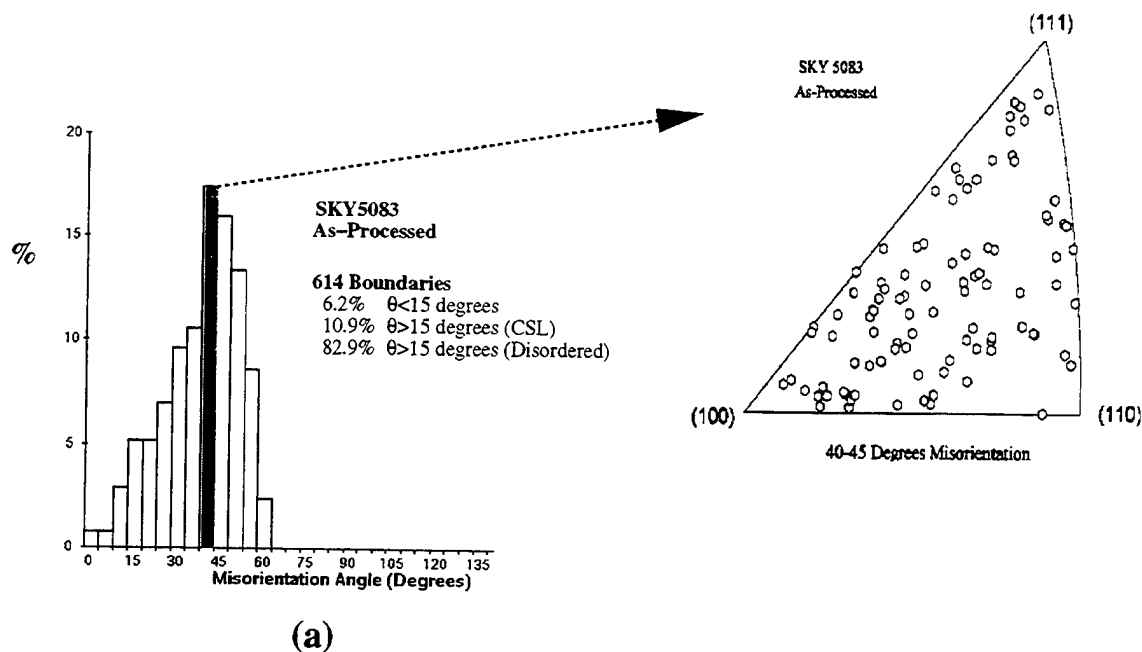


Figure 7.4. Boundary misorientation angle graphs and grain misorientation texture plots for (a) as-processed and (b) processed and annealed specimens. GMT plots are shown for the misorientation range where the peak fraction of boundaries was observed. There is a shift upward in this range with prolonged annealing. The GMT plots illustrate that the boundaries are primarily disordered.

rotation axes for grain boundaries in the misorientation range in which the peak fraction of boundaries was observed. In Figure 7.4 (a) this misorientation range is 40° - 45° . There are three low-index CSL relations in this misorientation range; $\Sigma 21b$, $44.8^\circ/\langle 211 \rangle$, $\Sigma 23$, $40.5^\circ/\langle 311 \rangle$ and $\Sigma 29a$, $43.6^\circ/\langle 100 \rangle$. Boundaries near low-index CSL relations have been reported to be associated with cusps of lower interfacial energy due to the high order of atomic registry at the interface of the two adjacent crystals [Ref. 30]. Data from the GMT for the as-processed material indicate that boundaries may be grouped around the $\langle 100 \rangle$ axis preferentially. The quantitative results, however, show that only a modest increase (1.0% actual compared to 0.66% for random using the Brandon criterion) over the random number of the CSL boundary associated with the $\langle 100 \rangle$ rotation axes in this misorientation range, $\Sigma 21b$, exists. In 7.4 (b) the GMT plot for material annealed 11 hours at 535°C is shown for a misorientation range of 45° - 50° . There are four low-index CSL relations in this misorientation range; $\Sigma 11$, $50.0^\circ/\langle 110 \rangle$, $\Sigma 15$, $48.2^\circ/\langle 210 \rangle$, $\Sigma 19b$, $46.8^\circ/\langle 111 \rangle$ and $\Sigma 29b$, $46.4^\circ/\langle 221 \rangle$. The quantitative data show that there are fewer $\Sigma 15$ and $\Sigma 29b$ boundaries than predicted by random while boundaries near the $\Sigma 11$ and $\Sigma 19b$ CSL relations exist at a level about 1.5 times random.

An analysis of the microtexture and mesotexture in deformed regions is summarized in Figure 7.5 (a) through (c). The data are presented in order of increasing deformation strain-rate utilized in the tensile testing. At the lowest strain-rate, nominally 10^{-4}s^{-1} , the mechanical test data indicated deformation was likely occurring due to GBS with $m \approx 0.5$. The microtexture plot in Figure 7.5 (a) is consistent with GBS in that a randomization of the cube texture present at the onset of straining (following temperature stabilization) without the formation of new components. The accompanying grain boundary misorientation histogram shows essentially the same boundary misorientation distribution as present in the undeformed material. As mentioned in a previous chapter, GBS has been observed to result in such a random distribution of misorientation regardless of the initial distribution following extensive GBS. This is thought to occur due to grain rotations and LAB coalescence during the GBS

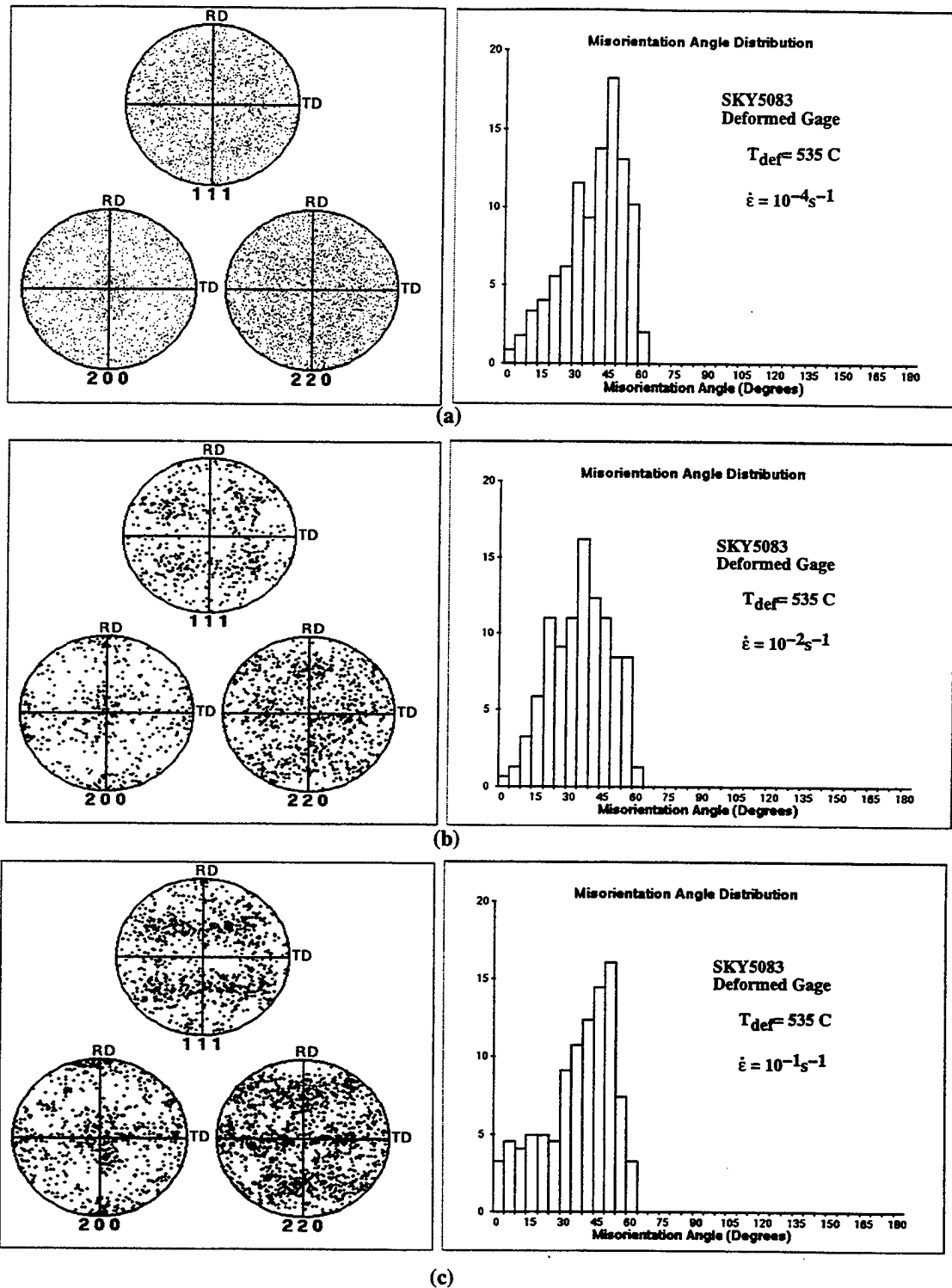


Figure 7.5. Discrete pole figures and boundary misorientation graphs for deformed gage regions in specimens with various strain rates; (a) 10^{-4} s^{-1} , (b) 10^{-2} s^{-1} , and (c) 10^{-1} s^{-1} . The transition of deformation modes from GBS in (a) to (predominantly) slip is shown by the formation of $\langle 111 \rangle$ fiber texture in (c).

process.

In Figure 7.5 (b) the micro- and mesotexture is shown for an intermediate strain rate where the mechanical test data indicated a transition to the solute drag controlled, $m \approx 0.33$ regime (although GBS may still be occurring). Figure 7.5 (c) shows the distinct formation of a $\langle 111 \rangle$ fiber texture indicating that deformation is likely occurring primarily by slip processes. There is a larger fraction of LAB's observed, possibly due to accumulation of dislocations into networks and the lack of LAB coalescence from rotations due to GBS. The fraction of boundaries near the twin orientation, $\Sigma 3$, $60^\circ / \langle 111 \rangle$, has increased to approximately 4%.

E. DISCUSSION AND OBSERVATIONS

Data from this study shows that the boundaries present following TMP and the apparent post-TMP static recrystallization are primarily disordered, high-angle boundaries with high interfacial energy character. There is little deformation- or recovery-induced texture or microstructure apparent following recrystallization, possibly due to rapid recovery kinetics and an insufficient volume fraction of fine particles to inhibit boundary migration. As a result, recrystallization occurs rapidly, and the data here indicate recrystallization is complete though the thickness of the processed material sheet within 30 minutes following heating to the annealing (deformation) temperature. Grain growth following recrystallization is apparent in the data and is likely a significant detriment to the superplastic flow behavior of this alloy. The coarsening of the grain size prior to the onset of deformation by GBS may be responsible for the limited (low) strain-rate regime at which region II behavior is observed. Sherby and Wadsworth illustrated the importance of grain size in optimizing peak strain rates for GBS in superplastic flow [Ref. 2]. Their development of a phenomenological expression for a peak strain rate for superplastic flow for a given set of microstructural conditions has been modified to incorporate phenomenological expressions for superplastically processed Al-Mg developed by McNelley and Salama [Ref. 50] in the following derivation:

An equation for deformation by grain boundary sliding involving accommodation by

grain boundary diffusion may be written:

$$\dot{\epsilon}_{gbs} = A_{gbs} \left(\frac{b}{L}\right)^3 \left(\frac{D_{gb}}{b^2}\right) \left(\frac{\sigma}{E}\right)^2 \quad (1)$$

where $\dot{\epsilon}_{gbs}$ is the strain rate for grain boundary sliding controlled deformation, A_{gbs} is a constant, b is the Burger's vector, L is the mean linear intercept grain size, E is the Young's modulus, σ is the flow stress, and D_{gb} is the grain boundary diffusivity. A similar equation for deformation by glide-controlled dislocation creep followed by low temperature deformation of processed Al - 10.0 wt%Mg - 0.1wt% Zr [Ref. 59] may be written:

$$\dot{\epsilon}_\perp = D_s \frac{K_g}{\alpha_g^3} \left[\sinh \alpha_g \frac{\sigma}{E} \right]^3 \quad (2)$$

where $\dot{\epsilon}_\perp$ is the strain rate for glide-controlled creep, α_g is the value of $(\sigma/E)^{-1}$ at the onset of power law breakdown, K_g is a factor related to the solute drag forces upon dislocations, and D_s is the lattice diffusivity. For $\alpha(\sigma/E) < 1$ equation (2) may be written:

$$\dot{\epsilon}_\perp \approx D_s K \left[\frac{\sigma}{E} \right]^3 \quad (3)$$

The peak strain rate value for the point of transition from GBS to slip creep based on equations (1) and (2) may be obtained by setting equations (1) and (3) equal and simplifying;

$$\frac{\sigma}{E_{\dot{\epsilon}_{SPmax}}} = \left[\frac{A_{gbs} D_{gb} b}{K D_s L^3} \right]^{2/3} \quad (4)$$

and substituting into equation (1) for (σ/E) to obtain:

$$\dot{\epsilon}_{SFmax} = \frac{[A_{gb} b D_{gb}]^{7/3}}{[K D_s]^{4/3}} \left[\frac{1}{L^7} \right] \quad (5)$$

The peak strain rate for GBS controlled superplastic flow for solid solution Al-Mg alloys is then expected to be highly sensitive to grain size.

A recent study utilized optical microscopy and TEM in examining the superplastic behavior of another commercial, superplastic 5083 alloy, manufactured by Alusuisse Co., Zurich, Switzerland, suggested that modifications to increase the recovery rate may be desirable for improved superplastic response[Ref. 128].

Results from the present study indicate that while rapid recovery kinetics may facilitate the recrystallization process, following recrystallization and the formation of new HAB's and nearly strain-free grains, the distribution of boundaries present result in a significant driving force for grain growth and highly mobile boundaries. Given the forming temperatures utilized for this alloy, $\approx 0.8 T_m$, unless modifications to the alloy are made to increase the volume fraction of the dispersoids to assist in retarding boundary motion, engineering the TMP schedule to retard recovery kinetics may be more desirable. Retention of deformation induced structure and production of a boundary distribution of lower interfacial energy character in the as-processed material may assist in achieving refinement to a smaller grain size and retarding grain growth during post-TMP annealing thereby improving the superplastic flow behavior for this alloy.

VIII. GRAIN BOUNDARY DEVELOPMENT FOLLOWING ALTERNATE THERMOMECHANICAL PROCESSING IN COMMERCIAL, SUPERPLASTIC 7475 ALUMINUM

A. INTRODUCTION

Aluminum alloy 7475 is a high strength ($UTS > 500$ MPa), light-weight material utilized extensively in military and aerospace systems in many primary structural applications due to the strength and high fracture toughness requirements of aircraft designers. Successful superplastic processing of 7075/7475 aluminum alloys has been accomplished [Refs. 10-15 in WPHM] via thermomechanical processing following the original "Rockwell" process discussed earlier in chapters I., V., and VI. Researchers have attributed the transition to superplastically-enabled microstructures in the 7075/7475 alloys to grain refinement by discontinuous recrystallization involving particle stimulated nucleation (PSN) [Ref. 47]. Modifications of the Rockwell-type TMP route applied to processing of 7075/7475 aluminum have been reported by Hamilton and Paton [Ref. 129]. All of these modifications involve an intermediate annealing treatment to control the distribution and size of second-phase and dispersoid particles in order to influence the PSN process and boundary migration kinetics during the reported discontinuous recrystallization.

Lee and McNelley [Ref. 130] proposed an alternate TMP for these alloys involving a moderate aging schedule to achieve a finer dispersion of smaller ($0.2\mu\text{m}$) second-phase particles to inhibit the PSN process and utilized subsequent warm rolling at 300°C . The TMP was intended to facilitate microstructural refinement via continuous recrystallization. Current research in Japan reported recently by Sato, Gemba, and Kuribayashi [Ref. 131] and Yang, Miura, and Sakai [Ref. 132] utilized a moderate temperature TMP schedule and a post-TMP pre-deformation (or two-step forming process) to produce a continuously-recrystallized microstructure and achieve improved superplastic performance in a 7475 aluminum alloy processed by Sumitomo-Kaiser Ltd (SKY7475). Peak elongations of over 700% were

reported at a strain rate of $3.0 \times 10^{-3} \text{ s}^{-1}$ with a deformation temperature of 798K (525°C) and a strain-rate sensitivity exponent of $m \approx 0.58$. Based on their TEM observations of the unrecrystallized, post-TMP and recrystallized, post-SPF microstructures the authors attributed observed microstructural refinement to the transition of boundaries consisting of high-density dislocation tangles into high-angle grain boundary structures assisted by GBS.

The objective of the present study is to analyze the grain boundary character of two of the available commercially-processed, superplastic 7475 alloys and compare the results to a laboratory-produced, optimally-processed 7475 alloys provided by the research department of Superform, USA, Inc, Riverside, California a subsidiary of ALCAN International. The latter material has been reported to exhibit improved superplastic forming characteristics. Data from the as-processed, commercial 7475 alloys should reveal the grain boundary structure following a Rockwell-type TMP schedule. Analysis of the grain boundary character data for alternate processing routes may provide insight into the role of grain boundary structure in the mechanical response of processed 7XXX alloys in the superplastic regime.

B. ALLOY CHEMICAL AND MECHANICAL DATA

Superplastically processed aluminum alloy 7475 material was provided in sheet form by Superform, USA, Inc. The materials provided and examined consisted of a laboratory processed (ALCAN BEST) 7475 aluminum alloy in 1.5 mm sheet, commercially-processed, superplastic 7475 aluminum manufactured by KOBE Steel, Ltd., Tochigi, Japan, supplied in 2.0 mm sheet, and commercially-processed, superplastic ACL7475 aluminum manufactured by SUPERFORM, USA, Riverside, California, and supplied in 1.5 mm sheet. Chemical composition data for the commercial alloys examined are shown in Table 8.1.

Mechanical testing data is shown in Table 8.2. Tension testing was conducted within a temperature range of 500°C to 515°C. Results indicate that the higher superplastic elongation for the available commercial superplastic 7475 alloys was observed in the ACL

	Zn	Mg	Cu	Cr	Fe	Si	Ti	Mn	Al
KOBE 7475 T4 SP Manuf. No. 0-41540	5.51	2.28	1.53	0.19	0.08	0.05	0.02	0.01	bal
ACL 7475 T762 SP Manuf. No. 872960	5.83	2.20	1.67	0.19	0.08	0.04	0.03	0.01	bal

Table 8.1. Chemical composition (wt%) data for the 7475 alloys examined.

7475T762SP alloy at a value of approximately 300% and occurs at a modest SPF strain rates of approximately $1.0 \times 10^{-3} \text{ s}^{-1}$ and a temperature of approximately 500°C . The laboratory processed ALCAN BEST material (details of the TMP are proprietary and were not disclosed) exhibited improved superplastic response [Ref. 127] with a peak elongation of approximately 1000% at a strain rate marginally higher than that utilized in testing the commercial alloy ACL 7475.

Material	$T_{\text{def}} (^\circ\text{C})$	Deformation Strain Rate (s^{-1})	Tensile Elongation
ACL 7475 T762 SP	515	1.3×10^{-3}	310%
ALCAN 7475SP BEST	515	2.0×10^{-3}	$\approx 1000\%$

Table 8.2. Mechanical test data for the materials examined in this study.

C. EXPERIMENTAL PROCEDURE

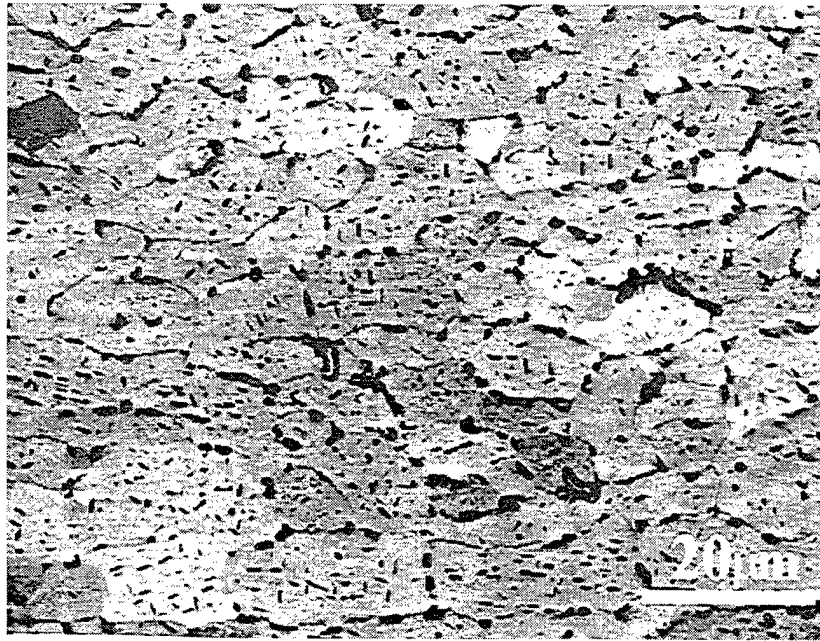
Specimens were extracted from the as-received sheet materials for BSE/EBSD examination in the as-processed condition and also for static annealing and subsequent BSE/EBSD examination. All specimens were sectioned in a manner consistent with that described in earlier chapters, examined at the $t/2$ region, and analyzed utilizing EBSP methods previously described. BSE micrographs were obtained near the regions examined for

purposes of detailing grain morphology, calculating of MLI values, and illustrating the size and dispersion of the second-phase and dispersoid particles present. A low accelerating voltage of 5 KV was again utilized to image the microstructure in the BSE mode of the SEM. Post-EBSD examination analysis of the data was accomplished in the manner described previously using the system software.

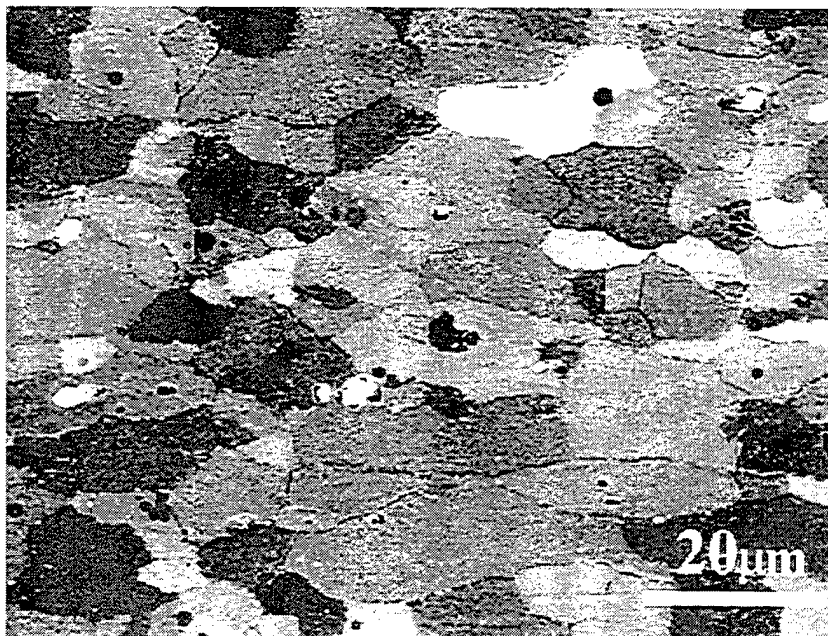
D. MICROSTRUCTURE

Figure 8.1 and Figure 8.2 show BSE micrographs illustrating the microstructure present in the as-processed and the processed and annealed materials, respectively. Average grain size determination using the MLI method previously discussed was accomplished for specimens examined. The results are summarized in Table 8.3. The microstructure present in the as-processed ACL 7475 specimen is shown in Figure 8.1 (a) and may be described as an equiaxed grain morphology and uniform, fine grain size. The average grain size for this specimen was measured as 9.4 μm . Several precipitate phases are evident at the relatively low magnification of the micrographs. An elongated, needlelike dispersion in dark contrast and a dispersion of smaller, spheroidally-shaped particles with light contrast (presumably a copper-containing phase) are evident throughout the material. Additionally, somewhat larger spheroidally-shaped particles, are present, located preferentially along grain boundaries. Other phases, particularly chromium-containing ultra-fine particles, may exist but are not evident at the magnifications employed here.

Figure 8.1(b) shows the grain structure in the as-processed ALCAN BEST specimen. The grain morphology here is somewhat more elongated than that in Figure 8.1 (a) with a broader range in grain size also evident. The aspect ratio of the grains reveals the rolling direction (horizontal in all figures) and the thickness of the pancaked grains is somewhat less than in Figure 8.1 (a) suggesting that this material may have been processed to a higher total strain. The average grain size for this material was estimated to be 8.3 μm . A higher degree of grain contrast is apparent and the volume fraction of precipitates evident appears to be

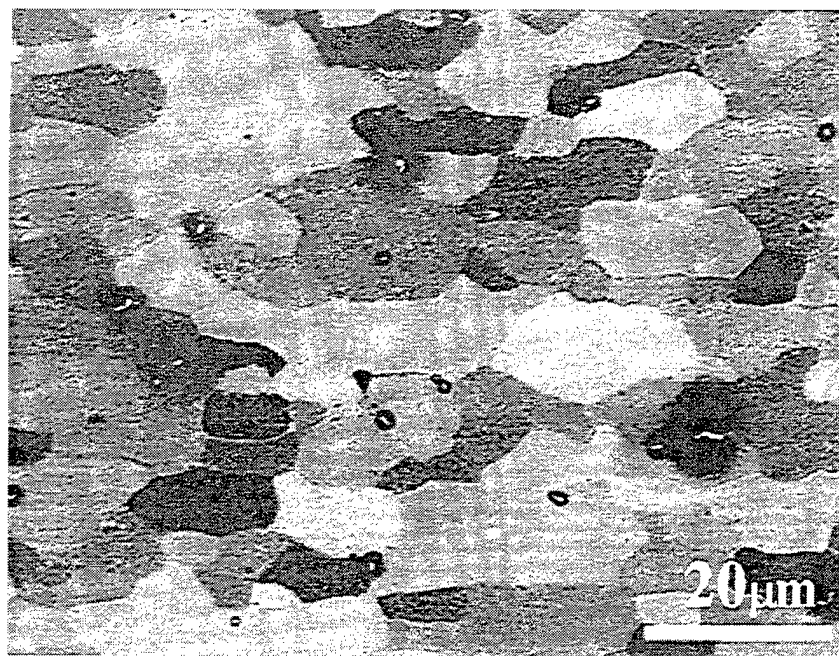


(a)

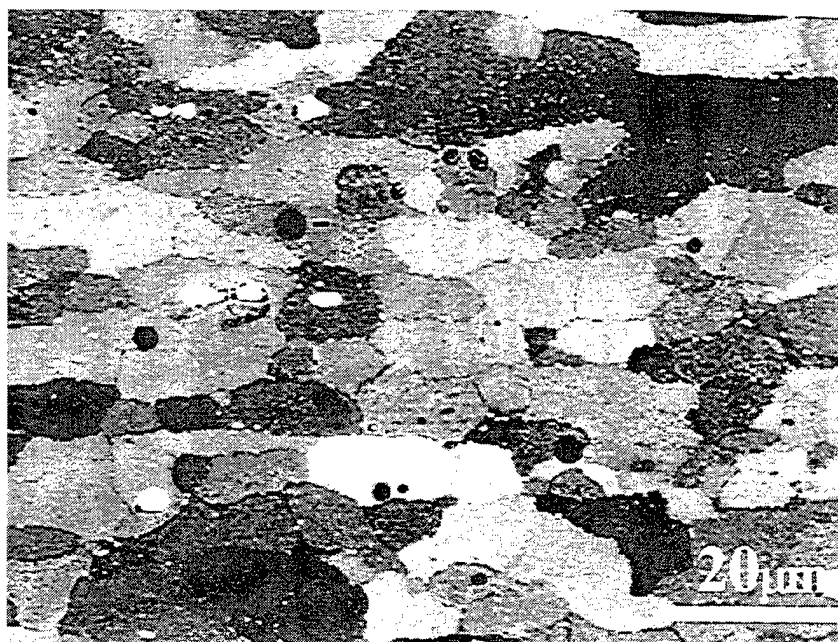


(b)

Figure 8.1. Backscatter electron images taken near the EBSD examination regions in as-processed; (a) ACL 7475SP and (b) ALCAN BEST 7475. The rolling direction is horizontal.



(a)



(b)

Figure 8.2. Backscatter electron images taken near the EBSD examination regions in processed and statically annealed specimens of; (a) KOBE 7475SP and (b) ALCAN BEST 7475. Annealing was conducted at 450C for one hour. The rolling direction is horizontal.

lower.

Figure 8.2 (a) shows the microstructure evident in the KOBE 7475 material following a one hour anneal at 450°C. The grain morphology is elongated in the rolling direction and static grain growth has occurred, from an average grain size of 10.5µm in the as-processed material to 12.5µm in the annealed material shown in this micrograph. Grain contrast is pronounced. The grain size distribution appears to be bi-modal with larger, elongated grains (presumably original grains "pancaked" by rolling) and smaller, equiaxed recrystallized grains. The grain structure present in the annealed specimen of the ALCAN BEST material is shown in Figure 8.2 (b). Some coarsening of precipitate particles is evident and static grain growth, from 8.3µm (the average grain size in the as-processed material) to 9.5µm has occurred. Most grains appear equiaxed and of uniform size.

Average Grain Size ($d_{av} = 1.774 \times \text{MLI}$)	As-Processed	Processed and Annealed at 450C for 1 Hour
ACL 7475 T762 SP	9.4µm	9.8 µm
KOBE 7475 T4 SP	10.5µm	12.5 um
ALCAN 7475SP BEST	8.3µm	9.5µm

Table 8.3. Summary of the average grain size data for specimens examined.

E. MICROTTEXTURAL AND MESOTEXTURAL RESULTS

Figure 8.3 illustrates the EBSD examination results for the as-processed ACL 7475 material. Microtextural data from the t/2 region examined reveals a distinct cube, {100} <001>, texture component (peak intensity of 5.7 times random) in the (200) pole figure. Other recrystallization components are evident including orientations near R_1 , {124} <211>, as shown in the $\phi_2=25^\circ$ window of the discrete Euler plot and near Q, {013} <231>, shown in the $\phi_2=15^\circ$ window of the discrete Euler plot. Recrystallization components near R are

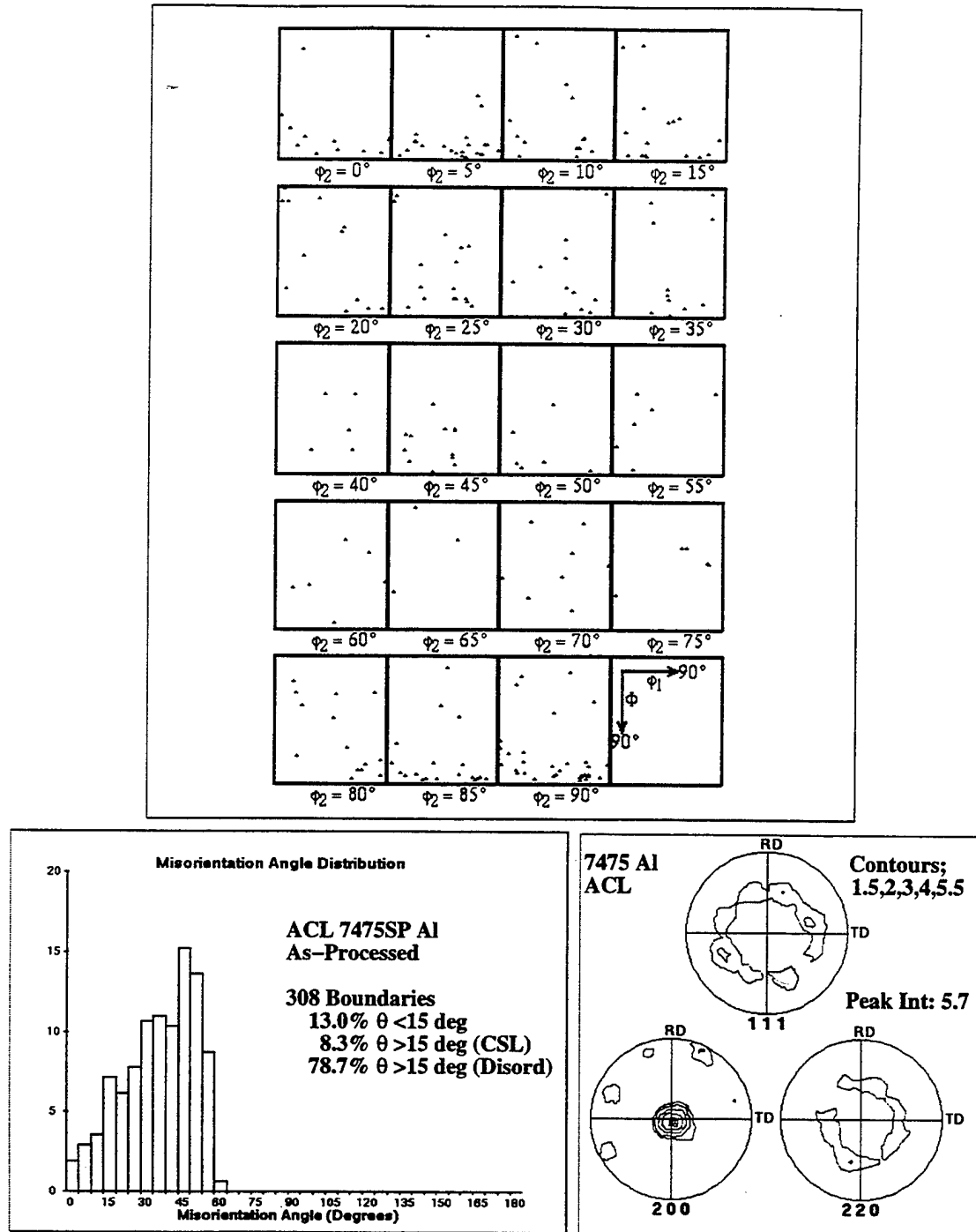


Figure 8.3. Discrete Euler plot, contour pole figure, and boundary misorientation angle histogram for data collected at the $t/2$ region in as-processed ACL 7475SP material.

originate from nucleation sites at grain boundaries while Q recrystallization orientations are thought to originate from shear bands in a manner similar to the origin of cube orientations. These microtextural data would suggest that the material is recrystallized at the mid-plane in the processed sheet and these data are consistent with a discontinuous recrystallization mechanism. There is little evidence of deformation components in the textural data. Furthermore, the textural data suggest that the TMP scheme employed may have included a post-rolling anneal, or rolling at an elevated temperature due to the intensity of the texture. Additionally, since weak to random levels of texture would be expected if PSN was the predominant recrystallization mechanism, nucleation of new grains from cube sites and grain boundaries (rather than particles) may have dominated the recrystallization process.

The misorientation distribution for the ACL 7475 material is flat for boundaries of greater than 15° misorientation (HAB's). All misorientation ranges are well populated (a fraction > 0.08) with the exception of boundaries near 60° misorientation. Low-angle and moderately misoriented boundaries constitute 0.13 of all boundaries and the fraction of HAB's satisfying the Brandon criterion to low-index CSL relations is less than expected for a cubic material with random orientations. Quantitative boundary data is summarized later in Table 8.4.

Micro- and mesotextural data for the KOBE 7475 specimen examined is shown in Figure 8.4. The material is more weakly textured with a peak intensity of 2.86 times random. There is no discernable concentration of orientations with the exception of the rotated cube recrystallization orientation, $\{100\} \langle 310 \rangle$, indicative of nucleation near particles [Ref. Nes]. The data provides evidence that recrystallization is complete through the mid-plane following TMP and that nucleation from particles in a manner consistent with PSN theory is likely dominating the recrystallization process. The associated mesotextural data reveal essentially a random distribution of misorientation with nearly half of all boundaries lying in the 40° - 50° misorientation range where boundaries of high mobility and interfacial energy levels

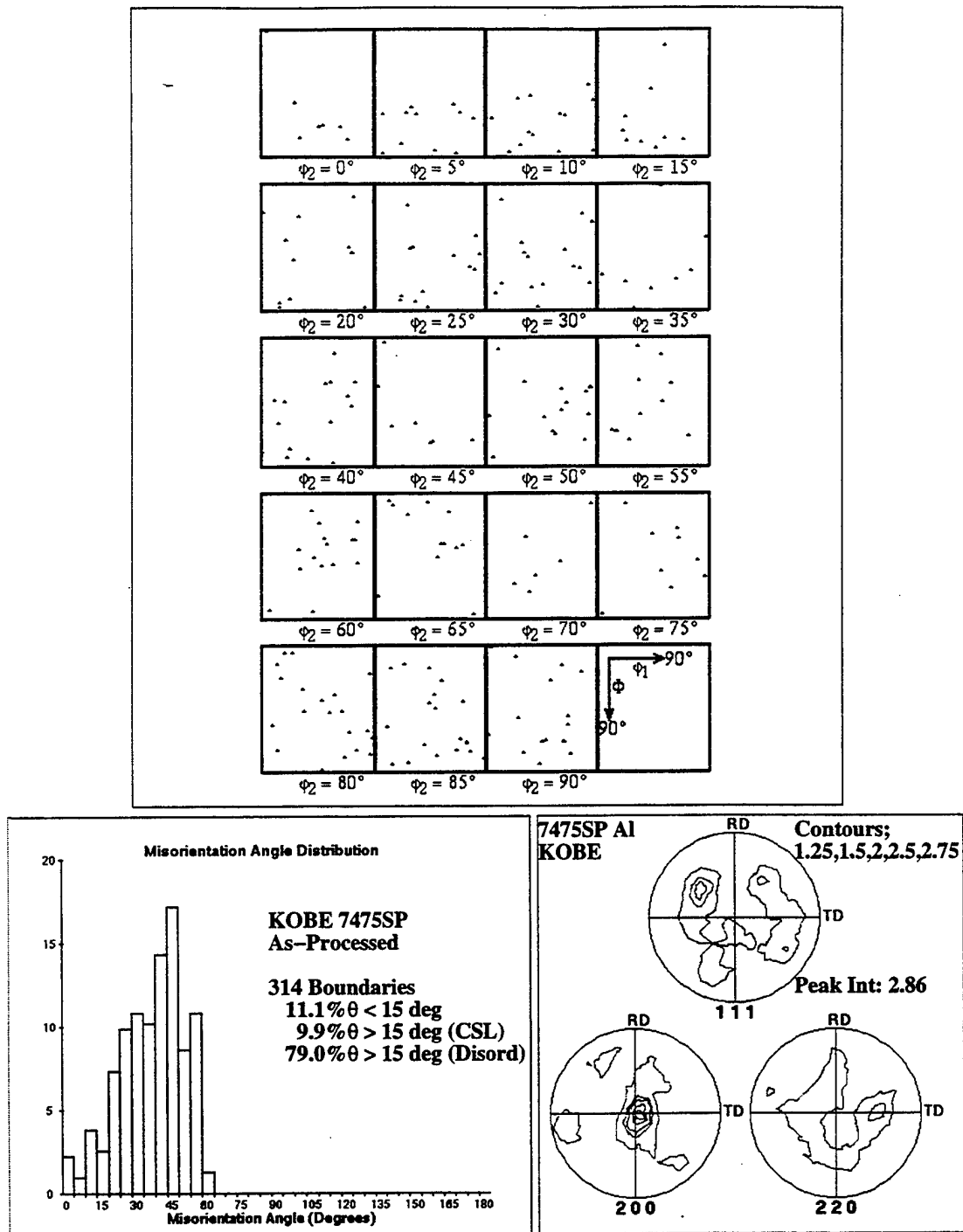


Figure 8.4. Discrete Euler plot, contour pole figure, and boundary misorientation angle histogram for data collected at the $t/2$ region in as-processed KOBE 7475SP material.

would be expected to appear.

Figure 8.5 shows the EBSD examination results for the as-processed ALCAN BEST material. The texture present is weak with a peak intensity of only 2.08 times random. The distribution of orientations in Euler space is largely random with no distinguishing concentration of orientations. There are a few orientations near deformation components (brass, S, and copper) and the recrystallization component (cube). Recrystallization involving PSN is again suggested by the textural data. The misorientation distribution is essentially random, with over 81% of all boundaries being disordered HAB's. The persistence of some deformation orientations in the textural data is consistent with the microstructural data from BSE microscopy showing the presence of some elongated original grains (with orientations near deformation texture components) surrounded by (presumably) recrystallized smaller grains (with random orientations if PSN is the predominant recrystallization mechanism).

The summary of data for examination of all three materials following the one hour anneal at 450°C is shown in Figure 8.6. Results are similar in each of the three materials examined in that the texture evident in the discrete data is weak and the mesotextural data is near random. The distinguishing feature of the data for annealed specimens is the evolution of microtexture in the ACL 7475 material. The moderately strong cube texture evident in the as-processed ACL 7475 material has weakened with annealing and the associated boundary misorientation distribution has evolved from the flat distribution observed previously and has approached the random distribution predicted by Mackenzie for adjacent cubes. The weakening of texture in this material suggests that the cube texture evident in the as-processed material may be due to the presence of original grains of cube orientation and generational cube orientation development [Ref. 126] and that recrystallization by PSN was incomplete at the mid-plane in the processed material.

F. DISCUSSION

Data from examination of the mid-plane regions in the 7475 materials reveal that the

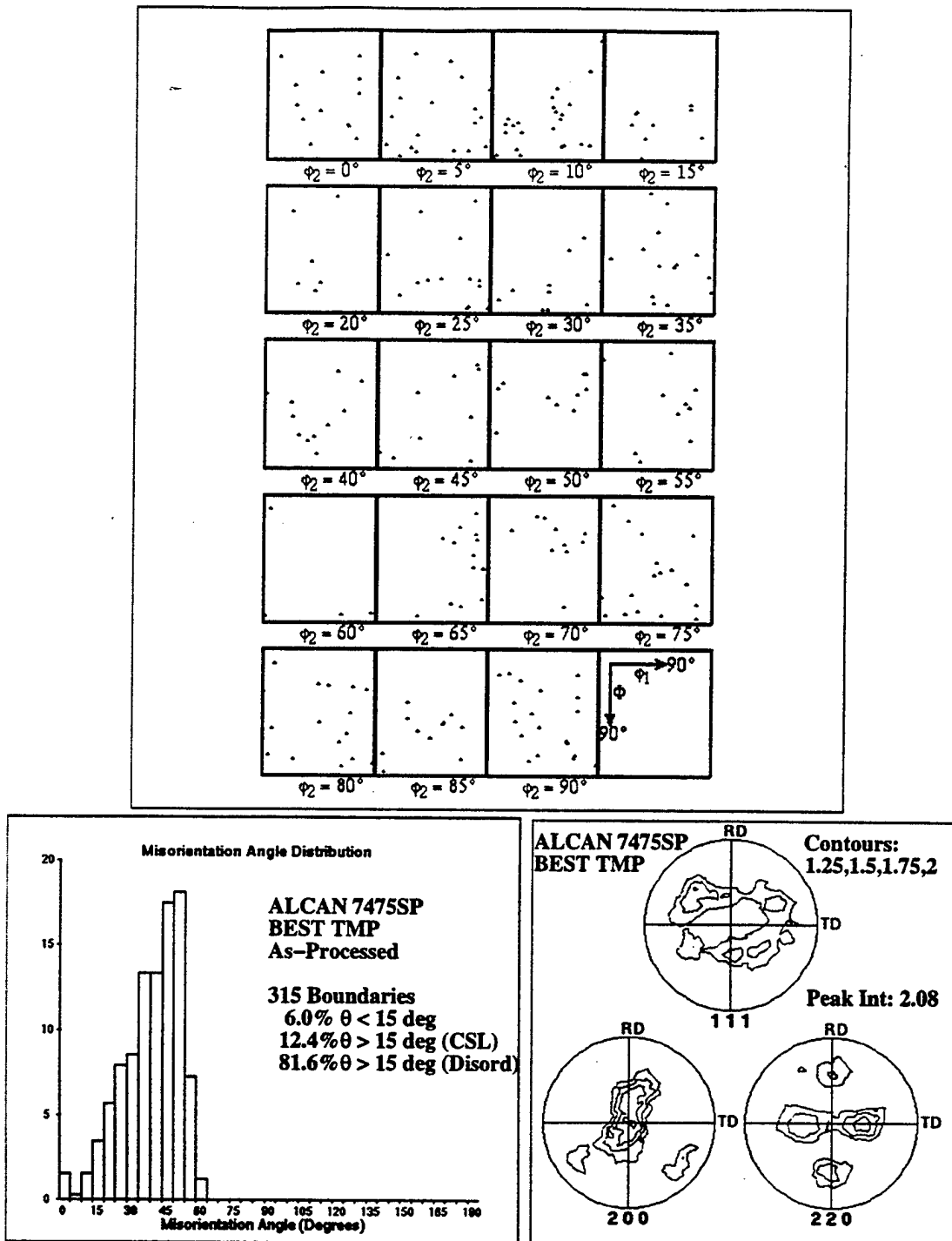


Figure 8.5. Discrete Euler plot, contour pole figure, and boundary misorientation angle histogram for data collected at the $t/2$ region in as-processed ALCAN 7475SP processed to the manufacturer's BEST TMP route.

7475 Al	As-Processed KOBE 7475T4-SPF	As-Processed ACL 7475T76-SP	As-Processed ALCAN BEST TMP	KOBE 7475T4-SPF Annealed 1Hr @ 450C	ACL 7475T76-SP Annealed 1Hr @ 450C	ALCAN BEST TMP Annealed 1Hr @ 450C
Total Number of Boundaries	314	308	315	277	316	319
% with $\theta < 15^\circ$ [2.3]	11.1	13.0	6.0	5.8	7.0	7.8
% with $\theta > 15^\circ$ and CSL ($\Sigma < 31$) [11.3]	9.9	8.3	12.4	10.5	11.0	9.3
% with $\theta > 15^\circ$ and disordered [86.4]	79.0	78.7	81.6	83.7	82.0	82.9
% $\Sigma 3$ [1.53]	2.0	2.6	2.9	1.8	1.9	1.3
% $\Sigma 5$ [1.07]	1.3	1.3	1.0	0.7	0.6	1.3
% $\Sigma 7$ [0.86]	1.0	0.3	1.0	0.7	0	1.3
% $\Sigma 9$ [0.88]	0.6	2.0	0.7	2.2	1.3	1.6
% $\Sigma 11$ [0.68]	0.3	0	0.7	0.4	0.6	0
% $\Sigma 13a/b$ [0.59]	0.7	0	1.4	1.1	0	1.0
% $\Sigma 15$ [0.82]	2.0	0	1.0	1.1	1.3	1.0
% $\Sigma 17a/b$ [0.51]	0.3	0	0	0	1.0	0.3
% $\Sigma 19a/b$ [0.48]	1.3	0	0.7	0.4	0.3	0.3
% $\Sigma 21a/b$ [0.66]	0	0	0.7	0.4	0.3	0.3
% $\Sigma 23$ [0.43]	0	0.9	0.3	0.4	1.9	0.3
% $\Sigma 25a/b$ [0.48]	0.3	0.3	0.7	0.4	1.3	0.3
% $\Sigma 27a/b$	0	0	0.7	0.7	0	0
% $\Sigma 29a/b$	0	0.6	1.0	0.4	0.3	0.3

Table 8.4. Summary of boundary character data for 7475 aluminum specimens examined. The number in brackets [] indicates the % of CSL boundaries satisfying the Brandon criterion for random rotations [Ref. 79].

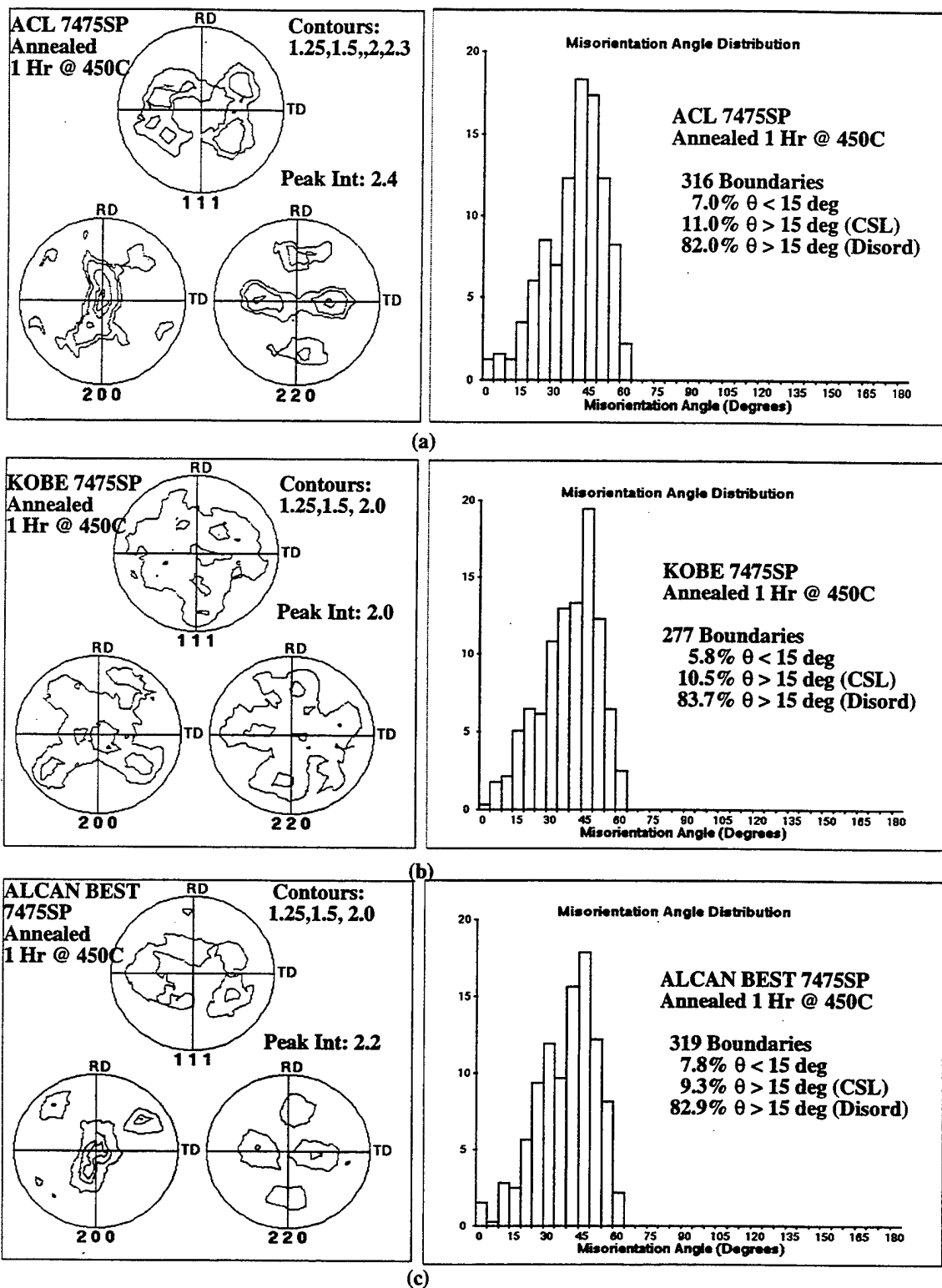


Figure 8.6. Microtextural and mesotextural plots for data from examination of annealed specimens: (a) ACL 7475T76SP, (b) KOBE 7475T4SP, and (c) ALCAN BEST TMP.

microstructural response to the Rockwell-type processing schedule in the ACL 7475 and KOBE 7475 commercial alloys is the initial formation of a moderate to strong cube texture in the as-processed condition and grain boundary misorientation distributions generally reflecting a random distribution but consisting of a higher fraction of HAB in the 15°-35° misorientation range. Variations in the intensity of the cube texture may be attributed to the relative contribution of nucleation sites from regions around larger particles, shear or transition bands between elongated original grains, cube grains, and near grain boundaries. Orientations of nuclei developed in the deformation zone around non-deforming particles are thought to be produced in a random fashion while cube grains are thought to nucleate new cube orientations and transition/shear bands are also thought to be responsible for the formation of cube orientations [Ref. 126]. Differences in the post-processing tempering treatments given to each alloy may also contribute to the subtle differences in the microtexture observed in the processed alloys.

Following static annealing the texture diminishes concurrently with the sharpening of the misorientation distribution toward a random distribution dominated by HAB's in the 35°-55° range. Studies have reported that when PSN is active in the formation of recrystallized (sub)grains the resulting orientations are random [Ref. 126]. This was discussed earlier and is thought to be due to the random development of the nuclei in the deformation zone around large particles, following Humphrey's theory [Ref. 25]. The diminishment of texture is consistent with a dominance of PSN in the recrystallization process and suggests that, at the mid-plane in the *as-processed* sheet material, the recrystallization process may be incomplete. Data from the comparative EBSD examinations reveal that the alternate route utilized by the manufacture following the BEST TMP resulted in a static discontinuous recrystallization similar to the KOBE and ACL commercial 7475 alloys examined. Microstructural refinement to a smaller grain size was achieved in the BEST TMP route and the smaller grain size is likely responsible for the improved superplastic behavior of the material.

Since most SPF methods would include a preheat time of a duration sufficient to

complete the microstructural transition observed in the annealed specimens in this study, the microstructure and boundary character data for the *annealed* specimens may be assumed to be that of the superplastically-enabled microstructure responsible for the observed mechanical behavior. Similarities in the boundary character data for the annealed specimens suggest that the three 7475 alloys examined follow a similar recrystallization scheme and that the differences in the mechanical response for the three alloys examined may be attributed to the degree of grain refinement achieved. This is because the boundaries dominating the misorientations distribution in each case reflect boundaries of high-interfacial energy character and high mobility. Such boundaries are thought to readily support accommodation processes during GBS. Flow softening due to grain refinement has been discussed earlier and would be expected to result in improved superplastic performance.

Evidently the distribution of grain boundary misorientation and the degree of order at boundaries following discontinuous recrystallization involving the formation and migration of high-angle boundaries consistently follows the orientation distribution for the overall microstructure and the predicted random distribution of boundary misorientation (and number of boundaries fulfilling low-index CSL relations) results.

Nevertheless, in material refined by recrystallization involving the formation of new HAB's the controlling deformation mechanism is thought to be [Ref. 130] dislocation generation and motion which result in a lower strain rate sensitivity value, m , while continuous refinement processes, such as those observed in the Al-10.0%Mg-0.1%Zr and SUPRAL alloys, involve higher recovery rates and yield higher m values and improved superplastic response at lower deformation temperatures. One obstacle for manufacturers following alternate processing to form unrecrystallized, refined microstructures for low-temperature SPF of 7475 alloys is the relatively high flow stresses encountered at the more moderate forming temperatures. Higher flow stresses in SPF translate to increase SPF gas pressures and result in more costly forming apparatus and methodologies.

IX. SUMMARY OF RESULTS - THE INFLUENCE OF GRAIN BOUNDARIES IN SUPERPLASTIC ALUMINUM ALLOYS

A. ALTERNATE MICROSTRUCTURES FOR SUPERPLASTICITY IN ALUMINUM ALLOYS

It has been recognized that there are at least two microstructural transformation routes which result in superplastically-enabled aluminum alloys [Ref. 2, 22, 32, 45-47]. Following Doherty [Ref. 61] these microstructural transformations may be described as either Gibbs I or Gibbs II type. Gibbs I reactions are analogous to first-order phase transformations and are the recrystallization processes which include heterogeneous nucleation and subsequent growth of new grains by the migration of newly-formed high angle grain boundaries. Large changes occur in the stable end-orientations from slip-induced plastic flow that form the deformation microtexture (DM) occur and this results in the disappearance of the deformation texture and appearance of recrystallization texture components. The nature of recrystallization texture has been a subject of much interest and has been discussed in terms of either oriented nucleation or oriented growth [Ref.23-24, 69, 110].

Gibbs II reactions are characterized by more gradual changes that occur homogeneously in the DM and, as a result, the associated refinement processes have been described as continuous or in-situ recrystallization or as extended recovery [Ref. McN,D,Or/Nes]. These reactions proceed without the formation and migration of new high angle boundaries, with boundary development occurring through short-range reactions including recovery of individual dislocations, subgrain coalescence, and subboundary migration. Orientation changes from those present in the DM are small and the deformation microtexture persists through the evolution of microstructure. The driving force for both transitions is a reduction in the stored strain energy from the increase in dislocation density during prior deformation.

Data from the present studies show that, while grain refinement occurs in either

process, the two transition mechanisms result in distinctly different distributions of grain boundaries that may not be described in terms of differences which exist in the resultant texture. Figures 9.1 and 9.2 illustrate the fraction of all boundaries with boundary misorientations less than 15° in as-processed and in processed and annealed specimens of the aluminum alloys examined. A significantly higher fraction of low angle (0° - 5°) and moderately misoriented boundaries (5° - 15°) is observed in as-processed materials, and the resulting mean misorientation, θ , in as-processed materials is higher in those materials observed to follow a Gibbs I type of transformation. Following Humphreys [Ref. 25], if the mean misorientation resulting in the DM is low a Gibbs I reaction (such as discontinuous recrystallization) would be possible only if a particular subgrain were present with a sufficiently large size and low misorientation to become unstable. Bi-modal second phase and dispersoid distributions present in the microstructures of the materials which transform by continuous processes here would likely inhibit the required boundary mobility. Furthermore, the misorientations in the microstructures here are large (the average misorientation of all boundaries less than 15° misorientation was 10.6° in annealed Al-10%Mg-0.1Zr, TMP6, material). With such a high mean misorientation the DM would be more stable and a discontinuous reaction would therefore not be expected.

It should be noted that the regions examined in the as-processed SKY5083 and 2519 materials were not fully recrystallized based on the observed microtexture, and yet the fraction of LAB's/MMB's was small. The development of a significant fraction of moderately-misoriented structures in the DM may be evidence that refinement processes by Gibbs II (continuous) transformations are initiated early in deformation processing. In the data collected from the as-processed SUPRAL 2004 material the high fraction (0.23) of LAB's and MMB's were collected at an orientation spacing of $0.5\mu\text{m}$ while the thickness of the pancaked grains was approximately $3\mu\text{m}$ and therefore the moderately-misoriented boundaries were developed as deformation-induced structures.

The observed disparity in the frequency of LAB's and MMB's for Gibbs I and Gibbs

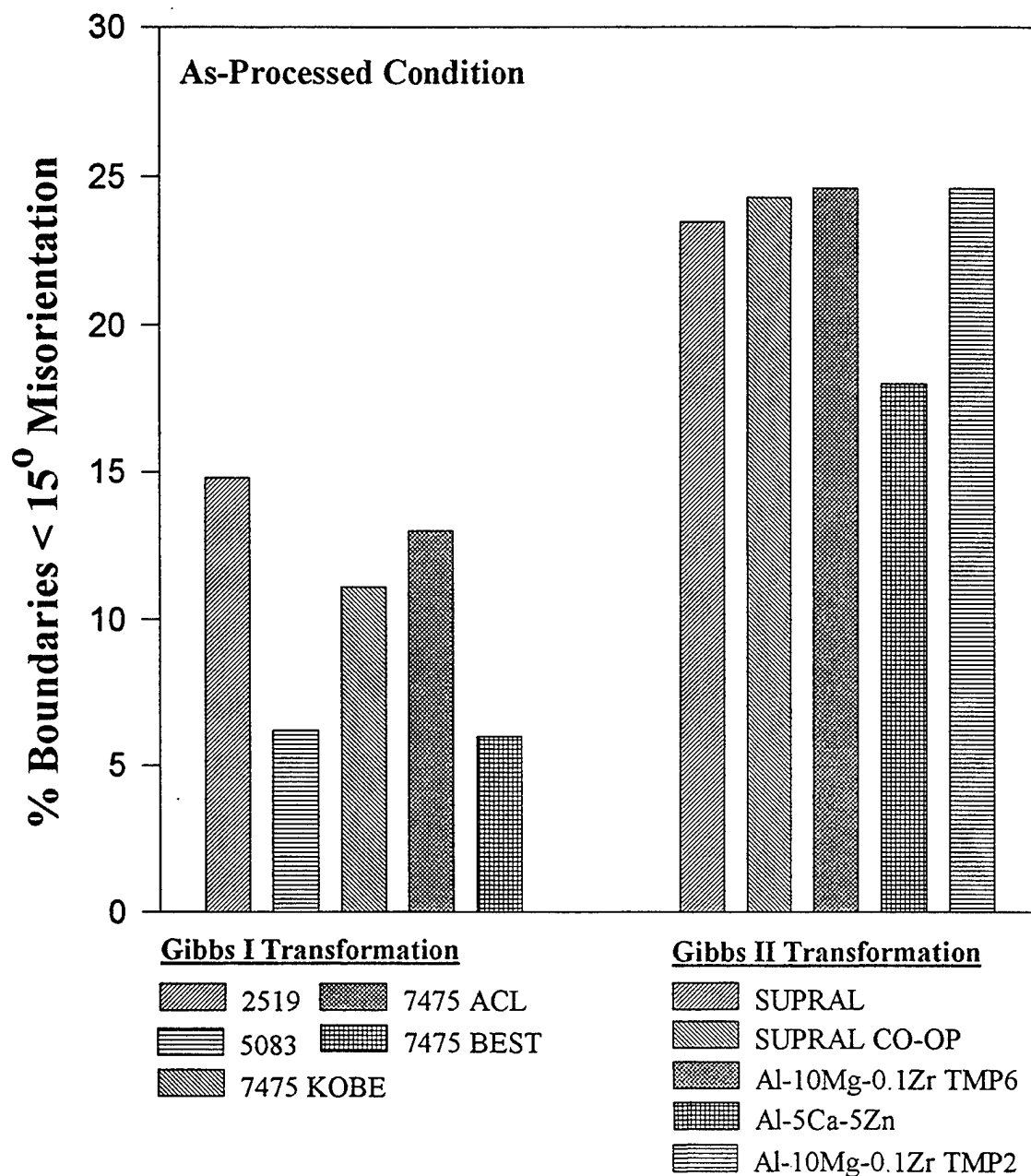


Figure 9.1. Histogram illustrating the population of low angle and moderately misoriented boundaries in as-processed materials examined. Classification of the transformation mechanism for microstructural refinement following Doherty [Ref. 61] is indicated.

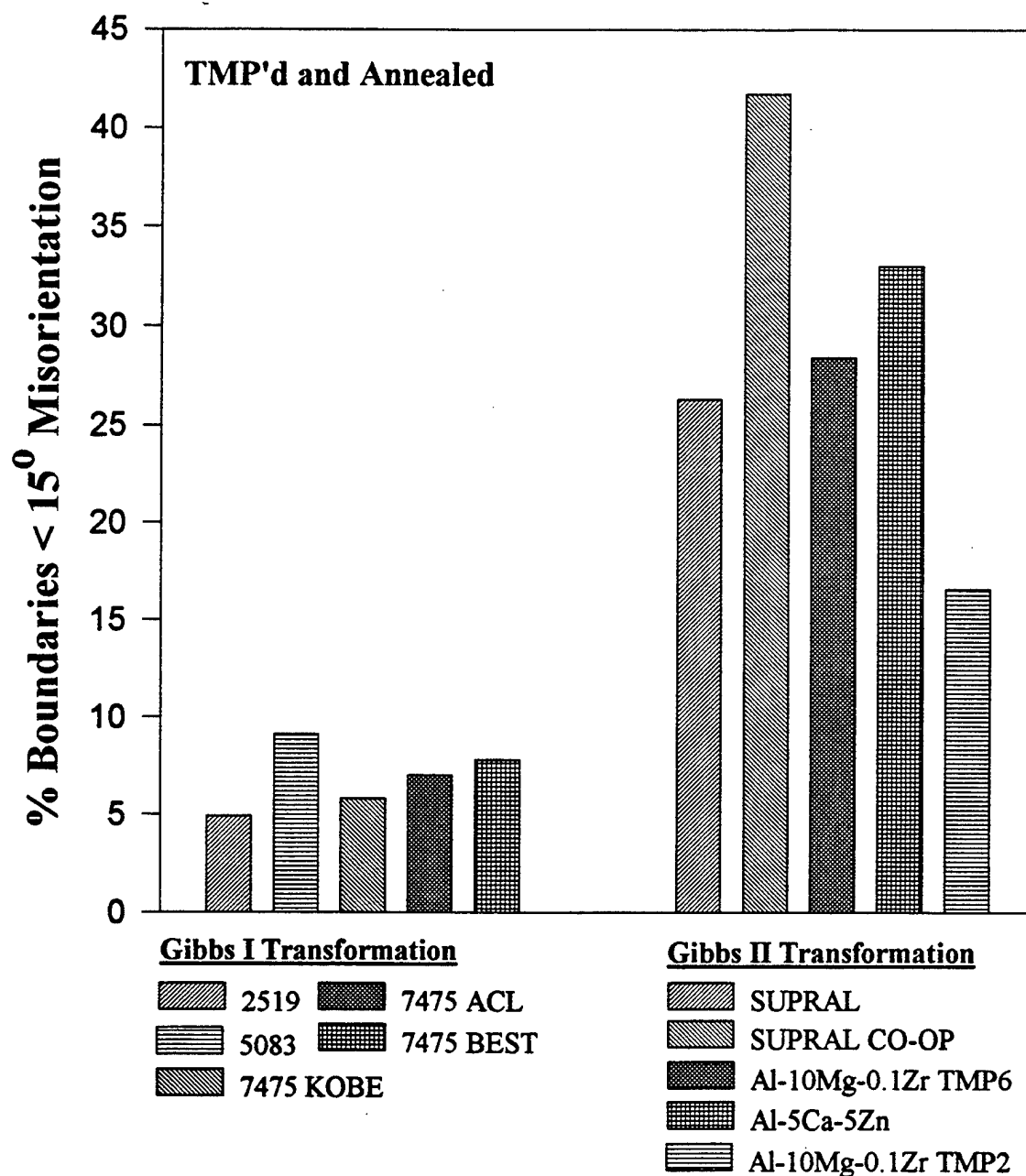


Figure 9.2. Histogram illustrating the population of low angle and moderately misoriented boundaries in materials TMP'd and annealed. Materials classified as transforming by a Gibbs II type mechanism illustrated retained deformation texture (and no evidence of a recrystallization texture) consistent with homogeneous microstructural refinement.

II transformations is more pronounced following static annealing as illustrated in Figure 9.2. The fraction of MMB's is observed to remain constant or to increase for materials which evolve by continuous refinement processes. Additionally, the fraction of LAB's and MMB's in materials observed to form recrystallization textures decreases. The SKY5083 and 2519 materials were observed to complete the recrystallization process at the mid-plane of the processed sheet in this data based on textural evidence. The decrease in the number of LAB's in those materials may be explained in terms of subgrain coalescence and annihilation by advancing reaction fronts of growing grains.

The tendency toward a more pronounced bi-modal character of the boundary misorientation distribution during annealing is observed to be characteristic of materials which are resistant to a Gibbs I transformation, even for extensive static annealing treatments. This is seen in the Al-10%Mg-0.1Zr data in Figure 4.8 and the SUPRAL 2004 data in Figure 5.5. Figure 9.3 illustrates the annealing behavior of a superplastic Al-5%Ca-5%Zn material [Ref. 133]. The examination of this material was conducted using identical EBSD analysis methods and illustrates an extreme case where an aluminum alloy microstructurally refined via a Gibbs II process (based on accompanying microtextural data, not shown here, showing the presence of only deformation texture components) is resistant to discontinuous processes even during prolonged annealing at high homologous temperatures.

Figure 9.4 illustrates the relative population of *disordered* HAB's that *do not* satisfy Brandon nearness criterion to low-index CSL relations. Grain boundaries produced following the Gibbs I transformations, including discontinuous recrystallization processes aided by PSN in the aluminum alloys in this study following processing by a Rockwell-type TMP schedule, are observed to be predominantly disordered, high angle boundaries. As discussed earlier, these boundaries are expected to have high interfacial energy and mobility. The most highly mobile boundaries most readily in the discontinuous processes resulting in microstructures dominated by high-angled, disordered types. Boundary misorientation distributions resulting from the Gibbs I transformations appear to have the peak fraction of boundaries near 40°-45°

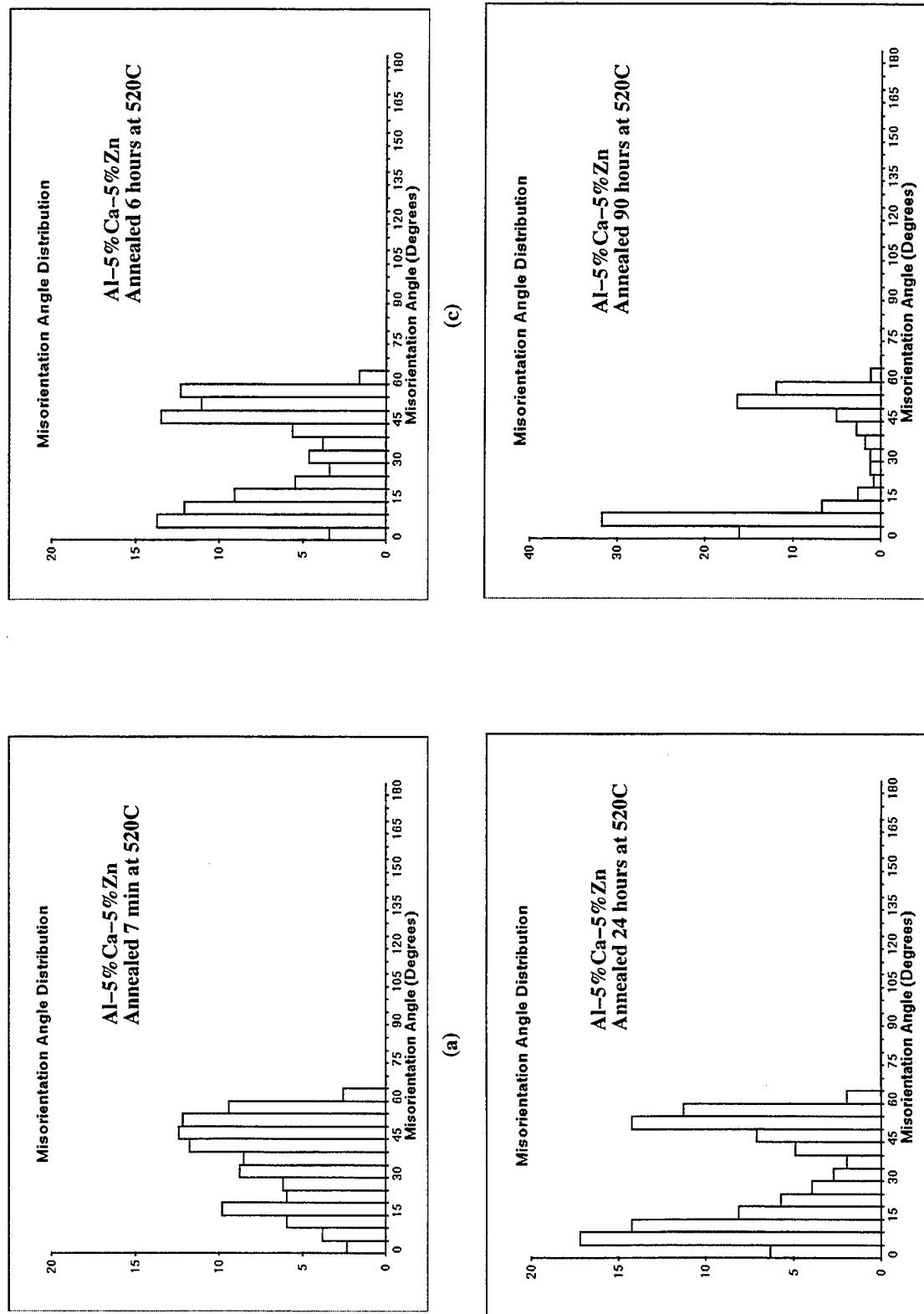


Figure 9.3. Boundary misorientation histograms illustrating the static annealing behavior of a superplastic Al-5%Ca-5%Zn alloy [Ref. 133].

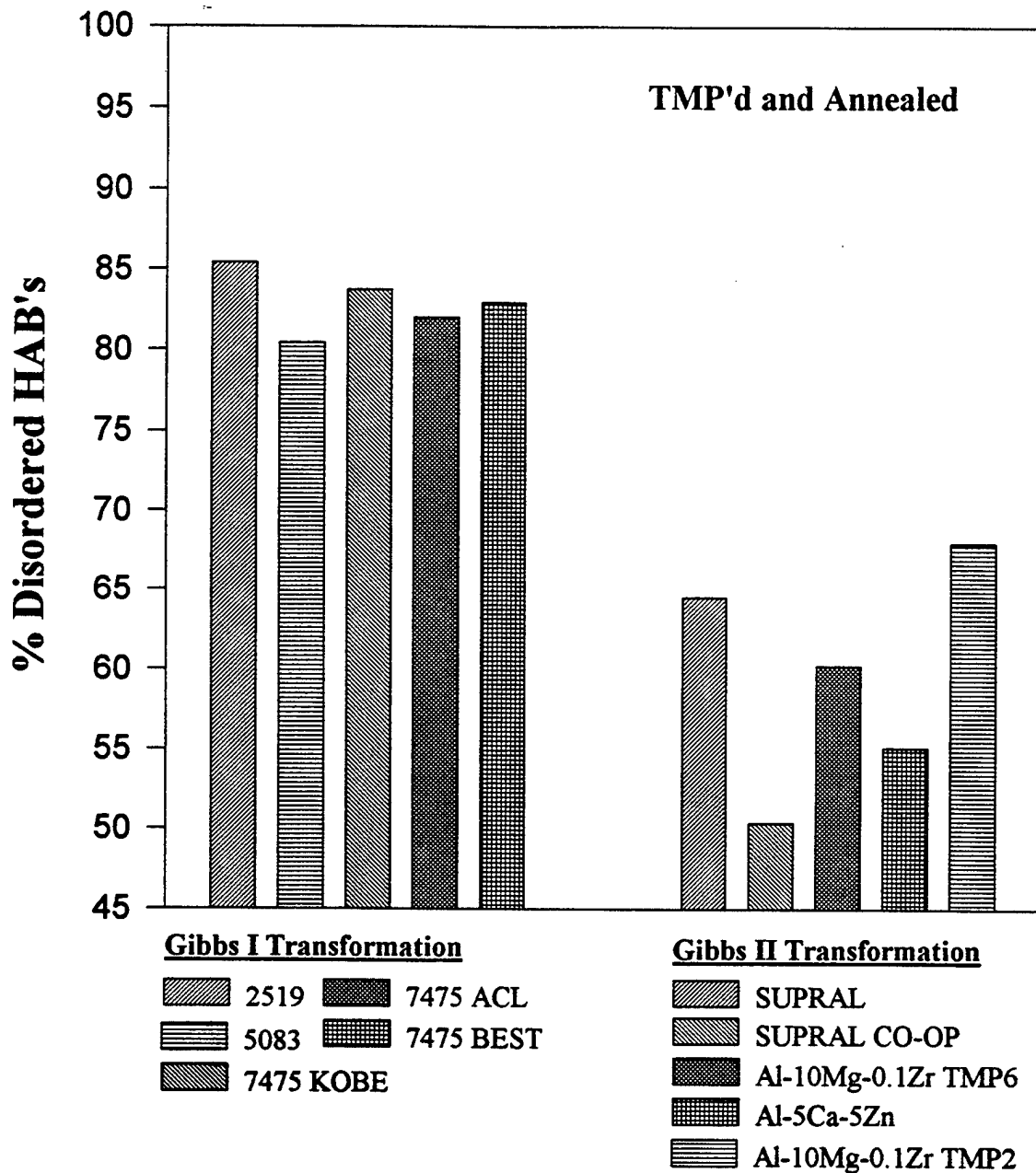


Figure 9.4. Histogram illustrating the population of disordered HAB's (>15 degrees and not near CSL relations up to $\Sigma 49$). Recrystallization mechanisms involving a Gibbs I type process result in microstructures consisting of predominantly disordered HAB's.

misorientation similar to that present in the random misorientation distribution of Mackenzie [Ref. 112].

The distribution of boundary misorientation following discontinuous recrystallization is observed to reflect the random distribution for the orientations present in the microstructure, or uncorrelated misorientation distribution, particularly in the lower misorientation ranges ($\theta \leq 20^\circ$). Figure 9.5 illustrates the ratio of the observed, correlated grain boundary misorientation distribution to the expected uncorrelated distribution for alloys examined. The data suggest that the large fraction of MMB's developed in continuously refined microstructures may not be explained by the differences in the preferred orientations when comparing deformation textures and recrystallization textures. These data indicate that MMB's developed are related to local reactions consistent with the short-range nature of Gibbs II reactions and continuous refinement processes. The data also emphasize that boundary misorientations present in the microstructures of materials transformed by discontinuous processes are near random in nature given the preferred orientation reflected in the uncorrelated misorientation distribution.

The overall fraction of boundaries near low-index CSL misorientations observed in materials examined in the as-processed condition is shown in Figure 9.6. Data for materials examined in other conditions is consistent with data in Figure 9.6. The *overall* fraction of boundaries near low-index CSLs does not vary significantly from random levels for any alloy. Based on these data there appears to be little significance of the *overall number* density of low-index CSL boundaries. Individual, twin-related CSL boundaries, particularly the first-order twin boundary, $\Sigma 3$, may be quite important in the mechanical behavior as evidenced in the test results of the Al-10%Mg-0.1Zr material processed with the shorter inter-pass anneal time (schedule TMP2). In that case, large differences in the superplastic elongation (compared to the TMP6 processed materials) were ascribed to the development of a large fraction of nearly immobile twin boundaries.

Based on qualitative observations during EBSP examination, significantly higher

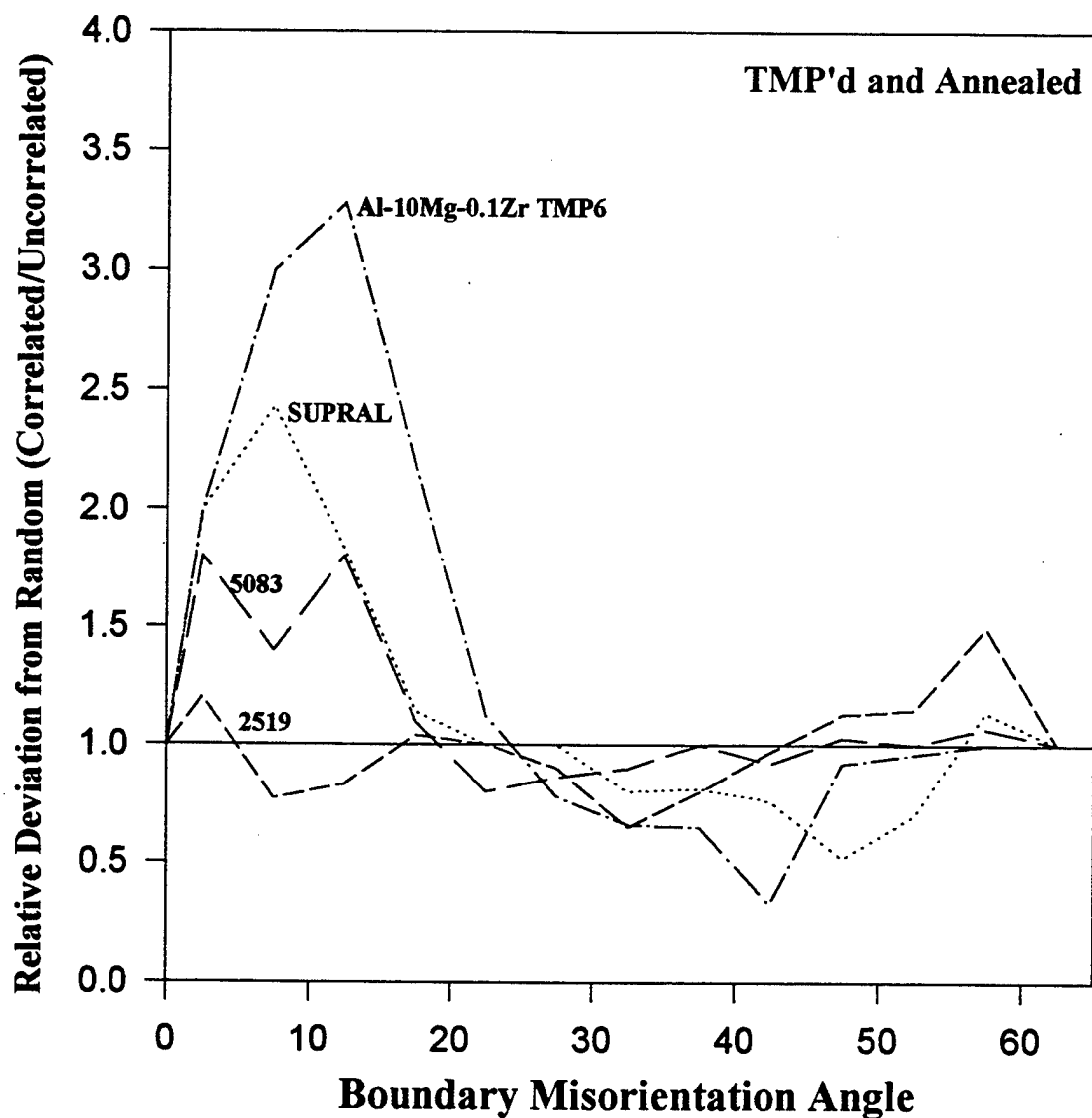


Figure 9.5. Graph of the ratio of the fraction of boundaries in the correlated data and the fraction in uncorrelated data versus misorientation angle. The uncorrelated data approximates the random distribution for the data set given the preferred orientation present. The deviation apparent in the excess number of MMB's following a Gibbs II-type transformation is indicative of mechanistic rather than random processes.

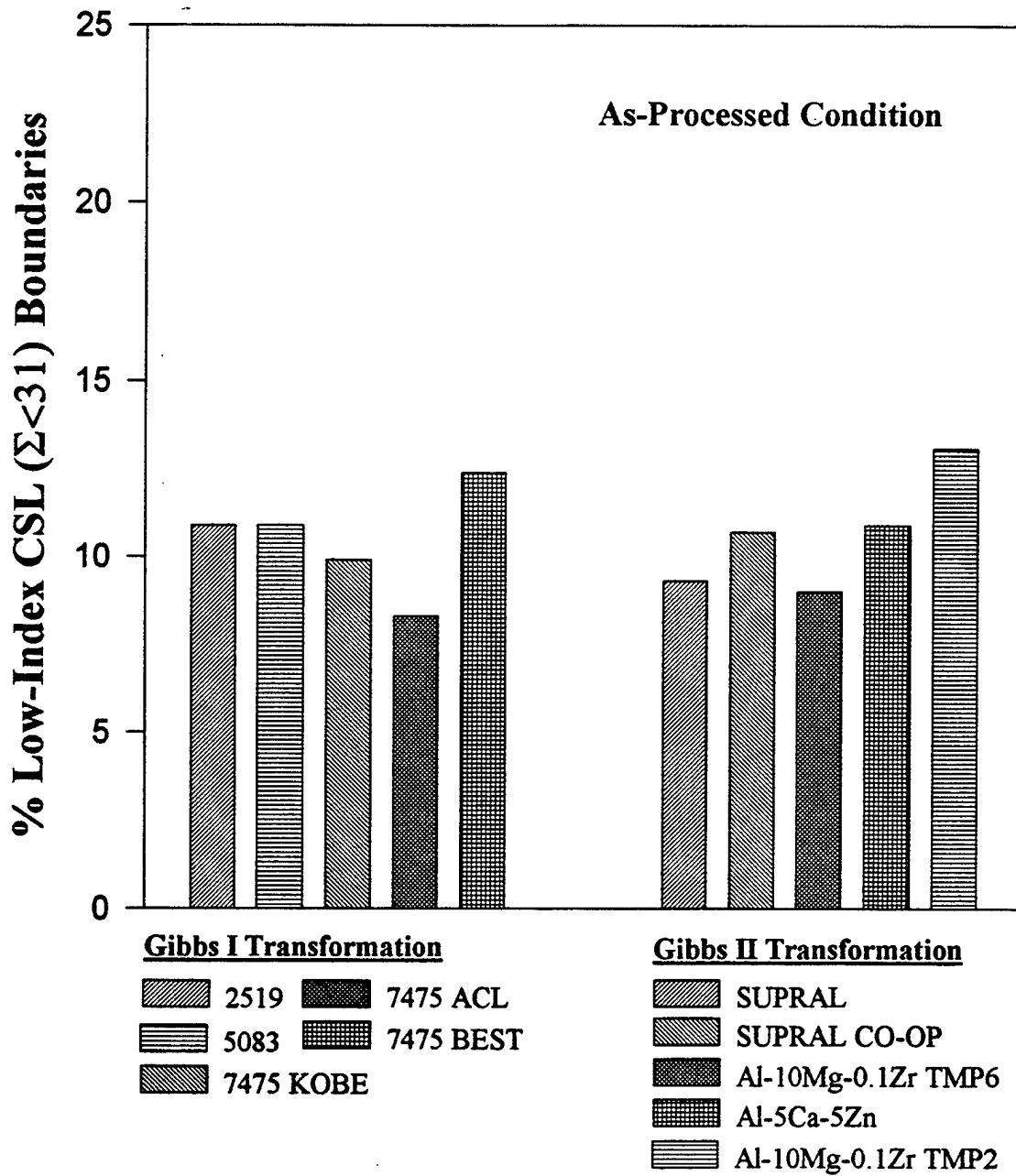


Figure 9.6. Histogram illustrating the population density of boundaries fulfilling the Brandon criterion for nearness to low-index CSL relations. The frequency of these boundaries was essentially unchanged in all alloys examined regardless of process condition or strain. Data for as-processed materials is shown here.

residual stored strain energy is present in materials transforming by continuous processes than exists in microstructures of discontinuously recrystallized materials. This is evident in the sharper, higher intensity diffraction images of the discontinuously recrystallized materials. The more complete reduction in stored strain energy following a Gibbs I process is also reflected in the higher interfacial energy character of the boundaries produced.

The alternate microstructures developed following Gibbs I and II transformations both appear to support superplastic deformation in the GBS regime (the influence of differences in the grain boundaries present on the GBS process is discussed in the next section). Grain refinement to a smaller grain size was postulated by Salama [Ref. 6] for continuous processes. Based on the data of this research, refinement to finer grain size may be facilitated in the case of continuous processes as the boundaries present would be expected to have more limited mobility and reduced tendency for static grain growth. Effective dispersion of pinning dispersoids is particularly important in the case when average boundary mobility is high.

B. GRAIN BOUNDARY EVOLUTION DURING SUPERPLASTIC FLOW

It has been previously widely accepted that a predominance of disordered, high angle boundaries is a prerequisite for extensive superplastic flow [Ref. 2, 22, 32]. However, the materials where micro- and mesotextural data indicate refinement by continuous processes shows that microstructures containing up to one-third MMB's in the boundary misorientation distributions exhibit extensive superplastic flow. Furthermore, this response is observed at lower deformation temperatures and higher strain rates than materials containing primarily disordered, high angle boundaries. Additionally, EBSP examination of superplastically deformed regions of materials deformed in the GBS regime shows that, regardless of the initial grain boundary misorientation distribution present in the refined, superplastically-enabled microstructures at the onset of GBS, following extensive GBS the misorientation distribution and boundary character evolve to a common misorientation distribution with

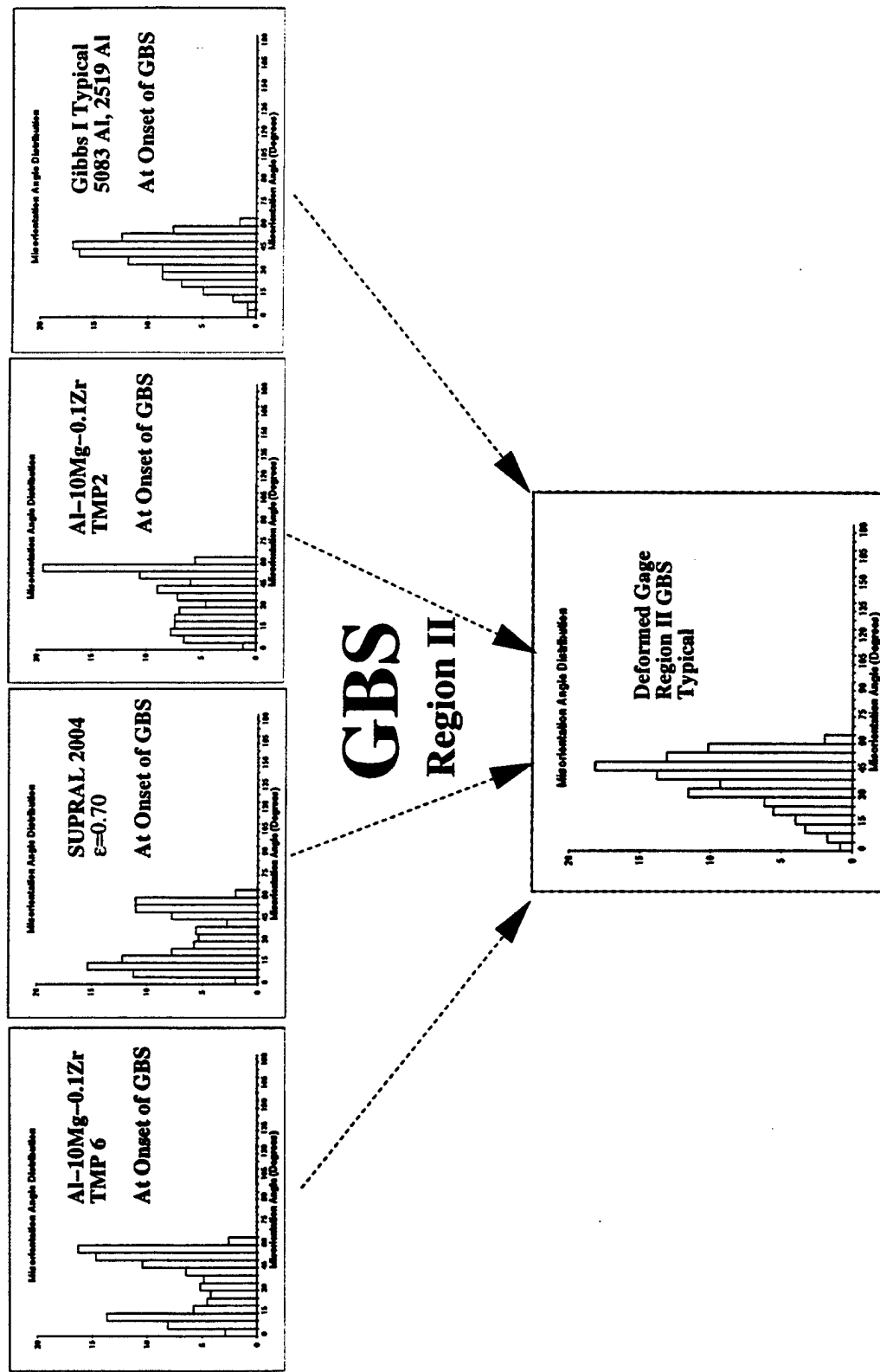


Figure 9.7. Grain boundary misorientation histograms of various superplastically-enabled microstructures near the onset of GBS are shown to transition to a common misorientation distribution following significant GBS in region II.

most boundaries possessing misorientations in the 35° to 50° range.

Figure 9.7 illustrates the evolution of grain boundary misorientations observed in materials from the onset of GBS and then following extensive superplastic flow with deformation conditions corresponding to region II. Here, GBS is thought to be responsible for most of the deformation and peak superplastic elongations are observed. In materials refined statically, the superplastically-enabled condition shown is a processed and briefly annealed condition (similar to duration of pre-heating to the SPF temperature). In SUPRAL 2004, where the transformation to a superplastic microstructure is observed to be strain-assisted, the onset of GBS was taken at a strain of $\epsilon=0.70$ where the microstructural refinement is thought to be complete (microtextural examination of material deformed to higher strains showed evidence of GBS as discussed earlier in Chapter V.). In each case the grain boundary misorientation distribution evolves to one similar to the random distribution predicted by Mackenzie. Randomization of the texture during GBS, previously reported [Ref. 108], was observed in these studies concurrent with the apparent randomization of the mesotexture.

Data from Hales, McNelley, and McQueen [Ref. 51] revealed that limited dynamic grain growth was observed in the Al-10%Mg-0.1Zr TMP6 processed material following superplastic deformation in the GBS regime (from a grain size of $\approx 2.0 \mu\text{m}$ in the undeformed grip region to $2.3 \mu\text{m}$ in the deformed gage region, all boundaries were included in the calculation). Therefore the evolution in the bi-modal misorientation distributions evident in the materials refined by Gibbs II-type reactions cannot be explained in simple terms of annihilation and coalescence of LAB's /MMB's and grain boundary shear along only disordered, HAB's ("hard" boundaries following Dingley and Pond [Ref. 29]). If that were the case the observed dynamic grain growth would be expected to be greater based on the high fraction of MMB's. Data suggest that GBS of the recovered microstructures (with a characteristic bi-modal distribution of grain boundary misorientation) present following a Gibbs II transformation proceeds readily at moderate superplastic deformation rates (10^{-3}s^{-1}

to 10^{-2}s^{-1}). Based on these data, the following comments and observations are made concerning GBS of these microstructures:

- Grain rearrangement to produce a boundary misorientation distribution similar to that evidenced in that of the deformed regions may occur immediately prior to the grain boundary shear process and GBS may then proceed in a uniform fashion, such as the sliding of individual grains as described by Raj and Ashby [Ref. 17]. Such rearrangement would not be expected to occur readily in microstructures typical of those observed following Gibbs II transformation. Additionally, such rearrangement would be expected to be identifiable in the microtextural data. Data from the isochronal study of deformed regions in SUPRAL 2004 presented in Chapter V illustrated that the bi-modal misorientation distribution of the (dynamically) refined microstructure persisted up to the onset of GBS, as evidenced by the commencement of randomization of the deformation texture.
- GBS may proceed in alternate manners, based on the ability to slide of the boundaries. In refined microstructures with a predominance of hard boundaries which are thought to slide readily [Ref. 30], sliding of individual grains may dominate the GBS process. This would be the case for grain boundary misorientation distributions observed following discontinuous (Gibbs I) processes. It is not possible to conclude that such sliding of individual grains is a slower process because of the disparity in grain size between the microstructures following Gibbs I and Gibbs II reactions. Theories describing superplastic flow in terms of grain boundary sliding as the rate-controlling process have been presented by Beere [Ref. 134].
- Grain rotations occurring during the GBS process may result in the coalescence of MMB's and the formation of new HAB's.
- Low-angle boundaries serve as effective sinks for dislocations produced during accommodation of the grain boundary shear and accommodation at grain junctions. The disappearance of LAB's following extensive GBS may be explained by coalescence

with migrating boundaries.

- The nearly random distribution of boundary character which is observed in all cases in regions following grain boundary sliding suggest that GBS is a turbulent process which does not likely occur in an orderly manner. Sliding by grain groups or cooperative grain boundary sliding (CGBS) [Ref. 135-136] may occur early in the GBS process but the homogenization of microtexture and mesotexture and the absence of LAB's and MMB's evident in deformed regions may indicate that such groups are subsequently broken-up following extensive GBS.
- In view of the significant change in the misorientation distribution observed in the materials microstructurally refined by Gibbs II-type transformations the GBS process may be viewed as a recrystallization mechanism in that the predominantly recovered microstructure is transformed into a microstructure with a grain boundary distribution characteristic of a Gibbs I transformation containing primarily high angle, disordered boundaries.

Figure 9.8 illustrates the evolution of grain boundary misorientation during deformation under conditions (higher strain rate or lower deformation temperature) outside of region II where a transformation to dislocation glide-controlled deformation becomes significant. The conditions for the Al-5%Ca-5%Zn material were a deformation temperature of 520°C and a strain rate of $1.0 \times 10^{-1} \text{s}^{-1}$. The conditions for the 2519 aluminum were a deformation temperature of 300°C and a strain rate of $1.0 \times 10^{-4} \text{s}^{-1}$ and the deformation conditions for the SKY5083 material were a deformation temperature of 535°C and a strain rate of $1.0 \times 10^{-1} \text{s}^{-1}$. Microtextural evidence of the early stages of formation of <100> fiber textures was observed in the deformed regions in these materials.

The distinguishing feature in the grain boundary misorientation distributions present here is the retention or build-up of still more LAB's and MMB's. This may be explained by the absence of extensive grain rotations associated with GBS which may consume LAB's. Dislocation glide processes may also result in the accumulation of gliding dislocations into

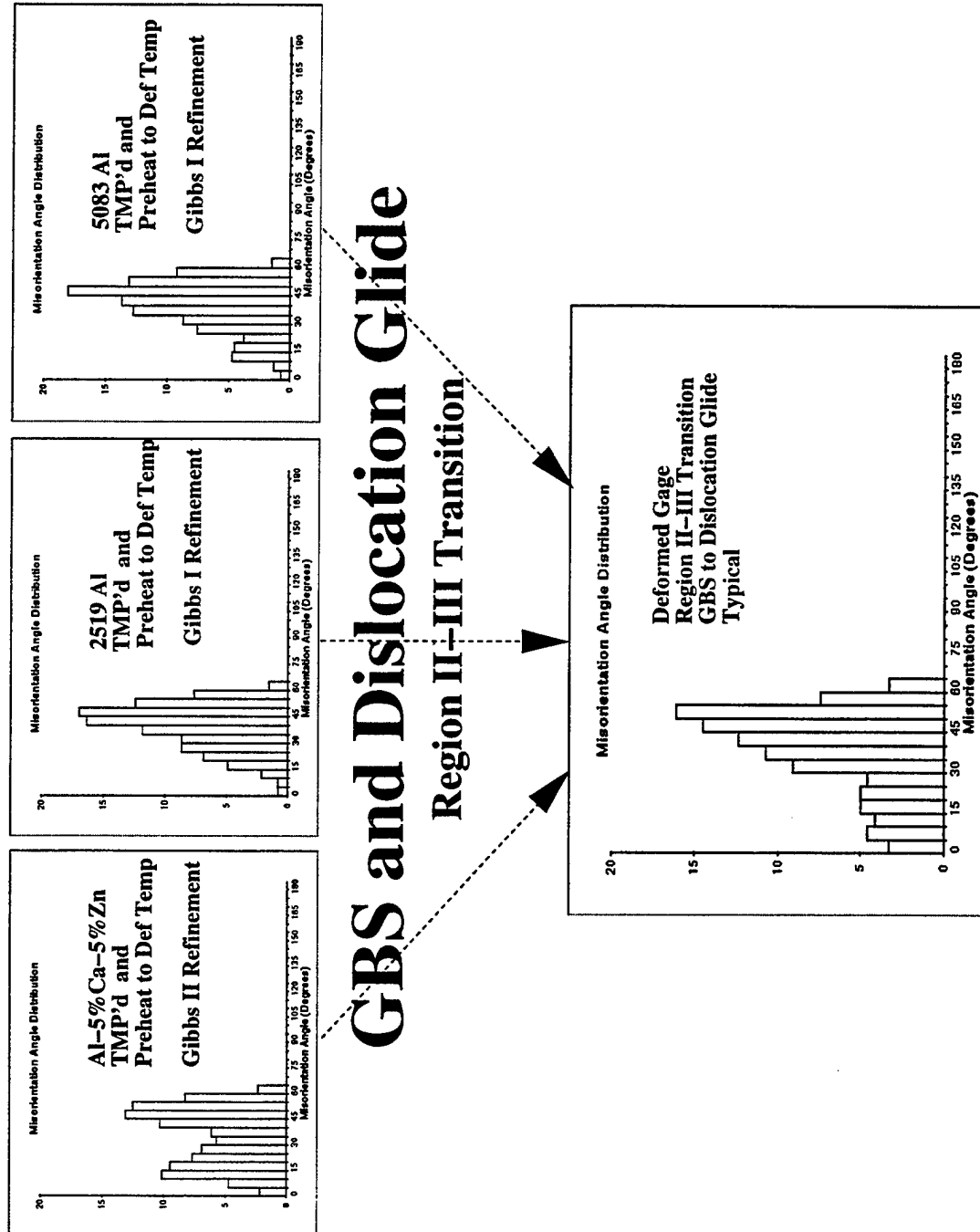


Figure 9.8. Grain boundary misorientation histograms of various superplastically-enabled microstructures are shown to transition to a common misorientation distribution following deformation conditions in the transition region II-III. A buildup or retention of LAB's and MMB's distinguishes the resulting misorientation distribution here from that for deformation in region II where GBS is thought to be primarily responsible for the deformation strain.

LAB dislocation arrays where subsequent climb and rearrangement of the dislocation arrays results in refinement of such networks, a decrease in the separation distance of dislocations and a resultant increase in boundary misorientation.

The overall fraction of grain boundaries satisfying Brandon criteria for nearness to low-index CSL relations does not vary significantly from random. Although variation in grain boundary sliding rates has been reported for some special HAB's, there was no evidence here that, with the exception of the twin boundary ($\Sigma 3$) which is known to be nearly immobile and not slide readily, such boundaries influence the GBS process in superplastic deformation of aluminum alloys. Twin boundaries, if present in a significant fraction, were shown to inhibit the deformation behavior in the Al-10%Mg-0.1Zr alloy, as discussed in Chapter IV.

X. CONCLUSIONS

1. Following the deformation stage of TMP for superplastic behavior, aluminum alloys 2519, 5083, and 7475 are observed to recrystallize by a heterogenous or discontinuous (Gibbs I type transformation) mechanism, by the formation and migration of high-angle boundaries. Grain boundaries developed following such a reaction are predominantly disordered, mobile, high-angle boundaries of high interfacial energy character. The grain boundaries are primarily 35° to 50° in misorientation and the overall grain boundary misorientation distribution follows the Mackenzie distribution for randomly oriented cubes. The high mobility of such boundaries may facilitate grain boundary sliding by individual grains; however, static grain growth due to rapid boundary migration limit superplastic elongations due to flow hardening.
2. Microstructural refinement in processed SUPRAL 2004 and Al-10wt%Mg-0.1wt%Zr materials is observed to follow a continuous, Gibbs II type transformation and to result in grain boundary distributions of lower interfacial energy character. The distributions contain significant fractions (≈ 0.25) of low-angle ($\theta \leq 5^\circ$) and moderately-misoriented ($5^\circ < \theta \leq 15^\circ$) boundaries. These grain boundary distributions are observed to be bi-modal, with peaks centered near 10° and 45° misorientation. The fractions of these boundaries exceed the expected values from random processes even given the preferred orientation present. These boundaries may therefore be attributed to short-range mechanisms involving dislocation-boundary and boundary-boundary interactions. The bi-modal character of the grain boundary misorientation distribution is observed to become more pronounced with static annealing. Enhanced grain refinement and increased superplastic elongations at higher deformation rates are observed for these processed alloys.
3. Alternate microstructures and distributions of grain boundaries present following Gibbs I or Gibbs II transformations support GBS processes in superplastic flow of aluminum alloys.

Following extensive superplastic elongations these different distributions of grain boundary misorientation, however, are observed to evolve to a common misorientation distribution which is similar to the random distribution predicted by Mackenzie. The randomization of mesotexture is observed to develop concurrent with the randomization of microtexture.

4. Evidence indicates that the moderately-misoriented grain boundaries developed during Gibbs II transformations are actually present as features of the DM prior to annealing. Such features include dislocation walls formed by entanglement and accumulation of dislocations with resulting misorientations corresponding directly to those of the LAB's and MMB's that become apparent upon annealing. These boundaries are observed in as-processed SUPRAL 2004 material, and were previously thought to develop by processes such as subboundary coalescence assisted by concurrent straining and resulting in a gradual increase in misorientation. Development of moderately-misoriented regions in the DM may be characteristic of continuous microstructural refinement processes.

5. There is no evidence that non-twin related, special grain boundaries near low-index CSL relations influence the microstructural refinement processes for superplastic aluminum alloys. Additionally, there is no evidence that non-twin related, low-index CSL grain boundaries influence the grain boundary sliding process for superplastic flow. A significant fraction of twin and near-twin grain boundaries may limit superplastic flow due to the restricted mobility of such boundaries in supporting accommodation processes for GBS.

LIST OF REFERENCES

1. Hamilton, C.H., "NATO-AGARD Lecture Series on Superplasticity", *Superplastic Sheet Forming*, No.168, pp. 2.1-2.24, 1989.
2. Sherby, O.D. and Wadsworth, J., "NATO-AGARD Lecture Series on Superplasticity", *Advances and Future Directions in Superplastic Materials*", No. 168, pp. 3.1-3.23, 1989.
3. Bengough, G.D., *Journal Institute of Metals*, Vol. 7, p. 123, 1912.
4. Rosenhain, W., Haughton, J.L., and Bingham, K.E., *Journal Institute of Metals*, Vol. 25, p. 261, 1920.
5. Pearson, C.E., *Journal of the Institute of Metals*, Vol. 54, p. 111, 1934.
6. Salama, A.A.S., *Analysis of Grain Refinement and Superplasticity in Aluminum-Magnesium Alloys*, Doctoral Dissertation, Naval Postgraduate School, Monterey, CA, December, 1987.
7. Underwood, E.E., *Journal of the Institute of Metals*, Vol. 14, p. 914, 1962.
8. Backofen, W.A., Turner, I.R., and Avery, D.H., *Transactions A.S.M.*, Vol. 57, pp. 981-989, 1964.
9. Avery, D.H. and Backofen, W.A., *Transactions A.S.M.*, Vol. 58, p. 551, 1965.
10. Alden, T.H., *Acta Metallurgica*, Vol. 15, pp. 469-480, 1967.
11. Lee D., *Acta Metallurgica*, Vol. 17, pp. 1057-1069, 1969.
12. Nabarro, F.R.N., *Proceedings on the Bristol Conference on Strength of Solids*, p. 75, 1948.
13. Herring, C., *Journal of Applied Physics*, Vol. 21, p. 437, 1950.
14. Coble, R.L., *Journal of Applied Physics*, Vol. 34, p. 1679, 1963.
15. Lifshitz, I.M., *Soviet Physics J.E.T.P.*, Vol. 17, p. 909, 1963.

16. Ball A. and Hutchison, M.M., *Metal Science Journal*, Vol. 3, pp. 1-7, 1969.
17. Raj, R. and Ashby, M.F., *Metallurgical Transactions A*, Vol. 2, pp. 1113-27, 1971.
18. Mukherjee, A.K., *Materials Science and Engineering*, Vol. 8, pp. 83-89, 1971.
19. Ashby M.F. and Verall, *Acta Metallurgica*, Vol. 21, pp. 149-163, 1973.
20. Gifkins, R. C., *Metallurgical Transactions A*, Vol. 7A, p. 1225, 1976.
21. Arieli, A. and Mukherjee, A.K., *Materials Science and Engineering*, Vol. 45, pp. 61-70, 1980.
22. Edington, J.W., *Metallurgical Transactions. A*, Vol. 13A, pp.703-715, 1982.
23. Haasen, P., *Metallurgical Transactions A*, Vol. 24A, pp. 1001-1015, 1993.
24. Haasen, P., *Proceedings on Recrystallization Conference, The Generation of New Orientations During Primary Recrystallization of Single Crystals*, TMS, pp. 17-26, 1990.
25. Humphreys, F.J., *Acta Metallurgica*, vol. 25, pp. 1323-1344, 1977.
26. Berger A., Wilbrandt P.J, Ernst F., Klement, U., and Haasen, P., *Progress in Materials Science*, Vol. 32, pp. 1-95, 1988.
27. Sutton, A.P. and Balluffi, R.W., *Acta Metallurgica*, Vol. 25, No. 9, pp. 2177-2201, 1987.
28. Wolf, D., *Journal Physique*, Vol. 46, pp. C4 -197, 1985.
29. Dingley, D.J. and Pond, R.C., *Acta Metallurgica.*, Vol. 27, pp. 667-682, 1979.
30. Pumphrey, P.H., *Grain Boundary Structure and Properties*, edited by D.A. Smith and G.A. Chadwick, Academic, New York, 1974.
31. Wadsworth, J. and Pelton, A.R., *Scripta Metallurgica*, Vol. 18, pp. 384-92, 1984.
32. Langdon, T.G., *Materials Science and Engineering*, Vol. A137, pp. 1-11, 1991.
33. INFORM, Company Literature, SUPERFORM, USA, Inc., Riverside, CA, Issue 2,

- 1996.
34. INFORM, Company Literature, SUPERFORM USA INC., Riverside, CA, Issue 1, 1996.
 35. INFORM, Company Literature, SUPERFORM USA, Inc. Riverside, CA, Issue 3, 1996.
 36. Lucas, G., Journal of Metals, Vol. 149, No. 5, pp. 29-30, 1996.
 37. McBride, J.K., Sanders, R.E., and Reavis, H.G., Journal of Metals, Vol. 48, No. 6, pp. 18-20, 1996.
 38. INFORM, Company Literature, SUPERFORM USA, Inc. Riverside, CA, Issue 4, 1996.
 39. Bampton, C.C. and Edington, J.W., Metallurgical Transactions A, Vol. 13A, pp. 1721-1727, 1982.
 40. Pilling, J. and Ridley, N., Acta metallurgica, Vol. 34, pp. 669-679, 1986.
 41. Tait, R.A. and Taplin, D.M.R., Scripta Metallurgica, Vol. 13, pp. 77-82, 1980.
 42. Mukherjee, A.K., Annual Review in Materials Science, Vol. 9, p. 191, 1979.
 43. Sherby, O.D., Caliguiri, R.D., Dayali, E.S., and White, R.A., *Advances in Metal Processing*, edited by J.J. Burke, R. Mehranlian and V. Weiss, p. 133, Plenum Press, 1981.
 44. Pearce, R., "NATO-AGARD Lecture Series on Superplasticity", *Superplasticity- An Overview*, No. 168, pp. 1.1-124, 1989.
 45. Grimes, R., "NATO-AGARD Lecture Series on Superplasticity", *The Manufacture of Superplastic Alloys*, No. 168, pp. 8.1-8.16, 1989.
 46. Watts B.M., Stowell M.J., Baile B.L., Owen D.G.E., *Metals Science Journal*, Vol. 10, No. 6, pp. 189-197, 1976.
 47. Paton, N.E., and Hamilton, C.H., US Patent 4 092 181, 1978.
 48. Wadsworth, J., Palmer, I.G., Crooks, D.D. and Lewis, R.E., Proceedings of the

Second International Al-Li Conference, edited by E.A. Starke and T.H. Sanders, p. 111, AIME, Warrendale, PA, 1983.

49. Pu, H.P., Liu, F.C., and Huang, J.C., *Metallurgical Transactions A*, vol. 26A, pp. 1153-1166, 1995.
50. McNelley, T.R., Michel, R.J., and Salama, A., *Scripta Metallurgica*, Vol. 23, pp. 1657-1662, 1989.
51. Hales, S.J., McNelley, T.R., and McQueen, H.J., *Metallurgical Transactions A*, Vol. 22A, pp. 1037-1047, 1991.
52. Crooks, R., Hales, S.J. and McNelley, T.R., *Microstructural Refinement via Continuous Recrystallization in a Superplastic Aluminum Alloy*, Proc. on Int'l. Conference on Superplasticity and Superplastic Forming, TMS, 1988.
53. McNelley, T.R., and Hales, S.J., *Grain Boundary Misorientation Distribution and Superplasticity in Al-10Mg-0.1Zr*, Conference on Superplasticity and Superplastic Forming, TMS, 1995.
54. Holloman, J.H., Transactions AIME, Vol. 162, p.268, 1945.
55. Sherby, O.D. and Burke, P.M. Progress Materials Science, Vol. 13, p. 325, 1967.
56. Weertman, J., Transactions AIME, Vol. 218, p. 207, 1960.
57. Wu, M.Y. and Sherby, O.D., Acta Metallurgica, Vol. 32, p. 1561, 1984.
58. Sherby, O.D. and Wadsworth, J., *Deformation Processing and Structure*, G.Krauss editor, American Society for Metals, Metals Park, OH, 1982.
59. McNelley, T.R., Salama, A.A., and Kalu, P.N., *Constitutive Equations for the Behavior of Superplastic Al-Mg Alloys*, Advances in Superplasticity and Superplastic Forming, N. Chandra, H. Garemetani, and R.E. Goforth editors, TMS, 1993.
60. Doherty, R.D., Gottstein, G., Hirsch, J., Hutchison, W.B, Lucke, K., Nes, E., and Wilbrandt, P.J., *Report on Panel on Recrystallization Textures: Mechanisms and Experiments*, ICTOM8, J.S. Kallend and G. Gottstein editors, TMS, 1988.
61. Doherty, R.D., *Theories of Nucleation and Growth During Recrystallization*, Proceedings on Third International Conference on Recrystallization, Monterey,

California, Pending Publication.

62. Hansen, N. and Juul Jensen, D., *Metallurgical Transactions A*, Vol. 17A, p. 253, 1986.
63. McNelley, T.R., Crooks, R., Kalu, P.N., and Rogers, S.A., *Materials Science and Engineering*, Vol. A166, p.135, 1993.
64. Li, J.C.M., *Recrystallization, Grain Growth and Textures*, H. Margolin editor, SAM, Metals Park, OH, 1966.
65. Humphreys, F.J., *Recovery, Recrystallization, and Grain Growth - Stability and Instability of Cellular Microstructures*, Proceedings on the Third International Conference on Recrystallization, 1996.
66. Nes, E., *Materials Science and Engineering*, Vol. 13, p. 2052, 1978.
67. Nes, E., *Materials Science and Engineering*, Vol. 13, p. 211, 1979.
68. McQueen, H.J., Knusstad, N.R., and Solberg, J.K., *Scripta Metallurgica*, Vol. 19, p. 73, 1985.
69. Beck, P.A., Sperry, P.R, and Hu, H., *Journal Appl. Physics*, Vol. 21, pp. 420, 1950.
70. Gottstein, G., *Acta Metallurgica*, Vol. 32, No. 7, pp. 1117, 1984.
71. Bishop, G.H. and Chalmer, B., *Scripta Metallurgica*, Vol. 133, No. 2, 1968.
72. Read, W.T. and Shockley, W., *Physics Review*, Vol. 78, p. 278, 1950.
73. Bragg, W.L., *Proceedings Physics Society*, Vol. 52, p. 54, 1940.
74. Burgers, W.G., *Proceedings Physics Society*, Vol. 52, p. 52, 1940.
75. Bollman, W., *Philosophical Mag.*, Vol. 16, p. 363, 1967.
76. Brandon, D.G., *Acta Metallurgica*, Vol. 14, pp. 1479, 1966.
77. Dechamps, M., Baribier, F., and Marrouche, A., *Acta Metallurgica*, Vol. 35, No.1, p. 101, 1987.

78. Ishida, Y. and McLean, M., *Philosophical Mag.*, Vol. 27, p. 1125, 1973.
79. Grimmer, H., Bollman, W., and Warrington, D.H., *Acta Crystallogr.*, Vol. 30, p. 197, 1974.
80. Warrington, D.H. and Boon, M. *Acta Metallurgica*, Vol. 23, p. 599, 1975.
81. Goodhew, P.J., *The Relationship Between Grain Boundary Structure and Energy, Grain Boundary Structure and Kinetics*, R.W. Balluffi editor, ASM, Metals Park, OH, 1979.
82. Watanabe, T., Fuji, H., Oikawa, H., and Arai, K.J., *Acta Metallurgica*, Vol. 37, p. 941, 1989.
83. Furley, J. and Randle, V., *Materials Science and Technology*, Vol. 7, p. 12, 1991.
84. Inman, M.C. and Tipler, H.R., *Metallurgical Review*, Vol. 8, p. 105, 1963.
85. Hasson, G. and Goux, C., *Scripta Metallurgica*, Vol. 5, p. 889, 1971.
86. Sutton, A.P. and Baluffi, R.W., *Acta Metallurgica*, Vol. 25, No. 9, p. 2177, 1987.
87. Frank, F.C., *Symposium on Plastic Deformation of Crystalline Solids*, Pittsburgh, PA, p. 150, 1950.
88. Wilbrandt, *On The Mechanisms of Twinning in the Annealing Texture Formation*, ICTOM8, J.S. Kallend and G. Gottstein editors, TMS, p. 573, 1988.
89. Aust, K.T. and Rutter, J.W., *Transactions AIME*, Vol. 215, p. 820, 1959.
90. Shewmon, P.G., *Recrystallization, Grain Growth and Textures*, p. 165, H. Margolin editor, SAM, Metals Park, OH, 1966.
91. Clark, M.A. and Alden, T.H., *Acta Metallurgica*, Vol. 21, p. 1195, 1973.
92. Biscondi M and Goux, C., *Mem. Science Review Metals*, Vol. 65, p. 167, 1968.
93. Weinberg, F., *Transactions AIME*, Vol. 212, p. 808, 1958.
94. Randle, V., *Acta Metallurgica*, Vol. 43, No.5, p. 1741, 1995.

95. Cullity, D.D., *Elements of X-Ray Diffraction*, Addison-Wesley, Reading, Mass., 1978.
96. Alam, M.N., Blackman, M., and Pashley, D.W., *Proceedings of the Royal Society*, Vol. 221A, p. 224, 1954.
97. Daaland, O. and Nes, E., *Acta Metallurgica*, Vol. 44, No.4, p. 1389, 1996.
98. Dingley, D.J., *Scanning Electron Microscopy*, Vol. 11, p. 74, 1984.
99. Randle, V., Ralph, B., and Dingley, D.J., *Acta Metallurgica*, Vol. 36, p. 267, 1988.
100. Humphreys, F.J., *Experimental Technology for Microtexture Determination*, Eighth International Conference on Texture in Metals, J.S. Kallend and G. Gottstein editors, TMS, 1988.
101. Course Literature, Orientation Imaging Academy, Tex Sem Laboratories, Inc., Provo, Utah, 1995.
102. Wright, S.I., Adams, B.L., and Kunze, K., *Metallurgical Transactions A*, Vol. 24A, p. 819, 1993.
103. Randle, V., *Microtexture Determination and Its Applications*, The Institute of Metals, London, UK, 1992.
104. Skjervold, S.R. and Ryum, N., *Acta Metallurgica*, Vol. 43, No. 8, p. 3159, 1995.
105. McNelley, T.R. and McMahon, M.E., *Journal of Metals*, Vol. 46, p. 58, 1996.
106. Voort, G.F.V., *Mettalography-Principles and Practice*, McGraw-Hill, NY, 1984.
107. Bunge, H.J., *Texture Analysis in Materials Science*, Butterworths, London, UK, 1982.
108. Bricknell, R.H. and Edington, J.W., *Acta Metallurgica*, Vol. 27, No. 8, p. 1303, 1979.
109. Matthies, S. and Vinel, G.W., *Physica Status Solidi*, Vol. 112, p. 111, 1982.
110. Hatherly, M. and Hutchinson, W.B., *An Introduction to Texture in Metals*, The Institute of Metals, Monograph No. 5, London, UK, 1979.

111. Wright, S.I. and Adams, B.L., *Textures and Microstructures*, Vol. 12, p. 65, 1990.
112. Mackenzie, J.K., *Biometrika*, Vol. 45, p. 229, 1958.
113. Kronberg, M.L. and Wilson, H.F., *Transactions AIME*, Vol. 85, p. 501, 1949.
114. Hirsch, J. and Lucke, K., *Acta Metallurgica*, Vol. 36, No. 11, p. 2883, 1988.
115. Barrett, C.S. and Massalski, J.B., *Structure of Metals*, McGraw-Hill, NY, 1966.
116. Berger, A., Wilbrandt, P.J., Ernst, F., Klement, U., and Haasen, P., *Progress Materials Science*, Vol. 37, p. 1, 1988.
117. Orsund, R. and Nes, E., *Scripta Materialia*, Vol. 23, p. 1187, 1989.
118. Kassner, M.E. and McMahon, M.E., *Metallurgical Transactions A*, Vol. 18A, p. 835, 1987.
119. Kim, W.J, Taleff, E., and Sherby, O.D., *Scripta Materialia*, Vol. 32, No. 10, p. 1625, 1995.
120. Pu, H.P., Lui, F.C., and Huang, J.C., *Metallurgical Transactions A*, Vol. 26A, p. 1153, 1995.
121. Kallend, J.S., and Davies, G.J., *Texture*, Vol. 1, p. 51, 1972.
122. Juul-Jensen, D., *Acta Metallurgica*, Vol. 43, No. 11, p. 4117, 1995.
123. Peet, B., *Thermomechanical Processing of an Al Alloy 2519 and an Assessment of Its Superplastic Response*, Masters Thesis, Naval Postgraduate School, Monterey, CA, March, 1995.
124. Stancy, S., *Assessment of Grain Refinement by Microtexture Analysis in Thermomechanically Processed Al Alloy 2519*, Masters Thesis, Naval Postgraduate School, Monterey, CA, December, 1995.
125. Zohorsky, P., *Study of Precipitation and Recrystallization in Al Alloy 2519 by Backscattered Electron Imaging Methods*, Masters Thesis, Naval Postgraduate School, Monterey, CA, March, 1995.
126. Nes, E., Vatne, H.E., Daaland O., Furu, T., Orsund, R., and Marthinsen, K.,

Physical Modelling of Microstructural Evolution during Thermomechanical Processing of Aluminum Alloys, Proceedings of the Fourth International Conference on Aluminum Alloys, T.H. Sanders and E.A. Starke editors, GIT, Atlanta, 1994.

127. A.J. Barnes, Private Communications, Superform, USA, Inc., 1996.
128. Verma, R., Friedman, P.A., Ghosh, A.K., Kim, S. and Kim, C., *Metallurgical Transactions A*, Vol. 27A, p. 1889, 1996.
129. Hamilton, C.H., Bampton, C.C., and Paton, N.E., *Superplastic Forming of Structural Alloys*, TMS-AIME, Warrendale, PA, 1982.
130. McNelley, T.R., Lee, E.W., and Mills, M.E., *Metallurgical Transactions A*, Vol. 17A, p. 1035, 1986.
131. Sato, F., Gemba, K., and Kuribayashi, K., *Effect of Pre-Deformation on Continuous Recrystallization in 7475 Al Alloy*, Superplasticity in Aluminum Materials, S. Hori, M. Tokizane, and N. Furushiro editors, JSRS, Tokyo, 1991.
132. Sakai, T., and Miura, H., *Microstructural Evolution During Dynamic Recrystallization in Bicrystalline or Polycrystalline Materials*, Hot Workability of Steels and Light Alloy-Composites, H.J. McQueen, E.V. Konopleva, and N.D. Ryan editors, TMS-CIM, Montreal, 1996.
133. Perez-Prado, T., Unpublished Research, CSIC, Madrid, Spain, August, 1996.
134. Beere, W., *Journal of Materials Science*, Vol. 12, p. 2093, 1977.
135. Zelin, M.G. and Mukherjee, A.K., *Journal of Materials Science*, Vol. 13, p. 1258, 1994.
136. Zelin, M.G., Dunlap, M.R., Rosen, R., and Mukherjee, A.K., *Journal of Applied Physics*, Vol. 74, No. 8, p. 4972, 1993.

INITIAL DISTRIBUTION LIST

1. Defense Technical Information Center.....2
8725 John J. Kingman Rd., STE 0944
Ft. Belvoir, Virginia 22060-6218

2. Dudley Knox Library.....2
Naval Postgraduate School
411 Dyer Road
Monterey, California 93943-5101

3. Mr. A.J. Barnes.....1
Superform USA, Inc.
P.O. Box 5375
Riverside, California 92517-5375

4. Dr. Steven J. Hales.....1
NASA-Langley Research Center
M/S 188A
Hampton, Virginia 23681

5. Prof. T.R. McNelley.....2
Code ME/Mc
Naval Postgraduate School
700 Dyer Road
Monterey, California 93943-5000

6. Special Agent Thomas P. McMahon.....1
6253 South Cook Drive
Littleton, Colorado 80121

7. Professor Amiya K. Mukherjee.....1
University of California
Department of Chemical Engineering and Materials Science
Davis, California 95616-5294

8. CDR. Michael E. McMahon.....2
6253 So. Cook Drive
Littleton, Colorado 80121

9. Prof. Alan G. Fox.....1
Code ME/Fx
Naval Postgraduate School
700 Dyer Road
Monterey, California 93943-5000
10. Prof. M.E. Kassner.....1
Department of Mechanical Engineering
Rogers Hall-204
Oregon State University
Corvallis, Oregon 97331